



UNIVERSITAT DE  
BARCELONA

# The Central Asia collision zone: numerical modelling of the lithospheric structure and the present-day kinematics

Lavinia Tunini



Aquesta tesi doctoral està subjecta a la llicència **Reconeixement- NoComercial – SenseObraDerivada 3.0. Espanya de Creative Commons.**

Esta tesis doctoral está sujeta a la licencia **Reconocimiento - NoComercial – SinObraDerivada 3.0. España de Creative Commons.**

This doctoral thesis is licensed under the **Creative Commons Attribution-NonCommercial-NoDerivs 3.0. Spain License.**

# **The Central Asia collision zone: numerical modelling of the lithospheric structure and the present-day kinematics**

Ph.D. thesis presented at the Faculty of Geology of the University of Barcelona  
to obtain the Degree of  
Doctor in Earth Sciences

Ph.D. student:

**Lavinia Tunini**<sup>1</sup>

Supervisors:

**Dra. Ivone Jiménez-Munt**<sup>1</sup>

**Prof. Dr. Manel Fernández Ortiga**<sup>1</sup>

Tutor:

**Prof. Dr. Juan José Ledo Fernández**<sup>2</sup>

<sup>1</sup> Institute of Earth Sciences Jaume Almera

<sup>2</sup> Department of Geodynamics and Geophysics of the University of Barcelona



This thesis has been prepared at the  
Institute of Earth Sciences Jaume Almera  
Consejo Superior de Investigaciones Científicas (CSIC)

March 2015

Alla mia famiglia

La natura non ha fretta, eppure tutto si realizza. – Lao Tzu



## Agradecimientos

En mano tenéis un trabajo de casi 4 años, 173 páginas que no hubieran podido salir a luz sin el apoyo de quienes me han ayudado durante este camino, permitiendo acabar la Tesis antes que la Tesis acabase conmigo.

En primer lugar quiero agradecer mis directores de tesis, Ivone Jiménez-Munt y Manel Fernández. Gracias por haberme dado la oportunidad de entrar en el proyecto ATIZA, de aprender de la modelización numérica, de participar a múltiples congresos y presentaciones, y, mientras, compartir unas cervezas. Desde el primer año, desde el máster, con todas esas reuniones semanales, me habéis enseñado a investigar concentrándome en el objetivo, a focalizarme en cada paso para llevar a cabo el proyecto y a no perder el ánimo cuando una revisión duraba más de lo previsto. También me habéis dado muchas recomendaciones para escribir un paper en la mejor manera posible y a darle la importancia adecuada a cada palabra, y aunque sé que ahora mismo estáis deseando que ponga un punto o una coma más, os quiero decir que seguiré intentando escribir frases menos “a la italiana”. Ivone, quiero agradecerte también todas las veces que, con tu calma y sonrisa, has conseguido infundirme ánimos, calmar los nervios y seguir adelante, y por las barbacoas y comidas en tu casa que me han hecho sentirte aún más cercana. Espero que estés contenta de esta experiencia como directora y que te lleves un buen recuerdo de tu primera estudiante de doctorado. Manel, gracias por todo el tiempo dedicado, por los consejos y por evitar que transmitiera mi estrés a los papers, que no es bueno.

Gracias también a Juan José Ledo Fernández, por haber aceptado ser el tutor de esta Tesis y haber seguido el trabajo desde el principio, y a Juan Carlos Afonso, por darme la oportunidad de hacer una estancia provechosa en Australia y permitirme utilizar el LitMod, el programa que ha permitido el desarrollo de buena parte de esta Tesis.

Big thanks also to Peter Bird, for allowing me to use his SHELLS program and for being there every time we needed an advice.

Agradezco también el ICTJA y al CSIC por poner a mi disposición la infraestructura para desarrollar la Tesis y a todo el personal del departamento e del Instituto.

En particular, quiero agradecer a Jaume Vergés. Jaume, gracias no solo por todo lo que me has enseñado científicamente sino también porque me has hecho creer en mi trabajo en un momento en el que había perdido la confianza.

Un gracias gigante a mis compañeros de despacho, si, a ambos, Alberto y Yan. Gracias por el soporte moral, por aguantar mis altibajos y por todas las conversaciones a puerta cerrada del despacho 300. Ánimo que os falta poco a vosotros también.

Gracias a otros compañeros o ex-compañeros del Jaume Almera, con los cuales he compartido momentos de todo tipo dentro y fuera del centro, y con algunos también dentro y fuera de España: Mar, Vinyet, Charlotte, Laura, Giovanni, Sofia, Juan, Stefania, Alexandra, Erika, Emilio, Daniel, Ana, Mireia, Candela, Chusa, Beatriz, Guiomar, Raquel, Helena, Siddique, Massimiliano, Stephanie, Juandi, Israel. Gracias por el Thanks God is Friday, por esa copa, ese café, esa fiesta, esos whatsapp cuando estaba en la tierra de los canguros, ese viaje, la convivencia en ese piso, los findes en el Almera desierto aparte de nosotros. Gracias

por esas muchas cosas que han enriquecido los años vividos en Barcelona más allá del doctorado.

Un gracias enorme a mis hermanas de Barcelona (aunque, precisamente, de Barcelona no son), que han compartido este viaje conmigo desde el principio: Ileana, Alba y Chiara. Sé que os tendré siempre en mi vida, en cualquier lugar que nos encontremos en el futuro. Ai miei amici sparsi qui e là, con i quali, mi basta una telefonata ed è come se ci fossimo visti ieri. A mis amigos esparcidos por el mundo con los cuales me basta una llamada y es como si nos hubiéramos visto ayer. Francesco, Laura, Elisa, Alicia, Marta, Vanessa, gracias, por los ánimos y por estar siempre ahí. Ai miei amici di sempre, che ogni volta che tornavo a casa mi han fatto sentire come se non fossi mai partita.

In ultimo, ma al primo posto per me, un grazie speciale alla mia famiglia, che mi ha sempre dato supporto in ogni decisione, mi ha insegnato a seguire la mia strada e a non mollare mai. A voi, che bene o male avete dovuto ingerire un bel po' del dietro le quinte del mio lavoro, è dedicata questa Tesi.

## **Funding:**

The author of this Thesis has benefited from a four-year FPI grant awarded by the Spanish Government between 2010 and 2014. The FPI was supported by the ATIZA project, which was funded by the Ministerio de Economía y Competitividad with reference CGL2009-09662-BTE. The author was also granted within the framework of the EEBB (short-term stays) with a 2-month stay at GEMOC ARC National Key Centre, Macquarie University (Sydney, Australia) from 1<sup>st</sup> June to 31<sup>st</sup> July 2012.

# CONTENTS

Summary	v
<b><u>Part I: Introduction and geological framework</u></b>	<b>1</b>
<b>Chapter 1: General Introduction</b>	<b>3</b>
1.1 Background and motivation	3
1.2 Objectives	7
<b>Chapter 2: Geological setting</b>	<b>9</b>
2.1 Central Asia	9
2.2 The Arabia-Eurasia collision zone	10
2.3 The India-Eurasia collision zone	14
2.4 The Arabia-India inter-collision zone	17
<b><u>Part II: Present-day lithospheric structure</u></b>	<b>21</b>
<b>Introduction</b>	<b>23</b>
<b>Chapter 3: Method: The integrated geophysical-petrological modelling</b>	<b>24</b>
3.1 Mantle temperature distribution	25
3.2 Mantle thermal conductivity	26
3.3 Densities	28
3.4 Potential fields	29
3.5 Mantle seismic velocities	30
3.6 Elevation	30
3.7 Sub-lithospheric anomalies	31
3.8 Mantle characterization	31
<b>Chapter 4: The Zagros orogen</b>	<b>38</b>
4.1 Data	40
4.1.1 Regional geophysical data	40
4.1.2 Crustal structure and depth to the Moho	42

4.1.3	Depth to the lithosphere-asthenosphere boundary	44
4.1.4	Mantle seismic velocities	44
4.1.5	Lithospheric mantle composition	46
4.2	Results	48
4.2.1	Crustal structure	49
4.2.2	Lithospheric mantle structure	49
4.2.1	Changing the lithospheric mantle composition	58
4.3	Discussion	60
4.3.1	Geophysical-petrological versus pure-thermal approaches	60
4.3.2	Crustal geometry	61
4.2.1	LAB geometry and compatibility with tomography models	62
4.4	Concluding remarks	63
<b>Chapter 5: The Himalaya-Tibetan orogen</b>		<b>65</b>
5.1	Data	67
5.1.1	Regional geophysical data	67
5.1.2	Previous studies on the crustal and lithospheric mantle structure	69
5.1.3	Upper mantle P-wave tomography	73
5.2	Results and discussion	74
5.2.1	Crustal structure	74
5.2.2	Lithospheric mantle structure	78
5.2.3	Mantle seismic velocities	81
5.2.4	Lithospheric structure variations along the strike of the Himalaya-Tibetan orogen	83
5.3	Concluding remarks	89
<b>Part III: Neotectonic modelling of Central Asia</b>		<b>91</b>
<b>Introduction</b>		<b>93</b>
<b>Chapter 6: Method and model construction</b>		<b>96</b>
6.1	Model domain and faults	97
6.2	Model inputs. Lithosphere and thermal structure	100

6.3	Plate motion and boundary conditions	102
6.4	Model constraints	104
<b>Chapter 7: Results</b>		<b>109</b>
7.1	Reference model	109
7.2	Change in the rheological parameters	115
7.3	Change of the lithospheric mantle thickness in NE-Tibet	119
7.4	Changing the velocity conditions in the south-eastern boundary	123
<b>Chapter 8: Discussion and concluding remarks</b>		<b>129</b>
8.1	Discussion	129
8.2	Concluding remarks	133
<b><u>Part IV: General conclusions</u></b>		<b>135</b>
<b>Chapter 9: General conclusions</b>		<b>137</b>
<b>List of figures and tables</b>		<b>143</b>
<b>References</b>		<b>151</b>



## Summary

The Central Asia region is dominated by one of the largest areas of distributed deformation on Earth, which spans eastern Turkey, northern Middle East, central and south-eastern Asia, covering the central and eastern sectors of the Alpine-Himalayan mountain belt. It is composed by the Zagros orogen in the western sector and the Himalaya-Tibetan orogen in the eastern sector, which are the results of the subduction of the Tethys oceanic lithosphere towards the NNE and the subsequent collisions between Arabia and India plates with the Eurasia plate during the Cenozoic. The strong and resistant Archean-to-Proterozoic shields of Arabia and India plates collided with the complex mosaic structure of the Eurasian ancient margin, which was formed by different Gondwana-derived continental blocks accreted by Late-Mesozoic time. The collisions resulted in tectonic escapes toward lateral regions (in Anatolia and south-eastern Asia), oblique convergence in the Zagros fold-and-thrust belt, the formation of the Makran accretionary wedge, convergence in the Hindukush, shortening in the Himalaya, Karakorum and Tibetan Plateau, and the development of two syntaxis at the edge of the Indian sub-continent. In addition, the Zagros and Himalaya-Tibetan orogens are excellent examples of diffused deformation, with wide deforming areas in the continent interiors, and the development of other mountain belts further north with respect to the Arabia-Eurasia and India-Eurasia suture zones, such as Caucasus, Alborz, Kopet Dagh, Pamir and Tian Shan mountains.

The lithosphere structure plays an important role in controlling the surface deformation and its propagation to the continental interiors. The compositional and strength heterogeneities within the lithosphere directly affect to the tectonic behaviour of the region and, hence, to the evolution of the orogenic systems. This thesis focalizes on the characterization of the present-day lithospheric structure of the Zagros and the Himalayan-Tibetan orogens and the role of the lithospheric structure and rheology in the accommodation of the deformation related to the Arabia and India convergence against Eurasia.

By combining geophysical and petrological information, the crust and upper mantle of the Zagros and the Himalaya-Tibetan orogens have been characterized from the thermal, compositional and seismological point of view. Four 2-D lithospheric profiles (two crossing the Zagros orogen and other two crossing the Himalaya-Tibetan orogen) have been modelled down to 400 km depth, in which the resulting crust and upper mantle structure are constrained by available data on elevation, Bouguer anomaly, geoid height, surface heat flow and seismic data including tomography models. In the Zagros orogen, the results on the crustal thickness show minimum values beneath the Arabia platform and Central Iran (42-43 km), and maximum values beneath the Sanandaj Sirjan Zone (55-63 km), in agreement with seismic data. Major discrepancies in Moho depth from those derived from seismic data are locally found in the Sanandaj Sirjan Zone (central Zagros) and Alborz Mountains where more moderate crustal thicknesses are modelled. Results on the lithosphere thickness indicate that the Arabian lithosphere is ~220 km thick along both profiles, whereas the Eurasian

lithosphere is up to ~90 km thinner, especially below the Central Iran and Alborz Mountains. The lithosphere-asthenosphere boundary (LAB) shows different geometries between the two transects. In the northern profile (northern Zagros), the LAB rises sharply below the Sanandaj Sirjan Zone in a narrow region of ~90 km, whereas in the southern profile (central Zagros), rising occurs in wider region, from the Zagros Fold-and-Thrust Belt to the Sanandaj Sirjan Zone. The best fit of seismic velocities ( $V_p$ ,  $V_s$ ) and densities requires lateral changes in the lithospheric mantle composition. Our results are compatible with Proterozoic peridotitic mantle compositions beneath the Arabian Platform, Mesopotamian Foreland Basin and the accreted terrains of Eurasia plate, and with a more depleted Phanerozoic harzburgitic-type mantle composition below the Zagros Fold-And-Thrust Belt and Imbricated Zone.

In the Himalaya-Tibetan orogen, the results show a Moho depth of ~40 km beneath the western Himalayan foreland basin, progressively deepening north-eastwards to ~90 km below the Kunlun Shan. Tarim Basin and Tian Shan show a nearly flat crust-mantle boundary at 50-65 km depth. The lithosphere-asthenosphere boundary lies at 260-290 km depth below the western Himalaya and Tibetan Plateau, Tian Shan and Altai Range, and it shallows to ~230 km depth below the southern Tarim Basin and to ~170 km below the Junggar region. The north-eastern Tibetan Plateau is underlined by a thinner lithosphere (LAB depth at ~120 km) with respect to its southern sector (LAB depth at ~280 km), confirming the results of previous 2D-geophysical integrated models carried out in this region. The modelled lithospheric mantle composition is generally compatible with a lherzolithic mantle-type, slightly changing to a more undepleted composition in the deep lithosphere beneath the Tarim Basin due to metasomatism. However, the mantle beneath Tian Shan, Junggar region and Altai Range is characterized by a FeO-MgO-rich composition, likely related to subduction slab-derived fluids, and the north-eastern Tibetan Plateau is highly depleted in MgO and enriched in FeO,  $Al_2O_3$  and CaO, as retrieved by xenolith samples. Our results of the geophysical-petrological study finally suggest that the Himalaya-Tibetan orogen is supported by a thick buoyant lithospheric mantle in the western profile and by a lithospheric mantle thinning in the north-eastern sector of the Tibetan Plateau along the eastern profile.

The combination of the present-day lithospheric structure of the Zagros and the Himalaya-Tibetan orogens with plate kinematics, geodetic observations and stress data allowed investigating the neotectonic deformation related to the collision of the Arabia and India plates against Eurasia. A geodynamic modelling technique based on the thin-sheet approximation has been used for this purpose. The crustal and lithospheric mantle thickness has been inferred from previous studies based on the combination of geoid and elevation data and thermal analysis. The surface velocity field, stress directions, tectonic regime and strain distribution are calculated after imposing velocity condition at the model boundaries and rheological parameters at the crust and lithospheric mantle.

The results allow obtaining a first order approximation of the velocity field and of the stress directions in the whole Central Asia, reproducing the counter-clockwise rotation of Arabia and Iran, the westward escape of Anatolia, and the eastward extrusion of the northern Tibetan Plateau by only imposing the convergence of Arabia and India plates respect to the

fix Eurasia. The simulation of observed extensional tectonics within the Tibetan Plateau requires, instead, a weaker lithosphere, which can be provided by i) a change in the rheological parameters or ii) reducing the lithosphere thickness in the NE-Tibet. Furthermore the temperature increase generated by the lithospheric thinning in the NE-Tibet would permit to reconcile the model with the high heat flow values and the low mantle seismic velocities observed in this area.

# **PART I:**

# **INTRODUCTION AND GEOLOGICAL FRAMEWORK**

---



## Chapter 1: General Introduction

### 1.1 Background and motivation

The study region of this Thesis is Central Asia, which spans from eastern Anatolia to eastern China and from the Oman Gulf and the Indo-Gangetic plain to the Caspian Basin and the Mongolian Altai Range (Figure 1.1). The Central Asia contains two of the most prominent deformed regions on Earth, which are the results of two tectonic events occurred during the Cenozoic: the Arabia-Eurasia and the India-Eurasia collision zones, formed after the NNE-wards subduction of Tethys oceanic lithosphere and the subsequent continental collisions of Arabia and India plates with the south-western and southern margins of Eurasia plate, respectively. The Arabia-Eurasia collision seems to have begun sometime between  $\sim 35$  and  $\sim 23$  Ma, whereas India's collision with Eurasia is thought to have started between 55 and 45 Ma (Hatzfeld and Molnar, 2010).

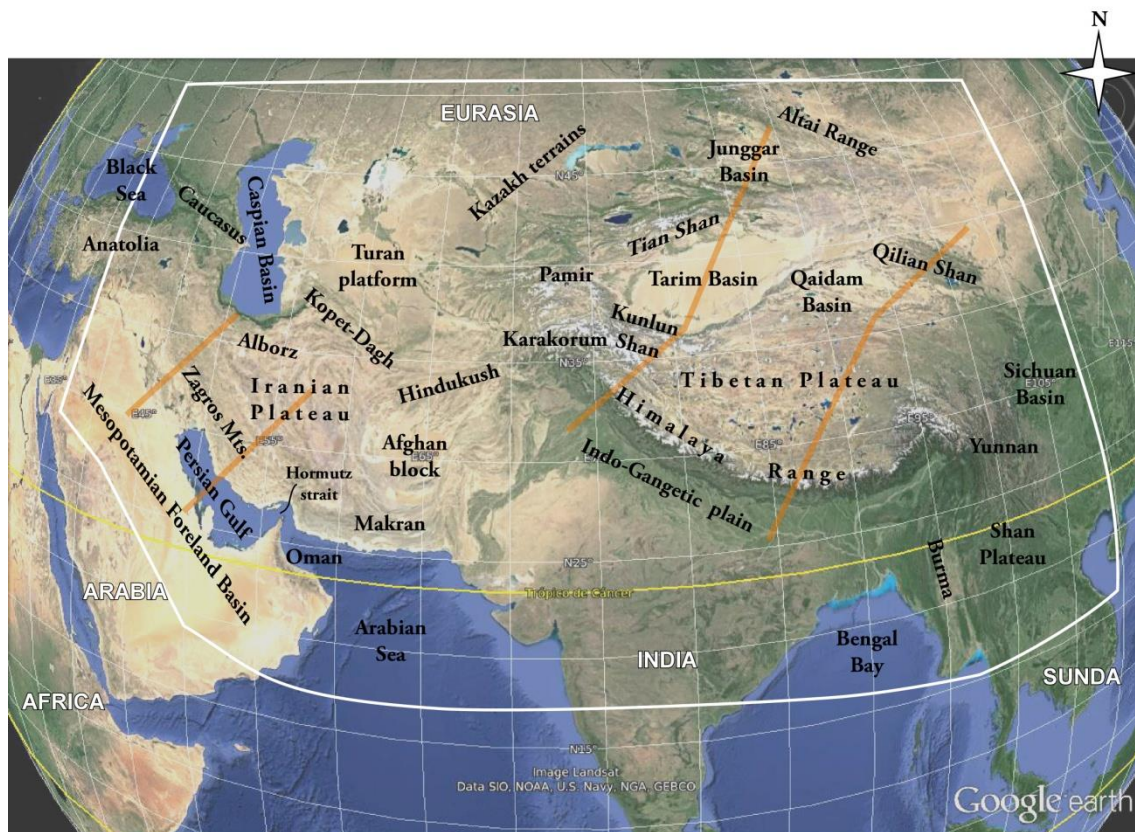


**Figure 1.1.** Topographic map of the study region (roughly defined by the white line). This Thesis shows the results on the present-day lithospheric structure along four profiles (orange lines) obtained by using an integrated geophysical-petrological methodology, and the study of the present-day deformation in the whole Central Asia obtained by applying a thin viscous sheet approach.

Both collisional processes have faced a strong lithosphere (beneath Arabia and India) with apparently weaker material that included segments of Andean-type margins

along the southern edge of the Eurasian plate. The Arabian platform plunges beneath the crust of central Iran, which has progressively become part of Eurasia, while the Indian shield has been underthrust beneath southern Tibet.

The tectonic convergence resulted in the westward escape of Anatolia, oblique convergence in the Zagros Mountains, formation of the Makran accretionary wedge, convergence and strike-slip movement in the Afghan block, convergence along the Himalaya Range and Karakorum, uplift of the Tibetan Plateau and crustal shortening across Asia, with the formation of different mountain ranges beyond the margins of both Iranian and Tibetan plateaus (Houseman and England, 1993; Kind et al., 2002; Li et al., 2008; Royden et al., 2008): Caucasus, Alborz, Kopet Dagh, Pamir, Kunlun Shan, Qilian Shan, Tian Shan and Altai mountain belts.

In this Thesis, the term *Zagros orogen* corresponds to the orogenic system resulted from the Arabia-Eurasia collision, which includes the Mesopotamian Foreland Basin, the Zagros Mountains, the Iranian Plateau, the Kopet Dagh, and the Alborz range; the term *Himalaya-Tibetan orogen* corresponds to the orogenic system resulted from the India-Eurasia collision, which includes the Himalaya Range, the Tibetan Plateau, and the orogenic belts surrounding the Tarim, Qaidam and Junggar basins.

As illustrated in Figure 1.1., the Zagros orogen is a NW-SE-trending orogenic system, extending for more than 1200 km from eastern Anatolia region to the Hormutz Strait in southern Iran. The Zagros Mountains represent the front of the collision zone, with the suture zone located along the Main Zagros Fault (Agard et al., 2006; Paul et al., 2006, 2010), but the continuous tectonic convergence propagated the deformation also to the continental interiors, and other mountain ranges formed along the ancient Eurasian margin, such as the Alborz Mountains in the north-west of Iran, and the Kopet Dagh in the north-east, at the southern edge of the Eurasian Turan Platform.

The Himalayan-Tibetan orogen is the highest and largest orographic system on Earth, located at the northern boundary of the Indian continent and characterized by an average topography of 4000-5000 m and several peaks over 8000 m (e.g., Mount Everest, 8848 m; K2, 8611 m). The India-Eurasia collisional process included different subduction and suturing episodes during the closure of the Tethys Ocean, which successively accreted continental terrains at the southern ancient Eurasian border, and finally culminated with the continental collision between the Indian and Eurasian plates. The convergence resulted in large amounts of thrusting and crustal thickening along the Himalaya Range, and broadly distributed deformation with the formation of the high Tibetan Plateau and of additional reliefs extending some 2000 km north of Indus-Tsangpo Suture, such as the Kunlun Shan and the Tian Shan to the north, and the Qilian Shan to the east.

Both the Zagros and the Himalaya-Tibetan orogens have been the subject of numerous researches, although with different focuses.

The Zagros Mountains have been widely investigated in the last decade because of its important hydrocarbon reserves that make it one of the most productive zones for oil and gas exploration. Geophysical surveys and tectonic studies focused on both the sedimentary cover and the basement units that configure the inner parts (Sanandaj-Sirjan and Urumieh-Dokhtar domains) of the Zagros Mountains, and provide good constraints for the topography of the crust-mantle boundary (e.g., Gök et al., 2008; Gritto et al., 2008; Sodoudi et al., 2009; Paul et al., 2006, 2010; Manaman et al., 2011).

The Himalaya-Tibetan region has been intensively investigated, especially from the beginning of the '80 when international seismic projects bloomed in the region to carry on multidisciplinary studies. The hot topic is the Tibetan Plateau, its formation and the mechanisms driving its broad and uniform regional uplift (England and Houseman, 1989; Molnar et al., 1993; Platt and England, 1994; Tapponnier et al., 2001; Jiménez-Munt and Platt, 2006). For this purpose, a large variety of geophysical acquisitions has been deployed especially in the eastern Tibetan Plateau: (1) deep seismic experiments (Zhao et al., 1993; Nelson et al., 1996; McNamara et al., 1997; Owens and Zandt, 1997; Huang et al., 2000; Haines et al. 2003; Tilmann et al., 2003; de la Torre and Sheehan, 2005; Shulte-Pelkum et al., 2005; Jiang et al., 2006; Monsalve et al., 2006; Chen and Tseng, 2007; Hétenyi et al., 2007; Nábelek et al., 2009; Zhao et al., 2011), (2) seismic tomography (Zhou and Murphy, 2005; Priestley et al., 2006, 2008; Li et al., 2008; Ren and Shen, 2008; Replumaz et al., 2010; Lei et al., 2011), (3) receiver functions studies (Vinnik et al., 2004; Wittlinger et al., 2004; Rai et al. 2006; Zhao et al., 2010; Zhang et al., 2012) (3) magnetotellurics (Unsworth et al., 2004; Spratt et al., 2005; Xiao et al., 2011), (4) potential fields (Braitenberg et al., 2000, 2003; Shin et al., 2007; Jiménez-Munt et al., 2008), and (5) geothermics (Wang 2001; Chung et al., 2005; Holbig and Grove, 2008). These studies focus on the upper part of the lithosphere and provide good constraints at least for the crustal structure across the orogen. However, like in the case of the Zagros orogen, the definition of the lithosphere-asthenosphere boundary (LAB) is more problematic due to the lack of direct observables and its more elusive nature (Eaton et al., 2009; Fischer et al., 2010).

Low seismic velocities and alkaline volcanism have been observed in both the Zagros and the Himalaya-Tibetan orogens suggesting the presence of a lithospheric mantle thinning (Chung et al., 2005; Maggi and Priestley, 2005; Jiménez-Munt and Platt 2006; Kumar et al., 2006; Alinaghi et al., 2007; Kaviani et al., 2007; Manaman and Shomaly, 2010; Zhao et al., 2010; Ceylan et al., 2012). In addition, sub-crustal mass deficits are required for the isostatic balance between crustal thickness, topography and potential fields, as inferred from integrated geophysical studies (Molinario et al., 2005; Jiménez-Munt et al., 2008; Motavalli-Anbaran et al., 2011; Jiménez-Munt et al., 2012). These studies consider the density of the lithospheric mantle only temperature-dependent and equivalent to the density of the underlying asthenosphere, corrected by thermal expansion. Phase changes are not contemplated and the lithospheric mantle is considered compositionally homogeneous.

However, recent works in petrology have shown the strong dependence of the mantle density on its compositional characteristics, as well as on temperature and pressure conditions. The chemical composition of the lithospheric mantle plays a fundamental role on controlling the buoyancy/rigidity characteristics of the lithosphere and its tectonic behaviour (Lenardic and Moresi, 1999; Poudjom-Djomani et al., 2001; Griffin et al., 2009).

The long-standing tectonic evolution of the Himalaya-Tibetan and of the Zagros orogen has likely modified the chemical composition of the lithospheric mantle, causing relevant changes in the geometry of the crust-mantle and lithosphere-asthenosphere boundaries. Up to date however, a quantified thermal and petro-physical characterization of the lithospheric mantle in the two orogens, consistent with geothermo-barometers and tomography models, has not been attempted.

This Thesis provides a first study of the relative contributions of temperature and composition on density and seismic velocities in the upper mantle beneath the Arabia-Eurasia and India-Eurasia collision zones. Geological, geophysical and petrological data are combined within an internally consistent thermodynamic-geophysical framework. The method allows incorporating lateral compositional variations in the lithospheric mantle, and the modelled crust and lithospheric mantle structures are constrained by available data on elevation, Bouguer anomaly, geoid height, surface heat flow and seismic data including receiver functions, and P- and S-wave tomographic models. The lithospheric models presented in this Thesis make compatible seismic and thermal modelling findings, and allow quantifying the effect of mineral physics on previous results from integrated thermal models.

Furthermore, the Arabia-Eurasia and India-Eurasia collisional processes are still on-going, and the high level of seismicity and GPS measurements attest the current strong tectonic activity in the whole Central Asia. Because the collision between India and Eurasia occurred before that between Arabia and Eurasia and because the average convergence rates between the former are higher (50–60 mm/yr since 45 Ma) than the latter (18–25 mm/yr since 25 Ma), associated widespread deformation differ between the Zagros and the Himalaya-Tibetan orogens (Hatzfeld and Molnar, 2010).

In addition to the present-day lithospheric structure, this Thesis also focalizes on the present-day deformation in the Central Asia through a thin-sheet approach. The applied geodynamic modelling technique allows inferring the surface velocities, stress directions, tectonic regime and strain distribution by applying velocity conditions to the model boundaries. The method allows rheology, faults and topography to be incorporated in laterally-varying crustal and lithospheric structure model. The aim is to understand how the Arabia and India convergence are accommodated within Eurasia and the role of the lithospheric structure and rheology of both the Zagros and the Himalaya-Tibetan orogens on the surface deformation.

## 1.2 Objectives

In order to characterize the present-day lithospheric structure and to investigate the neotectonic deformation in the Central Asia, I have defined the following objectives with their specific activities and tasks:

- I. To obtain 2D crust and upper mantle cross-sections in both the Zagros and the Himalaya-Tibetan orogens:**
  - a. Modelling the crustal structure along 4 profiles perpendicularly crossing the two orogenic systems: two profiles crossing the Arabia/Eurasia collision zone and two profiles crossing the India/Eurasia collision zone (localization in Figure 1.1). This task requires the compilation of all available structural and tectonic information about the selected regions and the definition of the physical parameters (density, thermal conductivity, radiogenic heat production) characterizing every geological domain.
  - b. Modelling the lithospheric mantle structure along the selected profiles, combining geophysical and petrological data. This task will allow the characterization of the lithospheric mantle in the Arabia-Eurasia and India-Eurasia continental collision zones, through the definition of the geometry of the lithosphere-asthenosphere boundary, mantle compositional variations, and distribution of mantle temperature, density and seismic velocity anomalies along the selected profiles.
- II. To characterize the nature of the lithospheric mantle beneath the Zagros and the Himalaya-Tibetan orogens**
  - c. Inferring the bulk composition of the lithospheric mantle compatible with geophysical observations by using available information from xenoliths and petrological studies in the study regions.
  - d. Checking the sensitivity of the model results to lateral variations of the lithospheric mantle composition.
  - e. Analysing the lithosphere structure and mantle composition variations along the strike of each orogen by compare the results obtained along the modelled profiles.
- III. To obtain a neotectonic model of the deformation in the Central Asia that combines the present-day lithospheric structure with plate kinematics, GPS observations and fault activities.**
  - f. Construction of the lithosphere structure and thermal regime obtained from a recent work and incorporation of the results from this Thesis

- g. Definition of the main tectonic features in the study area (active faults, plate boundaries etc.).
- h. Investigating the effect of the rheology, boundary conditions, and lithospheric structure on the predicted surface velocities, stress orientations and tectonic regime.

This Thesis has been structured in four Parts: I) Introduction and geological framework; II) Present-day lithospheric structure; III) Neotectonic modelling of Central Asia; IV) General conclusions.

The first part (Part I) is composed of two chapters illustrating the objectives of the Thesis (this Chapter) and providing an overview of the tectonic and geological settings of the study area (Chapter 2).

The second part (Part II) is dedicated to the present-day lithospheric structure in the Zagros and the Himalaya-Tibetan orogens. It is composed of three chapters (Chapters 3-5). Chapter 3 illustrates the integrated geophysical-petrological approach used to characterize the crust and upper mantle structures down to 400 km depth (LitMod-2D, Afonso et al., 2008). Chapters 4 and 5 show the resulting lithospheric structures in the Zagros and the Himalaya-Tibetan orogens depth from a thermal, compositional, seismological and density viewpoint.

The third part (Part III) is dedicated to the study of the neotectonic deformation in Central Asia, and it is structured in three chapters. Chapter 6 describes the methodological approach and the data considered in the study (SHELLS, Bird et al., 2008). Chapter 7 present the results for different neotectonic models changing the rheological parameters, friction coefficient on faults, boundary conditions and lithospheric mantle thickness. The pros and the cons of several models are discussed in Chapter 8. The different models and their results on the deformation patterns in Central Asia are analysed in order to delineate some conclusions.

Finally, Part IV includes one Chapter (Chapter 9) illustrating the overall conclusions of this Thesis.

## Chapter 2: Geological setting

This chapter is thought to provide a geological large-scale overview of the study area. After a brief introduction to the whole Central Asia region (Section 2.1), a close up on the Arabia-Eurasia (Section 2.2) and India-Eurasia (Section 2.3) collision zones allows, then, to detail the main tectonic features of the Zagros and Himalaya-Tibetan orogenic systems, which are the main subjects of this Thesis.

### 2.1 Central Asia

The Central Asia region is dominated by one of the largest areas of distributed deformation on Earth, which spans eastern Turkey, northern Middle East, central and south-eastern Asia, covering the central and eastern parts of the Alpine-Himalayan mountain belt. It is composed by the Zagros orogen in the western sector and the Himalaya-Tibetan orogen in the eastern sector, resulting from two continental collisions occurred during the Cenozoic. The strong and resistant Archean-to-Proterozoic shields of Arabia and India plates collided with the complex mosaic structure of the Eurasian ancient margin, which was formed by different Gondwana-derived continental blocks accreted by Late-Mesozoic time.

The two collisional events caused re-organization of the different terrains over a large territory (Molnar and Tapponnier, 1975). Many tectonic processes acted upon a relatively weak lithosphere between rigid blocks. The lithospheric weakness is related to major pre-existing structures as suture zones and/or large-scale fault zones between the accreted micro-continents (Audet and Bürgmann, 2011).

For the sake of simplicity, in this chapter the Central Asia region is divided into 3 major zones (Figure 2.1): (1) the Arabia-Eurasia collision, (2) the India-Eurasia collision, (3) the Arabia-India inter-collision zone.

The Arabia-Eurasia collision zone includes the eastern Arabian plate, and the Zagros orogenic system up to the northern ranges of the Caucasus, the Alborz and the Kopet Dagh. The India-Eurasia collision zone includes the Indian plate and the Himalaya-Tibetan orogenic system. The two collision zones are separated by the rigid Afghan block, bordered to the south by the Makran subduction zone and to the north by the Hindukush region (Figure 2.1).

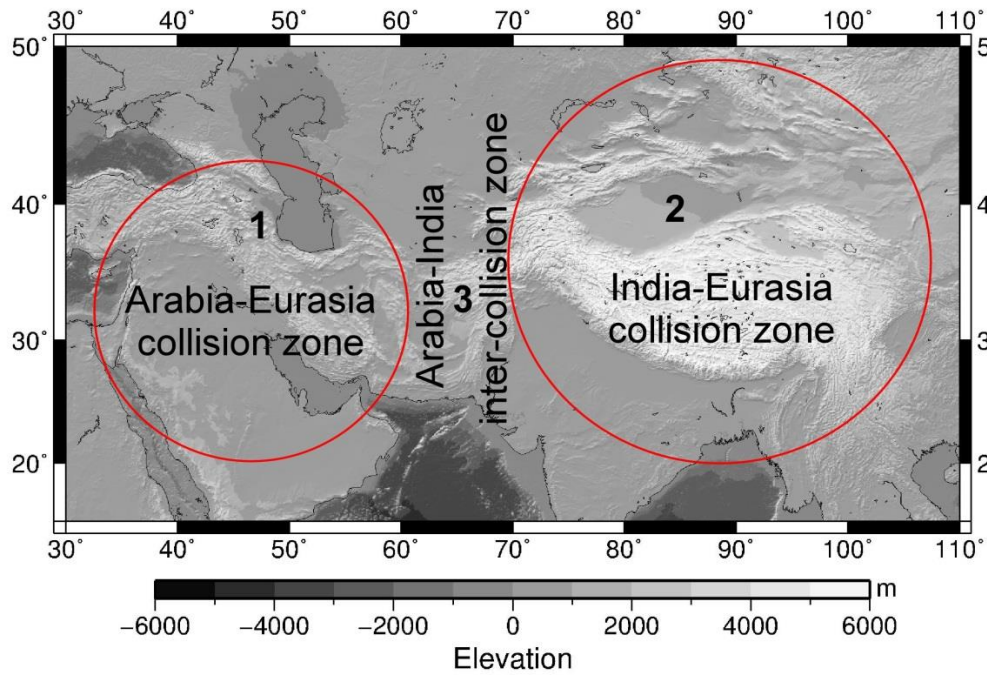


**Figure 2.1.** Topography map of the Central Asia region and localization of the three major zones selected to introduce the geodynamic and tectonic setting. The shaded relief has been obtained from ETOPO1 database (Amante and Eakins, 2009).

## 2.2 The Arabia-Eurasia collision zone

The Arabian plate is one of the youngest lithospheric plates, having originated ~25 Ma when rifting from the Gulf of Aden and the Red Sea split off a fragment of the African continent. It is composed of the Arabian Shield in the western sector and the Arabian Platform in the eastern part (Figure 2.2). The Arabian Shield is formed by a Neoproterozoic basement, with Archean and Paleoproterozoic rocks that locally are tectonically intercalated (Stern and Kröner, 1993; Stern and Abdelsalam, 1998; Hargrove et al., 2006). The shield was variably above sea level after ~750 Ma, and repeatedly uplifted and depressed, developing unconformities and continental sedimentary basins. The crystalline basement in the eastern Arabian Plate is also Neoproterozoic, but appears to have a geologic history different to that of the Shield. After ~750 Ma, eastern Arabia stabilized as a neo-craton (Stern and Johnson, 2008), overlain by a shallow marine environment, and since then has subsided more or less continuously to accommodate up to 10 km of sediments (Sandvol et al., 1998; Konert et al., 2001; Mokhtar et al., 2001). Phanerozoic sedimentary rocks dominate the Arabian Platform, forming a succession which is progressively younger and thicker away from the Shield. The uplift associated with the Red Sea and the mantle processes which have operated since the onset of the rifting in the Gulf of Aden (the past 25 million years) resulted in a gentle tilt of the Arabian plate toward the north and east (Stern and Johnson, 2008). Cenozoic basalts are unconformably emplaced on the crystalline

basement and Phanerozoic sedimentary rocks in the western and north-western parts of the Arabian plate (Stern and Johnson, 2008, 2010).

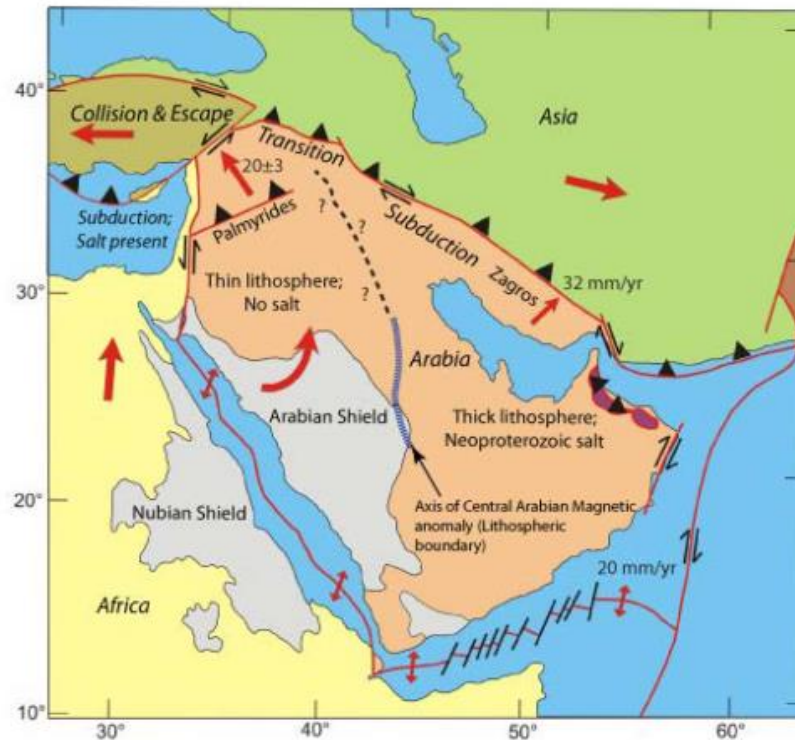


**Figure 2.2.** Simplified map of the Arabian and surrounding plates, with plate boundaries (red) and convergence vectors (red arrows). Grey areas represent exposed basement. Figure from Stern and Johnson (2008).

Since its separation from Africa the Arabian plate has rotated anticlockwise and drifted north, currently at a rate of 2–3 cm/year (Bird, 2003). The process of northward drift led to the closure of the Tethys Ocean, lasting from Late Cretaceous to Neogene (Vergés et al., 2011; Mouthereau et al., 2012, McQuarrie and van Hinsbergen, 2013) and its subduction beneath Eurasia. The subsequent continental collision beneath the Arabia and Eurasia plates propagated from north-west to south-east (Agard et al., 2011) and formed the Zagros mountain belt, extending from eastern Turkey to the Hormuz Strait for more than 200 km (Figure 2.3).

From the tectonic point of view, the Zagros mountain belt includes five structural domains, separated by significant thrust faults (Figure 2.3). The Mesopotamian Foreland Basin and its continuation in the Persian Gulf, formed by the flexure of the Arabian plate in front of the Zagros Fold-and-Thrust Belt (ZFTB). The Fold-and-Thrust Belt (or Simply Folded Belt) is separated from the foreland basin by the Main Frontal Fault (MFF), creating a structural uplift of several kilometres, involving basement rocks and folding of the thick cover succession (Sepéhr and Cosgrove, 2004; Sherkati et al.,

2006; Emami et al., 2010, Casciello et al., 2009). The sedimentary rocks were deposited in an extensional and passive margin setting during Paleozoic and most of the Mesozoic periods followed by compression and flexural basin development starting in the Late Cretaceous times (Beydoun et al., 1992; Homke et al., 2009 and Koop and Stoneley, 1982 among others). The higher density and the presence of Neoproterozoic salt in the eastern sector Arabian plate, i.e. east of the so-called Central Arabian Magnetic Anomaly (Figure 2.2), allowed the platform sediments to be scraped off to form the Zagros fold-and-thrust belt due to the reduced friction on the plate interface.

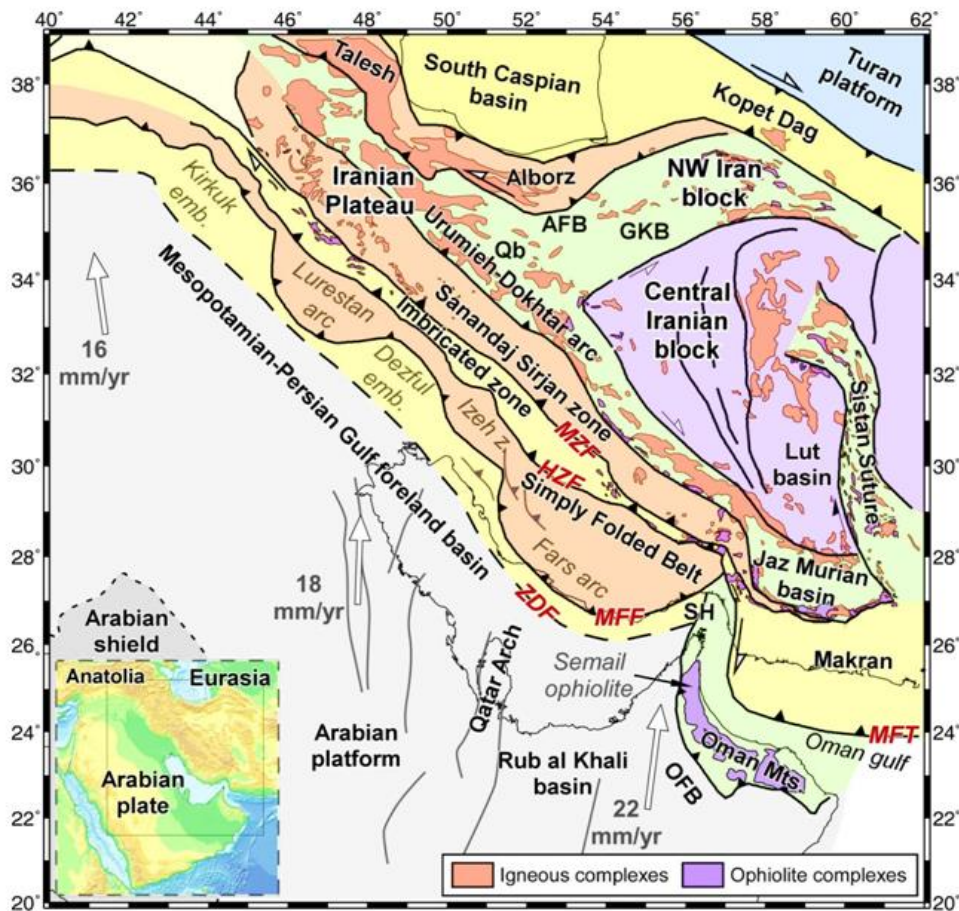


**Figure 2.3.** Structural map showing the main tectonic units of the Zagros Mountains and adjacent areas (modified after Jiménez-Munt et al., 2012). The colours assigned to the different tectonic units are not related to age or lithology, but are used to highlight their limits. White arrows correspond to the relative plate velocities of the Arabian plate with respect to a fixed Eurasian plate. ZDF: Zagros deformation front; MFF: Main Frontal Fault; HZF: High Zagros Fault; MZF: Main Zagros Fault; Qb: Qom basin; GKB: Great Kabir basin; and AFB: Alborz foredeep basin; OFB: Oman foreland basin; SH: Strait of Hormuz; MF: Minab Fault; MFT: Makran Frontal Thrust.

The Imbricated Zone (IZ), bounded by the High Zagros Fault (HZF) to the southwest, is a highly deformed domain, involving multiple tectonic thrust sheets composed of sedimentary, radiolaritic and ophiolitic rocks, which represent the distal cover rocks of the Arabian plate, as reconstructed in Vergés et al. (2011). The Sanandaj Sirjan Zone (SSZ) is an Iranian continental block involving Palaeozoic to Cretaceous sedimentary and metamorphic rocks. It has been documented that this region was an active Andean-like margin characterized by calc-alkaline magmatism (Berberian and Berberian, 1981) during the mid-Jurassic/ Early Cretaceous. The Sanandaj Sirjan zone is thrust to the SW, on top of the Main Zagros Fault (MZF). The Tertiary Urumieh Dokhtar Magmatic Arc (UDMA) is interpreted to be a subduction-related arc that has been active since Late Jurassic (Berberian and King, 1981; Berberian et al., 1982) and is thrust to the NE above the Central Basin in Iran.

The Central Iran Basin (east Iran) is filled by a 6-8 km thick Neogene sedimentary succession above Eocene volcanics and Cretaceous and Jurassic rocks (Morley et al., 2009). To the north, the Alborz Mountains were formed by the collision with Eurasia after the Paleo Tethys Ocean subduction, which culminated in Triassic times (Berberian and King, 1981; Sengör et al., 1988). The tectonic history is later characterized by a Late Cretaceous-Paleocene thrusting event followed by Eocene back-arc extension during early-middle and late Eocene (Allen et al., 2003) (Figure 2.5). The South Caspian Basin represents the deepest basin in the world with more than 17 km thick Oligocene-Recent sedimentary succession, mildly folded and thrust as a result of the Arabian-Eurasia collision (Egan et al., 2009). The subduction of the South Caspian basin below the Apsheron–Balkhan sill in to the north and the Talesh region to the west since 2–5 Ma is also a result of the tectonic convergence between Arabia and Eurasia plates (Jackson et al. 2002; Allen et al., 2002; Masson et al. 2006; Hollingsworth et al. 2008).

Toward the north-west, the Zagros orogen is connected with the Eastern Anatolian Accretionary Complex (EAAC), located between two former subduction arcs, the Pontide and the Bitlis-Poturge (Keskin, 2003). The complex resulted from northward subduction of the Tethys oceanic lithosphere as well as of lithospheric mantle beneath the Bitlis-Poturge Massif (Sengör et al., 2003; Rizaoglu et al., 2009). The slip on the East Anatolian fault and the post-collisional volcanism in eastern Anatolia (Keskin, 2003) are associated with the oblique collision in this region. Slab break-off and delamination of the mantle lithosphere have been proposed to explain the uplift of the Turkish Plateau (Keskin, 2003; Sengör et al., 2003). The same mantle processes would explain also the change over time of the volcanism throughout the Turkish and Iranian plateaus. The earliest volcanism following the closure of the Neo-Tethys Ocean was calc-alkaline until the Late Miocene. By 6– 8 Ma, the volcanism became widespread and changed to alkaline (Pearce et al., 1990). This variation is interpreted as resulting from slab break-off processes by Ghasemi and Talbot (2006). Therefore, despite the change from subduction to continental collision, the tectonics of the Turkish and Iranian

plateaus is still driven by deep processes affecting the upper mantle (Hearn and Ni, 1994; Agard et al., 2011).

## 2.3 The India-Eurasia collision zone

The India plate (Indian Shield) is a mosaic of various Precambrian tectonic provinces, assembled between mid-Archean and Neo-Proterozoic times (Braun and Kriegsman, 2003; Meert et al., 2010). All these amalgamated tectonic domains are separated by major shear zone systems, some of which represent collision sutures (Chetty and Santosh, 2013). Figure 2.4 shows the geological map of the Indian Shield with the age and exposure of the Precambrian basement. Archean rocks dominate the southern and eastern sectors, but are also present in the north-west as relatively small patches. Sedimentation in the Aravalli and Eastern Ghat orogens took place during the late Proterozoic. The NNE-trending, 100–200 km wide, Eastern Ghat mobile belt experienced high-grade metamorphism in the Late Proterozoic, when it finally accreted to the Indian shield. A region of massive Cretaceous flood basalts, the Deccan Volcanic Province (DVP), is considered as a consequence of the separation of India from the Seychelles microcontinent (a Gondwana-derived continental block) (Rajesh and Mishra, 2004 and references therein). The break-up of Gondwanaland occurred ~140 Ma (earliest Cretaceous) and corresponds to the beginning of the northern drift of the Indian plate towards Eurasia (Kumar et al., 2007).

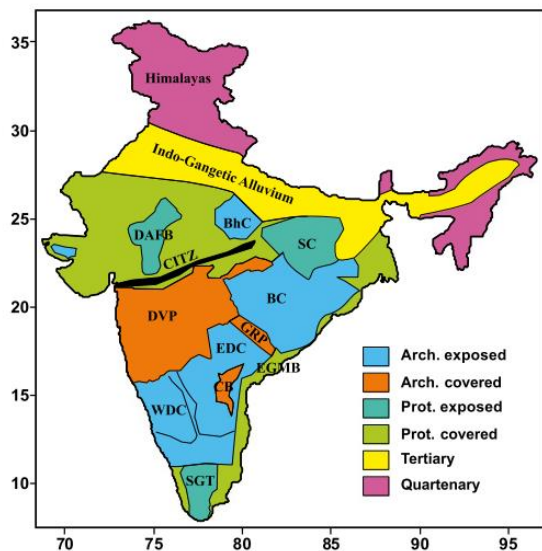


**Figure 2.4.** Geological map of the Indian Shield showing the age and exposure of the Precambrian basement. SGT: Southern Granulite Terrain; WDC: Western Dharwar Craton; EDC: Eastern Dharwar Craton; EGMB: Eastern Ghat Mobile Belt; CB: Cudappah Basin; DVP: Deccan Volcanic Province; GRP: Godavari Rift Province; BC: Bhandara Craton; SC: Singhbhum Craton; BhC: Bundhelkhand Complex; DAFB: Delhi Aravalli Fold Belt; CITZ: Central Indian Tectonic Zone. Figure from Rajesh and Mishra (2004).

The northern drift of the Indian plate culminated 55 and 45 Ma with the continental collision with the Eurasian southern margin forming the Himalaya-Tibetan orogen (Hatzfeld and Molnar, 2010).

The Himalaya-Tibetan orogen (Figure 2.5) is a large amalgamation of crustal and lithospheric domains resulting from different continental collision processes throughout time. The Himalaya Range corresponds to the ancient northern margin of the Indian plate, strongly thrust and folded in three major tectonic slices: the Lesser Himalaya, the Greater Himalaya, and the Tethys Himalaya sequences. These units are separated from each other by major discontinuities, named, from south to north: (1) Main Boundary Thrust (MBT), carrying the Lesser Himalaya sequence over Quaternary molasses; (2) Main Central Thrust (MCT), separating the gneisses and migmatites of the Greater Himalaya from the Lesser Himalaya units; (3) Indus-Tsangpo Suture (ITS), representing the suture zone between India and Eurasia plates. Mesozoic island arc volcanic rocks and relics of the Tethys Ocean can be traced along the suture zone, overlain by deep sea sediments.

The active deformation front migrated southwards during the collision, from the Indus–Tsangpo suture to the present-day Himalayan front (Robinson et al., 2001; DeCelles et al., 2002). North of the Indus–Tsangpo suture, the Indochina (Indochinese peninsula and southern Tibetan Plateau) and Tibet blocks were parts of Eurasia when India collided. At the onset of the collision, the Indochina peninsula was located partially in front of the collision zone, as deduced from rotation poles and tectonic reconstructions (Briais et al., 1993; Leloup et al., 2001; Replumaz and Tapponnier, 2003), forming a compact block with the southern part of the Tibetan Plateau. To the west, this block has been thickened to form the southern Tibetan Plateau (Tapponnier et al., 2001), while to the east the Indochinese peninsula has been extruded south-eastward between 30 and 15Ma (Briais et al., 1993), sliding along the ancient Red River (Leloup et al., 2001).

Nowadays, the southern Tibetan Plateau is formed by the Lhasa terrain, which is the southernmost continental terrain accreted along the south-eastern Eurasia margin (Figure 2.5). It consists of a ~300 km wide band, narrowing westwards, formed by sedimentary units from Ordovician and Carboniferous to Triassic shallow marine clastic sediments, and a mid-Proterozoic to early Cambrian basement (Yin and Harrison, 2000). The Lhasa block collided with the Qiangtang terrain in the Jurassic (Dewey et al., 1988), although they are now separated by the Bangong-Nujiang Suture (BNS). The Qiangtang terrain forms a strip 1900 km long and ~300 km wide, delimited by the Bangong-Nujiang Suture in the south and by the Jinsha Suture (JS) in the north. It consists of Triassic to Jurassic stratigraphic sequences composed by metamorphosed mélangé complexes, shallow marine carbonates interbedded with terrestrial clastic and volcanoclastic strata, and intruded granitoids of 111-145 Ma (Yin and Harrison, 2000).

North of the Jinsha Suture, there is a relatively heterogeneous zone which is bounded to the west by the Altyn Tagh Fault (ATF) and its western propagation, the Karakax Fault. These two discontinuities divide the eastern micro-terrains of the Tibetan Plateau and the Kunlun Shan from the rigid Tarim block (Searle, 2010).

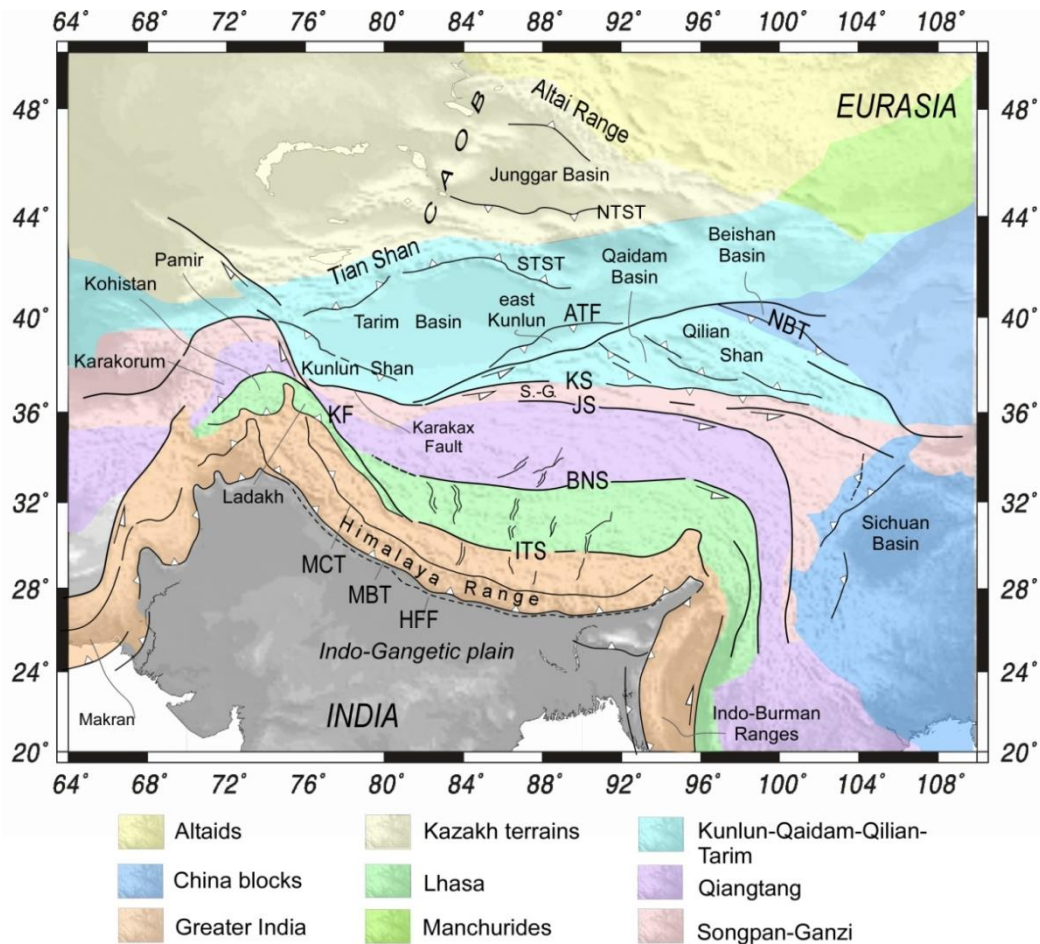


**Figure 2.5.** Tectonic map of the Himalaya-Tibetan Plateau and surrounding areas. The names for the different terrains (coloured areas) are taken from van Hinsbergen et al. (2011). ATF: Altyn Tagh Fault; BNS: Bangong Nujiang Suture; CAO: Central Asia Orogenic Belt; HFF: Himalaya Frontal Front; ITS: Indus-Tsangpo Suture; JS: Jinsha Suture; KF: Karakorum Fault; KS: Kunlun suture or fault; MBT: Main Boundary Thrust; MCT: Main Central Thrust; NBT: North Border Thrust; NTST: Northern Tian Shan Thrust; S.-G: Songpan-Ganzi; STST: Southern Tian Shan Thrust.

In the western sector of the Himalaya Range, approximately at 76°E longitude, the ITS zone is split in two parallel ranges, the Ladakh and the Karakorum, which are the westward prolongation of the Lhasa and Qiangtang terrains, respectively. The Ladakh forms a 500 km long and 25 km wide belt in continuity with the Kohistan arc. It is a Cretaceous-Early Tertiary batholith, composed by sheared greenschists that grades to basalts and granitoids; an andesitic unit, and plutonic rocks, ranging from gabbro, diorite, to granodiorite and leucogranites showing calc-alkaline geochemical affinities. The northern limit is marked by the Shyok Suture, with the thrusting of the Karakorum thrust sheet on top of the Kohistan and Ladakh units. The Tarim Basin, covering an area of nearly 600,000 km<sup>2</sup>, is the largest cratonic area in western China. Its Precambrian crystalline basement is inferred to be a fragment of the Rodinia Supercontinent (Lu et al., 2008 and references therein). It is covered by a thick sedimentary sequence, in

which the Permian strata consist of volcano-sedimentary sequences resulting from the flood basalt magmatism that affected the so-called Tarim Large Igneous Province ~290 Ma (i.e., the Tarim Basin and the western part of the Central Asian Orogenic Belt - CAOB-, including the Tian Shan, Junggar region and Altaids, Figure 2.5) (Xu et al., 2014). Despite the Permian magmatic event, the evolution of the Tarim Basin is characterized by almost continuous sedimentation since the neo-Proterozoic (Xu et al., 2014), whereas the Central Asian Orogenic Belt experienced subduction and accretion-related processes through the Paleozoic, being finally amalgamated with the Tarim craton in the Late Carboniferous (Wang et al., 2006, Zhang et al., 2012b).

The central-eastern sector of the Tibetan Plateau, from the Jinsha Suture northwards, is formed by: i) the Songpan-Ganzi terrain, formed by a thick sequence of deep marine Triassic strata; ii) the eastern Kunlun–Qaidam terrain and the Qaidam Basin, bounded to the north by the southern Qilian Suture, and dominated, in the south, by a broad Early Paleozoic arc, on which a younger and narrower Late Permian to Triassic arc was superposed (Yin and Harrison, 2000); and iii) the Qilian Shan, formed by complexly deformed Early Paleozoic arcs, which developed at the southern margin of the North China craton before it was offset by the Altyn Tagh Fault during the Cenozoic (Yin and Harrison, 2000).

## 2.4 The Arabia-India inter-collision zone

In the region between the Zagros and the Himalaya-Tibetan orogens there is the Afghan block, located between between 61°E and 65°E longitudes.

To the west of the Afghan block there is a north- to northwest-trending right-slip fault system accommodating the northward penetration of Arabia into Eurasia: the Sistan suture zone (Bonini et al., 2003; Yin, 2010). The Sistan suture zone (Figure 2.6) developed presumably during the Late Cretaceous (Zarrinkoub et al., 2010). During the Cenozoic, the E-W closure of the oceanic domain located between the Lut block (eastern Iran) and the Afghan block (Sistan Ocean) started and continued until Oligocene-Miocene times (Rezaei-Kahkhaei et al., 2010).

To the east of the Afghan block, the left-slip Chaman fault system in the easternmost Afghanistan accommodates the northward penetration of India into Eurasia. The Afghan block collided with India in the late Cenozoic (~5 Ma) and then it was extruded westward along the conjugate Herat and Chaman strike-slip faults (Tapponnier et al., 1981). The collision between the Afghan block and the India plate is thought to be related with the change in the kinematic pattern observed on the Eurasian side of the Arabia-Eurasia collision zone around 5 Ma (Austermann and Iaffaldano, 2013). Agard et al. (2011) suggested that prior to the Afghan-India collision, the crust in Central Iran was able to deform laterally to the southeast, transferring strain into Afghanistan. Once collision started, this process was no longer viable. Therefore, the escape transferred

toward the north, initiating a westward transport of the South Caspian basement (Hollingsworth et al., 2008) and a westward escape of Anatolia (McKenzie, 1972).

The Afghan block is bordered to the south by the Makran subduction zone and to the north by the Pamir-Hindukush region.

The Makran region represents an active subduction zone in which the oceanic lithosphere of the Oman Sea subducts northward beneath the Makran accretionary prism (Byrne et al. 1992). This region shows a relict accretionary prism onshore of middle-upper Miocene age and a younger (Miocene-Pliocene) active system developed offshore (Ellouz-Zimmermann et al., 2007). North of this belt, the Jaz Murian basin is considered the back-arc basin related to the Makran subduction zone, filled with Cenozoic deposits (Jiménez-Munt et al., 2012; and references therein).

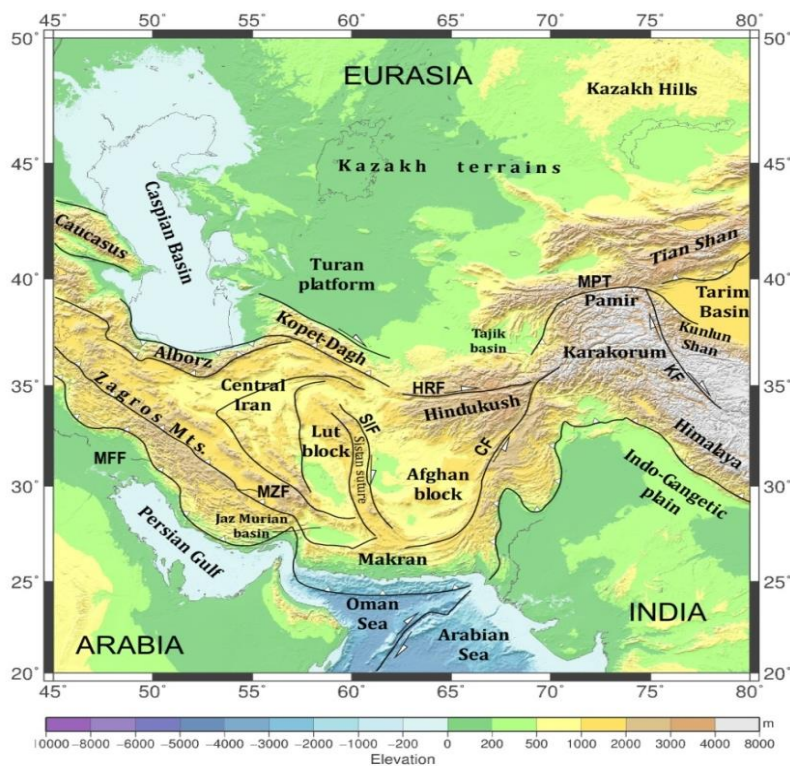


**Figure 2.6.** Topography map and main structural lines of the Arabia-India-Eurasia inter-collision zone. CF: Chaman Fault; HRF: Herat Fault; KF: Karakorum Fault; MFF: Main Frontal Front; MPT: Main Pamir Thrust; MZF: Main Zagros Fault; SIF: Sistan Fault.

The Pamir-Hindukush region originated from the accretion of micro-continents, arcs, and subduction-accretion complexes to the ancient Asian margin during the Paleozoic and Early Mesozoic (Burtman and Molnar, 1993; Schwab et al., 2004). Formed north of the western Himalayan Syntaxis, on the Asian (retro)continent, the

Pamir accommodated a high amount of Cenozoic crustal shortening over a short north-south distance (Schmidt et al., 2011; van Hinsbergen et al., 2011). Moving toward the north, the Pamir thrust over the Tajik-Afghan basin, then connected with the Tarim Basin. Currently the Pamir and the Hindukush are featuring intense intermediate depth (~90–250 km) seismicity in an intra-continental setting, testifying vigorous geodynamic processes in the mantle below (Schurr et al., 2014).

Finally, the Kazakh terrains and the epi-Variscan Turan Platform are located to the north of this deforming region and they are part of the stable Eurasia plate (Figure 2.6). The formers have been affected by the northward propagation of the deformation related to India-Eurasia collision, and, as a consequence, the Kazakh Hills in northern Kazakhstan have been subjected to denudation during the past 3 Ma (Smit et al., 2013 and references therein). The latter was a stable domain separated by the Gondwana-derived Central Iran block by the Paleo-Tethys Ocean. The Cimmerian orogeny closed the Paleo-Tethys Ocean and the Alborz and Kopet Dagh ranges which corresponds to the actual northern boundary of the Arabia-Eurasia collision zone, developed along the Paleo-Tethys suture zone (Sengör et al., 1988; Robert et al., 2014).



## **PART II:**

# **PRESENT-DAY LITHOSPHERIC STRUCTURE**

---



## Introduction

The temperature and the composition of the lithosphere are key parameters in modern lithospheric modelling, since they determine the physical properties (elasticity, rheology, density, etc.) which control the Earth's interior dynamics. A model of the thermal and compositional structure of the lithosphere provides crucial information for understanding the present-day lithospheric features and geodynamic processes.

Traditionally, the calculation of the lithospheric structure has been based on a 'pure' thermal approach, which considers that the density of the lithospheric mantle is only temperature dependent and equivalent to the density of the underlying asthenosphere, corrected by thermal expansion (e.g. in Zagros region, Molinaro et al. 2005; Motavalli-Anbaran et al. 2011; Jiménez-Munt et al. 2012; and in Tibet, Jiménez-Munt et al., 2008). Strong limitations of this approach are: (i) the lithospheric mantle is assumed to be homogeneous in composition, (ii) phase changes are not considered and (iii) the density of the asthenosphere is constant everywhere. A major restriction is that, the resulting lithospheric mantle structure cannot be directly compared with Pn-, Sn-, P- and S-wave velocities obtained from seismic experiments and tomographic models.

In contrast to previous studies, in this work, we apply a self-consistent petrological-geophysical approach (Afonso et al., 2008; Fulla et al., 2009), which integrates potential fields (gravity and geoid), isostasy (elevation), thermal equations (heat flow and temperature distribution) and mantle mineral physics. Hence, the calculated mantle density, thermal conductivity and elastic parameters ( $V_p$  and  $V_s$ ) depend on temperature, pressure and chemical composition through the equations of state. The Part II of this Thesis addresses the relative contributions of temperature and composition on density and seismic velocities in the upper mantle beneath the Arabia-Eurasia and India-Eurasia collision zones with the aim of (i) making compatible seismic and thermal model results; (ii) analysing the effect of mantle composition on the resulting lithospheric structures; (iii) discussing the differences on the lithospheric mantle composition and thickness along the strike of the two collisions, Arabia-Eurasia and India-Eurasia; and iv) calculating P- and S- mantle seismic velocity distributions and velocity anomalies along the two collisions, thus making the results comparable with published seismic tomography studies.

The methodology is illustrated in Chapter 3. The Section 3.2 is dedicated to illustrate the improved version of the thermal conductivity model on which I worked during a two months-long stay at Macquarie University (Sydney, Australia, on June-July 2012), and that has been implemented in the main code for the lithospheric models in the Himalaya-Tibetan orogen. The Section 3.7 illustrates the interdependency of the different mantle properties considered in the study, i.e. density, temperature, composition and seismic velocity.

Finally, Chapters 4 and 5 describe the data and the results obtained along the four selected profiles which cross the Zagros (profiles A-A', B-B') and the Himalaya-Tibetan (profiles C-C', D-D') orogenic systems, respectively.

## Chapter 3: Method: The integrated geophysical-petrological modelling

The methodology used in this work was based on the LitMod-2D code (Afonso et al., 2008), which combines geophysical and petrological data, in order to study the crust and upper mantle structures from a thermal, compositional, seismological and density viewpoint. The code allows calculation of the 2D distribution of temperature, density and mantle seismic velocities down to 400 km depth and the gravity and geoid anomalies, elevation, and surface heat flow (Figure 3.1). A forward modelling scheme is applied by comparing the model outputs (elevation, gravity and geoid anomalies, surface heat flow, and mantle seismic velocities) with observed data and modifying parameters and model geometry within the experimental uncertainties, until the best fit model is obtained.

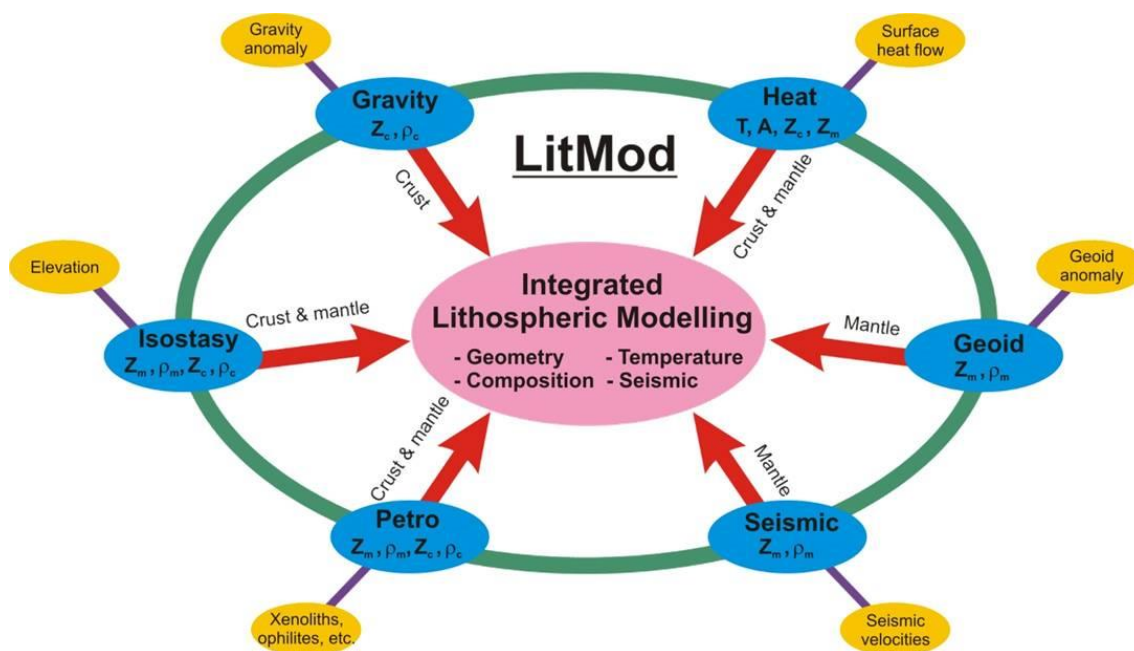


**Figure 3.1.** Simplified scheme of the LitMod program. A: radiogenic heat production;  $\rho_c$ : crustal density;  $\rho_m$ : lithospheric mantle density; T: temperature;  $Z_c$ : crustal thickness;  $Z_m$ : lithospheric mantle thickness.

The model domain is composed of multiple polygons, representing the different crustal and mantle bodies, to which a triangular finite element mesh is adapted. Each crustal body is associated with a single lithology, described by a set of thermo-physical parameters (density, thermal conductivity and volumetric heat production). Density and thermal conductivity can be pressure- and/or temperature-dependent, whereas, radiogenic heat production can be either constant or exponentially decreasing with depth. The geometry and properties of the crustal bodies are assigned according to the geological structure and constrained by existing data.

Once a particular structure is defined, the LitMod-2D code solves the following algorithms.

### 3.1. Mantle temperature distribution

Under the assumption of a purely conductive lithospheric domain, i.e. in the absence of convection/advection, the steady-state temperature distribution is calculated by solving the conductive heat transport equation expressed by

$$\nabla(-K\nabla T) - H(x, z) = 0 \quad (\text{Eq. 3.1})$$

where  $T$  is the temperature,  $K$  is the thermal conductivity ( $\text{Wm}^{-1}\text{K}^{-1}$ ),  $H$  is the radiogenic heat production ( $\text{Wm}^{-3}$ ),  $(x, z)$  horizontal and vertical Cartesian coordinates, and  $\nabla$  is the Nabla operator.

The boundary conditions are: i)  $0^\circ\text{C}$  at the surface; ii)  $1330^\circ\text{C}$  at the LAB, in agreement with thermo-physical models that use realistic rheologies (Shubert et al., 2001); and iii) no heat flow across the lateral boundaries of the model.

The mantle thermal conductivity, which is pressure/temperature-dependent, is calculated with the formula by Hofmeister (1999):

$$K_{(T,P)} = K^\circ \left(\frac{298}{T}\right)^a \exp\left[-\left(4\gamma + \frac{1}{3}\right) \int_{298}^T \alpha(T) dt\right] \times \left(1 + \frac{K'_0 P}{K_T}\right) + k_{rad}(T) \quad (\text{Eq. 3.2})$$

where  $K^\circ$  is the thermal conductivity at  $T=298\text{K}$  and  $P=1\text{atm}$ ,  $a$  is a fitting parameter ( $=1.25$ ),  $\alpha(T)$  is the thermal expansion coefficient which depends on the temperature,  $K_T$  is the isothermal bulk modulus ( $K'_0 = \frac{dK_T}{dP}$ ), and  $k_{rad}(T)$  is a function describing the radiative contribution to the thermal conductivity. Though  $K$  strictly varies with composition due to changes in thermodynamic parameters, chemistry, and relative proportions of the constitutive minerals, the thermal conductivity model from Hofmeister (1999), though being in agreement with experimental results for salts, silicates, and oxides, is not an explicit function of the composition. To solve this problem, a new thermal conductivity model (see Section 3.2) based on more recent results of experimental petrology, has been adopted in a second phase of this thesis, i.e. in the modelling of the profiles crossing the Himalaya-Tibetan orogen.

In the sub-lithospheric domain, the heat transfer is dominated by convection, and the vertical temperature distribution is assumed to follow an adiabatic gradient. The algorithm considers a 40 km-thick thermal buffer with a temperature of  $1400^\circ\text{C}$  at its base, in order to avoid unrealistic discontinuities between the conductive thermal gradient within the lithospheric mantle and the adiabatic thermal gradient within the asthenosphere. The temperature gradient between the thermal buffer and the base of the model is restricted to

$0.35 < dT/dz < 0.50^\circ\text{C}/\text{km}$ , which translates into maximum lateral temperature variations of  $\sim 120^\circ\text{C}$  at the base of the model. This is consistent with seismic observations on the topography of the 410-km discontinuity that indicate maximum temperature variations of a few hundred degrees at these depths (Afonso et al., 2008 and references therein).

### 3.2. Mantle thermal conductivity

As mentioned in the previous section, the heat is transferred by conduction within the lithospheric domain. Conductive heat transport in the Earth occurs via lattice vibrations and diffusive radiation. The input of heat excites vibrations of the nearby atoms. Because atoms are connected by chemical bonds, the vibrational energy is dissipated through lattice vibrations of adjacent atoms. A realistic model for thermal conductivity accounts for quantization of these lattice vibrations, called phonons. Heat is thus transferred through phonons colliding with each other and possibly with defects or grain boundaries ( $k_{lat}$ ). Because raising pressure raises vibrational frequencies and densification increases the chances of collision, the thermal conductivity increases as P increases or as T decreases. In addition to transport by conduction, a hot material produces blackbody radiation, which travels as an electromagnetic wave. Heat is diffused if the light (photons) emitted by one particle is partially scattered or partially absorbed by high-frequency transitions in neighbouring particles (radiative transfer). The thermal conductivity derived from the radiative transfer is defined as  $k_{rad}$ . Since this process occurs simultaneously with collisions of lattice phonons, the total conductivity  $k$  is the sum of  $k_{lat}$  and  $k_{rad}$ .

Furthermore, the radiative transfer can occur through two mechanisms of photons transport (Figure 3.2): i) Diffusive radiative transfer, involving emissions of photons by a hot grain, then absorbed by nearby warm grains, which, in turn, emit light according to their cooler temperatures, so each grain is both an emitter and a receiver; ii) Direct radiative transfer, when temperature increases rapidly in a short distance, hence a significant heat flux goes through the medium.

The radiative transfer, and therefore the thermal conductivity are strictly related to the optical properties of the mantle minerals, and also to the Fe-content.

In fact, thermal conductivity is controlled by the lifetime, or equivalently, the mean free path ( $\lambda$ ) of phonon–phonon collisions (Ziman, 1962): the more collisions there are, the shorter the mean free path and the smaller the conductivity. If physical scattering is negligible, mean free path is defined by:

$$\lambda \sim \frac{1}{A} \quad (\text{Eq. 3.3})$$

where  $A$  indicates the absorption coefficient. At the distance defined by the mean free path, half of the incident light is absorbed, i.e. stored in the solid. An opaque spectral region is a region with high back-reflection (photons are back-scattered, thus the light is extinguished in

short distance) and high absorbance. Opaque (=optically thick) mediums are characterized by  $k_{rad} = 0$ . The radiative transfer requires high transparency, and thus occurs under optically thin conditions.

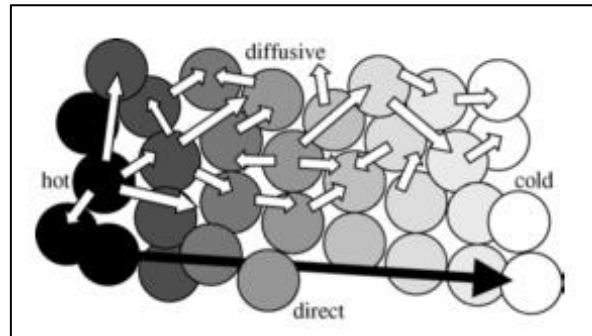


**Figure 3.2.** Schematics of diffusive vs. direct radiative transfer in an internally heated medium comprised of grains. In a low temperature gradient, each grain is effectively isothermal. The shades of the grains indicate the gradual temperature change. White arrows indicate diffusion. Black arrow denotes direct transfer of a photon from a hot to a cold grain: here, negligible interaction with the intervening grains occurs. Figure from Hofmeister (2005).

. The radiative transfer requires high transparency, and thus occurs under optically thin conditions. Radiative transfer also depends strongly and non-linearly on grain-size ( $d$ ) and on Fe-content ( $X$ ), since the absorption is controlled by the product  $dX$  (Beer's law) (Hofmeister, 2005). At low temperatures, high Fe-content enhances the diffusive radiative transfer ( $k_{rad,dif}$ ). However, the increase of  $d$  moves the maximum of  $k_{rad,dif}$  to low Fe-contents. Very Fe-rich minerals (opaque minerals) and very Fe-poor mineral (poor emitters) are both characterized by low  $k_{rad,dif}$ , thus the diffusive radiative transfer is maximum in moderated Fe-content (Hofmeister, 2005).

Furthermore, the thermal conductivity ( $k$ ) is directly related to the thermal diffusivity ( $D$ ) by:

$$D = \frac{k}{\rho C_p} \quad (\text{Eq. 3.4})$$

where  $\rho$  is density and  $C_p$  is heat capacity.

The equation (3.4) points out the strong dependency of the thermal conductivity on the composition, since both density and heat capacity are specific for every mineral phase.

As the reader can infer by this brief *excursus* on the heat transport mechanisms in the lithospheric mantle, a more realistic thermal conductivity model should take into account the chemistry and relative proportions of the mantle minerals.

As previously mentioned, the thermal conductivity model from Hofmeister (1999) does not explicitly consider the composition. Therefore, a new LitMod subroutine has been implemented to the code, in order to provide a more realistic model for the thermal conductivity. During my stay at Macquarie University (Sydney, Australia), I personally worked on the new Fortran subroutine which calculates the thermal conductivity following the model based on Grose and Afonso (2013).

The thermal diffusivity is derived from:

$$D(T) = a + b \exp(-cT) + d \exp(-eT) \quad (\text{Eq. 3.5})$$

with the tabulated coefficients for each mineral phase.

Then, the thermal conductivity is calculated by using equation (3.4).

The contribution of the radiative conductivity is a function of the temperature, composition, grain size, and optical properties of crystals (Hofmeister, 2005), and it is expressed by:

$$k_{rad}(T, d) = A \exp\left(\frac{(T-T_A)^2}{2x_A^2}\right) + B \left(\frac{(T-T_B)}{2x_B^2}\right) \quad (\text{Eq. 3.6})$$

where  $A$ ,  $B$ ,  $T_A$ ,  $T_B$ ,  $x_A$ ,  $x_B$  are all function of grain size  $d$  (further details in Grose and Afonso, 2013).

The new model of the thermal conductivity has been implemented in the updated version of the main program LitMod, which has been used for the modelling of the Himalaya-Tibetan orogen profiles (Chapter 5).

### 3.3. Densities

Stable mineral assemblages in the mantle are calculated using a Gibbs free energy minimization as described by Connolly (2005). The chemical composition is expressed in the NCFMAS system ( $\text{Na}_2\text{O}-\text{CaO}-\text{FeO}-\text{MgO}-\text{Al}_2\text{O}_3-\text{SiO}_2$ ). In this work, we used a modified version of the thermodynamic database of Holland and Powell (1998) (Afonso and Zlotnik, 2011). The resulting thermodynamic tables are generated by Perple-X (Connolly, 2005), describing densities, elastic and thermo-physical parameters of the end-member minerals. The asthenosphere has been considered to be compositionally homogeneous, due to its convective nature, whereas, the lithospheric mantle can show lateral compositional variations, depending on the geodynamic context of a certain region.

Within the crust, where mineral equilibria are not solved for, the density is calculated at each node of the mesh by using (Eq. 3.7) with an iterative process which stops when the density difference is  $\leq 0.01 \text{ kg/m}^3$

$$\rho_{(T,P)} = \rho_0 - \rho_0\alpha(T - T_0) + \rho_0\beta(P - P_0) \quad (\text{Eq. 3.7})$$

where  $\rho_0$  is the reference density at temperature  $T_0$  and pressure  $P_0$ ,  $\alpha$  is the thermal expansion coefficient and  $\beta$  is the compressibility.

### 3.4. Potential fields

Gravity calculations are performed by applying the Talwani's algorithm for polygonal bodies (Talwani et al., 1959) to the elements of the mesh, therefore considering both horizontal and vertical density variations. In order to avoid boundary effects, the models are extended horizontally  $1 \times 10^5 \text{ km}$  beyond the profile limits.

Due to the  $1/r^2$  dependency of the gravity field, where  $r$  is the distance to the density anomaly, gravity anomalies basically provide information on the density distribution at crustal and shallow depths (the short-wavelength part of the signal). Geoid height, on the other hand, is more sensitive to deeper density anomalies and to the topography of the LAB. Geoid anomaly is the height difference between two equipotential surfaces, indeed, and therefore it is a function of  $1/r$  instead of  $1/r^2$ , where  $r$  is the distance to the density anomaly (Turcotte and Schubert, 1982).

Geoid height is calculated converting the adjacent triangular elements of the mesh into rectangular prisms, then solving the integral of their gravity potential and substituting the result into the Brun's formula:

$$\Delta N = \Delta U / g_0 \quad (\text{Eq. 3.8})$$

where  $\Delta N$  is the geoid anomaly,  $\Delta U$  is the potential anomaly and  $g_0$  the normal gravity acceleration. Finally, the geoid anomaly obtained is expressed by:

$$\Delta N = \frac{G\rho}{g_0} \int_{x_1}^{x_2} \int_{y_1}^{y_2} \int_{z_1}^{z_2} \frac{1}{\sqrt{x^2+y^2+z^2}} dx dy dz \quad (\text{Eq. 3.9})$$

where  $G$  is the gravitational constant,  $\rho$  the rectangular prism density, and  $(x, y, z)$  the prism boundary coordinates. LitMod uses the method outlined by Zeyen et al. (2005), based on an analytical solution of equation (3.9), to obtain 2.5-D geoid heights along the model.

### 3.5. Mantle seismic velocities

Mantle seismic velocities are calculated as a function of composition, pressure and temperature. The calculation requires knowing the elastic moduli of each end-member mineral and the density of the bulk rock at the pressures and temperatures of interest.

While densities are obtained as described in Section 3.3, the elastic moduli of the aggregate (i.e., rock) are computed by a two-steps procedure as follows. The first step consists on applying a least squares procedure to infer the amounts of end-members (mole fractions) present in each stable phase. The moduli of each solution phase are then calculated as the arithmetic mean of the end-member moduli weighted by their respective molar proportions. In the second step, the elastic moduli of the bulk rock are computed following a Voigt-Reuss-Hill (VRH) average scheme:

$$M_B = \frac{1}{2} \left[ \left( \sum_{i=1}^n w_i / M_i \right)^{-1} + \sum_{i=1}^n w_i M_i \right] \quad (\text{Eq. 3.10})$$

where  $M_i$  and  $w_i$  are the moduli of the phases present and their volumetric fractions, respectively.

Finally, anelasticity effects are computed *a posteriori* as a function of the grain size, oscillation period, P-T conditions, and empirical parameters (further details in Afonso et al., 2008).

### 3.6. Elevation

According to the principle of isostasy, all regions of the Earth with the same elevation must have the same buoyancy when referenced to a common compensation level. LitMod assumes the compensation level at the base of the model, i.e.: the 410-km discontinuity. In order to estimate the absolute elevation one needs to perform a calibration with respect to a reference column. This reference column is taken at the middle ocean ridge (MOR), where elevation, petrogenetic processes and lithospheric structure are well-known. The elevation is calculated at each node of the mesh and its buoyancy is compared to the one at the MOR. The elevations above ( $E_a$ ) and below ( $E_b$ ) the sea level, are given respectively by:

$$E_a = \int_{L_{top}}^{L_{bottom}} \frac{\rho_b - \rho_l(z)}{\rho_b} dz - \varepsilon \quad (\text{Eq. 3.11})$$

$$E_b = E_a \frac{\rho_b}{\rho_b - \rho_w} \quad (\text{Eq. 3.12})$$

where  $L_{top}$  and  $L_{bottom}$  are, respectively, the upper and lower limit of the column,  $\rho_b$  is the mantle density at 400 km depth,  $\rho_l(z)$  is depth-dependent density,  $\rho_w$  is the water density (1030 kg/m<sup>3</sup>), and  $\varepsilon$  is a calibration constant which takes into account the average density

(according to the MOR composition and P-T conditions), the lithospheric structure and the elevation.

### 3.7 Sub-lithospheric anomalies

LitMod is able to consider thermal, compositional, or thermo-compositional anomalies relative to the surrounding sub-lithospheric mantle to explain seismic velocity anomalies imaged by tomography models.

In the case of thermal anomalies, the code assigns to the anomalous zone(s) the same composition as given to the asthenosphere (usually Primitive Upper Mantle, PUM), and recalculates the relevant physical parameters (density, seismic velocity, phase changes, and thermal conductivity) at P and  $T+\Delta T$  conditions,  $\Delta T$  being the prescribed temperature anomaly relative to the surrounding mantle. When the anomaly is compositional, the code calculates the relevant physical parameters at the T-P conditions, considering the prescribed chemical composition. Thermo-compositional anomalies can be related to lithospheric mantle bodies that have been detached and sunk into the asthenosphere and therefore, having a different temperature and composition than the surrounding asthenosphere. These sub-lithospheric anomalies can be coupled, when the density anomaly is transmitted to surface elevation, or decoupled, when density anomalies are not transmitted to surface elevation. Therefore, decoupled anomalies do not have effects on calculated isostatic topography but they do on gravity and geoid calculations.

### 3.8 Mantle characterization

As mentioned in Section 3.3 the LitMod approach defines the bulk composition by considering the relative amounts of the six major elements which compose the ~98% of the Earth's mantle: Na, Ca, Fe, Mg, Al, Si. These elements are used to define both the conductive and the convective mantle domains. Since the lithospheric mantle was formed by the differentiation of the primitive mantle that was residual after the Earth's core formation, it is geochemically different from the underlying asthenosphere. Commonly, the lithospheric mantle is relatively depleted in basaltic components, measured by lower Al-, Ca-, Fe-contents, and abundant in specific minor and trace elements (i.e. light rare-earth elements, Ti, Zr, Y). Due to its non-convective nature, the lithospheric mantle does not mix nor homogenize, but it preserves the fingerprint of large-scale tectonic events that involve fluid movement from the asthenosphere (tectonothermal events). Therefore, the degree of depletion, i.e. the degree to which a mantle composition have been modified by melt extraction, is highly variable from place to place, depending on the thermal history and on the formation mechanism.

In terms of major-element composition, calcium and aluminium are easily removed from the solid phase when mantle melting occurs (incompatible elements), while magnesium remains in the solid residue (compatible element). Iron is equally divided between both liquid and solid phases at relatively low pressures; however, at pressures  $\geq 3$  GPa, it prefers the residue at an increasing degree of melt extraction (Carlson et al., 2005). Therefore, element ratios involving Ca, Al, Mg and Fe are normally used to quantify the degree of depletion (Poudjom-Djomani et al., 2001). Depending on the P-T condition and on the bulk composition, different amounts of the major elements are accommodated in the four main mantle mineral phases (olivine, clinopyroxene, orthopyroxene, Al-rich phase). The physical properties of a solid assemblage thus depend not only on the volumetric proportions of the constitutive mineral phases and environmental variables (e.g., oxygen fugacity and stress/strain state) but also on their individual compositions (e.g., fayalite content in olivine).

Keeping this in mind, how can we select a NCFMAS? Which are the constraints for the lithospheric mantle composition? How does a selected NCFMAS affect the mantle densities and the seismic velocities?

The bulk composition of the lithospheric mantle can be represented as that of a peridotite, but tectonothermal processes can change this average composition considerably from one place to another, also affecting the physical properties of the lithospheric mantle. Thus, lithospheres with different tectonothermal histories are expected to have distinctive physical properties and different compositions.

The compositional heterogeneities of a peridotitic material in the upper mantle depend on the relative amounts of the three main constitutive minerals, i.e. olivine, pyroxenes, and an Al-rich phase which could be plagioclase, spinel, or garnet, depending on the equilibration pressure, and it typically defines the “facies” from which the samples have been recovered (e.g., garnet facies). By definition, a peridotitic rock can vary from almost 100% olivine (dunite) to ~40% olivine. Rocks with <40% olivine (e.g. pyroxenites, eclogites) are also important components of the lithospheric mantle. In addition, several studies (Hawkesworth et al., 1999; Gaul et al., 2000; Zheng et al., 2001; O’Reilly et al., 2001) show that the composition varies with the age of the lithospheric mantle, at least from Archean, to Proterozoic, and to Phanerozoic continental lithospheres. Data from mantle-derived xenoliths and garnet xenocrystals in volcanic rocks and exposed massifs document a secular compositional evolution of the lithospheric mantle through time, revealing a variation in Fe, Ca, Al contents from Archean to Phanerozoic times (Griffin et al., 2003, 2008; O’Reilly and Griffin, 2006; Poudjom-Djomani et al., 2001), as illustrated in Figure 3.3. The depletion in incompatible elements, in particular in Fe-content, has important consequences for geophysical properties, since it results in lower densities and higher seismic velocities (Artemieva, 2006; Poudjom-Djomani et al., 2001). In addition, considering the principle of isostasy, also the lithospheric thickness is expected to depend on the composition and therefore on the tectonothermal age. Most Archean lithosphere is thicker and cooler (today) than Phanerozoic lithosphere (O’Reilly and Griffin, 2006 and references therein).

Griffin et al. (2008) compiled estimates of the subcontinental lithospheric mantle composition, based on both garnet xenocrysts and the averages of well-studied xenolith suites.

Table 3.1 summarizes the characteristics for Archean (Archons), Proterozoic (Protons) and Phanerozoic (Tectons) lithospheric mantles.

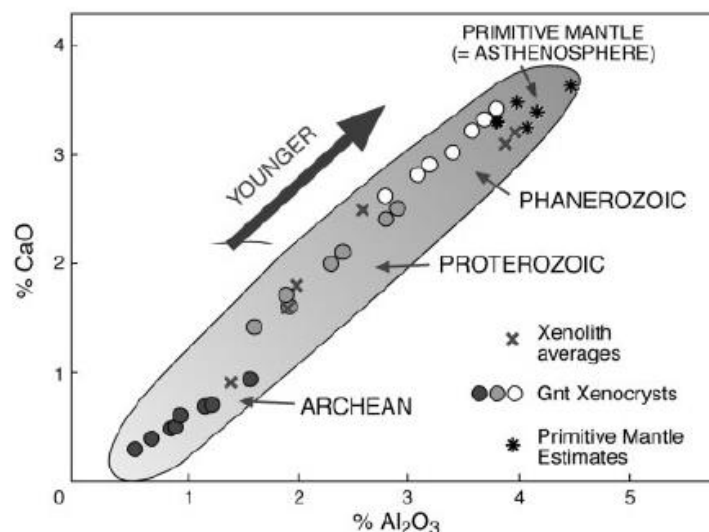


**Figure 3.3.** Secular evolution of subcontinental lithospheric mantle composition, using estimates for single areas based on garnet xenocrysts and xenolith suites and classified in terms of tectonothermal age (from Griffin et al., 2008).

**Table 3.1.** Lithospheric mantles are classified into Archons, Protons and Tectons in terms of the tectonothermal age (Janse, 1994; Griffin et al., 2003). Bulk compositions, expressed in weight %, come from Griffin et al. (2008) and references therein. PUM: Primitive Upper Mantle.

	Archons	Protons	Tectons	PUM
Age (x) [Ga]	x > 2.5	1 < x < 2.5	x < 1	--
thickness [km]	180 - 250	150 - 180	60 - 140	--
SiO <sub>2</sub> [%wt]	41.7 - 46.6	43.9 - 45.4	44.0 - 45.0	45.0 - 45.2
Al <sub>2</sub> O <sub>3</sub> [%wt]	0-30 - 2.2	0.64 - 3.7	2.3 - 3.9	4.0 - 4.5
FeO [%wt]	6.4 - 8.1	7.9 - 8.3	8.1 - 8.4	7.8 - 8.1
MgO [%wt]	43.8 - 50.4	39.9 - 4.6	38.7 - 41.4	37.8 - 38.3
CaO [%wt]	0.12 - 1.66	0.43 - 3.2	2.2 - 3.2	3.5 - 3.6
Na <sub>2</sub> O [%wt]	0.26 - 0.34	0.08 - 0.26	0.24 - 0.27	0.33 - 0.36

High depletion in Fe and Ca characterizes the Archean lithospheric mantle, which is mostly composed by Fe-poor harzburgites and lherzolites with high Mg/(Mg+Fe) ratios,

strongly subcalcic garnets, and high abundance of orthopyroxene, mainly enstatite, with typical modal fraction of ~32% (e.g. O'Reilly et al., 2001; Afonso et al., 2005). Clinopyroxene only reaches maximum values of ~3% (Zheng et al., 2001), whereas Mg-rich olivine ranges comprise modal fractions of ~60% in a typical Archean lithosphere (e.g. Siberia, Kaapvaal, Slave) (Gaul et al., 2000). These features support the interpretation of the Archean lithosphere as the product of high-degree partial melting, which has consumed most of the clinopyroxene during basalt extraction. As a consequence of this continuous Fe-removal, the solidus of the mineral assemblage rises while the mean density decreases. The combination of relatively low density, low Fe content, and low geothermal gradients, makes the Archean lithosphere stable and highly refractory. Unmodified Archean lithospheric mantle is unlikely to delaminate, or to melt extensively, and would be expected to persist even through major tectonic events. However, metasomatic processes could modify it through time, and this refertilization will affect its density and rheology.

Phanerozoic continental lithosphere shows the least degree of melt depletion, with high Ca and Al contents close to that of the undepleted asthenosphere (O'Reilly et al., 2001), abundance of clinopyroxenes (~20%) and garnets (~10%). Therefore, its density is relatively close to that of the asthenosphere. Refertilizations through metasomatic processes are commonly evidenced in mantle-derived xenoliths (Gaul et al., 2000). The Phanerozoic continental lithospheric mantle is, thus, less depleted, and commonly buoyant relative to the underlying asthenosphere when its geotherm is high, but will lose this buoyancy on cooling with major tectonic consequences (e.g. Poudjom Djomani et al., 2001; O'Reilly et al., 2001; Zheng et al., 2006).

In conclusion, the “young” regions located at plate boundaries, more likely to be affected by tectonic processes, are expected to be characterized by a Phanerozoic lithospheric mantle, whereas “old” (cratonic) stable areas, far from plate boundaries, are likely to be characterized by Archean mantle compositions.

The Zagros Mountains region and the Himalaya and Tibetan Plateau are located at plate boundaries and they have been affected by tectonic processes in Cenozoic time, then, in agreement with the distribution of the age of the last tectonothermal event (Figure 3.4) the composition of the lithospheric mantle should be Phanerozoic or neo-Proterozoic.

But, what does Phanerozoic composition mean? For Griffin and co-workers (2008) four different sets of NCFMAS elements can be defined as Phanerozoic mantle compositions, with density and P-wave velocities values varying, at 100 km depth, from 3365 kg/m<sup>3</sup> to 3385 kg/m<sup>3</sup> and from 8.20 km/s to 8.23 km/s, respectively. Similarly, nine different NCFMAS sets are included in the Archean mantle definition and six NCFMAS sets in the Proterozoic mantle. Furthermore, upper mantle processes like subduction, slab break-off, convective-removal, delamination, extensive melting, the presence of plumes, or metasomatic events, could have modified the tectonothermal age-classified composition, re-fertilizing an Archean keel or modifying Phanerozoic mantle material. Therefore, unless mantle xenoliths studies are available in the study region providing a local but direct picture of the subcrustal

domain, the identification of the lithospheric mantle bulk composition with the only clue of the age, remains a real challenge.

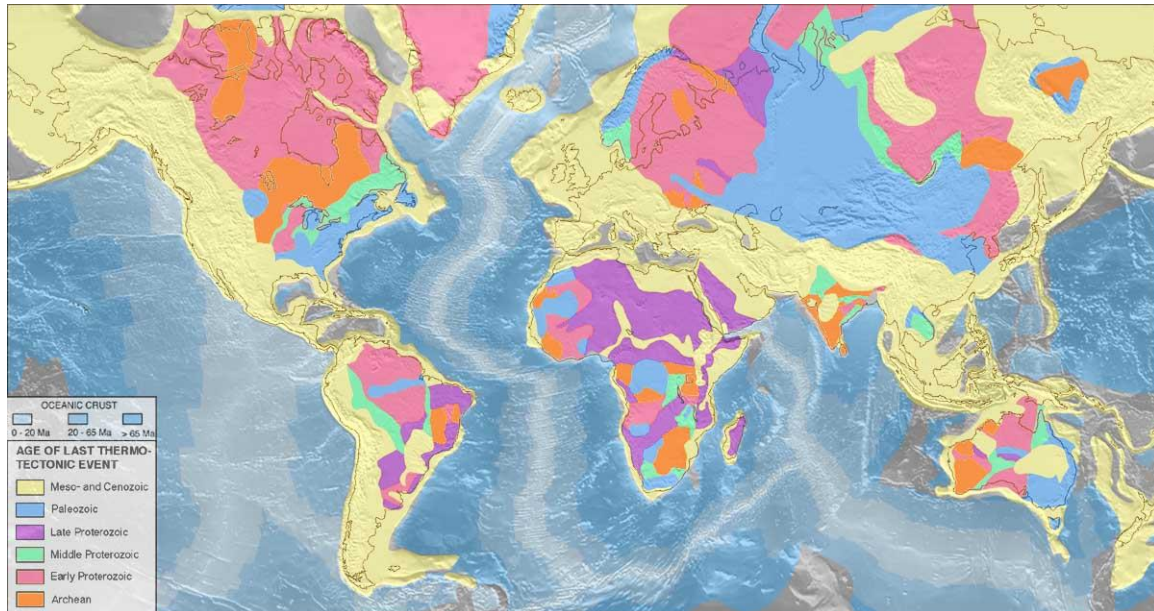


**Figure 3.4.** Classifications of the crustal domains in terms of the age of the last tectonothermal event. Figure from IUGS web page (<http://iugs.org/index.php>).

The lack of uniqueness in the values of physical properties, such as density or seismic velocities, as illustrated in Figure 3.5, is a further major problem in identifying the mantle composition of a certain region. Archean and Phanerozoic mantles, although being characterized by different density values (ranging from  $3285 \text{ kg/m}^3$  to  $3330 \text{ kg/m}^3$  and from  $3330 \text{ kg/m}^3$  to  $3365 \text{ kg/m}^3$ , respectively, for a 150 km-thick lithosphere), share the same range of values in seismic velocities, especially P-wave velocities.

The simultaneous fitting of all available geophysical and petrological observables (gravity anomaly, geoid height, surface heat flow, thermal conductivity, elevation, available xenolith data, and seismic velocities or seismic velocity anomalies), like in the LitMod approach, reduces the uncertainties associated with the modelling. However, recent works by Afonso et al. (2013a, b) analyse the non-uniqueness of the compositional space and the dissimilar sensitivities of physical parameters to temperature and composition, and show that a wide range of compositions can, equally well, explain multiple geophysical data. This work is based on a non-linear 3D multi-observable probabilistic (Bayesian) inversion approach which analyses the trade-off between temperature and compositional effects on wave velocities.

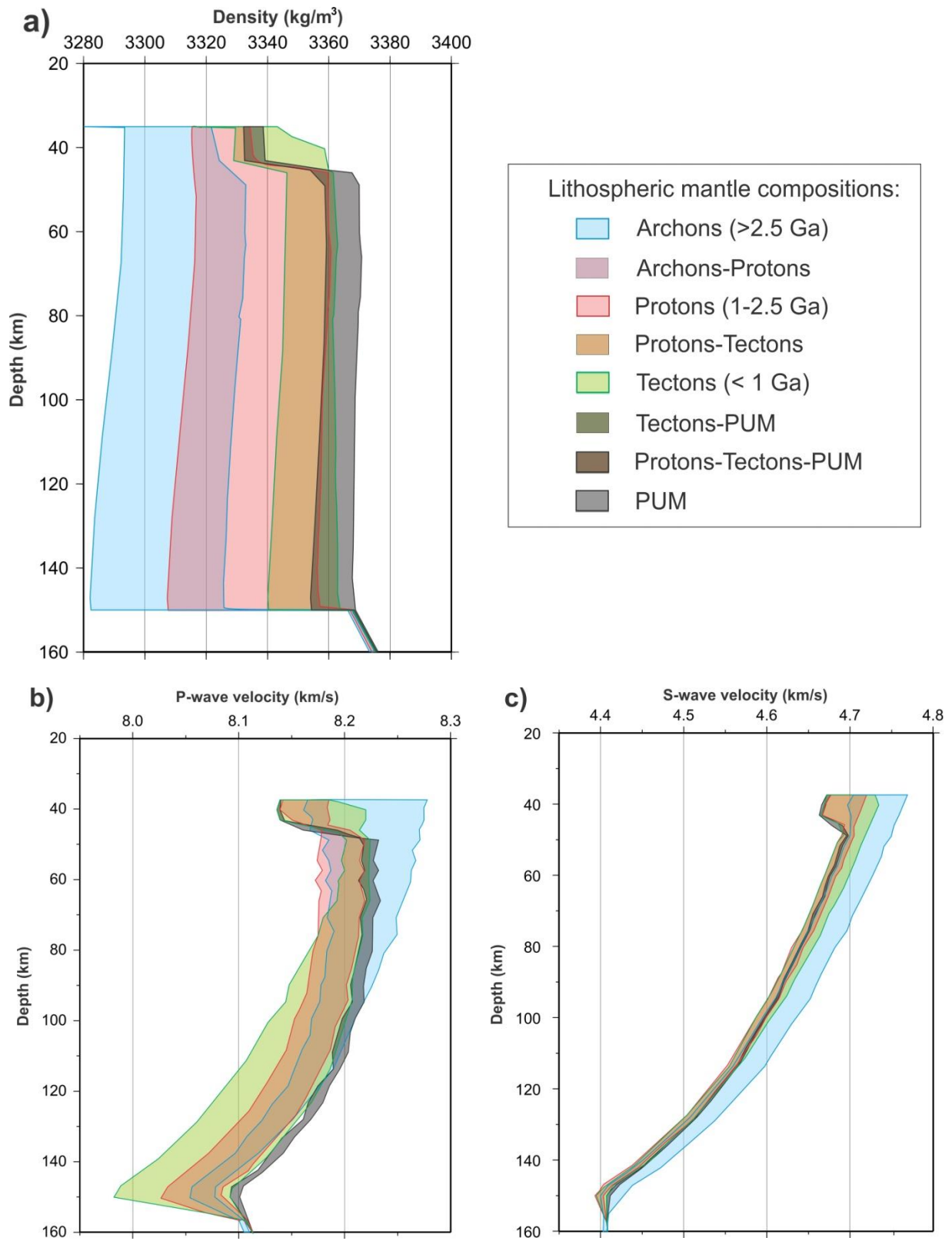


**Figure 3.5.** Density-depth (panel a) and velocity-depth (panels b, c) ranges for different lithospheric mantle compositions, calculated considering the Moho and the LAB discontinuity at 35 km and 150 km depth, respectively. Compositions are taken from Griffin et al. (2008). PUM: Primitive Upper Mantle.

Anderson and Isaak (1995) experimentally found that Mg- rich olivine (e.g. Fo92–94, typical of depleted mantle regions) has lower density but higher seismic velocity than Fe-rich olivine (e.g. Fo88–90, typical of more fertile mantle regions). A change in the forsterite content of olivine by 1% ( $=0.01XMg$ ) changes its density by 0.3% and its mean  $V_s$  by 0.22%.

Analytically, I found that seismic velocities, in particular P-wave velocities, are mostly controlled by the amount of  $Al_2O_3$  and MgO in the bulk composition. An increase of  $Al_2O_3$  content increases the density and moderates the seismic velocities. An increase of the MgO with respect to FeO decreases the density but increases the seismic velocities.

However, despite these considerations, the current integrated methodology applied in this Thesis does not allow resolving for the mantle compositions univocally. Chosen compositions in the modelled profiles are compatible with the global geochemical xenolith data and the tectonothermal age of the different domains, but the intrinsic problem of non-uniqueness of the compositional space remains.

## Chapter 4: The Zagros orogen

The Zagros Mountains are the result of the long-standing convergence between the Arabian Plate and Gondwana-derived tectonic fragments of the southern margin of the Eurasian Plate. The area has been the subject of numerous geophysical surveys and tectonic studies mainly focused on both the sedimentary cover and the basement units that configure the inner parts of the Zagros Mountains (Sanandaj Sirjan and Urumieh Dokhtar domains). During the last decade, many efforts have been devoted to unravelling the lithospheric structure and, particularly, in imaging the topography of the crust–mantle boundary (e.g. Paul et al. 2006, 2010; Gök et al. 2008; Gritto et al. 2008; Sodoudi et al. 2009; Manaman et al. 2011; see also Jiménez-Munt et al. 2012 for a thorough compilation on crustal thickness data).

Studies dealing with the subcontinental mantle structure are scarce and include global, regional and local teleseismic models (e.g. Maggi and Priestley 2005; Alinaghi et al. 2007, Kaviani et al. 2007; Manaman and Shomali 2010; see next sections for a more complete reference list). Results from these studies show fast mantle seismic velocities in the Arabian Plate and slower seismic velocities in Central Iran. Surface waveform tomography (Maggi and Priestley 2005) suggests a thin lithosphere beneath the Turkish–Iranian plateau probably related with partial delamination of an earlier thickened lithosphere. Tomographic cross-sections presented by Alinaghi et al. (2007) show northward-dipping high-velocity mantle anomalies beneath Central Iran, which can be interpreted as remnants of the subducted Neotethys oceanic lithosphere, as was later noted by Paul et al. (2010). Shomali et al. (2011) investigated the upper-mantle structure of the Zagros Mountains in southwest Iran, using traveltimes teleseismic tomography. The results show a thick (more than 200 km) continental lithosphere in the Arabian Platform, while very thin (or no) lithospheric mantle is seen in Central Iran. The authors also noted the presence of a disconnected cold NE-dipping oceanic slab or detached mantle lithosphere beneath Central Iran, suggesting a lithospheric delamination below the main Zagros fault (MZF).

The lithospheric mantle thinning below the Iranian Plateau was also proposed during the 1970s–1980s from earthquake distribution and focal mechanisms (Bird 1978) and from gravity and flexural studies (Snyder and Barazangi 1986). Integrated 2-D models combining lithostatic, gravity and thermal equations (Molinari et al. 2005; Motavalli-Anbaran et al. 2011) confirmed a pronounced lithospheric mantle thinning from the Arabian Plate to Central Iran along several lithospheric cross-sections. Jiménez-Munt et al. (2012) calculated the lithospheric structure of Iran with the aim of separating the regional/residual gravity anomalies. These authors used a 1-D approach combining geoid height and elevation data and considering the crust as a homogeneous layer with a constant average density and a temperature-dependent lithospheric mantle density. The authors also found that the Mesopotamian–Persian Gulf foreland basin is characterized by a thick lithosphere, which thins out drastically underneath the high Zagros and Central Iran.

A remarkable feature is that, all the previously referred lithospheric models in the region (e.g. Molinaro et al. 2005; Motavalli-Anbaran et al. 2011; Jiménez-Munt et al. 2012) are based on a ‘pure’ thermal approach. Conversely, in this work, I apply the method described in Chapter 3, the self-consistent petrological-geophysical LitMod modelling (Afonso et al., 2008; Fullea et al., 2009), which integrates potential fields (gravity and geoid), isostasy (elevation), thermal equations (heat flow and temperature distribution) and mantle mineral physics.

I present the crust and upper mantle structure down to 400 km depth along two transects across the Arabia–Eurasia collision from the Mesopotamian–Persian Gulf Foreland Basin (Arabian Foreland Basin) to Central Iran (Figure 4.1), whose location was selected based on the availability of data and previous works. Most of the content of this chapter has been published in Tunini et al. (2015) and I kept the original text when possible.

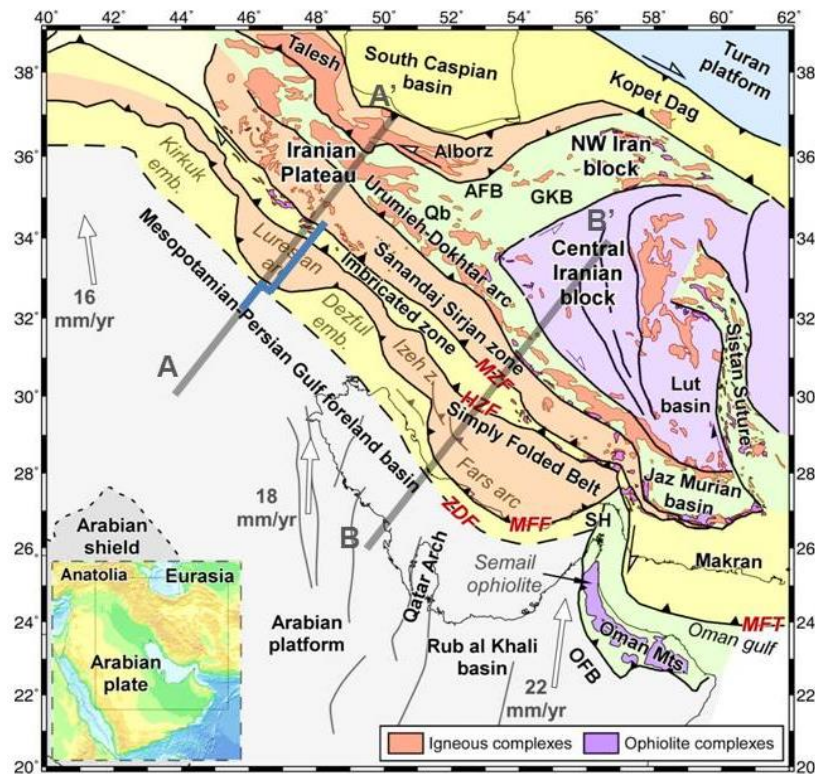


**Figure 4.1.** Structural map showing the main tectonic units of the Zagros Mountains and adjacent areas, including major igneous and ophiolitic complexes, and location of the selected profiles (thick grey lines) A-A' and B-B' (modified after Jiménez-Munt et al., 2012). The colours assigned to the different tectonic units are not related to age or lithology but are used to highlight their limits. White arrows correspond to the relative plate velocities of the Arabian plate with respect to a fixed Eurasian plate. Light-blue line indicates the balanced geological cross-section by Vergés et al. (2011). ZDF: Zagros deformation front; MFF: Mountain Frontal Fault; HZF: High Zagros Fault; MZF: Main Zagros Fault; Qb: Qom basin; GKB: Great Kabir basin; and AFB: Alborz foredeep basin; OFB: Oman foreland basin; SH: Strait of Hormuz; MF: Minab Fault; MFT: Makran Frontal Thrust.

## 4.1 Data

The modelling approach used in this study was constrained by four different types of data: 1) Elevation, surface heat flow, and potential field data collected from global databases. 2) Crustal structure and Moho depths derived from geological cross-sections and waveform inversion, receiver functions, and receiver functions coupled with surface wave analysis. 3) LAB geometry inferred from numerical models, seismic tomography models and, partly, from receiver functions. Since Moho and LAB depths contain intrinsic uncertainties depending on the experimental and modelling approaches, they were used to construct the initial lithospheric structure model and were then further modified within the uncertainties range. 4) Mantle seismic velocities inferred from seismic tomography models (global and regional) and from some seismic profiles. Due to the scarcity of xenolith suites in the study area, we estimated the composition of the lithospheric mantle, according to the crustal tectonothermal age of the different domains, following global studies (e.g., Griffin et al., 2003, 2009; O'Reilly and Griffin, 2006).

### 4.1.1 Regional geophysical data

Gravity data (Figure 4.2a) for Iran came from Getech 10 x 10 km grid data (<http://www.getech.com>), while in the rest of the region, the Bouguer anomaly was computed by applying the complete Bouguer correction to satellite free-air data (Sandwell and Smith, 1997) using the FA2BOUG code (Fullea et al., 2008) with a reduction density of  $2670 \text{ kg/m}^3$ . Geoid height data were derived from the Earth Geopotential Model EGM2008 (Pavlis et al., 2008) with spatial resolution of 5 min-arc. Long wavelengths ( $>4000 \text{ km}$ ) have been removed by subtracting spherical harmonics up to degree and order 9 to avoid deep density variations ( $>400 \text{ km}$ ). The obtained geoid anomaly is shown in Figure 4.2b with maximum amplitude of  $\sim 30 \text{ m}$  over a distance of 500 km between the Persian Gulf and SE-Zagros.

Surface heat flow measurements (Figure 4.3), although being particularly abundant in Red Sea, Gulf of Aden, Anatolia and Caspian Sea, are very scarce in Iran and the Arabian Platform (e.g., Förster et al., 2007; Lucazeau et al., 2010; Pollack et al., 1993; Rolandone et al., 2013). A total of three heat flow sites were available in the study region located over 100 km far from the selected profiles. Therefore, we are not considering surface heat flow as a constraint in our modelling.

Elevation data (Figure 4.4) come from 1x1-min arc resolution ETOPO1 (Amante and Eakins, 2009) global elevation model (<http://www.ngdc.noaa.gov/>). The Arabian Platform and the foreland basin show a smooth topography with a minimum in the Persian Gulf, whereas in the Zagros Mountains the elevation increases rapidly from sea level to 1500 m in the ZFTB, achieving an average of 3000 m of altitude in the Imbricate Zone and in the Alborz.

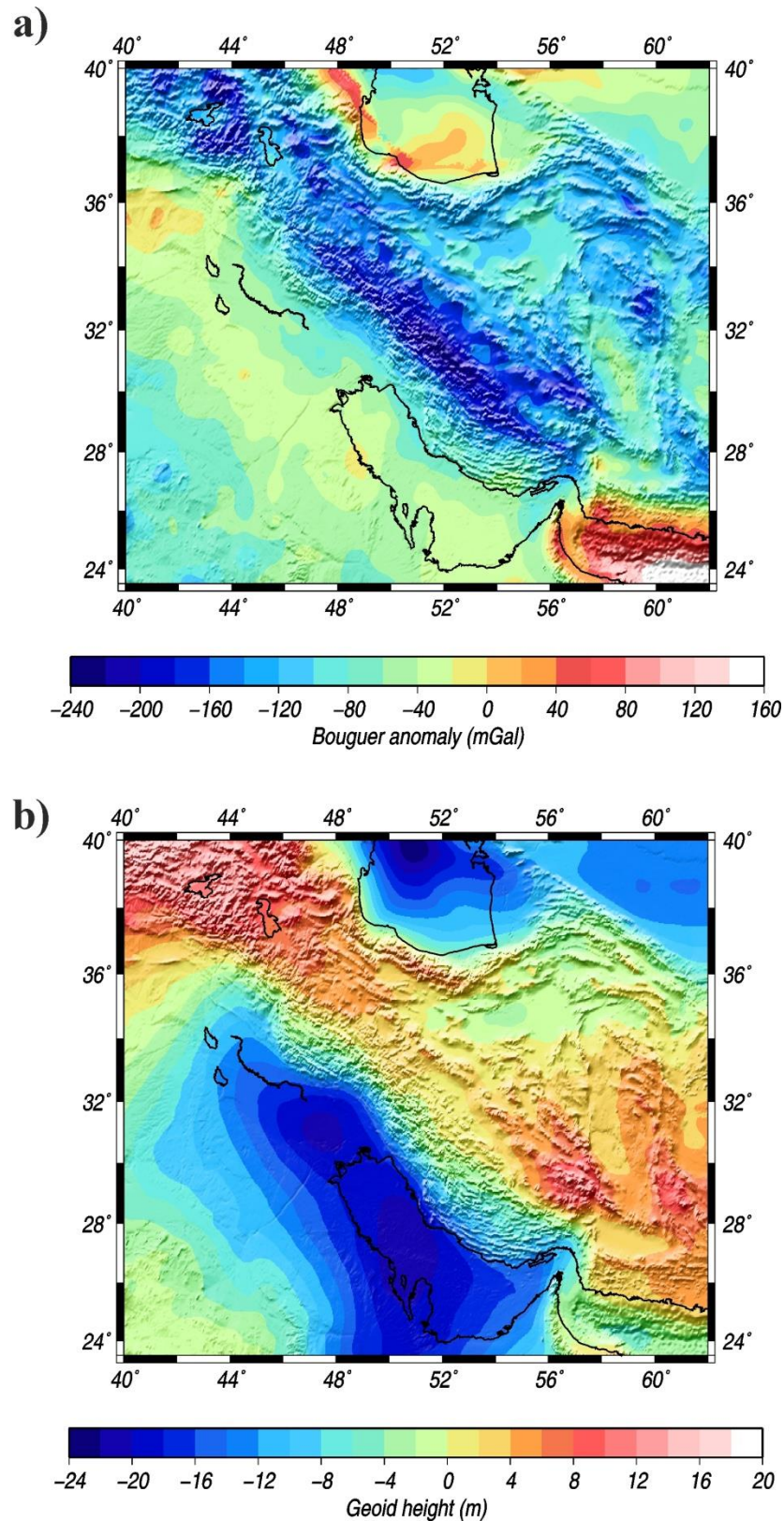


**Figure 4.2.** Potential fields in the study area. (a) Bouguer anomaly from Getech data in Iran and calculated from satellite free-air anomaly in the rest of the region (see text for details). (b) Geoid height from EGM2008 model. Spherical harmonics up to degree and order 9 have been removed. Shading indicates elevation.

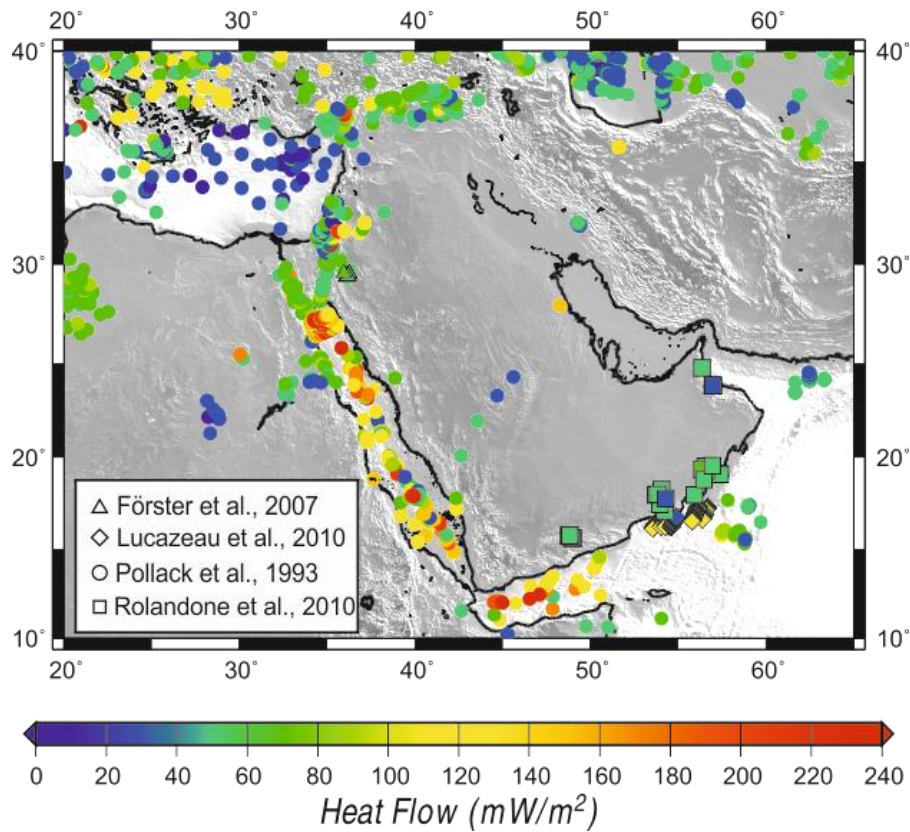


**Figure 4.3.** Heat flow measurements in the Arabian plate, Red Sea, Gulf of Aden, Eastern Mediterranean Sea, Anatolia region, Caspian Sea and Zagros Mountain region.

### 4.1.2 Crustal structure and depth to the Moho

Figure 4.4 shows a compilation of obtained Moho depth values inferred from seismic studies, using receiver functions and surface-wave dispersion analyses. Crustal thickness varies from 35 to 45 km in the Mesopotamian Foreland and Arabian Platform and between 44 and 69 km below the Zagros Mountains with the maximum values beneath the SSZ zone (Gök et al., 2008; Gritto et al., 2008; Nasrabadi et al., 2008; Paul et al., 2006 and 2010; Manaman et al., 2011). A crustal root is identified below the Alborz (Nasrabadi et al., 2008; Paul et al., 2010; Sodoudi et al., 2009; Radjaee et al., 2010), with the crust-mantle boundary at depths of 53 to 67 km. See also Jiménez-Munt et al. (2012) for a thorough compilation of crustal thickness data.

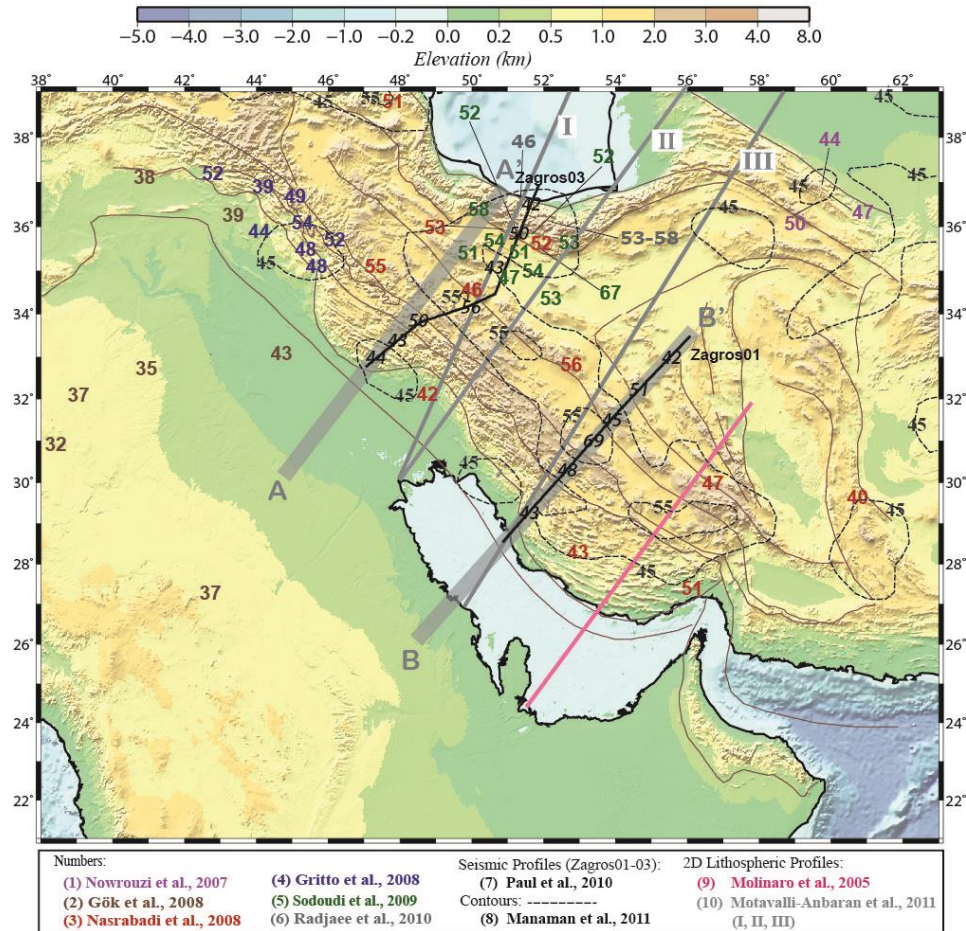


**Figure 4.4.** Topography map of the study area, crustal thickness values (numbers) and 2D-lithospheric modelling profiles (heavy continuous lines, grey and pink) from other studies (modified after Jiménez-Munt et al., 2012). Black dashed contours are the results from regional tomographic models (Manaman et al., 2011). Grey wide lines denote the localisation of A-A' and B-B' profiles of this study. Grey thin lines correspond to the main structural boundaries (see Figure 4.1).

The geological structure of the Zagros Mountains is outlined by different studies (e.g., McQuarrie, 2004; Mouthereau et al., 2007; Casciello et al., 2009; Emami et al., 2010; Vergés et al., 2011), detailing the stratigraphy of the Zagros Fold-and-Thrust belt and showing evidences for the compressive deformation affecting both the sedimentary cover and basement. We also used geological cross-sections, available from the geological maps by the National Iranian Oil Company (NIOC) to construct the shallower part of the profiles (7-10 km depth).

Our A-A' profile runs parallel to the geological cross-section by Vergés et al. (2011) and continues NE-wards, following approximately the northern seismic profile (Zagros03) by Paul et al. (2010), and southwards through the Mesopotamian Foreland Basin. Profile B-B' coincides with the southern transect (Zagros01) by Paul et al. (2006, 2010), and extends

south-westwards crossing the Persian Gulf (Figures 4.1 and 4.4) until it reaches the Arabian Platform.

### 4.1.3 Depth to the lithosphere-asthenosphere boundary

The LAB depth of the Arabia-Eurasia collision zone has been investigated by using numerical models integrating different geophysical data (Molinaro et al., 2005; Motavalli-Anbaran et al., 2011; Jiménez-Munt et al., 2012), and by using seismic techniques (Hansen et al., 2007; Mohammadi et al., 2013). Molinaro et al. (2005) show a profile crossing perpendicularly the southern Zagros (Figure 4.4) and propose a sharp lithospheric thinning below the range. Their results show that the LAB shallows from ~220 km beneath the Persian Gulf to ~100 km beneath the ZFTB, deepening again north-eastwards to depths of 140 km in Central Iran. Motavalli-Anbaran et al. (2011) present three SW-NE transects crossing Iran from the Arabian Platform to the South Caspian Basin and the Turan Platform. The results suggest that the lithospheric thinning (LAB depths of 100-120 km) affects the northern Zagros Mountains extending to Central Iran. Jiménez-Munt et al. (2012), show a thick lithosphere beneath the Persian Gulf and the ZFTB (180-220 km) thinning underneath the SSZ and Central Iran (160-140 km).

Results from receiver function studies reveal trends similar to the numerical models, but a consistently shallower LAB. Mohammadi et al. (2013) image the LAB at ~130 km depth beneath the ZFTB, ~150 km beneath the SSZ, and 80-85 km in Central Iran. In the Arabian Platform, Hansen et al. (2007) propose the base of the lithosphere as lying at ~160 km depth in the Arabian Shield-Platform boundary (~45°E longitude), shallowing north-eastwards to ~135 km depth.

### 4.1.4 Mantle seismic velocities

Figure 4.5 shows the Vp anomaly distribution along the selected profiles, resulting from a global tomography model based on P-wave arrival times. The global P-wave velocity model shown here has been obtained using the same method described in Bijwaard et al. (1998), incorporating additional earthquakes from 1995 to 2002 and arrival times (Villaseñor et al., 2003). In total, more than 14 million arrival times from 300,000 earthquakes were reprocessed using the EHB methodology (Engdahl et al., 1998). The ray paths corresponding to these new arrival times sample, mainly, the uppermost mantle with a resolution of  $0.5^\circ \times 0.5^\circ$  in area and 25-50 km in depth. Along the A-A' transect, a 50° NE-dipping boundary is interpreted as the Arabia-Eurasia boundary lying along the MZF. High velocity perturbations (>1%) are imaged, extending from the Arabian Platform to the MZF, reaching the ~200 km depth. A slab feature is dipping towards the NE beneath the Sanandaj Sirjan Zone. Along the B-B' transect, the maximum of the high velocity feature is localised beneath the Arabian

Platform and the Persian Gulf, until ~230 km depth. The lateral transition to the low velocity anomaly of the Central Iran is less abrupt than along the A-A' profile. Slight lateral velocity variations ( $\pm 0.2\%$ ) characterise the lithospheric mantle beneath the Zagros Mountains, and small features with inverse velocity can be observed in the shallower mantle below the MFF discontinuity (low velocity anomaly down to 50 km depth) and below the Imbricated Zone (high velocity at 50-100 km depth).

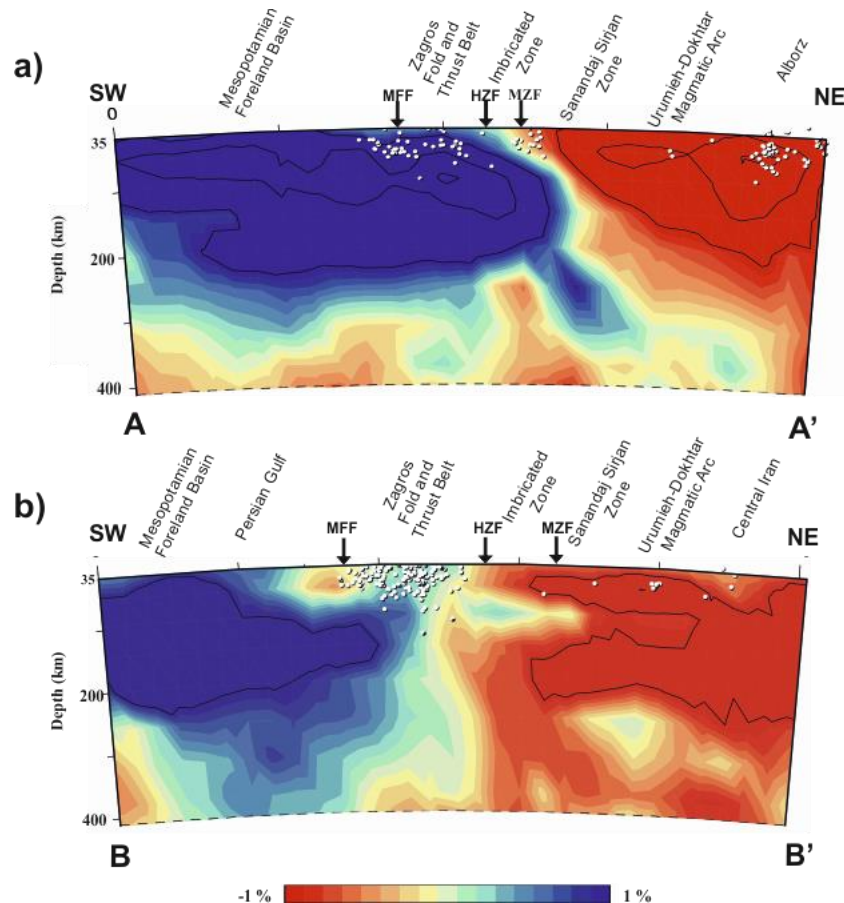


**Figure 4.5.** P-wave tomography along A-A' (a) and B-B' (b) profiles from 35 to 400 km depth. Global reference model used - AK135 (Kennett et al., 1995). HZF: High Zagros Fault; MFF: Main Frontal Fault; MZF: Main Zagros Fault.

The sharp change in seismic velocities in the Arabia-Eurasia collision zone is also observed in other published tomography profiles (Kaviani et al., 2007; Maggi and Priestley, 2005; Manaman and Shomali, 2010; Ritzwoller et al., 2002). The Arabian lithosphere is, overall, characterized by high seismic velocity, while the Iranian lithosphere is markedly slower. The transition between the two velocity domains is located, approximately, beneath the MZF. However, it is still unclear whether low velocities characterize only the lithospheric mantle beneath Central Iran or also the lithospheric mantle beneath the inner parts of the Zagros Mountains (UDMA and SSZ). Manaman and Shomali (2010) observed low velocities

below the Urumieh Dokhtar Magmatic Arc, whereas, Maggi and Priestley (2005) only observed them below Central Iran. Alinaghi et al. (2007) observed a change in the low velocities across the strike of the Zagros Mountains, with the high velocities of Arabia penetrating more into Iran in the NW Zagros than in the central Zagros (nearby our B-B' profile). Kaviani et al. (2007) found high S-wave velocities beneath the Zagros Mountains and low S-wave velocities in the shallow mantle below the SSZ and UDMA regions. According to the authors, the 0.5 km/s difference of  $V_s$  is, likely, due to a compositional change associated with high temperatures beneath the Sanandaj Sirjan and Urumieh Dokhtar Magmatic Arc. Simmons et al. (2011), using a multi-event location approach and 3D-ray tracing, imaged a fast-velocity anomaly beneath the Arabian Platform extending several kilometres beneath Iran at a depth of ~150 km, which is interpreted as the underthrusting of the Arabian lithosphere beneath Central Iran.

#### 4.1.5 Lithospheric mantle composition

Global data from mantle-derived xenoliths and garnet xenocrystals in volcanic rocks and exposed massifs document a secular compositional evolution of the lithospheric mantle through time, revealing a depletion in Fe, Ca, Al contents from Phanerozoic to Archean times (Griffin et al., 2003, 2009; O'Reilly and Griffin, 2006; Poudjom-Djomani et al., 2001). Depletion in incompatible elements, in particular Fe, has important consequences for geophysical properties, since it results in lower densities and higher seismic velocities (Artemieva, 2006; Poudjom-Djomani et al., 2001). In this work, we assume that the formation (or modification) of crust and mantle are broadly contemporaneous and, hence, we refer to the tectonothermal age of the crust in order to constrain the composition of the lithospheric mantle.

The age of the Iranian lithosphere is <50 Ma, whereas, available geochronological data indicate a Neo-Proterozoic age (540-850 Ma) for the Arabian Platform (Artemieva, 2006; Stern and Johnson, 2010). Therefore, we consider Proterozoic compositions for the lithospheric mantle beneath the Arabian Foreland Basin and a more fertile Phanerozoic composition for the lithospheric mantle below the Zagros Mountains.

Due to the scarcity of mantle-derived xenoliths in the study region, we adopted standard NCFMAS compositions from Griffin et al. (2009) for the lithospheric mantle bodies. The chosen compositions provide the best fit of seismic velocities, densities (elevation) and potential fields. The asthenosphere is considered to have a primitive upper mantle (PUM) composition (McDonough and Sun, 1995). In order to smooth the compositional change between the lithospheric mantle and the underlying asthenosphere, we introduced a layer of 10-20 km thickness with an intermediate composition between the asthenosphere and the corresponding lithospheric mantle above. Table 4.1 summarises the mantle compositions considered in this study.

**Table 4.1.** Chemical compositions used in the models for mantle bodies (see Figures 4.8 and 4.9).

<b>Mantle compositions in the NCFMAS system (%)</b>				
	<b>Mantle 1</b>	<b>Mantle 2</b>	<b>Mantle 3</b>	<b>Asthenosphere - PUM</b>
	<i>Pr3</i>	<i>Pr6</i>		
	<i>Proterozoic</i>	<i>Proterozoic</i>	<i>Pr3-Tc3*</i>	<i>Primitive Upper Mantle</i>
	<i>(Griffin et al., 2009)</i>	<i>(Griffin et al. 2009)</i>		<i>(McDonough and Sun, 1995)</i>
<b>SiO<sub>2</sub></b>	45.2	45.4	45	45
<b>Al<sub>2</sub>O<sub>3</sub></b>	2	3.7	3	4.5
<b>FeO</b>	7.9	8.3	7.9	8.1
<b>MgO</b>	41.6	39.9	42	37.8
<b>CaO</b>	1.9	3.2	1.9	3.6
<b>Na<sub>2</sub>O</b>	0.13	0.26	0.13	0.25
<b>Total</b>	98.73	100.76	99.93	99.25

\*Intermediate composition between Pr3 (Proterozoic) and Tc3 (Phanerozoic) from Griffin et al. (2009).

Figure 4.6 illustrates how lithospheric mantle composition affects the resulting density and seismic velocities in a 210 km thick lithosphere with a 42 km thick crust, which is a representative structure of the Arabian plate. All compositions show a density increase ranging from 10 kg/m<sup>3</sup> for Mantle 1 to 25 kg/m<sup>3</sup> for PUM around 50 km depth, related to the spinel-garnet phase transition. The spinel-garnet transition marks also an increase in P-wave velocities ranging from 0.05 km/s for Mantle 1 and 0.08 km/s for PUM, and an increase in S-wave velocities of 0.01-0.02 km/s. Down to this phase transition, the density and seismic velocity depth variations are very similar for all compositions, increasing with depth for density and P-waves and decreasing for the S-waves, until the LAB. The lighter composition corresponds to Mantle 1, which is ~12 kg/m<sup>3</sup> less dense than Mantle 3, ~ 27 kg/m<sup>3</sup> less dense than Mantle 2, and ~ 37 kg/m<sup>3</sup> less dense than PUM. Note that the density-depth evolution within the lithospheric mantle depends on the competing effects of temperature and pressure and, therefore, on the lithospheric structure. The depleted Mantle 1 is also markedly slow with respect to the other composition types, particularly, for the P-wave velocities, being ~0.04 km/s slower than Mantle 2 and 0.05 km/s slower than the fertile PUM.

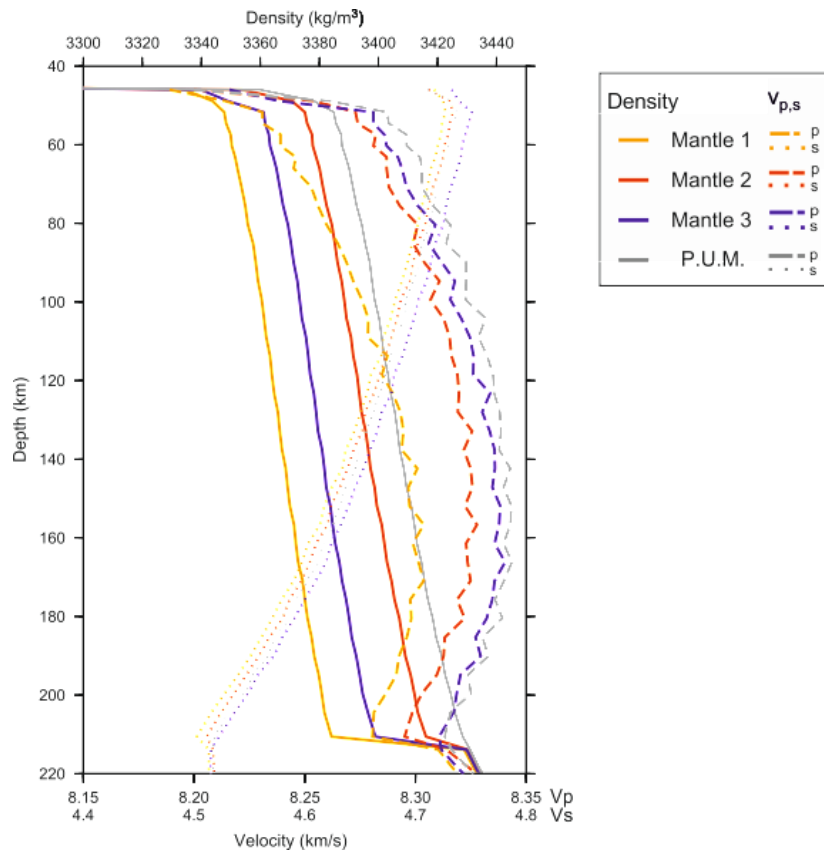


**Figure 4.6.** Density and velocity variations with depth for each mantle composition, considering a Moho discontinuity at 42 km depth and LAB at 210 km depth. Mantle compositions refer to Table 4.1.

## 4.2 Results

The forward modelling scheme required an initial model including the geometries of the crustal and lithospheric mantle bodies and their physical parameters. As a general procedure, we kept the initial crustal model (geometry and physical parameters) and we only modified it when strictly necessary, in order to fit the high frequency components of topography and gravity signals, after trying different mantle compositions and mantle bodies' geometries. Crustal modifications are always within the uncertainties associated with experimental data. The final lithosphere geometry, as well as chemical composition and physical parameters are assigned in order to obtain the best fit with all the observables (gravity, geoid, elevation, mantle seismic velocities and derived tomography models).

## 4.2.1 Crustal structure

The resulting best fit crustal models for the selected A-A' and B-B' profiles are shown in Figure 4.7. The different lithologies are characterised by the physical parameters detailed in Table 4.2. In the sedimentary cover, we distinguished Tertiary, Mesozoic and Palaeozoic sediments. The Sanandaj Sirjan Zone and the Urumieh Dokhtar Magmatic Arc are characterised by granitic and metamorphic complexes, differently distributed along the two profiles.

**Table 4.2.** Physical properties of the materials used in the modelling: depth-varying density  $\rho$ ; thermal conductivity  $K$ ; radiogenic heat production  $H$ . The heat production in the lithospheric mantle is  $0.02 \mu\text{W}/\text{m}^3$ .

<i>Material description</i>	<i>Density <math>\rho</math> [<math>\text{kg}/\text{m}^3</math>]</i>	<i>Thermal conductivity <math>K</math> [<math>\text{W}/\text{K}\cdot\text{m}</math>]</i>	<i>Heat Production <math>H</math> [<math>\mu\text{W}/\text{m}^3</math>]</i>
Cenozoic Sediments	2450-2580	2.0	1.0
Mesozoic and Imbricated Zone Sediments	2650	2.0-2.5	1.0
Paleozoic Sediments	2700	2.5	1.0
Granitoids - Melange	2730-2780	2.0-3.1	1.0-2.0
Metamorphic rocks	2850	2.0	0.5
Upper Crust	2820-2840	3.0	1.0
Lower Crust	2980-2995	2.2	0.4
High Dense Lower Crust	3500	2.0	0.25

The crystalline basement is represented by the upper-middle crust and the lower crust. Along the A-A' profile each of these layers is  $\sim 15$  km thick in the Arabian Platform and foreland basin, and they vary their relative thicknesses towards the NE. Along B-B' profile, the lower crust is considerably thicker than the upper-middle crust from the foreland basin to Central Iran, particularly, in the Sanandaj Sirjan Zone where the crust-mantle boundary reaches 63 km depth. In order to reconcile gravity, geoid and elevation data with the crustal thickness inferred from receiver functions (Paul et al., 2006 and 2010), we included a high density lower-crustal body at depths of  $\geq 50$  km, with a density of  $3500 \text{ kg}/\text{m}^3$ . This body would correspond to a 100% eclogitised lower crust, characterised by relatively low velocity and high density. Alternatively, we can also consider a  $\sim 10$  km shallower Moho which would require a slight modification of the upper and middle crustal bodies in this region.

## 4.2.2 Lithospheric mantle structure

The best fit models along the selected profiles are illustrated in Figures 4.8, 4.9, 4.10 and 4.11, with the crustal structures described previously and shown in Figure 4.7. The data

adjustments for both profiles are shown in Table 4.3. The Root Mean Square Error (RMSE) between observed and calculated data has been determined according to

$$\text{RMSE} = \frac{\left[ \sum_{i=1}^N (x_{(i)\text{obs}} - x_{(i)\text{calc}})^2 \right]^{1/2}}{N} \quad (\text{Eq. 4.1})$$

with  $x_{\text{obs}}$  and  $x_{\text{calc}}$  being the observed and calculated data, respectively, and  $N$  is the total number of points along the profile depending on the horizontal discretization.

**Table 4.3.** The RMSE between measurements and calculated data for the profiles A-A' and B-B' (see Figures 4.8 and 4.9) and test models (see Figure 4.12 in Section 4.2.3)

<b>Profile</b>	<b>Reference to Table 4.4 in Section 4.2.3</b>	<b>Bouguer anomaly (mGal)</b>	<b>Geoid height (m)</b>	<b>Topography (m)</b>
A-A' (Figure 4.8)		7.28	1.13	215.14
B-B' (Figure 4.9)		5.93	1.19	158.73
Archean lith. mantle (Figure 4.12)	Mantle a	67.83	4.05	2736.50
Proterozoic lith. mantle (Figure 4.12)	Mantle b	17.36	1.57	328.78
Phanerozoic lith. mantle (Figure 4.12)	Mantle c	25.67	2.89	1047.54

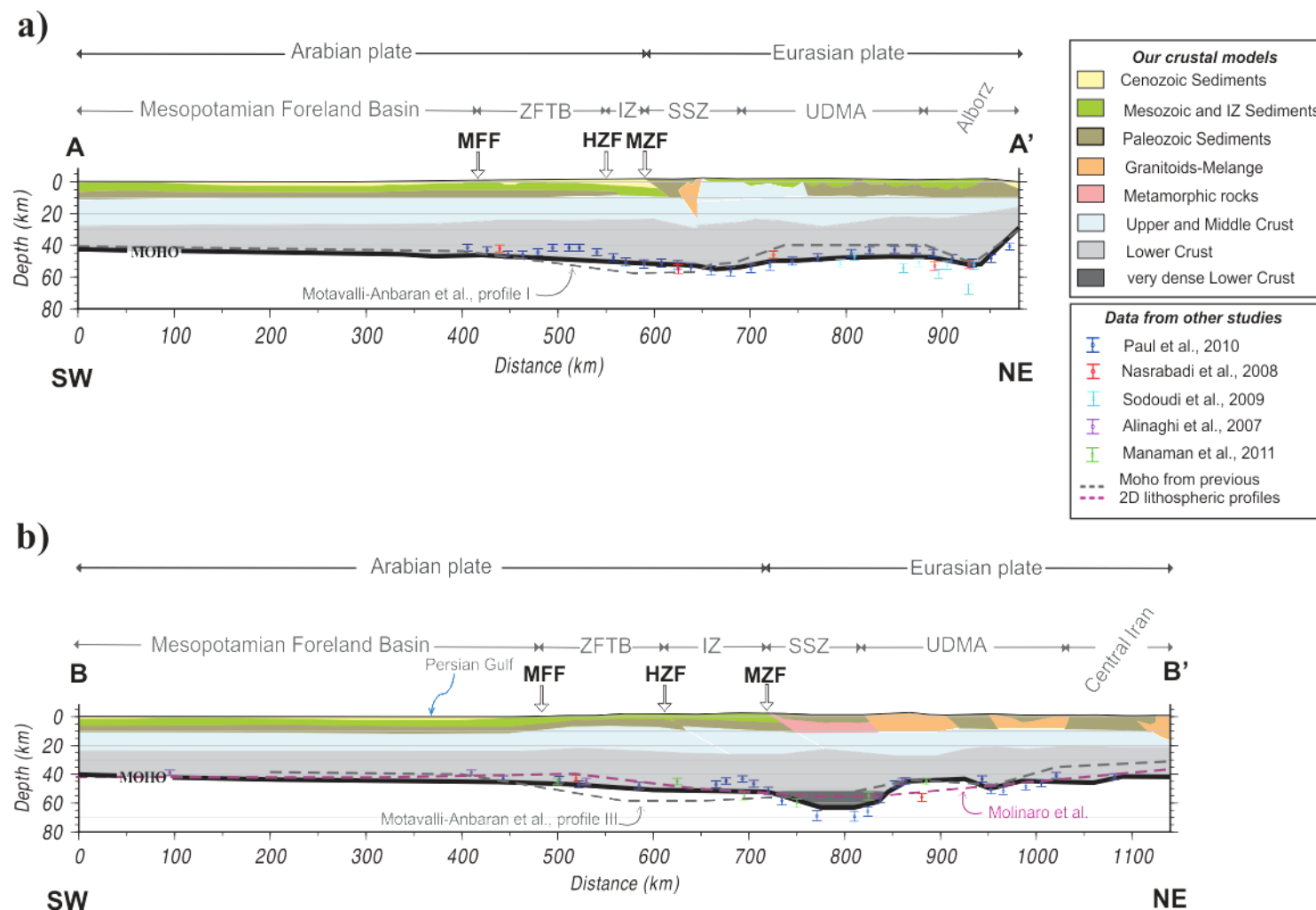


**Figure 4.7.** Crustal model for A–A’ (a) and B–B’ (b) profiles. Dashed lines indicate the Moho discontinuity from published 2-D lithospheric profiles (Molinari et al. 2005; Motavalli-Anbaran et al. 2011). Physical properties of crustal bodies are reported in Table 4.2. HZF: High Zagros Fault; IZ: Imbricated Zone; MFF: Main Frontal Fault; MZF: Main Zagros Fault; SSZ: Sanandaj Sirjan Zone; UDMA: Urumieh Dokhtar Magmatic Arc; ZFTB: Zagros Fold-and-Thrust Belt.

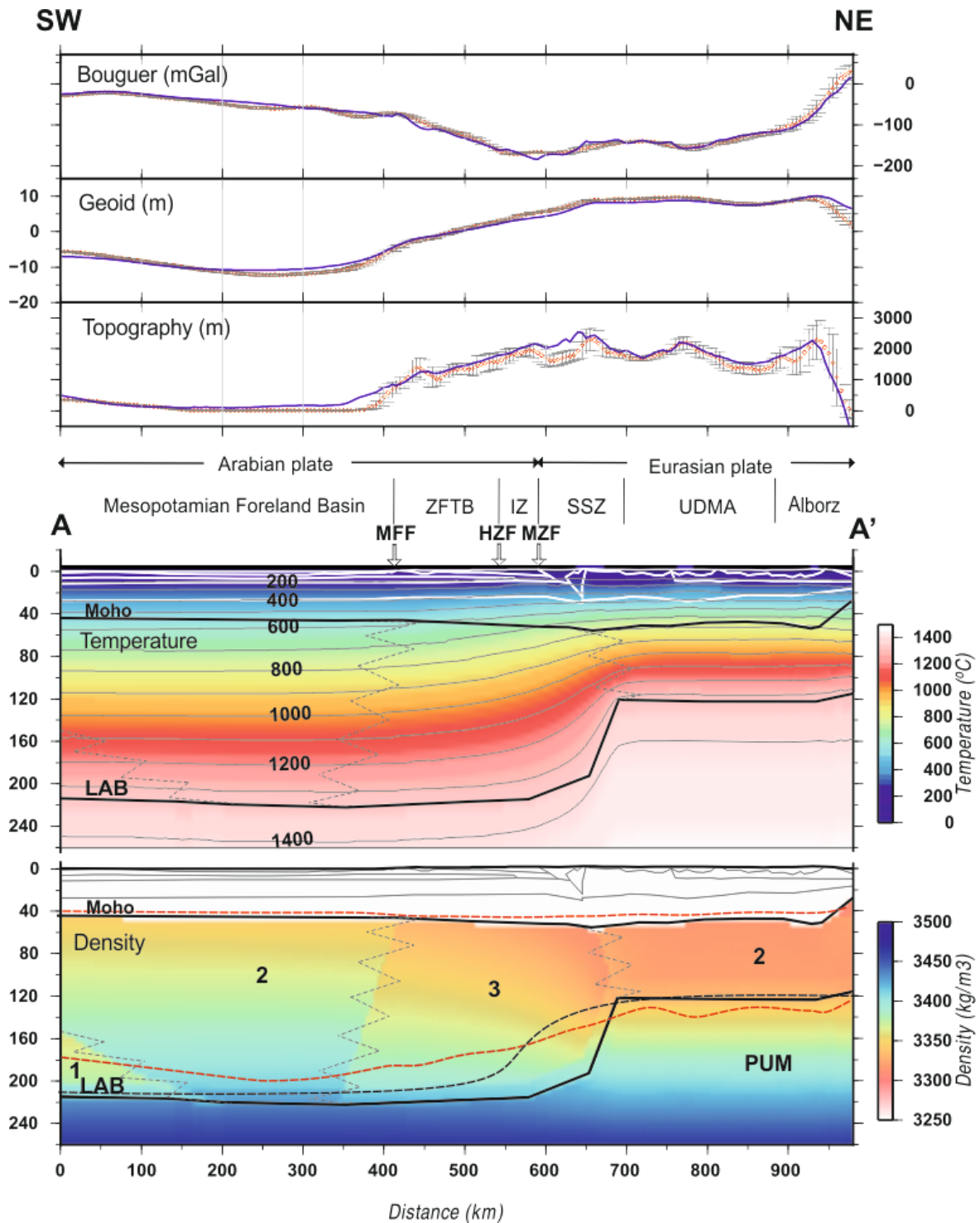


**Figure 4.8.** Modelling results for A-A' profile. Red dots denote measured values and vertical dispersion bars with the standard deviation calculated on a strip of 50 km. Continuous blue lines represent the calculated values from the model. Dashed grey lines represent the transition between different chemical compositions or mantle domains. Numbers indicate different mantle composition (Table 4.1). Discontinuous lines indicate Moho and/or LAB depth geometry from Motavalli-Anbaran et al. (2011) (profile I, black) and Jiménez-Munt et al. (2012) (red). HZF: High Zagros Fault; IZ: Imbricated Zone; MFF: Main Frontal Fault; MZF: Main Zagros Fault; SSZ: Sanandaj Sirjan Zone; UDMA: Urumieh Dokhtar Magmatic Arc; ZFTB: Zagros Fold-and-Thrust Belt.

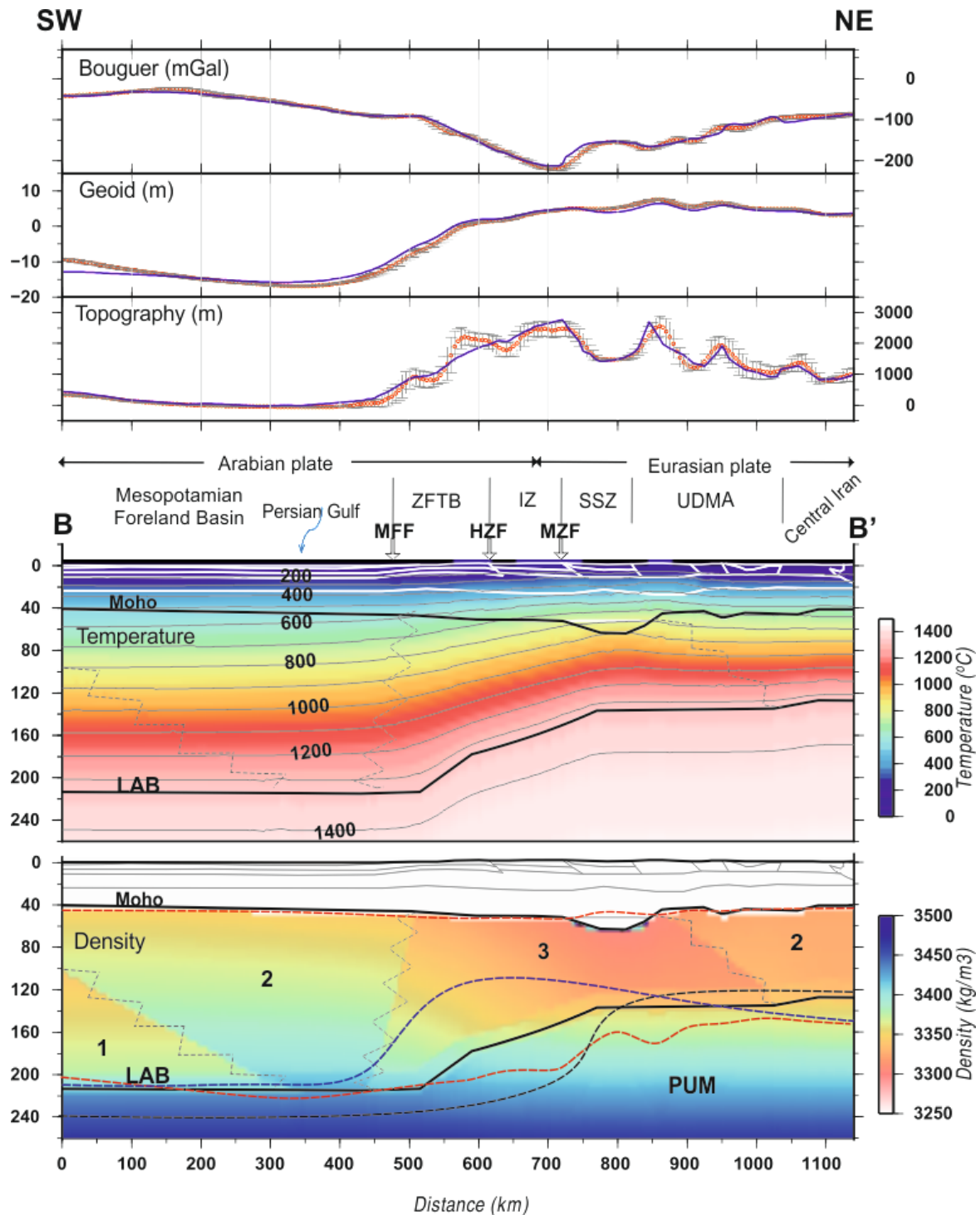


**Figure 4.9.** Modelling results for B-B' profile. Red dots denote measured values and vertical dispersion bars with the standard deviation calculated on a strip of 50 km. Continuous blue lines represent the calculated values from the model. Dashed grey lines represent the transition between different chemical compositions or mantle domains. Numbers indicate different mantle composition (Table 4.1). Discontinuous lines indicate Moho and/or LAB geometry by Molinaro et al. (2005) (purple), Motavalli-Anbaran et al. (2011) (profile III, black), and Jiménez-Munt et al. (2012) (red). HZF: High Zagros Fault; IZ: Imbricated Zone; MFF: Main Frontal Fault; MZF: Main Zagros Fault; SSZ: Sanandaj Sirjan Zone; UDMA: Urumieh Dokhtar Magmatic Arc; ZFTB: Zagros Fold-and-Thrust Belt.

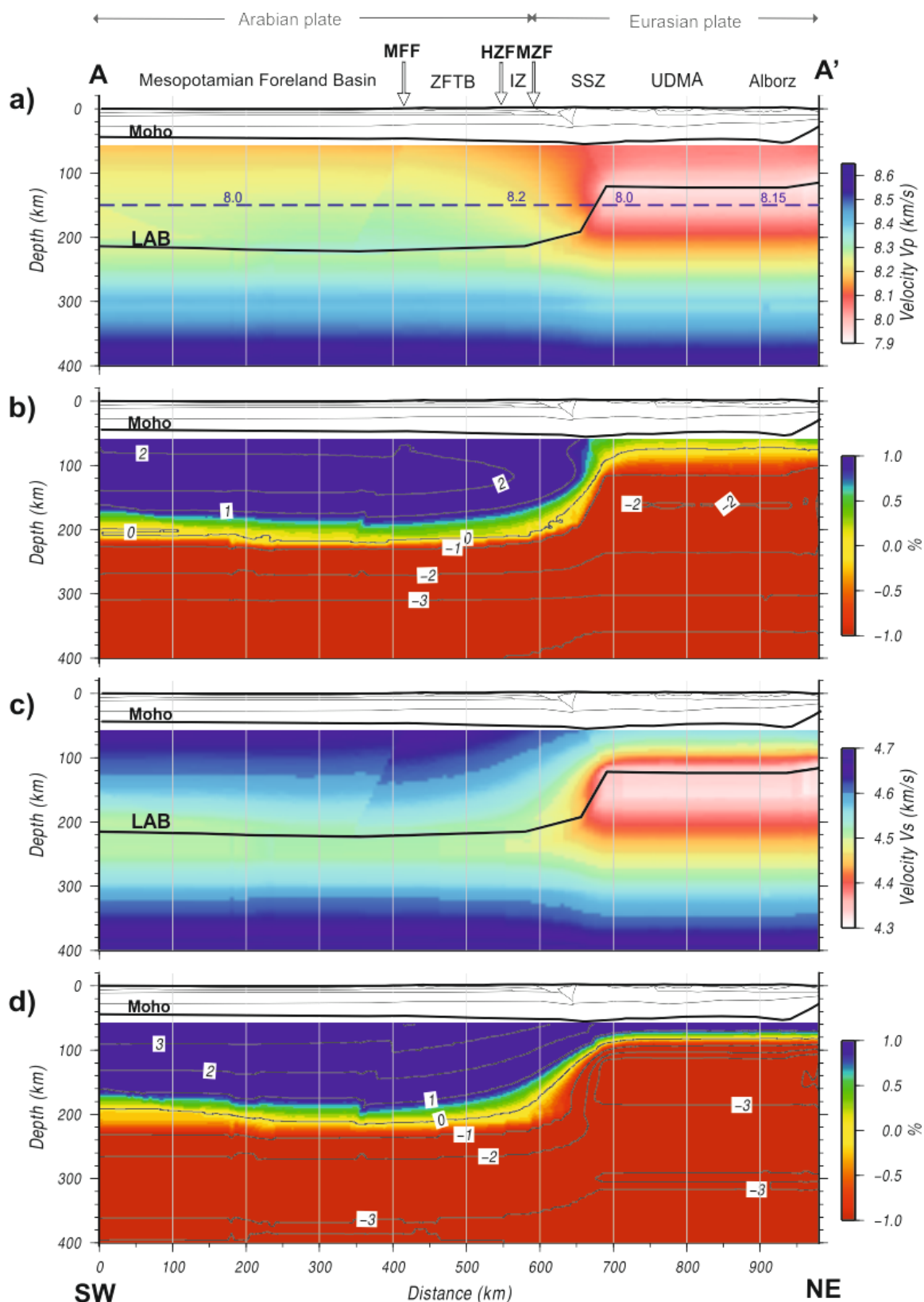


**Figure 4.10.** A-A' profile. (a) P-wave mantle velocity distribution; (b) P-wave seismic velocity anomaly with respect to AK135 reference velocity model (Kennett et al., 1995); (c) S-wave mantle velocity distribution; (d) S-wave seismic velocity anomaly with respect to AK135 reference velocity model (Kennett et al., 1995). Numbers along dashed line (in panel a) represent velocity values from tomography model by Simmons et al. (2011).

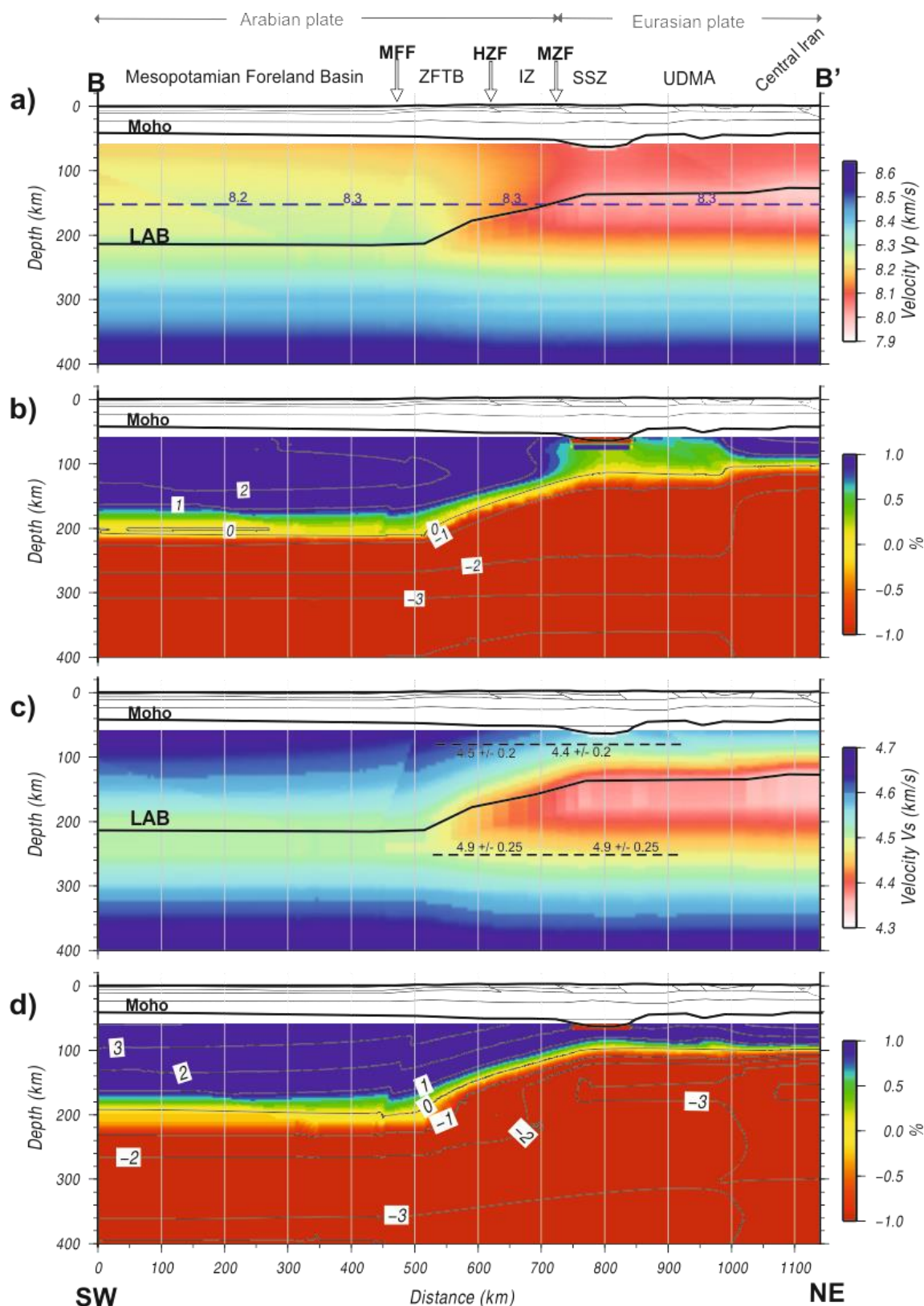


**Figure 4.11.** B-B' profile. (a) P-wave mantle velocity distribution; (b) P-wave seismic velocity anomaly with respect to AK135 reference velocity model (Kennett et al., 1995); (c) S-wave mantle velocity distribution; (d) S-wave seismic velocity anomaly with respect to AK135 reference velocity model (Kennett et al., 1995). Numbers along dashed blue and black lines represent velocity values from tomography model by Simmons et al. (2011) (panel a) and from Kaviani et al. (2007) (panel c).

### Mantle chemical composition

In order to fit the observables (gravity, elevation, geoid and seismic velocities), we considered three different lithospheric mantle compositions (Mantles 1, 2 and 3 in Table 4.1). The overall composition of the lithospheric mantle along both profiles falls into the lherzolitic field. However, slight changes in the bulk composition (0.2-2.1 wt% variation) have been considered along both transects according to the age-composition variations. The composition of the deep lithospheric mantle portion of the south-western Arabian Platform with Mg# ~90.4 (Mantle 1 in Table 4.1), changes progressively towards the Mesopotamian Foreland Basin to a mantle type richer in FeO, Al<sub>2</sub>O<sub>3</sub> and CaO with Mg# ~90.6 (Mantle 2 in Table 5.1). This composition is also assumed to be predominant in the accreted terrains of the Eurasian plate, including the Urumieh Dokhtar Magmatic Arc, Alborz and the Central Iran.

In the region below the Zagros Fold-and-Thrust Belt and the Imbricated Zone the composition is depleted in FeO, Al<sub>2</sub>O<sub>3</sub>, CaO and enriched in MgO (Mantle 3 in Table 4.1), resulting in a less dense lithospheric mantle. This depleted composition extends, partly, beneath the Sanandaj Sirjan Zone in profile A-A' and until the UDMA in profile B-B'. Although falling into the lherzolitic field, Mantle 3 composition shows similarities with respect to the harzburgite-type composition, observed in the ophiolitic complexes outcropping in the Imbricated and Sanandaj Sirjan Zones, the depletion being related to intense mantle melt extraction during subduction (Ghasemi and Talbot, 2006; Shervais, 2001; and references, therein). The mantle mineral assemblages vary according to the P-T conditions and to the main oxides composition. Olivine is, obviously, abundant everywhere (61-65 wt%), especially in its Mg-rich phase (48-49 wt%); the 22-30 wt% of the rocks is formed by pyroxenes and the residual 8-15 wt% by garnet, present already at shallow depths. Garnet phase increases with depth, although, depleted in Fe, Al and Ca elements. Mantle 3 is characterised by a lower content in garnet and pyroxene with respect to Mantle 2 and Mantle 1, especially at shallower levels, due to the depletion in Al<sub>2</sub>O<sub>3</sub> and CaO. The proposed enrichment in Al<sub>2</sub>O<sub>3</sub> and CaO towards Central Iran is in agreement with a recent geochemical study on xenolith samples from NE Iran (Su et al., 2014).

### Geometry and temperature-density distributions

A significant variation of the lithospheric mantle thickness is the most striking feature of the model outputs along both profiles (Figures 4.8 and 4.9). The LAB is located at ~220 km depth below the Mesopotamian Foreland Basin, rising up to ~125 km depth below the Sanandaj Sirjan Zone and the Urumieh Dokhtar Magmatic Arc and further NE towards the Alborz Mountains in profile A-A' (Figure 4.8), and towards Central Iran in profile B-B' (Figure 4.9). The main difference between both profiles is that in A-A' the thinning occurs over a very narrow region (<100 km width) starting in the contact between the Imbricated Zone and the Sanandaj Sirjan Zone (the MZF). In contrast, in profile B-B' lithospheric thinning occurs in the Zagros Fold-and-Thrust Belt (immediately north of the MFF) and extends north-eastwards over a 300 km wide region to the SSZ and the UDMA.

Temperature distributions are also similar in both profiles. The Arabian Foreland Basin is characterised by horizontal isotherms with moderate temperatures within the lithospheric mantle, with a Moho temperature of about 550°C. The lithospheric mantle thinning affecting the SSZ, UDMA, Alborz and Central Iran deflects the isotherms upwards, especially near the lithosphere-asthenosphere boundary. Along profile A-A', the Moho temperature beneath the Zagros Mountains increases from 650°C below the ZFTB and IZ to 750-800°C below the SSZ, and it continues, without significant variations, northwards towards the Alborz Mountains (Figure 4.8). Along profile B-B', the calculated Moho temperature increases from 600°C in the ZFTB to 800°C in the IZ, reaching a maximum of ~900°C in the Sanandaj Sirjan Zone, where the crust is thicker. In the UDMA and Central Iran, the Moho temperature is in the range of 650-700°C.

The density distribution within the lithospheric mantle depends on composition and P-T conditions. Along profile A-A' (Figure 4.8), low densities (~3310 kg/m<sup>3</sup>) are found beneath the UDMA and the SSZ, increasing to the SW beneath the IZ and the ZFTB, related to the sharp lithospheric thickening, even though the mantle composition is lighter. Maximum densities (~3430 kg/m<sup>3</sup>) are found in the Arabian plate due to both composition and mantle thickening. Along profile B-B' (Figure 4.9), the pattern of lateral density variations differs from profile A-A' and the lower densities are found beneath the SSZ and the IZ, due to the combined effects of high temperature associated with lithospheric thinning and thick crust, and chemical composition. As in profile A-A', the maximum densities correspond to the Arabian plate, with similar values.

#### Seismic velocity distribution (Vp and Vs)

Figure 4.10 shows the calculated seismic velocity (panels a, c) and seismic velocity anomaly distribution (panels b, d) for both P- and S-waves along profile A-A'. The velocity anomalies are calculated, with respect to the AK135 reference model (Kennett et al., 1995). Velocity variations related to compositional changes are smaller than those related to temperature and lithospheric thickness variations. P-wave velocities increase with depth within the lithospheric mantle and down to 400 km depth, whereas, S-wave velocities decrease with depth until the LAB and then increase again to the bottom of the model. The most remarkable feature is the sharp lateral change, observed in both P- and S-wave velocities, coinciding with the pronounced lithospheric thinning close to the plate suture. A low velocity anomaly characterises the regions with a thin lithosphere, where, Vp in the lithospheric mantle decreases from 8.10 km/s, at 60 km depth, to 7.95 km/s at the LAB and Vs decreases from 4.60 km/s to 4.35 km/s. In the Arabian plate, the lithospheric mantle velocities are, generally, higher ranging from 8.15 to 8.33 km/s for P-waves and from 4.50 to 4.68 km/s for S-waves. A similar trend in the distribution of seismic velocities is observed along profile B-B' (Figure 4.11) with small variations in the calculated Vp and Vs values. Low Vp and Vs velocities extend over a wider region than in profile A-A', related to the lithospheric mantle thinning, although, the anomalies show a lesser amplitude due to composition effects.

### 4.2.3 Changing the lithospheric mantle composition

Considering a compositionally homogeneous lithospheric mantle, we performed a number of tests along profile A-A' changing the mantle chemical composition in order to check the sensitivity of the model to these variations. Crustal structure (geometry and parameters) and LAB geometry are fixed. Figure 4.12 shows the obtained results along profile A-A', by considering compositions corresponding to Archean, Proterozoic and Phanerozoic lithospheric mantles (Table 4.4). The corresponding misfits between measured and calculated data are reported in Table 4.3.

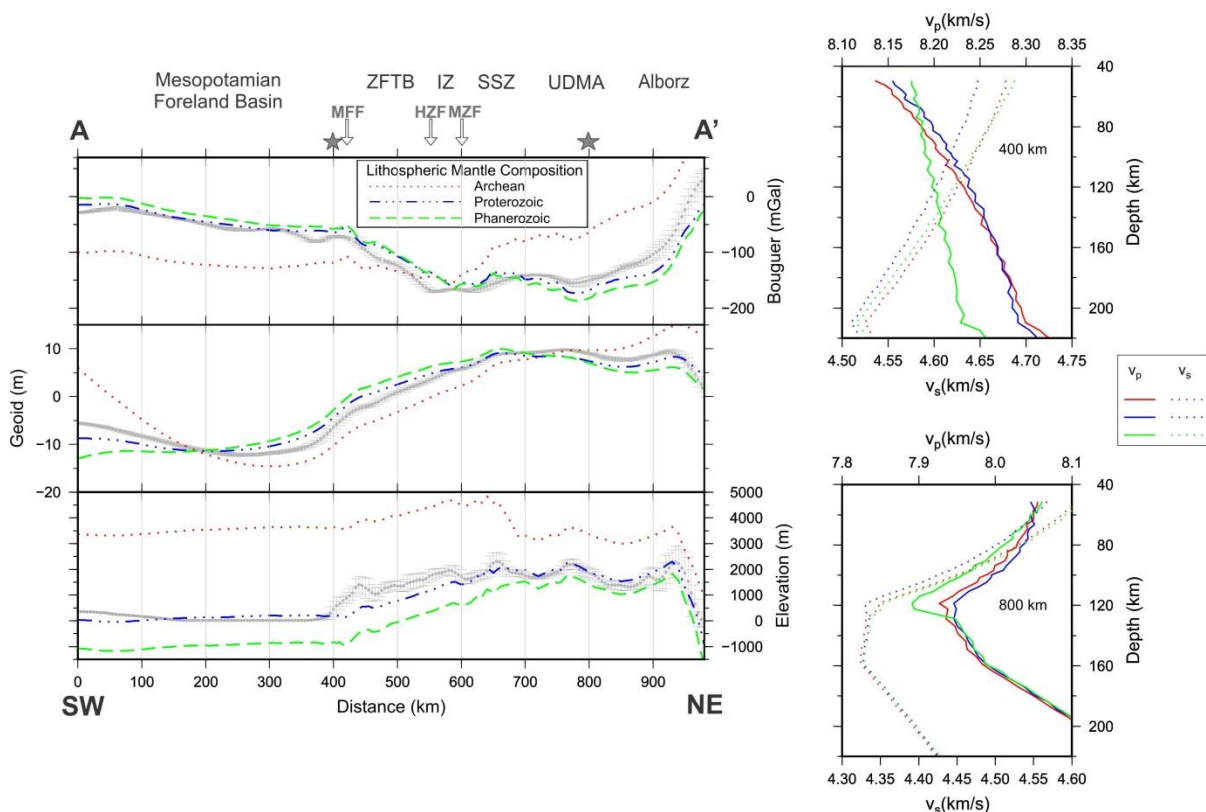


**Figure 4.12.** Calculated Bouguer and geoid anomalies, elevation, and seismic velocities for different lithospheric mantle compositions (Archean, Proterozoic, Phanerozoic) along the A-A' profile. Grey dots with error bars indicate the geophysical observables. Velocity profiles correspond to are calculated at 400 km (top right) and 800 km (bottom right) from the beginning of the profile.

As expected, the Archean lithospheric mantle composition results in a considerable uplift of the whole region, since it is highly depleted in incompatible elements (Al, Ca, Fe) and, therefore, is more buoyant. The calculated elevation exceeds the observed elevation by ~3000 m in the Foreland Basin, ~2000 km in the Zagros Fold-and-Thrust Belt and ~1500 m in the Eurasian part of the profile. The Phanerozoic lithospheric mantle composition is enriched in FeO, CaO and  $Al_2O_3$  and depleted in MgO, which results in a higher density. This composition fits, quite well, the elevations in the UDMA and Alborz Mountains, whereas, it

generates an increasing misfit towards the Arabian Foreland Basin, where the calculated topography is ~1000 m lower than observed. The best fit is obtained with a Proterozoic mantle composition, which is characterised by an intermediate depletion degree between Archean and Phanerozoic compositions, although, being highly enriched in FeO. A misfit of ~500 m in elevation is found in the Zagros Fold-and-Thrust Belt and the Imbricated Zone. Bouguer and geoid height anomalies reveal the same mass excess/deficit as elevation. Note that, fitting the observables with a homogeneous Proterozoic composition would require a noticeable thinning of the lithospheric mantle beneath the ZFTB and the resulting seismic velocities would be in disagreement with tomographic models.

Furthermore, we calculated the P- and S-wave velocity-depth distributions for each composition at 400 km and 800 km distance from the beginning of the profile, corresponding to the Arabian and Eurasian lithospheric mantles, respectively. Calculated  $V_p$  ranges from 8.12 km/s to 8.30 km/s in the thick Arabian lithospheric mantle, and from 7.9 km/s to 8.05 km/s in the thin lithospheric mantle beneath the magmatic arc. Similarly,  $V_s$  is in the range between 4.50 km/s and 4.70 km/s in the Arabian lithospheric mantle, and between 4.33 km/s and 4.60 km/s, in both locations, respectively. Interestingly, calculated  $V_p$  for Archean and Proterozoic compositions are similar but differ noticeably for Phanerozoic compositions. In turn, calculated  $V_s$  are similar for Archean and Phanerozoic and differ for Proterozoic compositions.

**Table 4.4.** Chemical compositions used in test models for mantle bodies (Figure 4.12).

<b>Mantle compositions in the NCFMAS system (%)</b>				
	<b>Mantle a</b>	<b>Mantle b</b>	<b>Mantle c</b>	<b>Asthenosphere - PUM</b>
	<i>Arc1</i>	<i>Pr6</i>	<i>Tc1</i>	<i>PUM</i>
	<i>Average Archean</i>	<i>Proterozoic</i>	<i>Average Phanerozoic</i>	<i>Primitive Upper Mantle</i>
	<i>(Griffin et al., 2009)</i>	<i>(Griffin et al. 2009)</i>	<i>(Griffin et al.,2009)</i>	<i>(McDonough and Sun, 1995)</i>
<b>SiO<sub>2</sub></b>	45.7	45.4	44.5	45
<b>Al<sub>2</sub>O<sub>3</sub></b>	0.99	3.7	3.5	4.5
<b>FeO</b>	6.4	8.3	8.0	8.1
<b>MgO</b>	45.5	39.9	39.8	37.8
<b>CaO</b>	0.59	3.2	3.1	3.6
<b>Na<sub>2</sub>O</b>	0.07	0.26	0.24	0.25
<b>Total</b>	99.25	100.76	96.05	99.25

These results show that lithospheric mantle density is particularly sensitive to the chosen bulk compositions, resulting in important variations in the calculated gravity and geoid anomalies and absolute elevation. The calculated seismic velocities appear to be more sensitive to lateral temperature variations (lithospheric thickness variations) than to the selected compositional variations.

It must be noted, however, that identifying mantle density with bulk composition and seismic velocities is a difficult problem, due to the lack of uniqueness. Recent works by Afonso et al. (2013a, b), based on a non-linear 3D multi-observable probabilistic (Bayesian) inversion approach, show that a wide range of compositions can, equally well, explain multiple geophysical data. Hence, deep temperature anomalies  $\leq 150^\circ\text{C}$  and compositional anomalies  $\Delta\text{Mg\#} < 3$  are not simultaneously resolvable, being the bulk  $\text{Al}_2\text{O}_3$  content a better compositional indicator than  $\text{Mg\#}$ . In consequence, the considered mantle chemical compositions are compatible with the geophysical observables, but it would be difficult to decide whether these compositions are unique.

### 4.3 Discussion

The numerical experiments carried out in this study are based on the combination of petrology, mineral physics, and geophysical observables, allowing for the self-consistent calculation of mantle physical parameters, such as density, thermal conductivity and seismic velocities and their related observables. At the same time, the incorporation of geological data and recently acquired seismic data reduced considerably the uncertainties inherent to previous lithospheric models in the region.

#### 4.3.1 Geophysical-petrological versus pure-thermal approaches

A noteworthy result is that the mantle density distributions obtained in this work differ, considerably, from those obtained from a pure-thermal approach (e.g., Jiménez-Munt et al., 2012; Motavalli-Anbaran et al., 2011; Molinaro et al., 2005). In the pure-thermal approach, the density of the lithospheric mantle depends only on temperature, such that  $\rho_m(z) = \rho_a(1 + \alpha(T_a - T(z)))$ , where  $\rho_a = 3200 \text{ kg/m}^3$  and  $T_a = 1330^\circ\text{C}$  are the density and temperature of the asthenosphere, respectively, and are constant everywhere, and  $\alpha = 3.5 \cdot 10^{-5} \text{ }^\circ\text{C}^{-1}$  is the thermal expansion coefficient. Accordingly, the density in the sub-crustal domain of the Mesopotamian Foreland Basin would vary roughly linearly from about  $3300 \text{ kg/m}^3$  at the crust-mantle boundary to  $3200 \text{ kg/m}^3$  in the LAB, keeping this value down to 400 km depth. Interestingly, despite the large differences in the density-depth distribution obtained from the two approaches, the corresponding lithospheric models show similar trends, in terms of lithospheric geometry. The reason for that is twofold: 1) On the one hand, although the resulting lithospheric mantle density from the geophysical-petrological approach is considerably higher than that from the pure-thermal approach, calculated elevations are comparable, because both approaches use different reference columns to calculate the lithospheric buoyancy. In the pure-thermal approach the reference column is the lithosphere at mid-oceanic ridges, with a constant sublithospheric density of  $\rho_a = 3200 \text{ kg/m}^3$  (e.g., Lachenbruch and Morgan, 1990). In the geophysical-petrological approach, the reference column is also the lithosphere at mid-oceanic ridges, but in this case, the sublithospheric mantle extends down to 400 km depth and the mantle density is calculated according to its

composition and P-T conditions; 2) On the other hand, the similarity in calculated elevations indicates that the predominant effect on lateral density variations is related to temperature rather than pressure and, in our case, composition.

As discussed later, although the results from our modelling are comparable with previous models, they show conspicuous differences in the crustal structure and LAB depth. Major differences in the crustal structure and Moho depth are encountered, with respect to the works by Molinaro et al. (2005) and Motavalli-Anbaran et al. (2011), partly, because these authors use a very simplified upper crust structure and different density contrasts. However, the obtained LAB depths do not differ much, except with respect to the location and sharpness of the mantle thinning. The modelling approach used by Jiménez-Munt et al. (2012) is remarkably simpler, since calculations are performed in 1D and both the crust and the lithospheric mantle are considered as homogeneous layers. Despite this simplicity, the main trends of Moho and LAB geometries are fairly reproduced although notable differences in the obtained values and short wavelength features were found.

### 4.3.2 Crustal geometry

The incorporation of geological cross-sections, based on geological field data along our modelled transects gives a better resolution on the shallow crustal structure. In addition, the significant amount of recent seismic experiments, allowed us to fairly constrain the Moho depth, by modifying the relative thickness of upper-middle crust and lower crust to simultaneously fit all the geophysical observables. Figure 4.7 displays the crust-mantle boundary inferred from previous studies, showing differences in crustal thickness exceeding 10 km among different authors and methods. Our crustal model along transect A-A' shows a crustal thickness of 42-43 km below the Arabian Foreland Basin, gradually increasing towards the Zagros Mountains. These values are similar to those proposed by Gök et al. (2008) and Nasrabadi et al. (2008). Maximum crustal thicknesses are obtained beneath the Sanandaj Sirjan Zone (55 km) and the Alborz Mountains (53 km) in good agreement with Paul et al. (2010) and Nasrabadi et al. (2008). Large discrepancies are obtained in the Alborz Mountains, relative to crustal thickness values proposed by Sodoudi et al. (2009), who proposed crustal thickness values up to 70 km. Along the B-B' transect, the Arabian Foreland Basin shows a similar crustal thickness to that in the northern transect, with values exceeding those proposed by Alinaghi et al. (2007), by 4-7 km. Across the Zagros and Central Iran, our results show a good agreement with previous studies. Major discrepancies are found below the Sanandaj Sirjan Zone where Paul et al. (2010) propose a maximum crustal thickness of 69 km, in contrast to 63 km, as inferred from our model. This exceptional crustal thickening is restricted to a region of ~150 km in width, and displaced relative to the higher elevations of the Imbricated Zone. Nevertheless, seismic data in this region show larger uncertainties than other areas, due to the lack of seismic stations and the consequent poor ray coverage (Paul et al., 2006). Note that, obtaining a very thick crust in this region requires considering a completely eclogitised lower crustal body, in order to simulate densities similar to the

uppermost mantle. If this body is not considered, the modelled Moho depth is of ~53 km, in good agreement to the values proposed by Manaman et al. (2011) from seismic data, and Molinaro et al. (2005) and Motavalli-Anbaran et al. (2011) from modelling. Slight discrepancies in resulting Moho depth values are found also between different receiver function studies (i.e. in the Alborz along A-A' profile, in the UDMA and IZ along the B-B' profile). In general, along both transects, our resulting Moho depth values are consistent with the results from Gök et al. (2008), which found ~42-45 km of crustal thickness in the Foreland Basin; from Gritto et al. (2008), which calculated Moho depth values between 44 km and 52 km in the NW Zagros; and from Radjaee et al. (2010), which found ~55 km below the Zagros Mountains and 53-58 km below the Alborz Mountains. Our values of Moho depth differ slightly from those proposed by Jimenez-Munt et al. (2012), being 3-5 km higher along profile A-A' (Figure 4.8) and practically coincident along profile B-B' (Figure 4.9).

### 4.3.3 LAB geometry and compatibility with tomography models

Numerous studies have highlighted the lower P- and S-wave velocities and the higher attenuation of Pn- and Sn-waves, below Central Iran and/or the internal parts of the Zagros Mountains, relative to the adjacent Arabian Platform (Villaseñor et al., 2001; Ritzwoller et al., 2002; Maggi and Priestley, 2005; Kaviani et al., 2007; Manaman and Shomali, 2010; Agard et al., 2011; Vergés et al., 2011). Low velocities and high attenuation are, usually, interpreted as implying relatively high temperatures. Our resulting lithospheric mantle geometry depicts a pronounced lithospheric thinning from about 215 km in the Arabian Platform to 125-130 km in the UDMA and Central Iran along both profiles. This lithospheric thinning has also been proposed in former lithospheric models (e.g., Molinaro et al., 2005; Motavalli-Anbaran et al., 2011; Jiménez-Munt et al., 2012). A main difference with these models is the location and sharpness of the lithospheric thinning. Profile A-A' shows similar results to those of Motavalli-Anbaran et al. (2011), in terms of sharpness but, in our model, lithospheric thinning occurs about 100 km farther to the NE. The location of this abrupt LAB rising in our model is the result of the best fit of all the geophysical observables in the region, including the location of the positive-negative velocity anomaly transition imaged in the tomography of Figure 4.5 (panel a). Differences with respect to the LAB geometry, proposed by Jiménez-Munt et al. (2012), are clear in both LAB and sharpness of lithospheric thinning (Figure 4.8). Prominent differences also appear when comparing our results along profile B-B' to those obtained by Molinaro et al. (2005) along a profile located 250 km further SE. According to these authors, the lithosphere thins very sharply from 210 km to about 100 km over a <80 km wide region beneath the Main Frontal Front, increasing steadily to values of 140 km beneath Central Iran. The lithospheric structure along B-B' proposed by Jiménez-Munt et al. (2012) shows a smoother lithospheric thinning, in terms of sharpness and a ~20 km thicker lithosphere beneath UDMA and Central Iran (Figure 4.9).

Caution must be taken when comparing calculated seismic velocities with tomography models and our calculated velocities should only be qualitatively compared to tomography

models. High velocities beneath the ZFTB are also observed in the tomography model by Manaman and Shomali (2010), obtained by using the partitioned waveform inversion method. In this case, the authors used an ad hoc regional reference model with low velocities characterising the lithospheric mantle below the UDMA and towards Central Iran, whereas, the highest velocities mark the lithosphere below the ZFTB and the foreland basin. This strong velocity contrast at 100-150 km depth, close to the suture zone, is also observed in other surface and body wave tomography studies (e.g. Villaseñor et al., 2001; Maggi and Priestley, 2005; Alinaghi et al., 2007; Kaviani et al., 2007). Our results are also in agreement with the absolute values of  $V_s$ , as calculated by Kaviani et al. (2007) in central Zagros (Figure 4.11, panel c) who, in reproducing a decrease in the shear-wave velocity values towards the Central Iran, found a low velocity zone, immediately below the Moho in the Sanandaj Sirjan Zone. A further discussion is required when comparing our results with the recent tomography model by Simmons et al. (2011). These authors show high  $V_p$  values (8.3 km/s) below the ZFTB and IZ, and also below the UDMA (Figure 4.11, panel a), allowing for the interpretation of the Arabian plate underthrusting the Eurasian lithosphere. Though our calculated seismic velocities in the same region (at 150 km depth) are lower than those proposed by Simmons et al. (2011) (Figure 4.11, panel a), we do not obtain any lithospheric-scale underthrusting feature when converting the calculated  $V_p$  values into  $\Delta V_p$  (%), relative to the AK135 reference model.

Finally, receiver function studies (Hansen et al., 2007; Mohammadi et al., 2013) show different LAB depth values, relative to those obtained in our models, indicating a shallower LAB in the whole area (~160 km depth in the Arabian Platform, ~130 km depth beneath the ZFTB, ~150 km beneath the SSZ, and 80-85 km in Central Iran). This discrepancy could be due to a misinterpretation of the horizon detected by receiver functions which, as suggested in a recent work by Yuan and Romanovicz (2010), probably corresponds to the sharp mid-lithosphere boundary, rather than to the more gradual lithosphere-asthenosphere boundary. Alternatively, as noted by Eaton et al. (2008), the definition of LAB depends on the observation method and, therefore, the thermal and seismic LABs are not forced to coincide.

## 4.4 Concluding remarks

I have presented new lithospheric models along two transects across the Arabia–Eurasia Plate boundary, combining geological, geophysical and petrological data within an internally consistent thermodynamic-geophysical framework. The approach allows calculations of absolute elevation, gravity anomaly, geoid height, surface heat flow and mantle seismic velocities and their comparisons with observations. The results obtained in this study allow us to make the following concluding remarks:

- The two modelled profiles (A-A' and B-B') reproduce the general trends of the Moho topography, obtained from previous seismic experiments reducing the uncertainties associated with the gathering of data with different provenance and regions with poor or null

data coverage. A highly eclogitized lower crust beneath the Sanandaj Sirjan Zone is required (central Zagros).

- The obtained LAB geometries reproduce a pronounced lithospheric mantle thinning from the Arabian to the Eurasian lithosphere in agreement with tomography and previous lithosphere models. However, conspicuous differences in terms of depth to the LAB, and sharpness and location of the lithospheric mantle thinning are encountered between the two selected profiles.

- Lateral changes in the composition of the lithospheric mantle are required to reproduce P- and S-wave seismic velocities from tomography models. Our results are compatible with a Proterozoic lherzolitic composition beneath the Arabian Platform, changing progressively to a more enriched composition beneath the Mesopotamian Foreland Basin and the Persian Gulf, and below the accreted terrains of the Eurasian plate (Urumieh Dokhtar Magmatic Arc and Central Iran). Below the Zagros Fold-and-Thrust Belt and the Imbricated Zone, a more depleted Phanerozoic harzburgitic-type mantle composition has been considered.

- Along-strike variations of the lithosphere structure are, mainly, related to the region where the lithospheric thinning occurs. In the NW Zagros region (Lurestan, profile A-A') lithospheric thinning is very sharp and located beneath the Sanandaj Sirjan Zone, coinciding with the Arabian-Eurasian plate suture (the Main Zagros Fault). In the central Zagros region (Fars, profile B-B') lithospheric thinning is smoother and affects a wide region of the NE-Arabian plate, including the Zagros Fold-and-Thrust Belt and the Imbricated Zone.

## Chapter 5: The Himalaya-Tibetan orogen

The Himalaya-Tibetan orogen is the result of ~270 My long tectonic convergence between India and Eurasia plates. The process included different subduction and suturing episodes during the closure of the Neo-Tethys Ocean, which successively accreted continental terrains at the ancient southern border of Asia, and finally culminated with the continental collision between the Indian and the Eurasian plates. The collisional process resulted in large amounts of thrusting and crustal thickening along the Himalaya Range, and broadly distributed deformation with the formation of the high Tibetan Plateau and of additional reliefs extending some 2000 km north of Indus-Tsangpo Suture, such as the Kunlun Shan and the Tian Shan to the north, and the Qilian Shan to the east.

The Himalaya-Tibetan region has been the object of numerous past and on-going researches, but which is the deep structure and which are the mechanisms supporting the high Tibetan Plateau are still debated questions. The chemical composition of the lithospheric mantle can play a fundamental role in controlling the buoyancy/rigidity characteristics of the lithosphere and its tectonic behavior (Lenardic and Moresi, 1999; Griffin et al., 2009). The long-standing tectonic evolution of the Himalaya-Tibetan orogen has likely modified the chemical composition of the lithospheric mantle, causing relevant changes in the geometry of the crust-mantle and lithosphere-asthenosphere boundaries. Up to date however, a quantified thermal and petro-physical characterization of the lithospheric mantle in the Himalaya-Tibetan orogen, consistent with geo-thermo-barometers and tomography models of the region has not been attempted. Previous geophysical studies put efforts in identifying the nature and composition of the deep unexposed part of the orogen, arguing for the presence of eclogites under Tibet (Schulte-Pelkum et al., 2003; Het al. et al, 2007), granulitic lower crust under the Himalaya Range (Nelson et al., 1996; Jackson et al., 2004) or under southern Tibet (Le Pichon et al., 1999; Priestley et al., 2008). However, though the contribution of chemical composition and phase transitions on the density and buoyancy of the lithospheric mantle are key aspects on the resulting lithospheric structure (Afonso et al., 2008; Fullea et al., 2009), no such analysis has been performed in the Tibet-Himalaya region, especially in its western sector.

In this chapter, I present a new 2D crustal and upper mantle cross-section in the Himalaya-Tibetan region (Profile C-C', Figure 5.1), which crosses, from India to Asia, the western Himalaya Range and Tibetan Plateau, the Tarim Basin, the Tian Shan and Junggar Basin, ending in the southern edge of the Altai Range. I apply the finite-element method described in Chapter 3 (LitMod-2D).

In order to discuss the along-strike variations of the lithospheric structure of the Himalaya-Tibetan orogen, I used the LitMod approach also to re-model the lithospheric profile by Jiménez-Munt et al. (2008). This profile crosses the eastern Himalaya Range and Tibetan Plateau, the Qaidam Basin, the Qilian Shan and Beishan units, ending in the North China cratonic block (profile D-D', Figure 5.1). Modelling the two transects with this new

methodology allows us i) analysing the effect of the mantle composition on the lithospheric structures; ii) discussing consistently the differences between the eastern and western Himalaya-Tibetan orogen, mainly on the lithospheric mantle composition and thickness; iii) calculating P- and S- mantle seismic velocity distributions and anomalies along the profiles, thus making the results comparable with published seismic tomography studies.

The obtained results are currently under review in a paper submitted to *Tectonics* (Tunini et al., under review) and I kept the original structure of the text when possible.

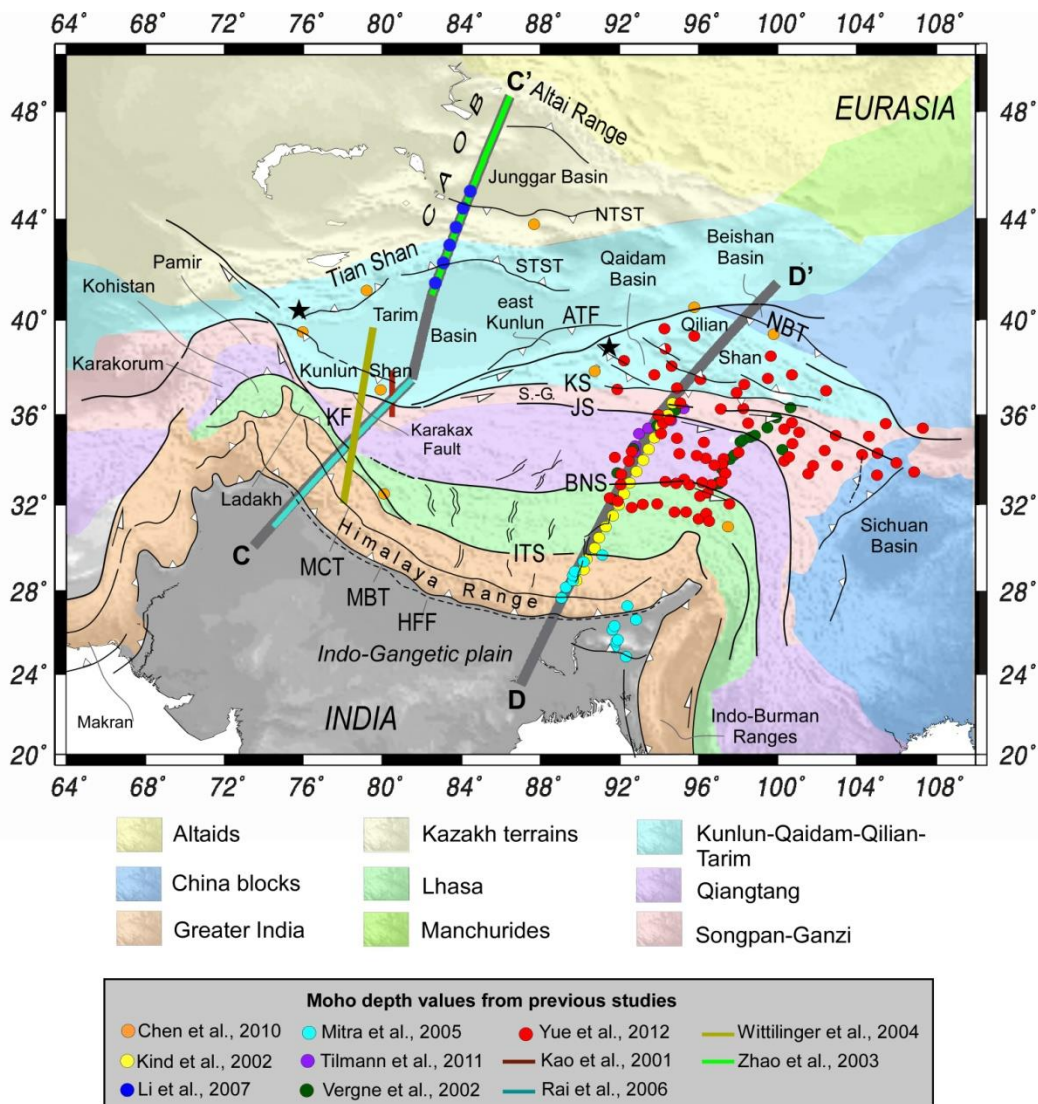


**Figure 5.1.** Tectonic map of the Himalaya-Tibetan Plateau and surrounding areas and Moho data from previous studies (color-coded symbols). Thick grey lines show the location of C-C' and D-D' profiles. Black stars indicate mantle xenolith suites localities from Bagdassarov et al. (2011) and Song et al. (2007) considered in this study. ATF: Altyn Tagh Fault; BNS: Bangong Nujiang Suture; CAO: Central Asia Orogenic Belt; HFF: Himalaya Frontal Front; ITS: Indus-Tsangpo Suture; JS: Jinsha Suture; KF: Karakoram Fault; KS: Kunlun Suture (or Kunlun fault); MBT: Main Boundary Thrust; MCT: Main Central Thrust; NBT: North Border Thrust; NTST: Northern Tian Shan Thrust; S.-G.: Songpan-Ganzi; STST: Southern Tian Shan Thrust.

## 5.1 Data

The elevation, surface heat flow, geoid and gravity observables derive from global databases. The geological cross-sections used for the tectonic structure come from recent published works. The information for constraining the crust-mantle topography, the LAB geometry and the composition of the lithospheric mantle, come mainly from numerical and seismic tomography models, and petrological studies.

### 5.1.1 Regional geophysical data

Elevation data (Figure 5.2, panel a) come from 1-min arc resolution ETOPO1 global elevation model (Amante and Eakins, 2009). The topography of the region is highly variable and characterized by steep gradients separating the topographic domains. The major plane areas, Tibetan Plateau, Tarim and Junggar basins, are surrounded by five different mountain ranges: the Himalaya and Karakorum ranges, with an average elevation of 4000-5000 m and several peaks over the 8000 m; the Tian Shan (~4000 m) and the Qilian Shan (~4500 m), located to the north and to the east of the Tarim Basin, respectively; the Kunlun Shan (~4000 m), located at the southern border near the Pamir region, and the Altai Range (2500-3000 m) extending at the northern and eastern border of the Junggar Basin.

The Bouguer anomaly (Figure 5.2, panel b) has been computed applying the complete Bouguer correction to satellite free-air data (Sandwell and Smith, 1997), using a reduction density of  $2670 \text{ kg/m}^3$  (Fullea et al., 2008). A strongest negative Bouguer anomaly of -500 mGal characterizes the entire Tibetan Plateau and the Himalaya-Karakorum ranges, gently smoothing towards the syntaxes, the Pamir and Beishan regions. The Tian Shan and Altai Range are characterized by values of ~-300 mGal, whereas the Tarim and Junggar basins show values between -100 and -200 mGal. Positive anomalies are only observed in the Indo-Gangetic plane (~50 mGal).

Geoid height data (Figure 5.2, panel c) derive from the Earth Geopotential Model EGM2008 (Pavlis et al., 2008), with 1x1 min-grid gravity anomaly data including spherical harmonic coefficients up to degree and order 2190. According to Bowin (2000), wavelengths larger than 4000 km were removed to obtain a residual geoid anomaly that reflects the density distribution of the first ~400 km of depth. The highest geoid height is observed along the Himalaya Range (~30 m), gradually decreasing towards the Beishan and towards the Karakorum. Minimum values are in the central Junggar Basin (~-22 m), and in the Tarim Basin (values between ~-10 m in the north-eastern sector and ~-2 m in the south-west).

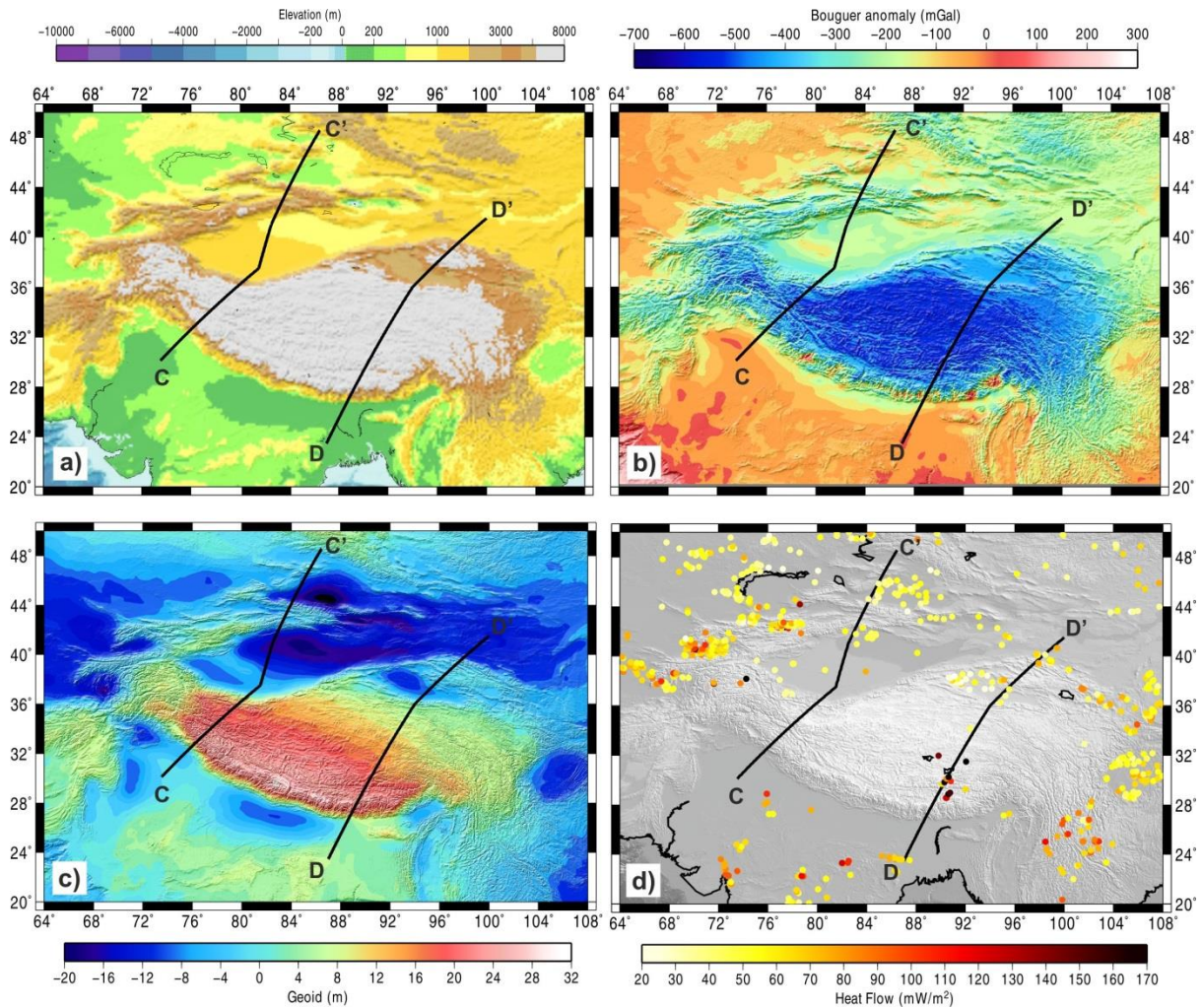


**Figure 5.2.** Geophysical observables in the study region. a) Topography; b) Bouguer anomaly calculated from global free-air anomaly (Sandwell and Smith, 1997) with 3D topographic correction; c) geoid height from filtered EGM2008 model; d) heat flow measurements from global dataset (Pollack et al., 1993).

Surface heat flow data (Figure 5.2, panel d) are taken from the global compilation by Pollack et al. (1993). Heat flow values are quite high in the eastern Tibetan Plateau, with peaks between  $180 \text{ mW/m}^2$  and  $194 \text{ mW/m}^2$ . Data show a high scatter, probably related to active groundwater flow and/or crustal melting as evidenced by the presence of numerous geysers, hot springs, volcanic, and anhydrous xenoliths (Nelson et al., 1996; Hacker et al., 2000; Jiménez-Munt et al., 2008). Few additional values are provided by two more recent papers which show  $\sim 60 \text{ mW/m}^2$  in the western Himalaya Range (An and Shi, 2007),  $55\text{-}60 \text{ mW/m}^2$  in the western Tibetan Plateau (An and Shi, 2007),  $44\text{-}55 \text{ mW/m}^2$  in the Tarim Basin (Wang, 2001; An and Shi, 2007),  $50\text{-}58 \text{ mW/m}^2$  in the Tian Shan (Wang, 2001; An and Shi, 2007),  $\sim 52 \text{ mW/m}^2$  in the Junggar Basin (Wang, 2001), and  $\sim 46 \text{ mW/m}^2$  in the Altai Range (Wang, 2001). These data are not included in Figure 5.2 (panel d) because they correspond to average regional values.

### 5.1.2 Previous studies on the crustal and lithospheric mantle structure

The crustal structure is relatively well defined by the large amount of geologic and geophysical investigations carried out in the Himalaya-Tibetan region especially in the last three decades. Table 5.1 details the main structural relationships among the different terrains along the profile. In contrast, the lithospheric mantle structure is still hardly constrained, due to the lack of direct observables and to its strong dependence on the lithosphere definition (seismic/thermal/elastic lithosphere; e.g., Eaton et al., 2009; Artemieva, 2011).

Li et al. (2006) summarize the results of about ninety seismic refraction/wide angle reflection profiles in a crustal thickness map of the mainland China. The map shows values of 70-74 km in the southern Tibetan Plateau, 60-68 km in the Himalaya Range and Qiangtang regions, gradually decreasing to 48 km towards the northeast (Qaidam Basin, Qilian Shan and Beishan Basin). Minimum values of crustal thickness are found in the Tarim (~44 km in its middle central zone) and Junggar (42-44 km) basins, whereas the Tian Shan is modelled with a 52-54 km-thick crust. The proximity of the crustal thickness contour lines in the western Tibetan region (Figure 4 in Li et al., 2006) suggests a lateral steep gradient of the Moho depth between the Tibetan Plateau and the Kunlun Shan, in agreement with results from seismic profiles (Wittlinger et al., 2004; Rai et al., 2006). Seismic experiments show that crustal thickness deepens from ~40 km beneath the Himalayan foreland basin to ~90 km beneath the western Qiangtang and Kunlun Shan (Rai et al., 2006). A remarkable Moho step (~20 km, Wittlinger et al. 2004; ~30 km, Rai et al., 2006) indicates the transition to the Tarim Basin, characterized by 50-60 km-thick crust (Kao et al., 2001; Wittlinger et al. 2004; Rai et al., 2006). Further north, Zhao et al. (2003) carried out an extensive study with wide angle seismic reflection/refraction surveys, magneto-telluric sounding and 2D density structure analysis across the Tian Shan and Altai Range. The results reveal the complexity of the crust-mantle transition zone beneath the Tian Shan, characterized by an interdigitated structure involving the upper, the middle and the lower crust layers. The crust-mantle boundary is located at depths of about 64 km beneath the Tian Shan, 55 km in the Junggar Basin, and 60 km in the southern Altai Range. More recently, another seismic experiment imaged the Moho discontinuity across the Tian Shan, from the northern Tarim Basin to the Junggar Basin (Li et al., 2007). The profile shows an averaged crustal thickness of 48 km in the Tarim Basin, 55-60 km in the Tian Shan and 50 km in the southern Junggar Basin, with no evidences of a crustal root, as usually expected in regions of tectonic shortening. All this crustal thickness data has been compiled on the recent publication by Robert et al. (2015).

**Table 5.1.** Lithology and structural relations among the different terrains along C-C' profile.

<b>Description</b>	<b>Lithology</b>	<b>Notes</b>	<b>References</b>
<b>Lesser Himalaya</b>	Precambrian metasediments, Paleozoic and Mesozoic sediments (carbonates, arenaceous and argillaceous); granitic intrusions, volcanics		Yin and Harrison (2000)
<b>Greater Himalaya</b>	Granitic intrusions, volcanics, gneisses, complex schists, Paleozoic and Mesozoic metasediments		Yin and Harrison (2000)
<b>Tethys Himalaya</b> (also called <b>Zaskar zone</b> )	Carbonate platform (Late Precambrian to Eocene sedimentary sequence), ophiolites, clasts and conglomerates derived from the uplifted Ladakh batholith to the north.		Searle et al (1988)
<b>Ladakh batholith</b> (+ <b>Kohistan arc</b> )	Cretaceous-Early Tertiary batholith, composed by: sheared greenschists that grades to basalts and sheared granitoids; andesitic unit; rhyolitic pyroclastic flows and volcaniclastic rocks; basalts intruded by calc-alkaline plutons; basalts and quartzites.		
<b>Qiangtang terrain</b>	Low to high grade metamorphosed melange complexes		
<b>Kunlun Shan</b>	Triassic flysch complex	Similar to the eastern Qilian-Songpan-Ganzi terrain	Wang et al. (2003) and references therein
<b>Tarim</b>	It is one of the largest Precambrian continental blocks in China. Neo-Archean to Paleoproterozoic metamorphic basement (granitoids plutons, granitic gneisses) covered by Mesoproterozoic sedimentary and volcanic deposits. In the north-western sector, Late Precambrian to Devonian shallow marine sediments are unconformably overlain by Late Paleozoic deposits (Carboniferous-Permian). At the northern margin of the Tarim craton, these deposits are continental Permian deposits, bimodal dikes and granitoids plutons arc/subduction-related. Finally the basin is filled with a thick foreland sequence of Mesozoic and Cenozoic continental sediments.	All the Precambrian and Mesoproterozoic units have been affected by the Late Mesoproterozoic / neo-Proterozoic tectono-thermal events related to the amalgamation and breakup of Rodinia supercontinent. Late Paleozoic magmatism at the northern margin of Tarim craton is thought to be the reflection of arc or subduction (the early Devonian northward subduction of the Southern Tian Shan Ocean below the Tian Shan).	Ju and Hou (2014); Wang et al. (2003) and references therein

**Table 5.1.** (continued)

Description	Lithology	Notes	References
<b>Tian Shan</b>	The southern Tian Shan is composed by allochthonous units of ophiolites and ophiolitic mélanges, locally containing relics of blueschists and HP-type granulite. The geochemical features of mafic rocks suggest a back-arc basin setting.	Central and southern Tian Shan are bounded by a northern suture corresponding to the Devonian closure of the Southern Tian Shan Ocean, and a southern suture corresponding to the Earliest Carboniferous closure of a back-arc basin. During the Silurian-Devonian, they constituted a single paleo-geographic unit, containing a volcanic arc in the northern part.	Charvet et al., (2011); Ju and Hou (2014)
	The central Tian Shan consists of Proterozoic gneiss and schist intruded by Paleozoic calc-alkaline granite. These older rocks are overlain by passive margin carbonate and continental clastics of Middle and Upper Proterozoic age.	The subduction led to the formation of a Middle Silurian to early Carboniferous magmatic arc along the southern margin of the Kazakhstan-Yili terrane. The closure of the South Tian Shan Ocean was possibly a diachronous, scissors-like process, which started in the east (early Devonian) and finished in the west.	Charvet et al. (2011); Wang et al. (2003) and references therein
	Northern Tian Shan: Upper Paleozoic (Late Devonian-Carboniferous) sedimentary sequence and abundant calc-alkaline volcanic and plutonic rocks.	The entire northern Tian Shan can be interpreted as a Late Paleozoic continental active margin bordering a southward-subducting oceanic domain located between the northern Tian Shan and the Junggar units. This subduction produced: 1) the Carboniferous volcanic arc to the east, the volcanic-arc plutonic and volcanic rocks of Yili unit to the west, and 2) trench-fill turbidites well preserved in the western area and ophiolitic mélange, forming a suture zone between the northern Tian Shan and Junggar units	Charvet et al. (2011)

**Table 5.1.** (continued)

<b>Description</b>	<b>Lithology</b>	<b>Notes</b>	<b>References</b>
<b>Junggar Basin and Junggar Accretional Belt</b>	<p>The basin is triangular in shape and filled with deposits thickening gradually from north to south. The basal Upper Permian deposits of the Junggar Basin are non-marine and were deposited within the subsiding foreland basin. Geological reconstructions suggest that the basement underlying the Junggar Basin consists of incompletely subducted, imbricated mid-Carboniferous oceanic crust and trench-wedge volcanoclastic sediment. To the north, the Junggar Accretional Belt consists mainly of accreted Devonian and Carboniferous sediments and volcanics with a few scattered Ordovician and Silurian rocks, and is a part of the south margin of the Altai Block. Dismembered ophiolites and associated cherts record the involvement of oceanic crust of the Paleo-Junggar Ocean. Calc-alkaline Paleozoic plutons formed between the Altai and Junggar mountains above the north dipping oceanic slab.</p>		Wang et al. (2003) and references therein
<b>Altai Range</b>	<p>The Altai Range includes a 12-km-thick early Paleozoic accretionary wedge, consisting of metamorphosed sandstone, shales, and minor limestones. Intercalated within these sedimentary sequences, there are mid-Paleozoic island arc volcanics and calc-alkaline intrusives. Gneissic rocks along the southern border are believed to comprise the Precambrian basement.</p>		Wang et al. (2003) and references therein

Seismic and thermal studies show that the western Tibetan Plateau has a lithosphere thickness of 180-220 km (An and Shi, 2006; Zhao et al., 2010), increasing westwards toward the Karakorum and Pamir regions. West of 80°E, the India-Eurasia plate boundary is located north of the Jinsha Suture, and it is expressed in the receiver functions profile by a jump in the LAB depth of ~50 km between the deeper Indian LAB and the Eurasian LAB (Zhao et al., 2010). Consistently to these results, P- and S-wave tomography studies show that the LAB below the Tarim Basin is relatively shallower and located at 150-200 km depth (Xu et al., 2002; An and Shi, 2006; Priestley and McKenzie, 2006; Lei and Zhao, 2007). Northwards, the Tian Shan belt is characterized by an even thinner lithosphere (120-170 km, Xu et al., 2002; 90-120 km Kumar et al., 2005), with higher temperatures (~1390°C at 150 km depth, An and Shi, 2006) and low velocities penetrating in the lower crust, which have been related to the upwelling of hot mantle anomalies (Xu et al., 2002 and references therein; Lei and Zhao, 2007).

### 5.1.3 Upper mantle P-wave tomography

Figure 5.3 shows a vertical cross-section of a P-wave global tomographic model obtained using the same method described in Bijwaard et al. (1998), but using a much larger arrival time dataset (Villaseñor et al., 2003).

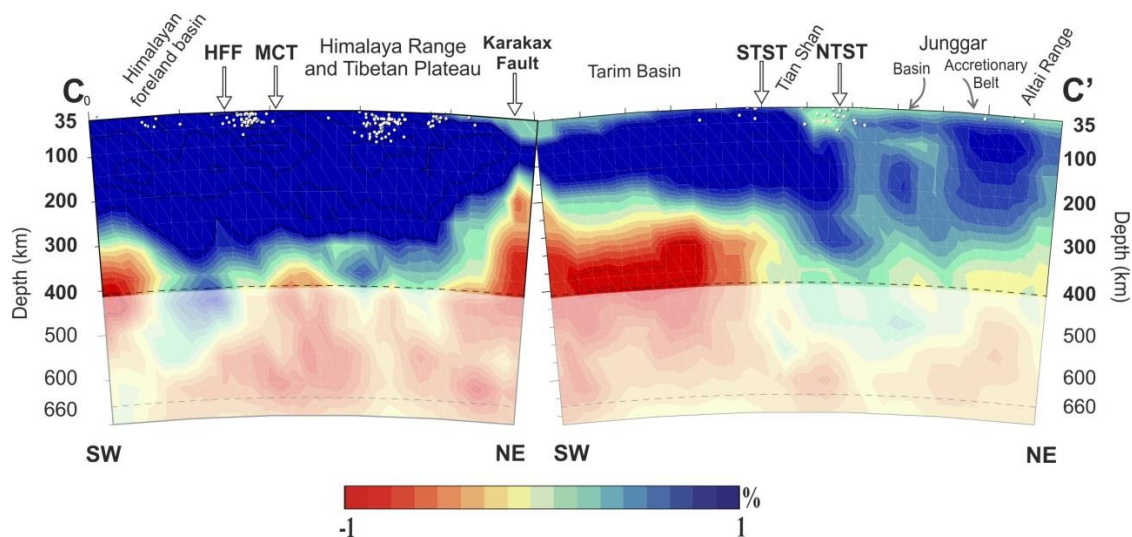


**Figure 5.3.** P-wave seismic tomography image along C-C' profile (see location on Figure 5.1) White circles represent the earthquakes used in the tomography (Engdhal et al., 1998). Contour lines interval: 1%. Global reference model used - AK135 (Kennet et al., 1995). HFF: Himalaya Frontal Fault; MCT: Main Central Thrust; NTST: Northern Tian Shan Thrust; STST: Southern Tian Shan Thrust.

The new dataset incorporates additional earthquakes from 1995 to 2002 listed in the International Seismological Centre's bulletins, and arrival times recorded at regional distances that were not used previously. In total, more than 14 million arrival times from 300,000 earthquakes, nearly 4 times the amount used by Bijwaard et al. (1998), were reprocessed using the EHB methodology (Engdahl et al., 1998). The ray paths corresponding to these new arrival times sample mainly the uppermost mantle and it is in this region where the resolving power of the new dataset is increased, allowing to image seismic velocity anomalies of the same resolution of the grid used for the tomographic inversion ( $0.5^\circ \times 0.5^\circ$  in area and 25-50 km in depth).

The tomography image shows a strong positive anomaly (up to 4%) beneath the Himalaya Range and the Himalayan foreland basin, vanishing to about 300 km depth. P-wave anomalies show progressive lower amplitudes north-eastwards, i.e. up to 2% below the Tarim Basin, and  $\leq 1\%$  in the Tian Shan, Junggar and Altai regions. The transition between positive and negative anomaly is located at  $\sim 220$  km depth beneath the Tarim Basin and  $\sim 320$  km depth beneath the Tian Shan. In the first 400 km depth of the profile, only one negative anomaly is imaged ( $\leq -1\%$ ), beneath the Tarim Basin.

## 5.2 Results and Discussion

### 5.2.1 Crustal structure

The large amount of published data on the crustal structure of the Himalaya-Tibetan region allowed us building a crustal model along the selected profile (C-C'). Density and thermal conductivity values for crustal bodies have been taken from previous studies (e.g. Wang, 2001, Wang et al. 2003; Zhao et al., 2003; Jiménez-Munt et al., 2008 and references therein). Density variations in depth are retrieved from seismic experiments (Owens and Zandt, 1997; Haines et al., 2003), wide angle seismic profiles (Zhang and Klemperer, 2005) and gravity data analysis (Zhao et al., 2003; Wang et al., 2004; Hetényi et al., 2007; Mishra et al., 2012). Radiogenic heat production has been taken from a global compilation carried out by Vilà et al. (2010). The tectonic structure is based on the tectonic map of Yin and Harrison (2000) and published geological cross-sections (Guillot et al., 2003; Wang et al., 2003; Wittlinger et al., 2004; Searle 2010; Charvet et al., 2011). Table 5.2 details the physical properties used in the modelling. Figure 5.4 shows the crustal model that better fits all the geophysical constraints. The crustal geometry has been constructed using the previous studies (described in Section 5.1.2 and Table 5.1) and modified within the data uncertainties.

**Table 5.2.** Physical properties of the different tectonic units used in the crustal model of Figure 5.4: density  $\rho$  (the range is due to its depth dependence); thermal conductivity  $K$ ; depth-varying radiogenic heat production  $H$ ;  $z$  is the depth in km. UC: upper crust; MC: middle crust; LC: lower crust.

	<b>Tectonic units</b>	<b><math>\rho</math></b> [kg/m <sup>3</sup> ]	<b><math>K</math></b> [W/K·m]	<b><math>H</math></b> [ $\mu$ W/m <sup>3</sup> ]
1	Himalayan foreland basin	2450 -2487	2.3	1.5 exp(-z/15)
2	India UC Lesser Himalaya	2635-2725	2.5	2.2 exp(-z/15)
3	Greater Himalaya	2645-3240	2.5	2 exp(-z/15)
4	Tethys Himalaya	2650	2.3	1.2 exp(-z/15)
5	Ladakh batholith	2720-2800	2.3	2 exp(-z/15)
6	Qiangtang	2610-3050	2.4	2 exp(-z/15)
7	Granitoid	2780	2.5	2
8	Tarim Basin sediments	2590-2780	2.2	1.2 exp(-z/15)
9	Junggar Basin sediments	2600-2690	2	1.2 exp(-z/15)
10	Kunlun Shan UC	2640-2880	2.5	2.2 exp(-z/15)
11	Tarim Basin UC	2720 -2790	2.5	2 exp(-z/15)
12	Tian Shan UC	2650-2725	2.3	2 exp(-z/15)
13	Junggar (Basin and Accretionary Belt) UC	2720-2800	2.5	2 exp(-z/15)
14	Altai Range UC	2720-2790	2.2	2 exp(-z/15)
15	India MC	2910-2990	2.3	0.3
16	Kunlun Shan MC	2900-3000	2.3	0.3
17	Tarim Basin MC	2800-2850	2.3	0.3
18	Tian Shan MC	2830-2940	2.3	0.3
19	Tian Shan and Junggar (Basin and Accretionary Belt) MC	2830-2950	2.3	0.3
20	India LC	3000-3180	2.1	0.2
21	Kunlun Shan LC	2910-3000	2.1	0.2
22	Tarim Basin LC	2990-3010	2.1	0.2
23	Tian Shan LC and Altai Range LC	2950-3000	2.1	0.2
24	Junggar (Basin and Accretionary Belt) LC	3000-3220	2.1	0.2

The resulting crustal model shows that the Himalayan Range (Lesser Himalaya and Greater Himalaya) and the Tibetan Plateau overthrust the relatively undeformed lower Indian crust as north as the Jinsha Suture (for more than ~860 km). The Greater Himalaya, in turn, is thrust by the Tethys sedimentary successions. The Tibetan Plateau is formed by a less than 100 km-wide area, including both the Ladakh batholith and the Qiangtang terrain. Both of them lay on top of the Indian middle-lower crust and are separated from the Tarim Basin by the north-verging Kunlun Shan. The Tarim Basin is characterized mostly by gently deformed strata, thrust below the southern Tian Shan. Further north, the Junggar Basin is characterized by similar tectonic structure, with the crustal layers dipping to the south beneath the northern Tian Shan. In the middle of the two basins, the compressive structure of the Tian Shan is modelled through two main discontinuities, the NTST (Northern Tian Shan Thrust) and STST (Southern Tian Shan Thrust) thrusts, and a crustal root which is almost flat (~50 km depth Moho), in agreement with Wang et al. (2003) and Li et al. (2007). The crust-mantle boundary is constrained by different seismic studies along the profile (Kao et al., 2001; Zhao et al., 2003; Wittlinger et al., 2004; Rai et al., 2006; Li et al., 2007; see Figure 5.1). The Moho discontinuity is deepening inwards, reaching almost 90 km below the Qiangtang terrain and the Kunlun Shan. A Moho step of ~35 km indicates the beginning of the Tarim lithospheric domain, characterized by an almost constant depth of the crust-mantle boundary (~50 km), in agreement with Wang (2001). The thickness of the sedimentary cover in the Tarim Basin is not completely homogeneous, and it is thrust on the edges (Mascle et al., 2012). Finally, the lower crust and middle crust layers are characterized by lateral variation in thickness and density along the profile, based on Zhao et al. (2003) (see Table 5.2).

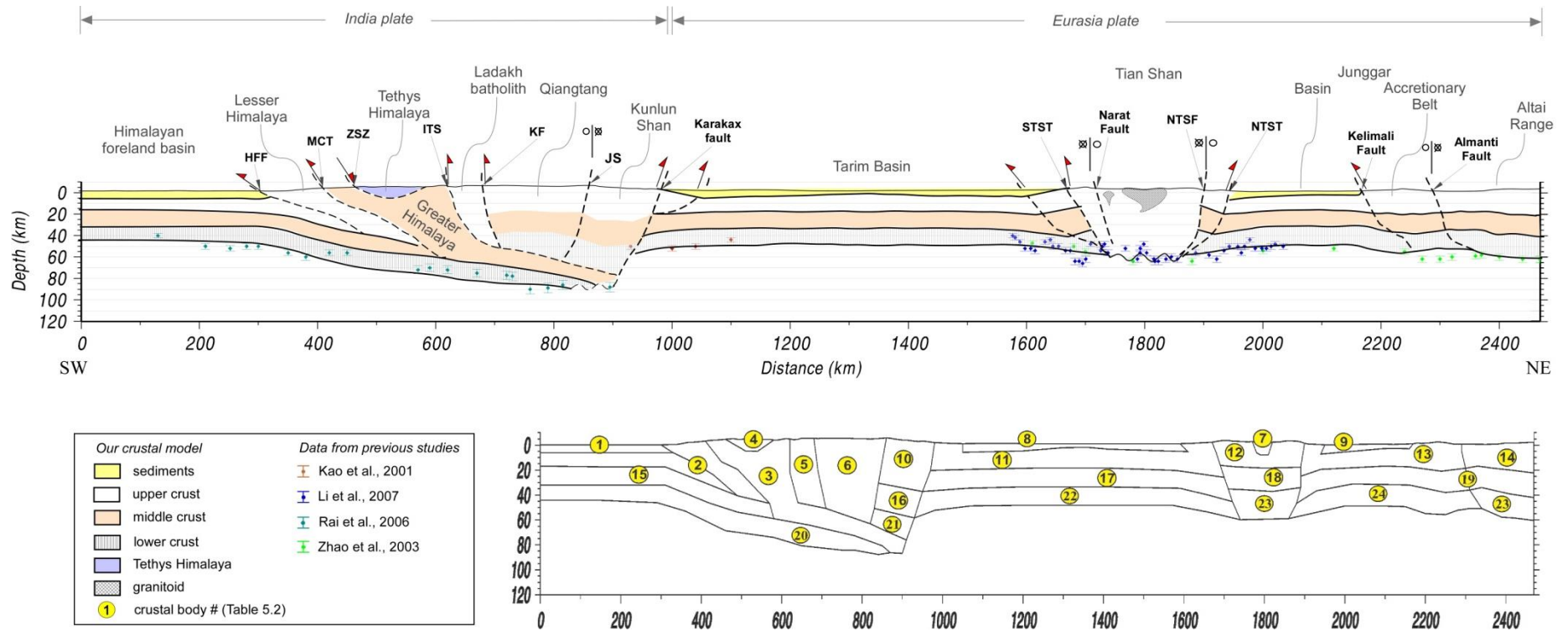


**Figure 5.4.** Crustal model of C-C' profile. Physical properties of the crustal bodies (numbers) are reported in Table 5.2. HFF: Himalaya Frontal Fault; ITS: Indus-Tsangpo Suture; JS: Jinsha Suture; KF: Karakorum Fault; MCT: Main Central Thrust; NTST: Northern Tian Shan Thrust; NTST: Northern Tian Shan Fault; STST: Southern Tian Shan Thrust; ZSZ: Zaskar Shear Zone.

## 5.2.2 Lithospheric mantle structure

The geochemical characteristics of the lithospheric mantle are defined by mantle xenoliths from Tian Shan (spinel lherzolites) (Bagdassarov et al., 2011), and Pamir (Hacker et al., 2005; Gordon et al., 2012) ranges. However, the compositional state of other lithospheric mantle domains, i.e. beneath the Himalaya Range and Tibetan Plateau, Tarim and Junggar basins, remains unclear. Mantle xenolith suites seem suggesting that the Tarim lithospheric mantle is formed by, at least partly, juvenile mantle material related to the Early Permian mantle plume event, which caused flood basalt magmatism covering nearly all the Permian strata in the Tarim Basin (Chen et al., 2014). Recently, Zhang and Zou (2013), by analysing chemical compositions of mafic dikes, argue for two distinct mantle domains in the Tarim Large Igneous Province: a long-term enriched continental lithospheric mantle of the Tarim domain in the south, and a more depleted lithospheric mantle of the Central Asian Orogenic Belt (CAOB) (i.e: Tian Shan, Junggar and Altai Range) region in the north, due to slab-derived fluids or subducted sediments.

Mineral assemblages in the lithospheric mantle have been computed using the NCFMAS major oxides approach. We have considered different mantle compositions on the basis of global scale xenolith and tectonothermal age data (Griffin et al., 2009), and available petrological studies on local mantle xenoliths (see Table 5.3 and xenolith suites localities in Figure 5.1). The asthenosphere is modelled through a highly fertile Primitive Upper Mantle (PUM, McDonough and Sun, 1995). In order to smooth the compositional change between the lithospheric mantle and the underlying asthenosphere, we introduced a 10-20 km-thick layer with an intermediate composition between the asthenosphere and the corresponding lithospheric mantle above. A thermal anomaly ( $\Delta T=70^{\circ}\text{C}$ ) has been introduced in the sub-lithospheric domain beneath the Tarim Basin to fit the low velocity anomaly observed in the P-wave tomography profile under the basin (Figure 5.3). Figure 5.5 shows the best fit model using the described conditions and the parameters summarized in Table 5.2 and compositions in Table 5.3.

In general, the resulting elevation, and gravity and geoid anomalies match the major observed trends along the profile. Local misfits in the Bouguer anomaly (15-20 mGal) are noticed at the southern edge of Tarim Basin, just after the Karakax fault, and in the elevation of the Junggar Basin and southern Altai Range (600-800 m), probably related to local crustal features not considered in our model. The calculated surface heat flow, ranging between 40 and 60 mW/m<sup>2</sup>, is not so well constrained owing to its scarcity and associated uncertainty, particularly along the SW-half of the profile. However, the results are consistent with the heat flow values from Wang (2001) and An and Shi (2007) illustrated in Section 5.1.1.

**Table 5.3.** Major elements composition in the NCFMAS system for the lithospheric mantle and asthenosphere domains used in the modelling (Figures 5.5 and 5.7). Mantle 2 and Mantle 4 derive from published petrological studies on mantle xenoliths. Gt: garnet; Lherz.: Lherzolite; Sp: Spinel.

<b>Mantle compositions in the NCFMAS system (%)</b>				
	<b>Mantle 1</b>	<b>Mantle 2</b>	<b>Mantle 3 - PUM</b>	<b>Mantle 4</b>
	Lherz. Average (Griffin et al., 2009)	Sp Lherz. (calculated from Bagdassarov et al., 2011)	Primitive Upper Mantle (McDonough and Sun, 1995)	Gt Lherz. (Song et al., 2007)
<b>SiO<sub>2</sub></b>	45.4	44.61	45	51.45
<b>Al<sub>2</sub>O<sub>3</sub></b>	3.7	2.57	4.5	4.64
<b>FeO</b>	8.3	9.03	8.1	8.89
<b>MgO</b>	39.9	41.37	37.8	24.56
<b>CaO</b>	3.2	2.26	3.6	8.82
<b>Na<sub>2</sub>O</b>	0.26	0.29	0.25	0.37
<b>Total</b>	100.76	100.13	99.25	98.73
<b>Mg#</b>	<b>90.6</b>	<b>89.04</b>	<b>89.3</b>	<b>83.1</b>

The best fit model (Figure 5.5) shows that the lithosphere thickness varies between 170 km and 290 km along the profile, with a kind of irregular “three-steps” geometry. Three relative minimums are located below the Himalayan foreland basin (230 km), the southern Tarim Basin (230 km) and the Junggar Basin (170 km); the maximum LAB depths being below the Kunlun Shan (300 km) and the Tian Shan (270 km). The transition between the India and Eurasia lithospheres occurs south of the Tarim Basin, just below the Karakax Fault, with a step in the LAB depth of about ~70 km, in agreement with Zhao et al. (2010). Further north, an additional thickening of the lithosphere (LAB depth at ~260 km) suggests that the Tarim lithospheric mantle extends below the Tian Shan, whereas the lithospheric mantle below the Junggar region is affected by mantle thinning (LAB depth at 170-180 km). These results are in agreement with Xu et al. (2002) who, by imaging velocity anomalies in the upper mantle, estimate that the lithosphere of the central and northern Tarim Basin is thicker (>200 km) relative to the southern sector, whereas low velocity anomalies suggest a lithospheric thinning below the Tian Shan and Junggar Basin. More recent seismic studies promote the lithospheric thinning hypothesis (Vinnik et al., 2004; Kumar et al., 2005), especially in the western sector of the Tian Shan, where the lithosphere thickness is only 90-120 km and suggests the presence of a little mantle plume. Our profile runs through the central-eastern Tian Shan sector, hence the thinning we image is just affecting the Junggar Basin.

The temperature distribution along the profile (Figure 5.5) shows upward deflections of the isotherms according to the increase of crustal thickness and the consequent higher radiogenic heat production, especially accentuated beneath the Tibetan Plateau, Tian Shan, and the Junggar Accretionary Belt. The temperature at the Moho discontinuity is ~700°C in the Himalayan foreland basin and Tarim Basin, 800-850°C in the Junggar Basin, ~900°C in the Himalaya-Tibetan Plateau region, Tian Shan, Junggar Accretionary Belt and Altai Range. The maximum temperature at Moho discontinuity is ~1000°C below the Kunlun Shan. These

Moho temperatures are in agreement with values obtained by field-based geothermal analysis and petrology studies (Liu et al., 2004; Bagdassarov et al., 2011). Our modelled temperatures match the temperatures estimated from seismic tomography in the western Himalaya-Tibetan region (An and Shi, 2007), except for the Tarim Basin and Tian Shan, where the authors predicted higher values ( $\sim 1390^{\circ}\text{C}$  at 150 km depth). These authors published a seismic-thermal lithosphere map where the LAB is located at 140-170 km depth beneath the Tarim Basin and Tian Shan (An and Shi, 2006), which is much shallower than predicted in our model (230-250 km) and the study by Wang (2001), where the lithosphere in the Tarim Basin is 250 km-thick.

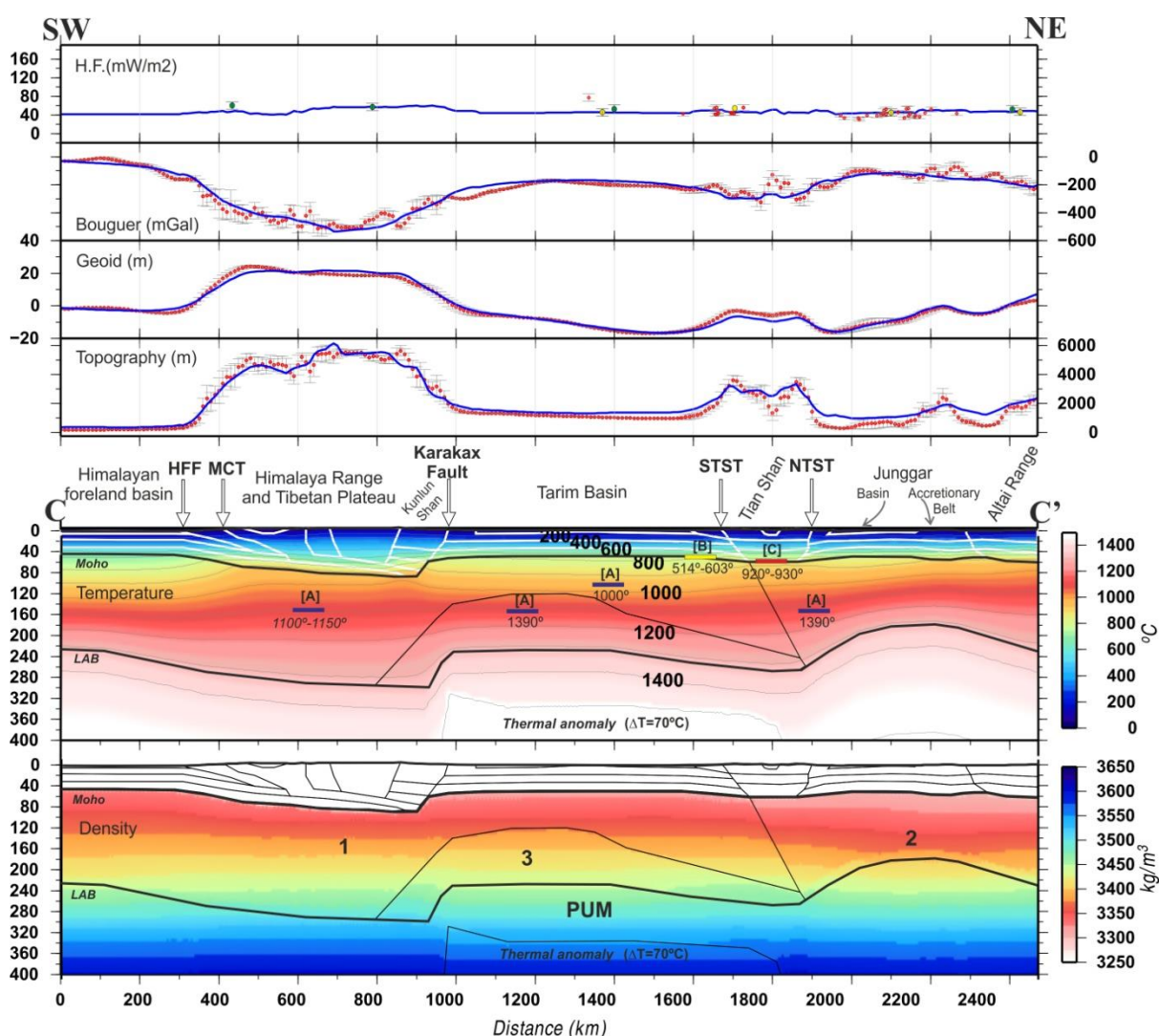


**Figure 5.5.** Modelling results along C-C' profile. Red dots represent the data and vertical dispersion bars the standard deviation calculated on a strip of 50 km for gravity, geoid and topography, and on a strip of 500 km for surface heat flow. Yellow and green dots are mean heat flow values from Wang (2001) and An and Shi (2007), respectively. Continuous blue lines represent the calculated observables from the model. Thick horizontal bars are temperatures from different studies ([A] An and Shi, 2007; [B] Liu et al., 2004; [C] Bagdassarov et al., 2011). Numbers indicate different mantle bodies defined by their own NCFMAS composition (Table 5.3). HFF: Himalaya Frontal Fault; MCT: Main Central Thrust; NTST: Northern Tian Shan Thrust; STST: Southern Tian Shan Thrust.

The lithospheric mantle density (Figure 5.5) is the result of the temperature, pressure and chemical composition, and their values range between 3350 and 3500 kg/m<sup>3</sup>. As a result of the compositional change and the thinning of the lithospheric mantle, the average mantle density decreases to values between 3300 kg/m<sup>3</sup> and 3400 kg/m<sup>3</sup> below the Junggar region. The sub-lithospheric mantle density increases continuously until values of 3600 kg/m<sup>3</sup>, due to the predominant effect of pressure.

### 5.2.3 Mantle seismic velocities

The LitMod-2D methodology allows calculating in a self-consistent way the elastic parameters of the mantle and therefore the P- and S- wave seismic velocities. Figure 5.6 shows the calculated mantle V<sub>p</sub> and V<sub>s</sub>, and their anomalies.

P-wave velocities within the lithospheric mantle range from 8.00 km/s at Moho depth below the Altaids (Junggar Accretionary Belt and Altai Range) to 8.50 km/s at LAB depth beneath the Tibetan Plateau and Kunlun Shan. In the sub-lithospheric domain, V<sub>p</sub> increases progressively with depth to values of ~8.75 km/s at 400 km deep. Beneath the Tarim Basin these values are slightly lower due to the pre-defined thermal anomaly. S-wave velocities within the lithospheric mantle vary between 4.5 km/s to 4.65 km/s, with the minimum and maximum located at LAB depth below the Junggar Basin and the Kunlun Shan, respectively.

The velocity anomalies are calculated assuming a 1D reference velocity model. Global seismic tomography commonly uses the AK135 reference model (Kennet et al., 1995), which represents a global average of seismic velocities corresponding to a simple stratified Earth with 35 km-thick crust and 120 km-thick lithospheric mantle. The thick crust of the Himalaya-Tibetan orogen (up to 90 km-thick; Rai et al., 2006), makes the AK135 unsuitable for a realistic analysis of the upper mantle anomalies in the region, especially at shallow levels. Therefore, we opted for calculating the mantle seismic velocity anomalies relative to a column selected along the profile. In order to reproduce the seismic anomaly distribution of the tomography profile in Figure 5.3, we selected the reference column following two criteria: i) its crustal and lithospheric thicknesses should be a representative average of the entire profile; ii) the seismic velocity anomalies of the tomography model (Figure 5.3) should be around zero.

Our reference column is selected in the Junggar Basin, at 2100 km distance in the profile. The resulting velocity anomalies (Figure 5.6) show positive values all along the profile down to 300 km depth in the lithospheric mantle, although with decreasing amplitude from southwest to northeast. The lithospheric mantle below the Himalayan foreland basin, Himalaya Range and Tibetan Plateau is cold and characterized by high positive (up to 2%) V<sub>p</sub> anomalies, penetrating down to ~300 km. This seismically-fast lithospheric mantle can be interpreted as the northward subducting Indian plate, in agreement with published tomography studies (e.g., Tilmann et al, 2003; Wittlinger et al., 2004; Li et al., 2008) and Figure 5.3. Beneath the Tarim Basin, the positive V<sub>p</sub> anomaly goes down to ~200 km depth,

and a low velocity zone in the sub-lithospheric domain, between 300 km and 400 km depth, marks the pre-defined thermal anomaly. Northwards, the Tarim lithospheric mantle plunging below the Tian Shan is in agreement with Poupinet et al. (2002), who imaged the Tian Shan sub-crustal lithosphere subducting beneath the northern Tian Shan.

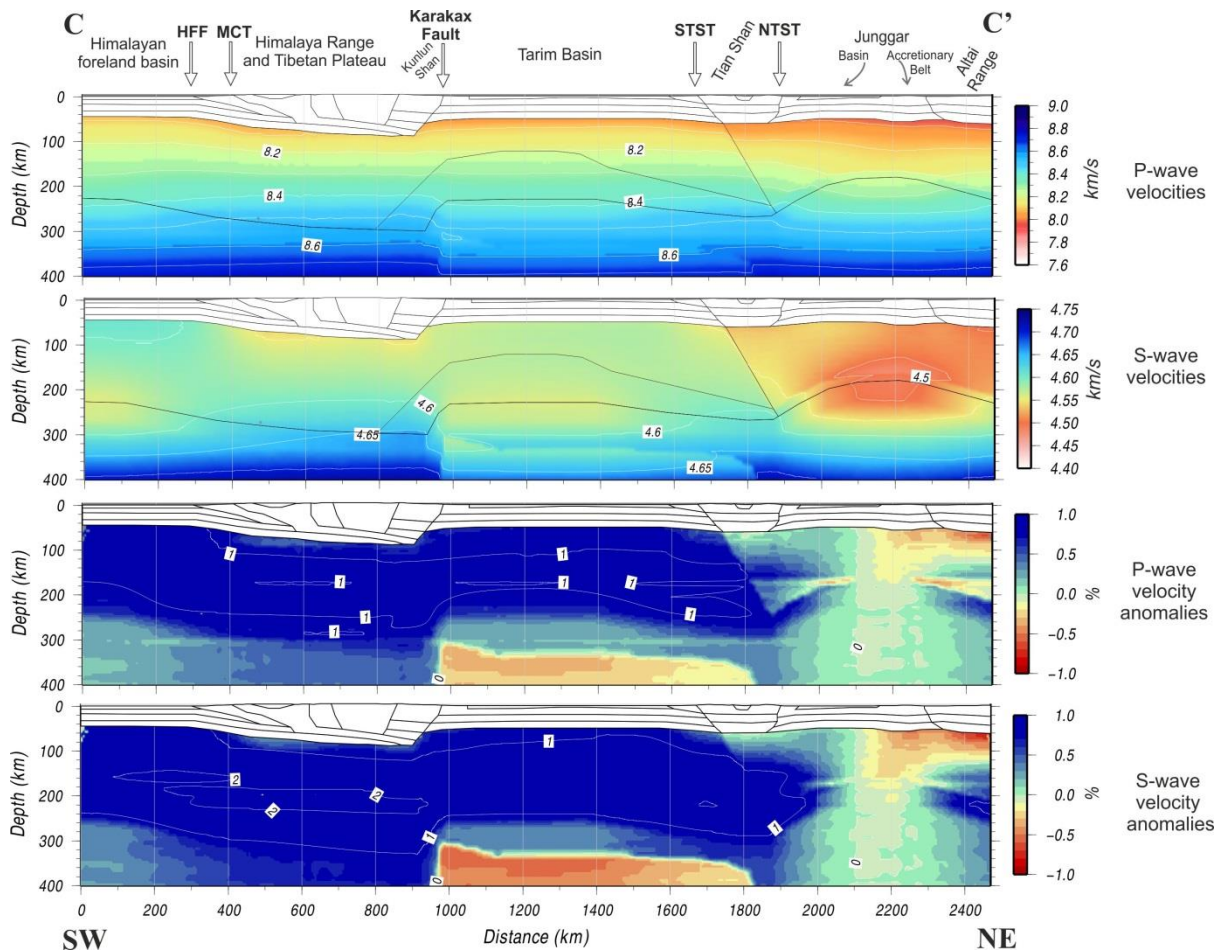


**Figure 5.6.** Resulting distribution of mantle seismic velocities and mantle seismic velocity anomalies for both P- and S-waves along C-C' profile. Velocity anomalies are calculated respect to the column at 2100 km from the beginning of the profile.

Our results show that the best fit model requires slight variations in the lithospheric mantle composition along the profile. Our model is compatible with i) a standard lherzolitic mantle composition (Mantle 1, Table 5.3) below the Himalayan foreland basin, Himalaya Range, and western Tibetan Plateau, and the uppermost mantle beneath the Tarim Basin; ii) a spinel-lherzolitic composition below the CAOB region (i.e. Tian Shan, Junggar, and Altai Range) (Mantle 2, Table 5.3); and iii) an undepleted mantle in the deepest portion of Tarim lithosphere, with a composition equivalent (at least in major oxides) to the primitive mantle of the underlying asthenosphere (Mantle 3-PUM, Table 5.3). The thermal anomaly located at 300-400 km depth beneath the Tarim Basin is probably the responsible of the enrichment in

incompatible elements (CaO and  $Al_2O_3$ ), calling for metasomatization of the lithospheric mantle by means of ascending asthenospheric fluids, according to the plume-lithosphere interaction hypothesis proposed by different studies (Zhang et al., 2010, Zhang and Zou, 2013, Xu et al., 2014).

The resulting lateral compositional changes, and the consequent seismic velocities and lithospheric thickness variations, suggest that three lithospheric domains can be recognized along the cross-section in the western Himalaya-Tibetan orogen: i) a subducting Indian lithosphere underlying the western Himalaya Range, Tibetan Plateau and Kunlun Shan, separated from the Eurasian lithosphere by a jump in both LAB and Moho discontinuities, clearly visible just below the Karakax fault; ii) the Tarim (Eurasian) lithospheric domain plunging northwards below the Tian Shan, with the deepest lithospheric mantle fertilized and underlined by a thermal sub-lithospheric anomaly between 300 and 400 km depth; and iii) a northern lithospheric domain beneath the northern Tian Shan, Junggar and Altai regions, also forming part of the Eurasian lithosphere.

## 5.2.4 Lithospheric structure variations along the strike of the Himalaya-Tibetan orogen

### Eastern Tibetan Plateau

Numerous studies (Kumar et al., 2006; Jiménez-Munt et al., 2006, 2008; Zhao et al., 2010; Ceylan et al., 2012) suggest the occurrence of a lithospheric mantle thinning beneath the north-eastern Tibetan Plateau, with the LAB located at 100-170 km beneath the north Lhasa and Qiangtang terrains. This thinning would explain the low P-, Pn- and S-, Sn-wave velocity anomalies, the low Rayleigh wave phase velocities and the high electrical conductivities observed in the region, suggesting a hot environment throughout the crust and upper mantle (Yue et al., 2012 and references therein). The 2D lithospheric thermal and density models, presented by Jiménez-Munt et al. (2008), along the D-D' transect (Figure 5.1 for location) agree with this hypothesis, proving the need of a thin and hot lithosphere to explain the high topography, gravity, geoid and crustal temperatures of the north-eastern plateau. We have re-modelled this profile using the same approach than for C-C' transect to investigate the relative importance of the mantle chemical composition on the density and buoyancy of the lithospheric mantle, and therefore on the resulting lithospheric structure. In the next paragraphs we present our results along the D-D' profile, and we discuss the differences between the western and eastern sectors of the Himalaya-Tibetan orogen.

Our best lithospheric model along the D-D' transect (Figure 5.7) confirms the thinning of the lithospheric mantle below the north-eastern Tibetan Plateau, being the LAB topography slightly different from the thermal model by Jiménez-Munt et al. (2008). The newly modelled Indian lithospheric mantle is up to 100 km thicker beneath the Himalaya Range, and 60-70 km thinner below the Lhasa terrain. Also, the lithospheric thinning between

the Lhasa and Qiangtang terrains is more gradual and, north of the Kunlun Suture the LAB is between 20 and 70 km deeper. The resulting thermal and density structures show that the north-eastern Tibetan Plateau is characterized by high temperatures ( $\sim 1050^\circ\text{C}$  the Moho temperature) and low densities ( $\sim 3310\text{--}3350\text{ kg/m}^3$ ). The results are compatible with a composition of the lithospheric mantle underneath the north-eastern plateau highly depleted in MgO and enriched in FeO,  $\text{Al}_2\text{O}_3$  and CaO (Mantle 4, Table 5.3), also retrieved by xenolith samples (Song et al., 2007). The olivine content is very low and the rocks are formed primarily by pyroxenes ( $\sim 80\text{ wt}\%$ ) and garnet ( $\sim 10\text{ wt}\%$ ). This composition could be the result of a metasomatic refertilization of a strongly depleted Archean lithospheric mantle, involving the introduction of Fe-, Ca- and Al-rich melts (Shi et al., 2010).

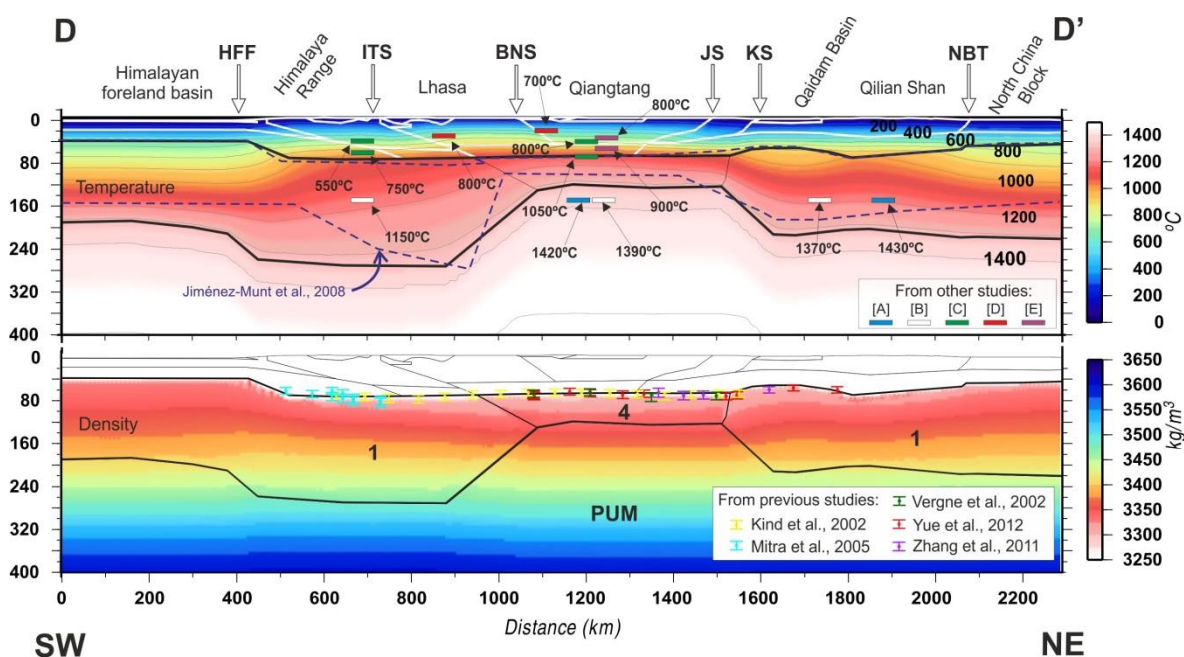


**Figure 5.7.** Modelling results along D-D' profile. Only small differences in the Moho depth have been applied to update the crustal thickness values of the previous model by Jiménez-Munt et al. (2008) (dashed line) with the most recent data (see text for details). Thick horizontal bars are temperatures taken from: [A] Priestley and McKenzie (2006); [B] An and Shi (2007); [C] Galve et al. (2006); [D] Mechie et al. (2004); [E] Hacker et al. (2000). BNS: Bangong Nujiang Suture; HFF: Himalaya Frontal Fault; ITS: Indus-Tsangpo Suture; JS: Jinsha Suture; KS: Kunlun Suture; NBT: North Border Thrust.

The resulting seismic velocities from our model are shown in Figure 5.8 (panels a, b), together with a section of the P-wave global tomographic model (panel c) obtained using the method described in Bijwaard et al. (1998) and the dataset from Villaseñor et al. (2003). The seismic tomographic model images strong positive anomalies (up to 4%) below the Himalayan foreland basin and the Himalaya Range, till the Indus-Tsangpo Suture, forming a sub-horizontal feature that we interpret as Indian lithospheric mantle. North of the suture, a slightly positive ( $\sim 0.2\text{--}0.4\%$ )  $V_p$  anomaly deeps to depths between 100 and 250 km below the Lhasa terrain, which could correspond to the Indian subducting slab. A slightly negative

( $\sim 0.4\%$   $V_p$  anomaly) anomaly is imaged between 150 and 250 km depth below the Qiangtang and Songpan-Ganzi terrains and between 250 km and 400 km depth below the Qaidam Basin. Our model is capable to reproduce the general distribution and shape of the seismic  $V_p$ -anomalies (with the reference column at 1500 km horizontal distance), with strong positive values below the Himalayan foreland basin, the Himalaya Range, and to the north below the Qaidam Basin, Qilian and North China Block. The lithospheric mantle of Lhasa and Qiangtang terrains is characterized by a  $\sim 0.6\%$  low velocity anomaly, vanishing beneath the LAB to the bottom of the model. These results are in agreement with the low velocity anomalies observed in P-, S- wave studies (Liang et al., 2004, Liang and Song, 2006; Huang and Zhao, 2006; Li et al., 2008; Liang et al., 2011, 2012; Pei et al., 2011; Zhang et al., 2012), although the amplitude of the anomalies differs depending on the tomography method used.

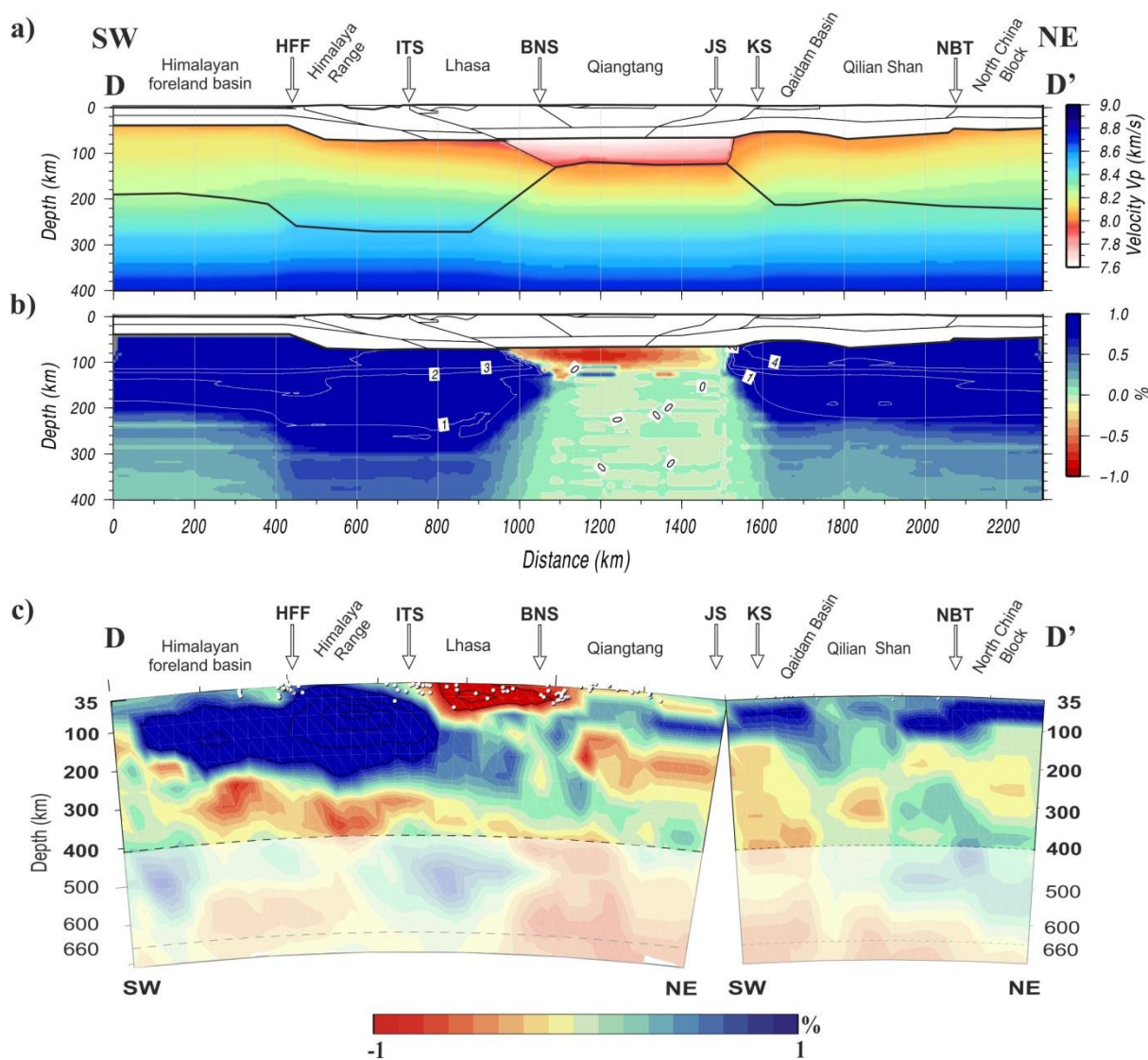


**Figure 5.8.** D-D' profile. (a) P-wave mantle velocities; (b) mantle velocity anomalies calculated respect to the selected column at 1500 km from the beginning of the profile; (c) P-wave seismic tomography image (see text for details).

Similarly to the western profile, the distinction between the Indian and the Eurasian lithospheres is noticed by changes in LAB topography and chemical composition. In our interpretation, the Indian lithospheric mantle is underthrusting the Tibetan Plateau up to the Bangong-Nujiang Suture discontinuity, whereas the lithospheric mantle below the Qaidam Basin, Qilian Shan and North China Block belongs to the Eurasian plate. In between, a transitional lithospheric mantle region, characterized by different composition and thickness, underlies the Qiangtang and (partially) the Lhasa terrains. This triple partition of the lithospheric mantle along the eastern transect follows the results of the receiver function study by Zhao et al. (2010), in which the transitional lithospheric region is defined as the “crush zone”, sandwiched between the India and the Eurasia plate.

The recent geophysical-petrological study of central Tibet by Vozar et al. (2014) shows lithospheric thickness values for the Qiangtang and Lhasa terrains (LAB depth at 80-120 km and at 140-220 km, respectively) similar to those obtained in our profile. The petrological results are also consistent with the presence of a compositional variation under the Tibetan Plateau, suggesting a fertile garnet-lherzolite lithospheric mantle below the Qiangtang, and a Fe-rich spinel-harzburgite lithospheric mantle below Lhasa. Since a wide range of compositions can equally well explain multiple geophysical data (Afonso et al. 2013a, b), we tested the compositions of Vozar et al. (2014) along our profile for the Qiangtang (garnet-lherzolite) and the India lithospheric mantle (Fe-rich spinel-harzburgite). The results, however, show a RMSE between calculated and observed data that is twice with respect to our model (Table 5.4). The increased amount of Fe in the India lithosphere results into a strong decrease of the elevation in the southern Tibetan Plateau and further misfits in geoid anomaly. A shallower LAB could overcome the difficulties, but it would produce a decrease in the positive seismic anomaly below the southern Tibetan Plateau, which works against seismic tomography results.

**Table 5.4.** The RMSE (Eq. 4.1) between measurements and calculated data for eastern profile (see explanations in the text).

<b>Profile D-D'</b>	<b>Bouguer anomaly (mGal)</b>	<b>Geoid (m)</b>	<b>Topography (m)</b>
Our model	25.3	3.6	314.5
Model with compositions from Vozar et al. (2014)	33.9	6.17	642.58

### Variations along the strike of the Tibetan Plateau

Our lithospheric models along the two profiles confirm the different mode of India-Eurasia collision from east to west (Huang and Zhao, 2006; Zhao et al., 2010; Zhang et al., 2012). In our interpretation India is underthrusting the whole Tibetan Plateau in the western

sector, whereas to the east the underthrusting is restricted to the north up to the Bangong-Nujiang Suture (Figure 5.9).

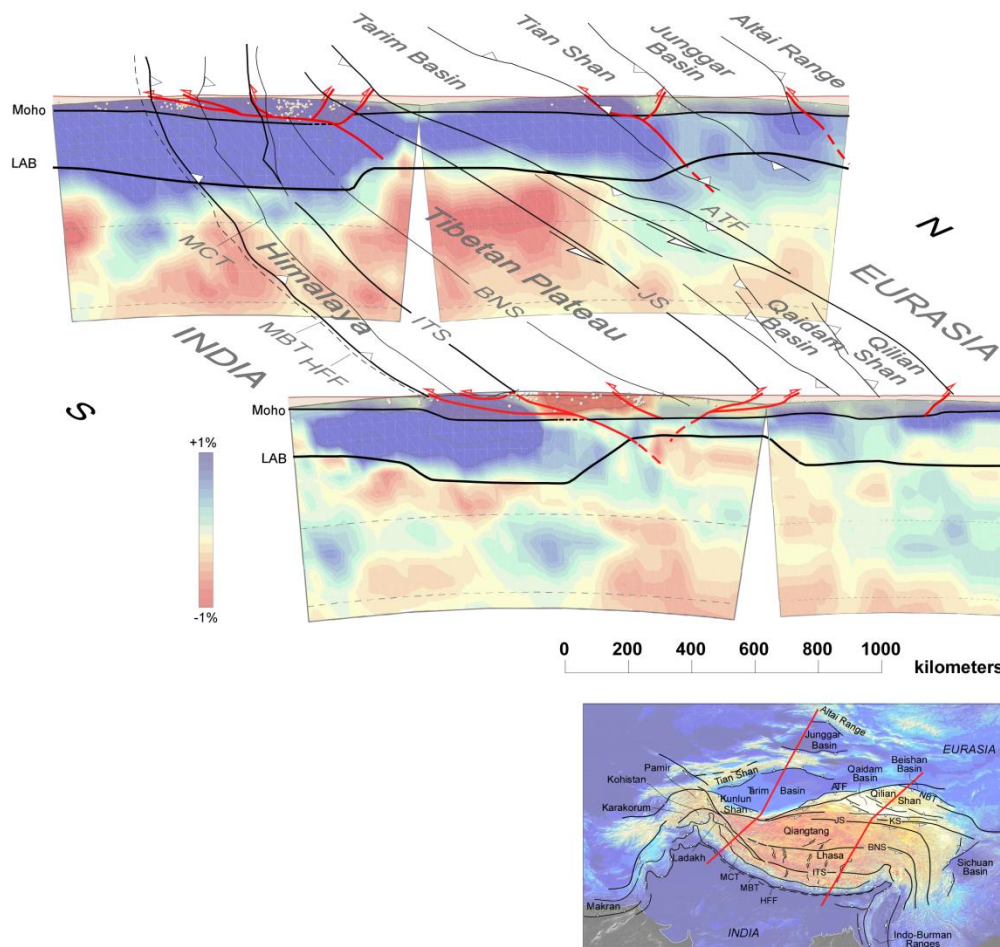


**Figure 5.9.** Simplified 3D diagram showing the resulting crustal and lithospheric structures from our modelling along the two studied profiles, superimposed to the seismic tomography. The Figure on the right lower corner is modified from Figure 1 in Jiménez-Munt et al. (2008).

Conspicuous differences in both crustal and lithospheric structures between the selected profiles are obtained: 1) The Tibetan Plateau (including Lhasa, Qiangtang, Songpan-Ganzi and Kunlun) is more than 1000 km wide along the eastern profile, whereas it narrows to less than 600 km between the Himalaya Range and the Tarim Basin along the western profile. 2) The thickening of the crust and the lithospheric mantle from the Himalayan foreland basin to the internal parts of the orogen is gradual in the west, whereas it is marked by a sharp step in the east. 3) The lithospheric mantle of the western transect is, in average, colder and thicker with respect to the eastern one. 4) A more fertile composition (high %  $\text{Al}_2\text{O}_3$  and low Mg#) results in smaller buoyancy (Watremez et al., 2013) and then, Mantle 4 in the north-eastern Tibet, is the least buoyant mantle. Conversely, Mantle 1 and Mantle 2, with a relatively low

content of FeO and Al<sub>2</sub>O<sub>3</sub> are more buoyant and, according to Watremez et al. (2013), stable through time, allowing for a better support of the high topography. This suggests that the support for the thickened lithosphere in the Himalaya-Tibetan orogen is favoured by a more depleted buoyant-like composition in the western sector, and by the thinning of the lithospheric mantle in the eastern Tibetan Plateau. 5) The relative enrichment of FeO, CaO and Al<sub>2</sub>O<sub>3</sub> of Mantle 4 in the north-eastern Tibet resembles supra-subduction zone mantle melts (Song et al., 2007), therefore it is consistent with the northward subducting Indian plate and the presence of a thinned lithospheric mantle, in agreement with other authors (England and Housemann, 1989; Molnar et al., 1993; Jiménez-Munt and Platt, 2006; Jiménez-Munt et al., 2008; Hatzfeld and Molnar, 2010). Finally, in order to analyse the effect of mantle composition on seismic velocities, we plot the depth variations of velocity and density for the four mantle compositions used in this study, considering a standard thickness of 210 km lithosphere and 42 km crust (Figure 5.10).

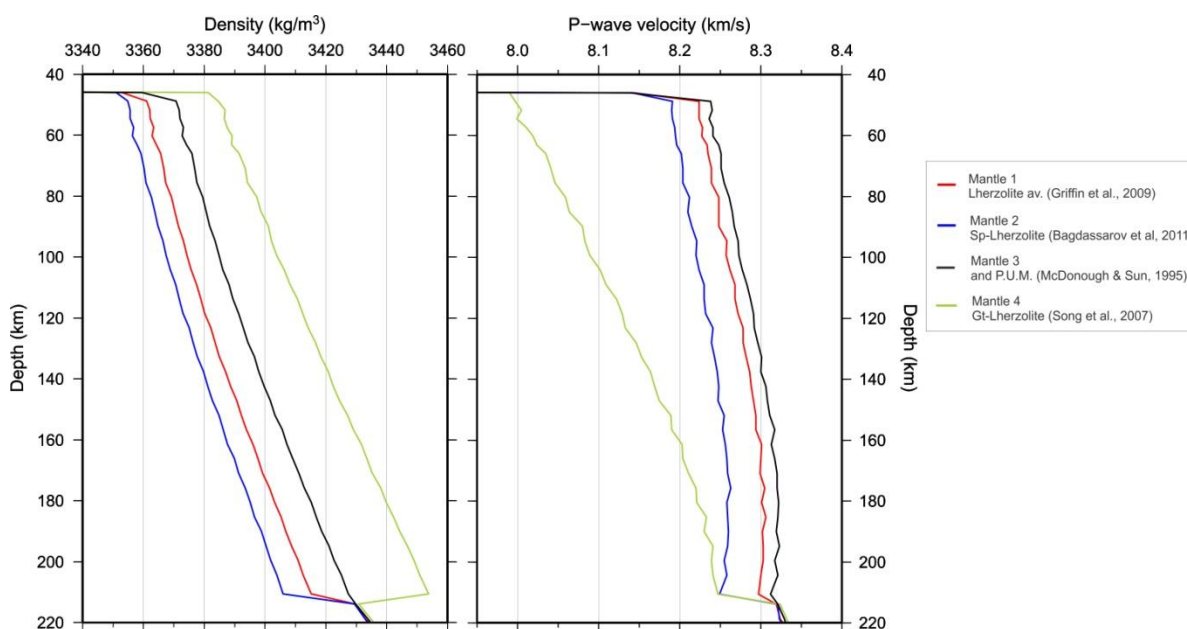


**Figure 5.10.** Density and P-wave velocity variations on depth for each composition, considering a flat model with parallel layers, where Moho and LAB discontinuities are located at 42 km and 210 km depth, respectively. Mantle composition names refer to Table 5.3.

Mantle 4 is characterized by the highest density, due to the high amount of garnet, but it shows the lowest V<sub>p</sub> values. This low V<sub>p</sub> is probably due to the small modal proportion of olivine in Mantle 4, which is the second fastest mineral in a four-phase lithospheric mantle (olivine, ortho- and clinopyroxenes, and garnet). Note that the lithospheric mantle of the north-eastern Tibetan Plateau (Mantle 4) is characterized by a strong depletion in olivine (only 10% wt), due to the insufficient amount of MgO in the considered bulk composition, and a significant amount of silica with respect to adjacent lithospheric mantle portions

(51.45% in Mantle 4 against 45.4% in Mantle 1). These characteristics suggest that this lithospheric mantle could have been affected by re-working processes involving crustal portions or subduction of continental crust.

In summary, our results are compatible with a composition that reflects the different and complex tectonic history of the area, including ongoing subduction of Indian and Tarim lithospheres, slab-induced mantle wedge asthenospheric flow, and subsequent interaction with the subjacent thinned lithospheric mantle in the north-eastern Tibetan Plateau and to the north of the Tian Shan region.

### 5.3 Concluding remarks

2D integrated geophysical-petrological modelling was performed along a profile crossing the western Himalaya Range, the Tibetan Plateau, the Tarim Basin, the Junggar and Tian Shan, ending at the southern Altai Range. Geological, geophysical and petrological data are combined within an internally consistent thermodynamic-geophysical framework, in which the density in the lithospheric mantle is a function of P-T conditions and chemical composition, taking into account mineral phase changes and lateral compositional heterogeneities. We compared the results with a new 2D lithospheric model along a transect crossing the eastern Himalaya Range and Tibetan Plateau, to consistently discuss the differences along-strike of the Himalaya-Tibetan orogen. The results obtained in this study allow us to make the following concluding remarks:

- Three lithospheric mantle domains have been identified in the western sector of the Himalaya-Tibetan orogen (C-C' profile): i) the Indian lithospheric mantle, which underlies the Himalayan foreland basin, the Himalaya Range and Tibetan Plateau, and the Kunlun Shan; ii) the Tarim (Eurasian) lithospheric mantle plunging northwards below the Tian Shan, and iii) a northern lithospheric (Eurasian) mantle domain beneath the northern Tian Shan, Junggar and Altai regions. Our results show that the India and Eurasia plates are separated by a sharp change in both LAB and Moho depths, coinciding with the Karakax fault at surface.

- The model shows that the Indian Moho is progressively deepening from ~40 km depth beneath the foreland, to ~90 km depth below the Kunlun Shan. Crustal roots are modelled in the Tian Shan and Altai ranges, with the crust-mantle boundary located at ~66 km and ~62 km depth, respectively. The lithosphere is 260-290 km-thick below the Himalaya and Tibetan Plateau (Indian LAB), gradually thickening towards the Kunlun, ~260 km below the Tian Shan Range, and ~240 km depth below the Altai Range, depicting a sort of irregular “three-steps” geometry of the lithospheric structure.

- A thermal anomaly is modelled beneath the Tarim Basin, below 300 km depth. This anomaly is likely linked to the enrichment in incompatible elements (CaO and Al<sub>2</sub>O<sub>3</sub>) of the deepest lithosphere mantle of the Tarim domain. Lateral compositional variations within the

lithospheric mantle are considered beneath the Central Asian Orogenic Belt, probably related to the metasomatism of Fe-, Mg-rich fluids from the subducted Tarim plate.

- In the eastern Himalaya-Tibetan Plateau along profile D-D', our results confirm that the eastern Tibetan Plateau is supported by a thick lithosphere (~280 km) in the south, and a thin lithosphere (~120 km) in the north, although the general shape of the LAB differs with respect to previous 2D-geophysical integrated models. The resulting lithospheric mantle composition beneath the north-eastern Tibetan Plateau is highly depleted in MgO and enriched in FeO, Al<sub>2</sub>O<sub>3</sub> and CaO, as retrieved by xenolith samples. The Indian lithosphere and the lithospheric domains to the north of the Tibetan Plateau are characterized by an average lherzolitic mantle.

- Our results suggest that the present-day lithospheric mantle structure of the India-Eurasia collision zone is laterally-varying along the strike of the Himalaya-Tibetan orogen, in terms of lithospheric thickness, lithospheric mantle density, temperature and composition. Our results also suggest that the orogen is supported by a thick buoyant lithospheric mantle in the western profile and by a lithospheric mantle thinning in the north-eastern sector of the Tibetan Plateau along the eastern profile.

## **PART III:**

# **NEOTECTONIC MODELLING OF CENTRAL ASIA**

---



## Introduction

Plate tectonics theory prescribes that most of the deformation on Earth is localized along a narrow belt around plate margins. However, how much deformation can be transmitted inside the plate is difficult to ascertain. The Central Asia region hosts wide deforming areas in which diffused or localized deformation occurs even hundreds of kilometres ahead of the Arabia-Eurasia and India-Eurasia plate boundaries.

One of the key parameters controlling the propagation of deformation to the continent interiors is the strength of the lithosphere (i.e. the total force necessary to deform the lithosphere at a given strain rate). Strength heterogeneities distributed laterally and in depth within the crust and lithosphere play an important role on defining the mode and localization of the deformation (Cook and Royden, 2008). The strength of the crustal rocks affects the spreading or migration of the mountain belts (Ghosh et al. 2006), but also mantle processes like subduction, slab tears or slab breakoffs have an impact on the surface motion. These mantle processes alter the distribution of the slab mass along the convergent margin, and drive lateral motion on the upper plate and/or affect the deformation of the margin and upper plate in time. The propagation to the continental interiors depends on the lithospheric strength and on the ability of the subducting lithosphere to propagate stress laterally (Capitanio, 2014 and references therein). Therefore, an accurate characterization of the surface deformation requires the knowledge of the structure and strength for both crust and upper mantle.

Using a geophysical-petrological approach (LitMod 2D, Chapter 3), we found that the lithosphere of the Zagros and the Himalaya-Tibetan orogens is characterized by lateral heterogeneities in terms of lithospheric and crustal thicknesses, lithospheric mantle density, temperature and composition (Chapters 4 and 5). It stands to reason that the lithospheric strength is also highly variable in these two orogens, being a function of composition, lithospheric thickness and geotherm. This study deals with the present-day deformation derived by the lateral strength variations not only in the two orogens, but in the whole Central Asia region. I investigate how the tectonic convergence of the Arabia and the India plates is accommodated within Eurasia and the relative contributions of the lithospheric structure, rheology, boundary conditions, and friction coefficient on faults on the predicted velocity and stress fields. For this purpose, I use a geodynamic modelling technique based on the thin-sheet approximation, which allows inferring the surface velocity field, stress directions, tectonic regime and strain distribution by applying velocity conditions to the boundaries of the model. The lithosphere strength is calculated by the lithosphere structure and thermal regime.

The thin-sheet approach has been widely used to study both the present-day (neotectonic) deformation in collisional settings (England and Molnar, 1997; Jiménez et al., 2001; Marotta, et al. 2001; Liu and Bird, 2002; Jiménez-Munt et al., 2003; Negredo et al., 2002, 2004; Barba et al., 2010; Howe and Bird, 2010; Cunha et al., 2012) and its evolution through time (England and Houseman, 1989; Sobouti and Arkani-Hamed, 1996; Jiménez-

Munt et al., 2005; Robl and Stüwe, 2005; Jiménez-Munt and Platt, 2006). In the Central Asia region, several studies have been published in the last two decades on the deformation related to the Arabian and Indian continental collisions. The numerical model proposed by Sobouti and Arkani-Hamed (1996) for the Iranian region shows that the deformation of this area is primarily controlled by the convergence between Arabia and Eurasia plates and by the presence of rigid blocks, i.e. Central Iran and the southern Caspian Basin, which control the observed crustal thickness and patterns of faulting. In the Tibetan Plateau, the numerical model by Jiménez-Munt and Platt (2006) explains the current elevation, the steep topographic margins, the E-W extension and the eastward extrusion with a rapid removal of the lithospheric root in the north-eastern sector. In the Amur region, i.e. to the north-east of the Central Asia, the neotectonic deformation has been investigated by Petit and Fournier (2005), using a thin-shell approach (Bird, 1999). These authors found that NE-SW compression is dominant in the western sector where the Amur plate faces the strong Eurasia plate, while SW-directed extrusion is allowed in the eastern sector due to the relatively weaker Pacific boundary. The same methodology was applied in the whole Himalaya-Tibetan orogen and in the south-eastern Asia by Vergnolle et al. (2007). The results show that the deformation in the compressional areas (Himalayas, Tian Shan, Altai Range) is well reproduced with strong coupling at the India/Eurasia plate contact, which allows the stresses to be transferred to the interior of Asia. However, south-eastward motions observed in north and south China require tensional, ocean-ward directed stresses, generated by gravitational potential energy gradients across the Indonesian and Pacific subductions.

These studies provide reliable insights on the deformation within the Arabia-Eurasia and India-Eurasia collision zones. However they focus only on specific parts of the Central Asia region. A neotectonic model considering the lithospheric structure and the rheology of the whole region, spanning from the Persian Gulf to the eastern China, has not been attempted so far.

Liu and Bird (2008) presented a kinematic model of the Persia-Tibet-Burma orogen which merges geological fault slip rates, stress/strain-rate directions and geodetic velocities. Their model is based on a kinematic modelling approach which uses the weighted-least-squares method to fit the internal velocity field within the model domain to available data and *a priori* constraints. Although it provides reliable constraining information on the kinematics within the Central Asia region, it does not investigate the relations between the observed motion and the forces affecting the motion. The model shows that the deformation is accommodated primarily in the frontal ranges (Zagros, Himalaya and Karakorum), in the Alborz, in the Kopet Dagh, and in the Makran subduction zone. The eastern and western segments of the India-Eurasia boundary (Burma and eastern Afghan block) are characterized by transpressive deformation and active faulting. Significant shearing is found also in the eastern margin of the Lut block, and joint strike-slip faulting and E-W extension characterize the Tibetan Plateau.

The study presented here should be considered a complementary work of Liu and Bird (2008), since the deformation observed roughly in the same region is predicted by using a geodynamic approach assuming rheologies and (velocity) boundary conditions.

I consider a rheological behaviour for both crust and upper mantle depending on temperature and strain rate. The model is laterally-varying in the crustal and lithospheric mantle thickness, elevation and heat flow. I use the lithospheric structure in the Central Asia region from Robert et al. (2015), derived by the combination of elevation and geoid data together with thermal analysis. The model shows a thinning of the lithospheric mantle in the Zagros orogen beneath the Sanandaj Sirjan Zone and the Urumieh Dokhtar Magmatic Arc, with the base of the lithosphere located at ~120 km depth, in agreement with the results along our A-A' and B-B' lithospheric profiles (Chapter 4). However, in the Himalaya-Tibetan orogen, though the lithospheric thickness of the southern and western part of the Tibetan Plateau is consistent with our previous findings, the northern sector of the plateau shows a very thick lithosphere, up to 340 km thickness against our 120 km-thick lithosphere in the north-eastern Tibet (profile D-D', Chapter 5). In the present study, I consider both a thick and thin lithosphere in the north-eastern Tibetan Plateau, in order to analyse the effect on the predicted surface velocity and stress fields.

A reference model is presented to show the neotectonic deformation in the Central Asia using the lithospheric structure from Robert et al. (2015). Changes in the rheological parameters, friction coefficient on faults and velocity conditions at boundary nodes will be then applied to see the effect on the predicted velocity, stress orientations and tectonic regime. The lithosphere thinning in the NE-Tibet will be also considered in the study. The quality of the models will be evaluated by comparing their predictions (long-term-average horizontal velocities, anelastic strain rates, integrated stresses and fault slip rates), with available data on seismic deformation, stress directions and GPS velocities.

This study is divided in three Chapters. Chapter 6 explains the thin-shell method used to perform the models (SHELLS, Bird 1999, Bird et al. 2008). I describe how the model has been constructed, defining the lithosphere and thermal structure and studying the motion of the surrounding plate to determine the boundary conditions. Finally, I present the data used to constrain the models. Chapter 7 describes the results for the reference model obtained by using the lithospheric and thermal structure from Robert et al. (2015) (Section 7.1). On the next three sections I present the results obtained by changing the rheology of the lithosphere (Section 7.2), the lithosphere mantle thickness in the north-eastern Tibetan Plateau (Section 7.3) and the boundary conditions in the south-eastern boundary of the Central Asia region (Section 7.4). Finally the pros and the cons of the different models are discussed in Chapter 8. The advantages and the limitations of the applied thin-shell approach in explaining the deformation patterns in the Central Asia region are analysed in order to delineate some conclusions.

## Chapter 6: Method and model construction

This study is based on the thin viscous sheet approach and I use the program SHELLS (Bird 1999; Bird et al., 2008) which simulates the deformation of a faulted lithosphere on a spherical Earth. Through considering the crustal and lithospheric mantle structure, regional elevation, surface heat flow and rheological behaviour for both crust and upper mantle depending on temperature, this program allows inferring the surface velocity field, stress directions, tectonic regime and strain distribution by imposing velocity conditions at the model boundaries. Modelling results are long-term-averaged horizontal velocities, anelastic strain rates, integrated stresses and fault slip rates, and they are constrained by geodetic velocities and available stress data.

The program is designed for neotectonic studies and the time scale considered in the modelling is much larger than that of the earthquake cycle, therefore, transient effects, such as elastic strain, are neglected. Model outputs should be considered as averages over several seismic cycles.

The SHELLS code works under the thin-sheet approximation which considers that: i) the vertical shear stresses are zero and therefore every column is locally supported (local isostasy); ii) the deviatoric stresses are assumed to vanish beneath the lithosphere, so there is no shear stress at the base of the lithosphere and no vertical variations of the horizontal velocity. This can be written as:

$$\sigma_{xz} = \sigma_{zx} = \sigma_{yz} = \sigma_{zy} = 0 \quad (\text{Eq. 6.1})$$

$$\dot{\epsilon}_{xz} = \dot{\epsilon}_{zx} = \dot{\epsilon}_{yz} = \dot{\epsilon}_{zy} = 0 \quad (\text{Eq. 6.2})$$

with  $\sigma$  and  $\dot{\epsilon}$  being the stress and strain rate tensors respectively.

These assumptions allow the deformation of the lithosphere to be treated in terms of vertically-averaged magnitudes. Therefore the momentum equations are vertically averaged along depth  $z$  within the plate.

A 2D finite element grid of spherical triangles is used to solve only the horizontal components of the momentum equation, whereas the radial (vertical) component of the momentum equation is represented by the isostatic approximation. The method is also considered a “2.5-dimensional” code since it performs volume integrals of density and strength in a lithosphere model with laterally-varying thickness of the crust and mantle-lithosphere, heat-flow and topography.

The temperature distribution is calculated under the steady-state conditions, considering only the vertical component of the heat conduction and solving the thermal equation in 1D. The system is considered being isostatically balanced with a 7 km-thick lithospheric column of the mid-ocean ridge at a bathymetry of 2.7 km.

The lithosphere strength is calculated from the lithosphere structure and thermal regime assuming a nonlinear rheology. At each depth, the yield stress is given by the lower of two competing processes: the frictional sliding or Mohr-Coulomb-Navier friction (dominant at low T and P) and the power law creep (dominant at high T and P, with different constants for crust and mantle).

The frictional sliding (brittle rheology) is given by:

$$\sigma_f = \mu_f (-\sigma_n - P_w) \quad (\text{Eq. 6.3})$$

where  $\mu_f$  is the coefficient of friction,  $\sigma_n$  is the normal stress, and  $P_w$  is the hydrostatic pore pressure.

The power-law creep or dislocation creep (ductile rheology) is given by (Kirby, 1983):

$$\sigma_{creep} = \left[ 2A \left( 2\sqrt{-\dot{\epsilon}_1 \dot{\epsilon}_2 - \dot{\epsilon}_2 \dot{\epsilon}_3 - \dot{\epsilon}_3 \dot{\epsilon}_1} \right)^{\frac{1-n}{n}} \exp\left(\frac{B+Cz}{T}\right) \right] \dot{\epsilon} \quad (\text{Eq. 6.4})$$

where  $\sigma_{creep}$  is the deviatoric stress tensor,  $\dot{\epsilon}$  is the strain rate tensor, T is the absolute temperature, z is the depth, n is the power law creep stress exponent, and A, B, and C are rheological parameters which are different for the quartz-diorite-dominated (feldspar-dominated) crust and dunite-dominated (olivine-dominated) mantle lithosphere. The term within the square root is the second invariant of the strain rate tensor. Parameter A is a constant, B in the crust is given by Q/nR, where Q is the molar activation energy and R is the gas constant, C is a proxy for the activation volume term,  $\sim(\rho g V_a)/nR$ , where g is the acceleration due to gravity and  $V_a$  is the activation volume.

Given a current strain rate tensor, the deviatoric stress tensor is calculated throughout the volume of the lithosphere using both frictional sliding and dislocation creep flow laws. At a particular depth, the yield stress is given by the lesser of the brittle and ductile strength.

In SHELLS, a model is essentially defined by the following inputs: (1) the model domain in a map view, i.e. the finite element grid formed by triangular spherical elements, and the traces and dips of the active (or potentially active) faults; (2) the lithosphere structure, i.e. the crust and lithospheric mantle thicknesses; (3) the elevation and surface heat flow; (4) the rheology of the crust and lithospheric mantle; (5) the velocity or lithostatic forces boundary conditions.

## 6.1 Model domain and faults

In this study the model domain spans between longitude 30°E and 109°E and latitude varying between 15°-30°N and 50°N (Figure 6.1).

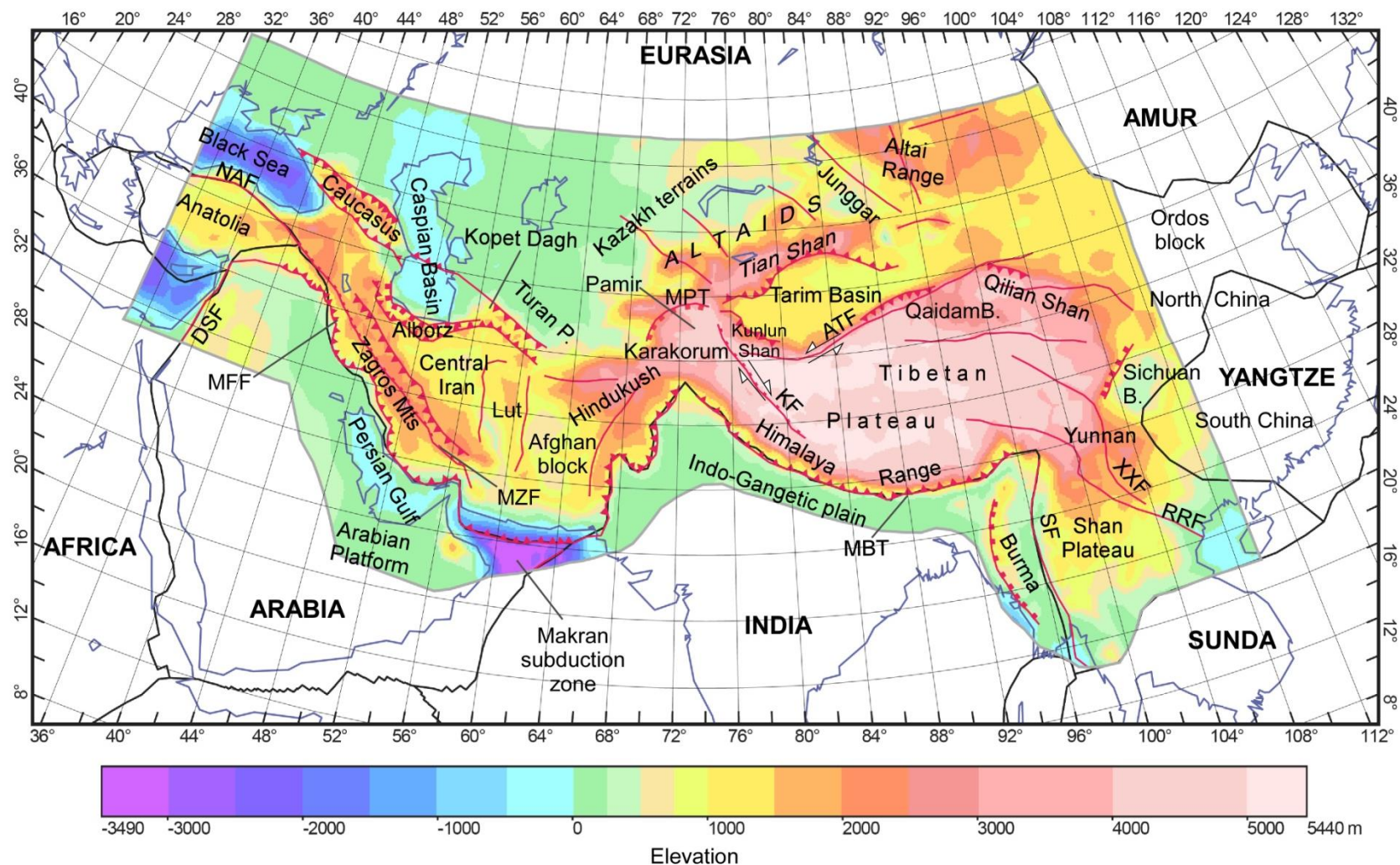


**Figure 6.1.** Plate boundaries (black thin lines) in the Central Asia region from PB2002 plate model (Bird, 2003). Colours indicate surface topography from ETOPO1 model (Amante and Eakins, 2009). ATF: Altyn Tagh Fault; DSF: Dead Sea Fault; MBT: Main Boundary Thrust; MFF: Main Frontal Front; MPT: Main Pamir Thrust; MZF: Main Zagros Fault; NAF: North Anatolia Fault; RRF: Red River Fault; SF: Sagaing Fault; XXF: Xiangshuihe-Xiaojiang Fault.

The southern boundary follows the north-eastern margins of Arabian and Indian plates, slightly extending into the southern terrains (Arabian Platform, and Indo-Gangetic Plain) in order to allow modelling deformation also along the frontal ranges (Zagros fold-and-thrust belt and Himalaya-Karakorum ranges).

The two-dimensional finite element grid consists of fault and continuum elements. Fault elements are defined by double nodes, by the dip and a lower friction coefficient ( $\mu_f$ ) with respect to the continuum elements which have a friction coefficient of 0.85. In this study, the finite element grid consists of 4467 continuum elements and 435 fault elements. I used the trace of major active faults in the Altai Range as reported by Holt et al. (2000), in the Himalaya-Tibet region by Taylor and Yin (2009), and in the rest of the area I referred to Bonini et al. (2003), Liu and Bird (2008) and references therein. Fault dips are assigned on the basis of available dip data or from geological cross-sections (Yin, 2006; Burchfiel et al., 2008; Burg et al., 2008; Guillot et al., 2003; Robert et al., 2009; Mosar et al., 2010; Charvet et al., 2011; Saura et al., 2011; Li et al., 2011; Ballato and Strecker, 2014; Robert et al., 2014): 20-25° for low angle faults; 30-35° for typical faults; 60-70° for high angle faults; 90° dip is assumed for strike-slip faults (Figure 6.2).

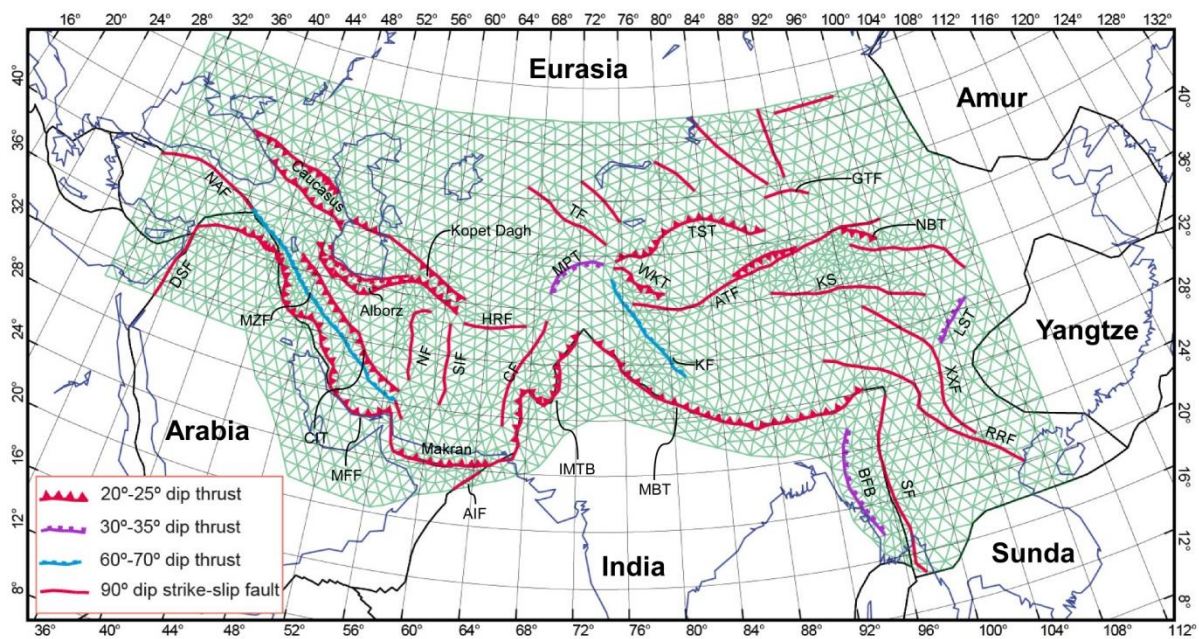


**Figure 6.2.** Finite element grid and faults in the study region. Plate boundaries (thin black lines) and plate names (bold characters) derive from PB2002 plate model (Bird, 2003). AIF: Arabia-India transform Fault; ATF: Altyn Tagh Fault; BFF: Burmese Fold Belt; CF: Chaman Fault; CIT: Central Iran Thrust; DSF: Dead Sea Fault; GTF: Gobi-Tian Shan Fault; HRF: Herat Fault; IMTB: Indus-Makran thrust belt; KF: Karakorum Fault; KS: Kunlun Suture (or Kunlun Fault); LST: Longmen Shan Thrust; MBT: Main Boundary Thrust; MFF: Main Frontal Front; MPT: Main Pamir Thrust; MZF: Main Zagros Fault; NAF: North Anatolia Fault; NBT: North Border thrust; NF: Nayband fault; RRF: Red River Fault; SF: Sagaing Fault; SIF: Sistan Fault; TF: Talas-Fergana fault; TST: Tian Shan Thrust; WKT: Western Kunlun Thrust; XXF: Xiangshuihe-Xiaojiang Fault.

## 6.2 Model inputs. Lithosphere and thermal structure

The SHELLS code (29th August 2006 version code) considers the elevation, the heat flow, the crustal thickness and the lithospheric mantle thickness as input data on each node of the finite element grid. Additionally, the program calls for two extra degrees of freedom in order to ensure local isostasy: a perturbation of the geotherm away of the steady-state and an anomaly in the vertically averaged density of the lithosphere (limited to the range  $\pm 50 \text{ kg/m}^3$ , Bird et al., 2008). These two extra data are interpreted, respectively, as transient effects of the thermal state of the lithosphere and as compositional changes within the lithosphere. They are necessary in order to preserve local isostasy fixing crust and lithosphere thicknesses, elevation and surface heat flow.

Topography, heat-flow, crust and lithospheric mantle thickness data come from the Central Eurasia lithospheric model by Robert et al. (2015). This model resulted from the combination of elevation, geoid anomaly and thermal analysis. The crustal and lithosphere structures (Figure 6.3) are calculated assuming local isostasy on a four-layer (sea water, crust, lithospheric mantle and asthenosphere) density model.

The crustal density increases linearly with depth between predefined values at surface and at the base of the crust. The lithospheric mantle density  $\rho_m$  is considered to be temperature dependent:

$$\rho_m(z) = \rho_a [1 + \alpha (T_a - T(z))]$$

where  $\rho_a$  is the density of the asthenosphere considered constant everywhere,  $\alpha$  is the thermal expansion coefficient,  $T_a$  is the temperature at the LAB and  $T(z)$  is the temperature of the lithospheric mantle at a given depth  $z$ .

Figure 6.3 shows that crustal thickening is not restricted but extends hundreds to thousand kilometres away from the collisional front, indicating transmission of tectonic stresses, and revealing the presence of stiff lithospheric blocks that remain almost undeformed within the collisional systems (Central Iran, Tarim Basin). The Zagros fold-and-thrust belt is characterized by  $\sim 200$  km thick lithosphere, whereas a thin to very thin lithosphere is observed in the internal regions of the Arabia-Eurasia collision zone. The region spanning between the Anatolia and the Afghan block, including the Central Iran, the Alborz, the Kopet Dag and the Lut block is characterized by a 100-130 km thick lithosphere, in agreement with previous studies (Molinaro et al., 2005; Motavalli-Anbaran et al., 2011), and with the results presented in the Part II of this Thesis (see Chapter 4). Conversely, the India-Eurasia collision zone shows a thicker lithosphere with respect to the Arabia-Eurasia region ( $>200$  km thick), reaching values of 340 km in the north-eastern Tibetan Plateau.

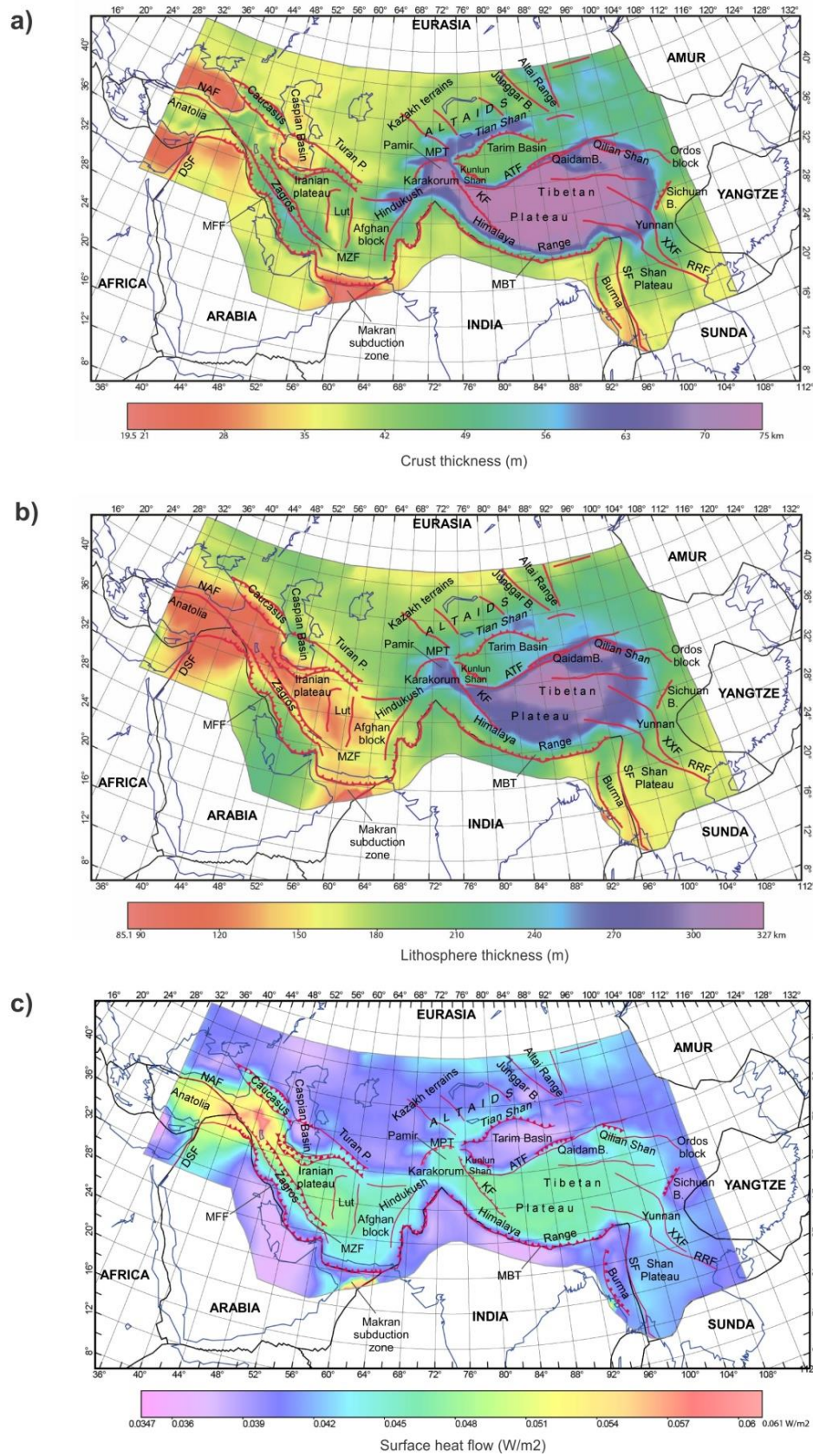


**Figure 6.3.** Input data for the neotectonic model. (a) Crustal thickness; (b) Lithosphere (crust + lithospheric mantle) thickness and (c) Surface heat flow in the Central Asia, derived from the combination of elevation, geoid anomaly and thermal analysis (Robert et al., 2015). Refer to the caption of Figure 6.2 for the fault names.

This lithospheric thickness is anomalously high and it contrasts with previous geophysical studies and tomography images suggesting a very thin to inexistent lithospheric mantle in this region (Kumar et al., 2006; Jiménez-Munt et al., 2008; Zhao et al., 2010; Liang et al., 2012) and with the results obtained in this Thesis along the D-D' lithospheric profile (Chapter 5). In this study I will consider both a thick and a thin lithosphere in the north-eastern Tibetan Plateau to analyse the effect of the thinning on the neotectonic deformation (Section 7.3).

### 6.3 Plates motion and boundary conditions

After more than four decades of the theory of plate tectonics, estimates of current plate motions continue to be broadly used for geological, geophysical and geodetic studies. Several studies model the present deformation by assuming rigid plates and estimate the plate angular velocity (e.g. NUVEL-1 from DeMets et al., 1990; PB2002 from Bird, 2003; MORVEL from DeMets et al., 2010). Increased shipboard, airborne and satellite coverage of the mid-ocean ridge system over time, earthquakes, slip directions and GPS stations velocities have enabled steady improvements in the precision and accuracy of estimates of plate angular velocities (position of the Euler pole and angular velocity).

In this study, I take the geometry of the plate boundaries from the PB2002 model. I have tested several Euler poles (e.g. Holt et al., 2000; England and Molnar, 2005; Liu and Bird, 2008; DeMets et al., 2010). Finally, I choose the Euler poles from Liu and Bird (2008) since they provide the best fits between the model-predicted velocities and stress orientations with the available GPS and stress data.

Six major plates compose the Central Asia region: Eurasia, Arabia, India, Sunda, Yangtze, and Amur (see Figure 6.1). Eurasia is considered as the reference plate (Eurasia-fixed reference frame) hence all the other plate's velocities are referred to it.

The Arabia plate, at the south-west corner of the study region, is moving NNE-wards, pushing against Eurasia at a rate 10-30 mm/yr increasing towards the south-east, consistent with the rate of 18-25 mm/yr inferred by geodetic measurements (Vernant et al., 2004). The India plate is advancing roughly NE-wards, twice faster than the Arabia plate, and with an increasing azimuth toward the east. The Sunda plate, located to the south-east of the study region, has been considered part of the Eurasia plate in some different plate models (e.g. NUVEL-1 from DeMets et al., 1990; or RM2 from Minster and Jordan, 1978), since the Eurasia/Sunda border only delimits an area with low seismicity and low anelastic strain rates. In the Eurasia reference frame, the Sunda plate is moving eastwards with respect to the Eurasia plate with velocities  $\leq 10$  mm/yr. The Yangtze plate, also called "South China" block, is an aseismic region of southern China (Giardini et al, 1999), bordered to the south by the Sunda plate, and to the north by the Amur plate (from longitude 124°E) and the deforming parts (Ordos and North China regions) of the Eurasia plate. Since GPS measurements do not detect relative motions larger than 2 mm/yr (Heki et al., 1999; Calais et al., 2003), the

Yangtze plate has been commonly considered a “kinematically” rigid unique block together with Ordos, North China and Amur regions moving eastwards with respect to Eurasia. However, other studies suggest that the Ordos block, Yangtze and North China regions are being extruded slightly faster than the Amur plate (Zhang et al., 1998; Shen et al., 2000; Petit and Fournier, 2005). In the PB2002 plate model, the boundary between Yangtze and Amur plates is a possible left-lateral transform fault. The boundary of Yangtze with the deforming parts of the Eurasia plate is not clearly represented by faults, but it delineates the low seismicity area of the Yangtze plate relative to the deforming Eurasia plate (Bird, 2003). Finally, the Amur plate, located in the north-eastern corner of the study region, delimits a block moving ESE-wards with respect to the Eurasia plate, between a left-lateral strike-slip fault system in the north-east (Stanovoy Mountains), and another strike-slip fault system in the southwest (Bird, 2003). The Amur plate is moving ~2 mm/yr relative to the Eurasia plate, slower than Yangtze and Sunda plates. This rate is slightly lower with respect to the rate estimated from MORVEL (DeMets et al., 2010), which is of 3-4 mm/yr.

Applying the Euler poles of Liu and Bird (2008; Table 6.1) the calculated velocities for the different plates respect to Eurasia are shown in Figure 6.4. These velocities are applied to the boundary nodes of the models shown in Sections 7.1, 7.2, 7.3. Changes in the velocity conditions are applied to the south-eastern boundary in the models shown in Section 7.4.

**Table 6.1.** Euler poles from Liu and Bird (2008) of the 5 tectonic plates in the Central Asia region referred to the fixed Eurasia plate.

Plate name	N-Lat (deg)	E-Lon (deg)	Rotation rate (deg Myr <sup>-1</sup> )
Amur	58.8	157.5	0.034
Arabia	26.22	22.87	0.427
India	28.56	11.62	0.357
Yangtze	61.21	142.00	0.206
Sunda	26.0	279.6	0.128

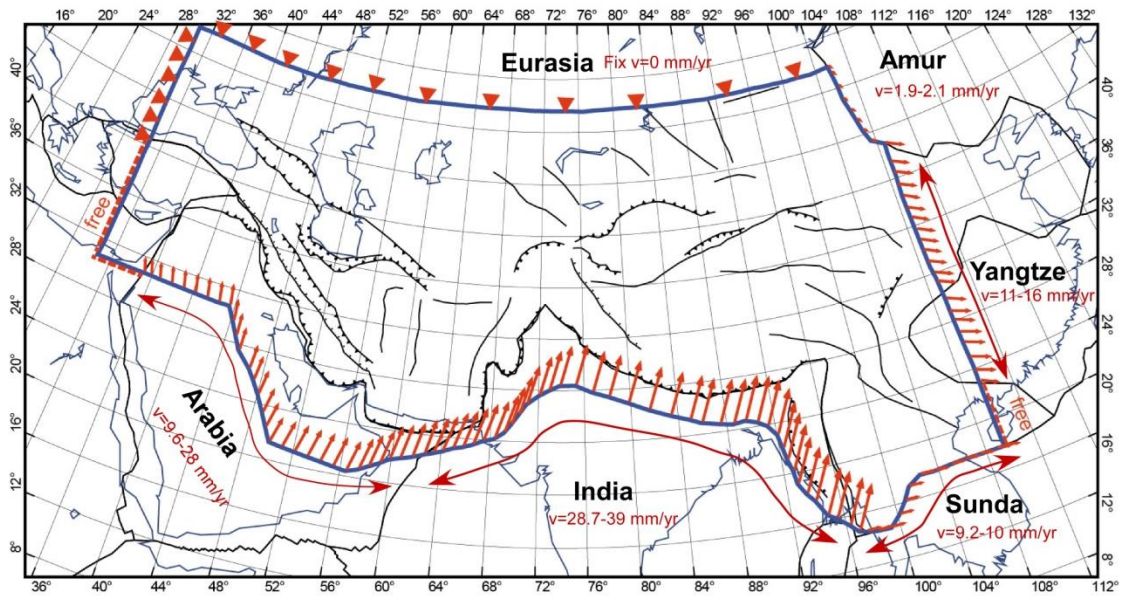


**Figure 6.4.** Velocity boundary conditions calculated using the Euler poles of Table 6.1 (Eurasia-fixed reference frame).

## 6.4 Model constraints

The SHELLS program predicts time-average horizontal velocities, anelastic strain rate, stress directions, tectonic regime and fault slip rates. To evaluate the quality of the modelling results we compare the model predictions with the surface velocities from geodetic studies, earthquake strain distribution, horizontal stress directions and tectonic regime.

Figure 6.5 shows the velocity field derived by GPS observations in Central Asia. In the western sector, GPS data (McClusky et al., 2003; Vernant et al., 2004; Reilinger et al., 2006; Masson et al., 2007; Tavakoli et al., 2008; Zarifi et al., 2013) reveal a rapid ( $\sim 20-30$  mm/yr) counter-clockwise motion of the Arabian Peninsula, Iran, Caucasus and Anatolia/Aegean regions. Agard et al. (2011) suggested that the counter-clockwise rotation and the westward escape of Anatolia are the indirect results of the collision between India and the Afghan block, occurred around 5 Ma. This collisional event is thought to generate the change of the kinematic pattern on the Eurasian side of the Arabia-Eurasia collision from an eastward (toward Afghanistan) to westward (toward Anatolia) escape, and also to play a role in the slowdown of convergence between Arabia and Eurasia (Austermann and Iaffaldano, 2013). In the Himalaya-Tibetan orogen the GPS velocities show that part of the NNE-ward penetration of India into Tibet is absorbed by eastward and southward transfer of material around the eastern end of the Himalaya (e.g., Holt et al., 2000; Wang et al., 2001; Zhang et al., 2004; Gan et al., 2007), forming a glacier-like flow zone that turns  $\sim 180^\circ$  clockwise around the eastern Himalaya syntaxis, and ends in the Shan Plateau with a fan-like front.

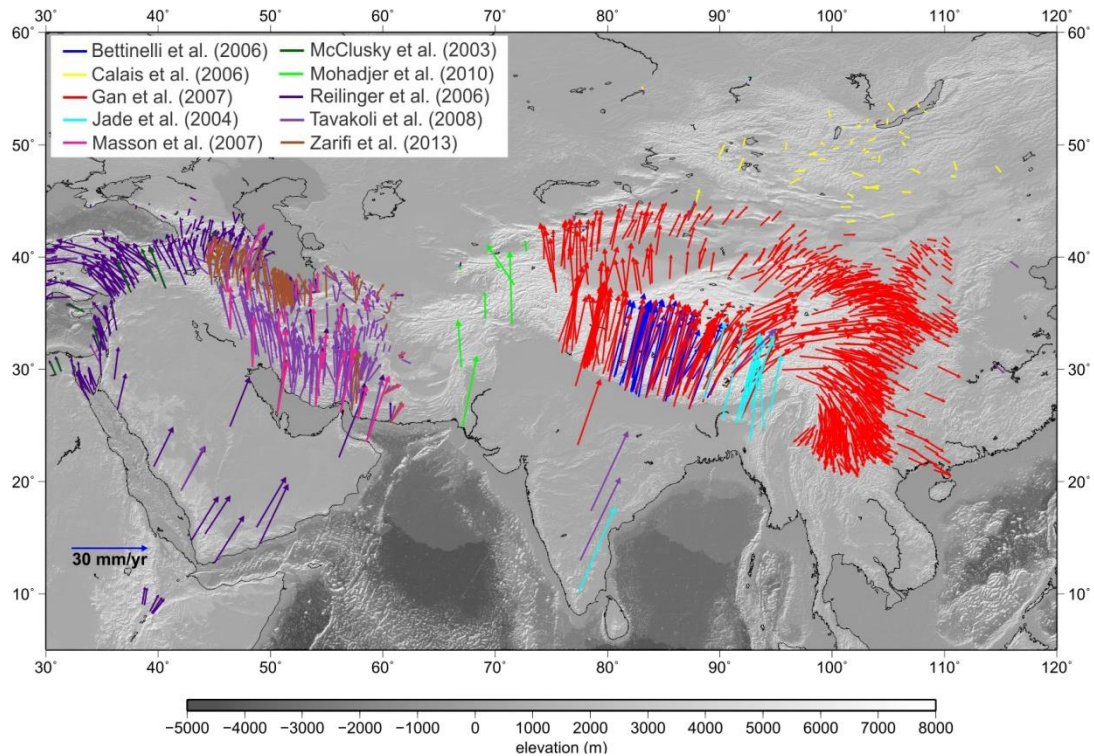


**Figure 6.5.** GPS velocities in the Eurasia reference frame. Note the more rapid convergence of India than Arabia with respect Eurasia, and the rapid westward escape of north-western Arabia, and the eastward and southward extrusion of material from the eastern Tibetan Plateau around the eastern Himalaya syntaxis.

Velocity vectors show that the average convergence rate is different between Arabia/Eurasia and India/Eurasia collision zones. In the former case, the current convergence rate is approximately 18-25 mm/yr in NNE direction (Sella et al., 2002; Vernant et al., 2004), with the deformation mostly accommodated along the main mountain ranges, the Alborz in the north and the Zagros in the south. Only 10% of the overall Arabia-Eurasia convergence rate is absorbed along N-S trending strike-slip faults which cross the Iranian Plateau (Vernant et al., 2004; Hatzfeld and Molnar, 2010). In the latter case, the convergent rate is higher, approximately 40-50 mm/yr between the Eurasia and India plates, directed NNE (Bettinelli et al., 2006; Calais et al., 2006), and ~20 mm/yr is absorbed only in the Himalayan front. The rest of the deformation is propagated northwards, producing crustal thickening and continuous mountain building. Finally, the Makran subduction zone accommodates  $19 \pm 2$  mm/yr, and transmits  $6 \pm 2$  mm/yr to the Kopet-Dagh (Vernant et al., 2004).

Earthquake depths provide valuable information about the style of local deformation and the brittle strength of the lithosphere. The distribution of the seismicity (Figure 6.6) reveals that both Arabia/Eurasia and India/Eurasia collision zones are the loci of numerous deadly earthquakes that attest to continuing tectonic activity (i.e.: Tabriz twin earthquakes, Iran, 11 August 2012, M6.3 and M6.4; Sichuan earthquake, eastern China, 12 May 2008, M8).

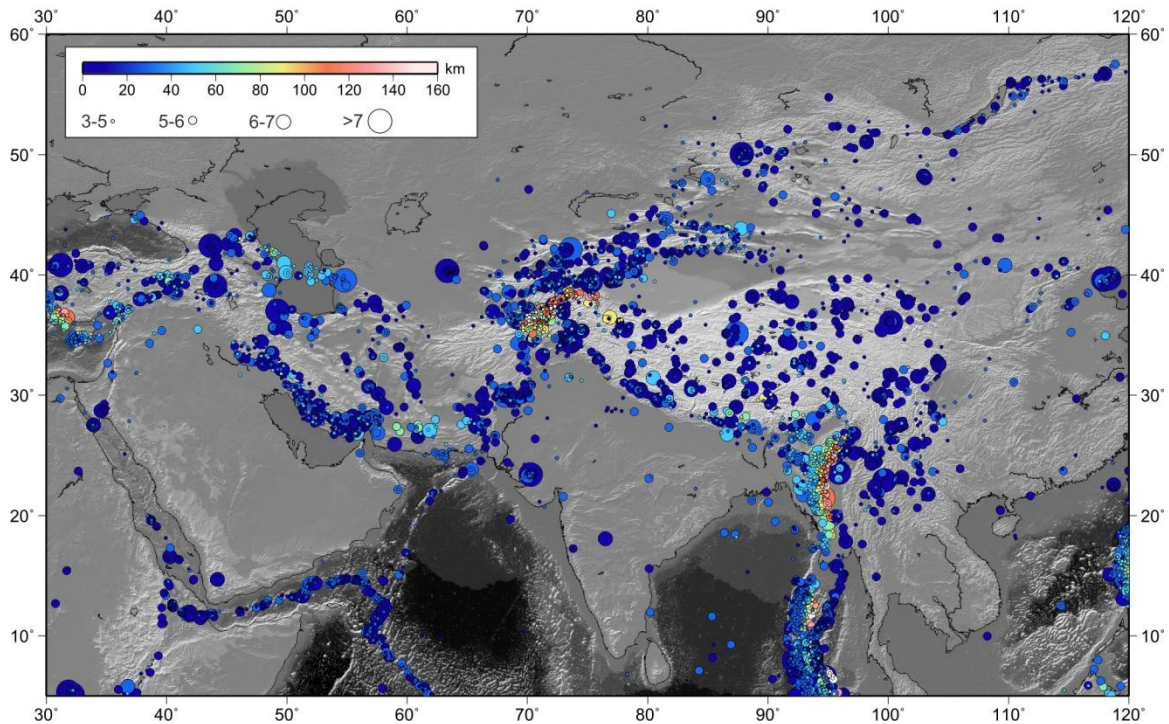


**Figure 6.6.** Distribution of earthquake with  $M > 3$  from Enghdal seismic catalogue (Enghdal et al. 1998). Colours indicate the depth of the seismic events and the size indicates the magnitude. The maximum magnitude in the Central Asia region is  $M = 7.9$ . Two larger earthquakes of magnitude  $M = 8.6$  and  $M = 9.0$  are located in the subduction zone south of Burma, at  $2^\circ\text{N}$  and  $3^\circ\text{N}$  latitudes respectively.

In the Arabia/Eurasia collision zone the seismicity is mostly concentrated in the belts surrounding the more stable, relatively aseismic, Central Iran, Lut and South Caspian blocks. The seismicity is shallow, and the crystalline basement deforms at up to depths of 20-40 km, but with the majority of the moderate-sized ( $M \sim 5-6$ ) earthquakes occurring in the lower sedimentary cover, between 5-10 km depth (Maggi et al., 2000; Talebian and Jackson, 2004; Tatar et al., 2004; Adams et al., 2009; Nissen et al., 2011). Nissen et al. (2011) propose that, since  $M \sim 5$  events typically affected either the sedimentary cover or the basement but not both, the salt deposits act as an effective barrier to rupture propagation at the base of the sedimentary succession. Focal mechanism solutions and other stress indicators show compressional regime along the Zagros fold-and-thrust belt (Figure 6.6), with a NNE-SSW direction of compression, perpendicular to the strike of the range, and further north, in the Kopet Dag, Alborz and Caucasus ranges. Strike-slip regime is also present, especially in the north-western Iran and around the Lut block, whereas extensional regime, with N-S direction of extension, characterizes the northern boundary of the South Caspian block, which is subducting beneath the Apsheron-Balkhan sill since  $\sim 5.5$  Ma (Priestley et al., 1994; Masson et al. 2005; Hollingsworth et al. 2008).

In the India/Eurasia collision zone the seismicity is significant, even higher than the Arabia/Eurasia collision zone, with large magnitude earthquakes ( $M_w \geq 8$ ). A Benioff

surface can be distinguished by the seismicity pattern south of the eastern Himalaya syntaxis, in the Burma region, shallow dipping eastwards with earthquakes at depths less than 200 km (Huang and Zhao, 2006; Li et al., 2008). Seismic tomography images show that the slab is confined to the upper mantle with a dip angle of  $\sim 60^\circ$ , sinking in the transition zone at southern latitudes (Li et al., 2008). The images show also low velocity zones beneath the Tengchong volcanic complex (located at  $25^\circ\text{N}$ ,  $98^\circ\text{E}$ ), confined at depths of  $\sim 150$  km, and beneath the Red River Fault (continuing into depths greater than 200 km). These anomalies seem to be respectively related to the eastward subduction beneath the Burma region and to upper mantle processes occurring beneath the South China Sea (Li et al., 2008). To the west, large to moderate-sized earthquakes occur at depths of 100 km or more beneath the western Himalayan syntaxis, Hindukush and Kunlun Shan. Fault plane solutions and tomography images show a Benioff surface steeply dipping down to 250 km depth (Chen and Yang, 2004; Negrodo et al. 2007). Some authors propose the presence of two slabs in the region, converging in the easternmost limit of the Hindukush: a steep northward subduction of the Indian lithosphere beneath the Hindukush and southward subduction of the Eurasian lithosphere under the Pamir, which together give the appearance of a laterally continuous subduction zone (Chatelain et al., 1980; Burtman and Molnar, 1993; Fan et al., 1994).

Stress data show a NS to NNE-SSW trending compressional regime in front of the Himalayan Range, perpendicular to the range, in the Qilian Shan, in the eastern Tian Shan and in the Altai Range, and a NS to NNW-SSE compression in the central and western Tian Shan and Pamir regions (Figure 6.7). Extensional and strike-slip features are observed throughout the Tibetan Plateau. Plate reconstructions show that extension in Tibet is due to a counter-clockwise rotation of nearly  $3^\circ$  of the Tibetan Plateau with respect to the Tarim Basin around a pole located in the northern segment of the Karakorum fault since the Miocene (van Hinsbergen et al., 2011). Since the observed displacement of the Tibet respect to the Tarim is negligible, the Tarim Basin should have rotated by a similar magnitude but in the opposite direction over the same time. Furthermore, the observation that the Altyn Tagh Fault and the Karakorum Fault can be simultaneously active only if Tibet was extending suggests that the onset of E-W extension in Tibet is contemporaneous with slip on the Karakorum Fault (14-12 Ma, van Hinsbergen et al., 2011 and references therein). Extension and strike-slip mechanisms characterize also the region around the eastern Himalaya syntaxis, to the west of the rigid Sichuan Basin, with a change from E-W to N-S direction of extension toward the east. Finally, the south-eastern portion of the Central Asia region is characterized by joint strike-slip and compressional tectonics in the Burma region and joint strike-slip and extensional tectonics are observed in the Yunnan and in the Shan Plateau.

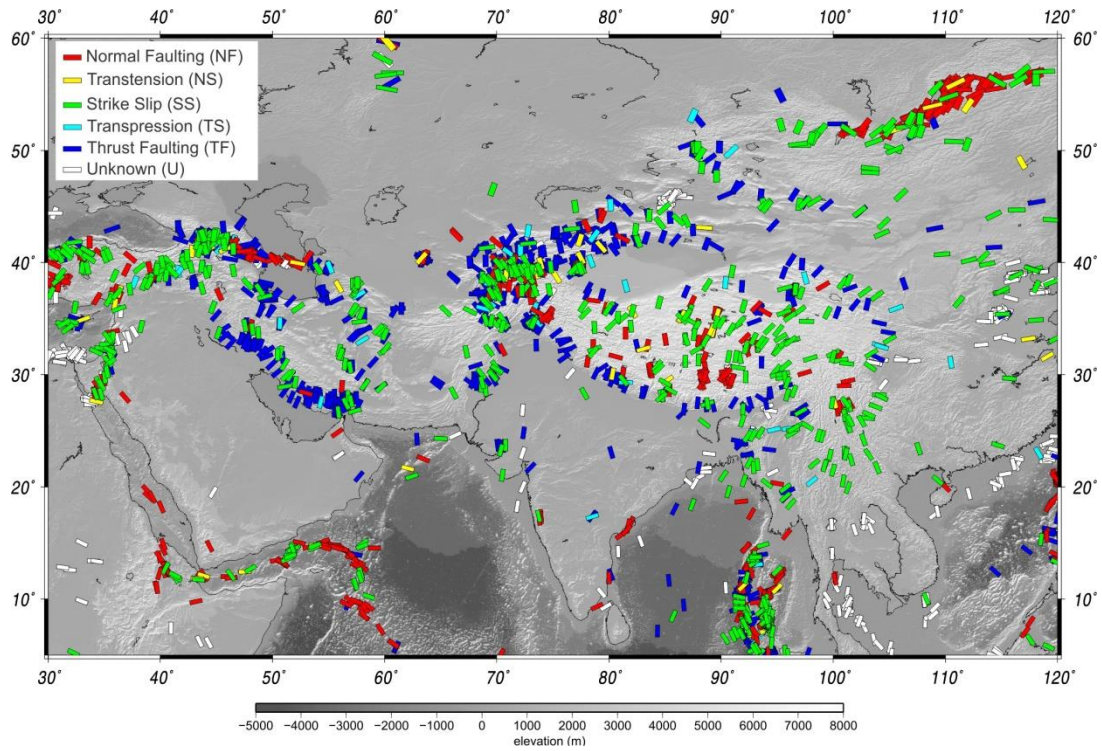


**Figure 6.7.** Stress data compilation in the Central Asia region extracted from the World Stress Map WSM2008 (Heidbach et al., 2008). Data have been filtered to quality C (stress orientations are accurate to within 25°). Depths are less than 50 km.

## Chapter 7: Results

This Chapter shows different models performed by changing the mantle rheology parameters, the friction coefficient on faults, the lithospheric mantle thickness in north-eastern Tibet and the velocity boundary conditions. The quality of the models has been evaluated by comparing their predictions (long-term-average horizontal velocities, strain rates, horizontal stress directions, tectonic regime, and fault slip rates), with available data on seismic deformation, stress directions and GPS velocities. Velocity vectors have been applied to the boundary nodes and they represent the motion of the tectonic plates (Arabian, Indian, Sunda, Yangtze and Amur plates) with respect to the Eurasia plate. The Euler poles used in the modelling are those described in Table 6.1.

### 7.1 Reference model

The reference model has been built by applying the lithospheric and thermal structure described Section 6.2 and the velocity conditions at the boundary nodes illustrated in Figure 7.1. The modelling parameters used are shown in Table 7.1.

Three different types of boundary conditions: (1) Eurasian plate fixed (velocity = 0 mm/yr) all along the northern boundary of the model and north of 40.4°N in the western border (thick, open triangles); (2) 'free', where normal tractions are equal to lithostatic vertical stress based on density and structure just inside the model boundary, along the SW corner and south of the eastern model boundary; and (3) moving according to the Euler pole of the tectonic plate of the boundary (Figures 6.4 and 7.1 and Table 6.1 ) (red arrows).

Figure 7.2 shows the vertical integral of viscosity in the region, with values ranging from  $10^{26}$  Pa·s·m to  $10^{30}$  Pa·s·m. By considering the lithospheric thickness  $\sim 10^5$  m, the resulting viscosities are between  $10^{21}$  to  $10^{25}$  Pa·s. More rigid blocks, characterized by higher viscosity values (Arabian Peninsula, Caspian Basin, Iranian Plateau - in Central Iran -, Turan Platform, Kazakh terrains, Indo-Gangetic plain, Altaiids, Tarim and Sichuan basins, Burma and Shan Plateau regions) surround a region rheologically weaker, which includes Anatolia, north-western Iran and the region south of Caucasus, Lut and Afghan blocks, Pamir region, Karakorum and Himalaya ranges, the whole Tibetan Plateau, the Qilian Shan and the southern corner of the Burma region. In these softer areas the vertical integral of viscosity ranges between  $6.3 \cdot 10^{26}$  and  $2.5 \cdot 10^{28}$  Pa·s·m, which means values of viscosity approximately ranging  $10^{22}$  Pa·s and  $10^{23}$  Pa·s.

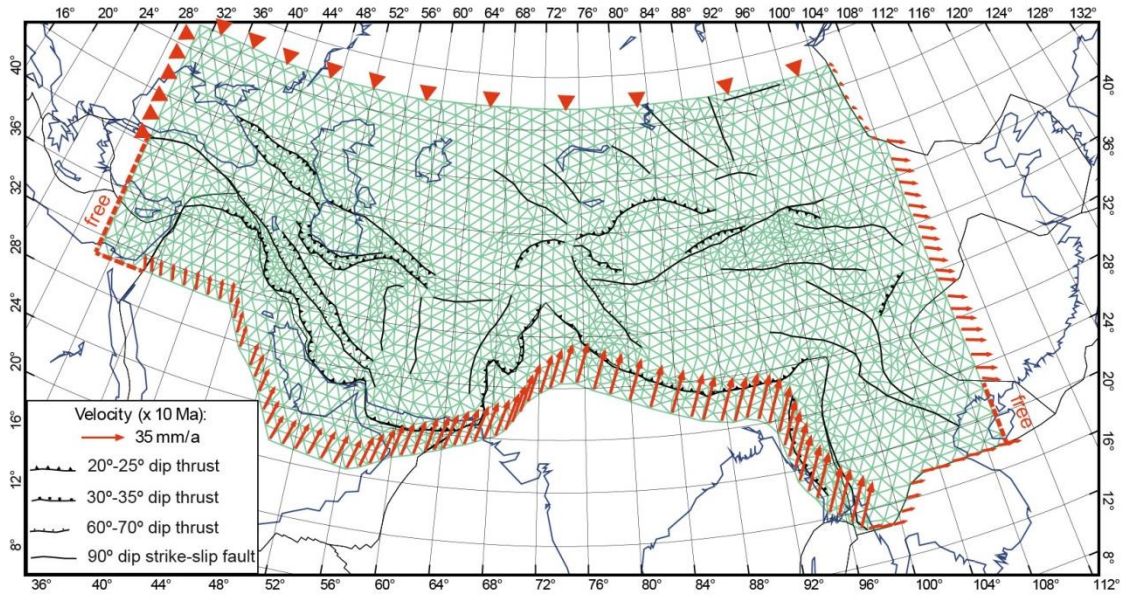


**Figure 7.1.** Finite element grid, fault traces and kinematic setting of the reference model. Coastline is shown in blue. Tectonic plate boundaries are shown in thin black line.

**Table 7.1.** Model parameters.

Model parameters	Reference model	
	values	units
Reference crustal density	2825	$\text{kg}\cdot\text{m}^{-3}$
Reference mantle density	3343	$\text{kg}\cdot\text{m}^{-3}$
Asthenosphere density	3200	$\text{kg}\cdot\text{m}^{-3}$
Water density	1031	$\text{kg}\cdot\text{m}^{-3}$
Surface temperature	15	$^{\circ}\text{C}$
Thermal conductivity, crust / mantle	2.7 / 3.2	$\text{W}\cdot\text{K}^{-1}\cdot\text{m}^{-1}$
Volumetric thermal expansion coefficient, crust / mantle	0 / $3.5\cdot 10^{-5}$	$\text{K}^{-1}$
Radioactive heat production, crust / mantle	$0.5\cdot 10^{-6}$ / 0	$\text{W}\cdot\text{m}^{-3}$
Temperature at LAB	1300	$^{\circ}\text{C}$
Friction Coefficient (in continuum elements)	0.85	
Dislocation creep strength, crust / mantle (ACREEP*)	$2.3\cdot 10^9$ / $9.5\cdot 10^4$	$\text{Pa}\cdot\text{s}^{-1/n}$
Dislocation creep activation energy/n/gas-constant, crust / mantle (BCREEP*)	4000 / 18314	K
Derivative of BCREEP with respect to depth, crust / mantle (CCREEP*)	0 / 0.0171	$\text{K}\cdot\text{m}^{-1}$
Maximum shear strength, crust / mantle (DCREEP)	$5\cdot 10^8$	Pa
Strain rate exponent in creep strength (1/n) (ECREEP*)	0.3333	

(\*) Equivalences with classical power-law creep parameters are:  $\text{ACREEP}=1/A$ ;  $\text{BCREEP}=Q/nR$ ;  $\text{ECREEP}=1/n$ ;  $\text{CCREEP}=\sim(\rho gV_a/nR)$ , with  $A$  the pre-exponential creep parameter,  $Q$  the activation energy,  $V_a$  the activation volume and  $n$  the power-law exponent (see Chapter 6).

Figure 7.3 shows the logarithm of the greatest principal strain rate, in colour, with the symbols indicating the strain rate tensors. The more rigid blocks identified in Figure 7.2, can be readily recognized in the strain-rate plot. The Caucasus, the Caspian Basin and the Arabian Platform behave rigidly and the strain derived from the Arabia-Eurasia convergence is accommodated in Anatolia, where the deformation is transpressive, to the south of the Caucasus and less in Zagros. The frontal part of the Zagros range is not deforming. The deformation is greater to the east of the Main Zagros Fault in the north-western and south-eastern Iran. From 56°E to 68°E, the Arabia-Eurasia convergence is accommodated mainly in the southern Lut block and in the northern Afghan block. The Makran subduction zone and the southern half part of the Afghan block have strain rate values ( $\sim 10^{-16} \text{ s}^{-1}$ ) comparable to those in the north-west Iran, Alborz and Kopet Dagh. Similar strain rates characterize also the Altaiids, the Burma and the Shan Plateau regions in the case of the India-Eurasia collision zone. The deformation derived by the India-Eurasia convergence is accommodated mostly in the Hindukush, Pamir and Karakorum, and in the southern Tibetan Plateau. The strain-rate in these areas is one order of magnitude higher than in the distant ranges (strain rate of  $\sim 10^{-15} \text{ s}^{-1}$  compared with  $\sim 10^{-16} \text{ s}^{-1}$  in the Altaiids and in the Qilian Shan), and the N-S contraction is dominant. As in the case of the Arabia-Eurasia collision zone, some rigid blocks show negligible deformation, i. e. the Indo-Gangetic plain, the Tarim, Qaidam and Sichuan basins, and the Shan Plateau.

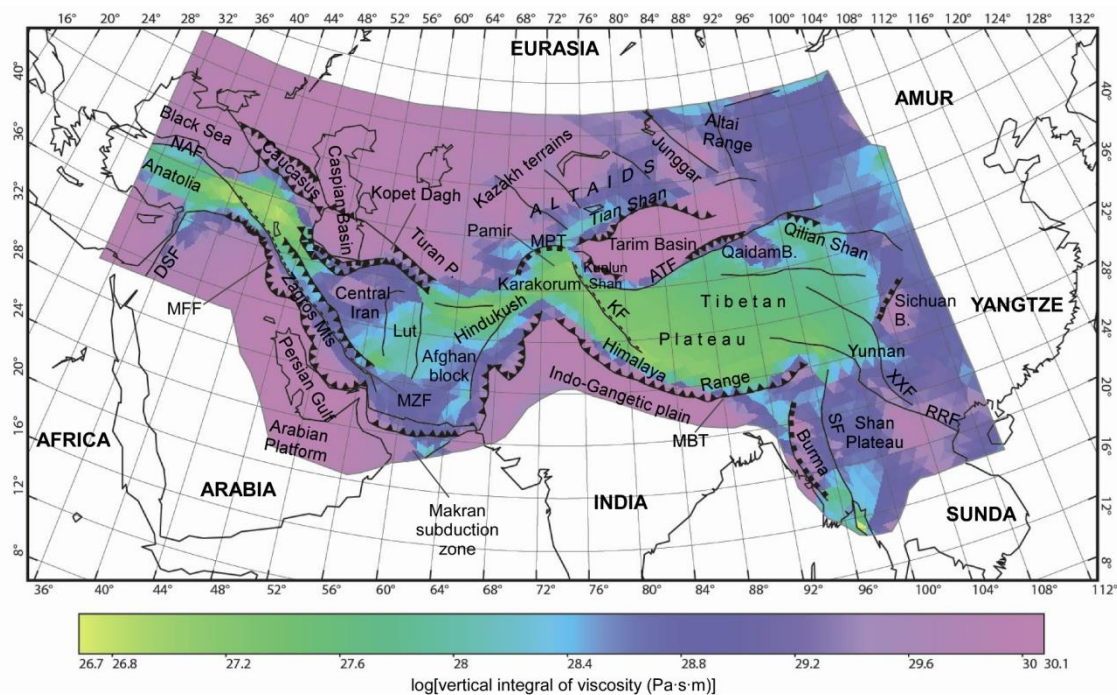


**Figure 7.2.** Vertical integral of viscosity in the study region for the reference model. Modelling parameters used are shown in Table 7.1. Friction coefficient on faults is  $\mu_f=0.1$ . ATF: Altyntagh Fault; DSF: Dead Sea Fault; MBT: Main Boundary Thrust; MFF: Main Frontal Fault; MPT: Main Pamir Thrust; MZF: Main Zagros Fault; NAF: North Anatolia Fault; RRF: Red River Fault; SF: Sagaing Fault; XXF: Xiangshuihe-Xiaojiang Fault.

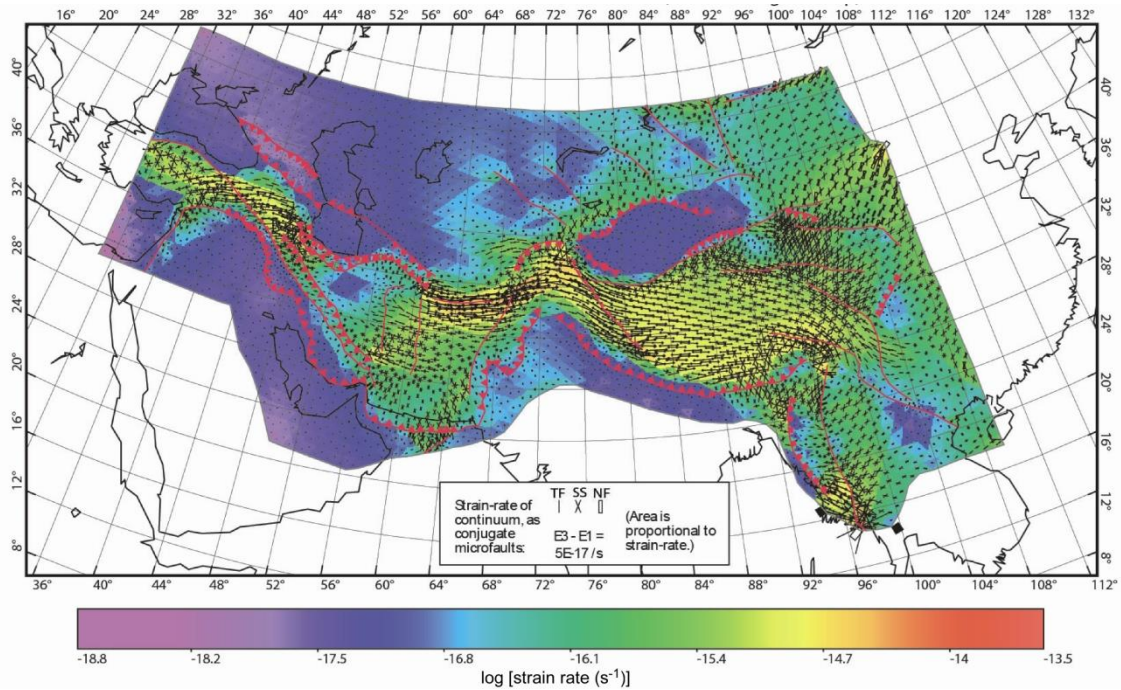


**Figure 7.3.** Long-term-average anelastic strain rate field. Straining due to slip rates of fault elements is not included. Coloured background shows logarithm of the magnitude of the greatest strain rate. Overlying icons show total strain rate tensor. The fault symbols are sized with an area proportional to the strain rate. Friction coefficient on faults is  $\mu_f=0.1$ . TF = thrust faulting; SS = strike-slip faulting; NF = normal faulting.

The predicted velocity vectors are shown in Figure 7.4 and compared with GPS-inferred velocities. The velocity field shows that the model reproduces the circular regional trend of the velocity observations for the Arabia-Eurasia collision zone, with the westward extrusion of the Anatolia and the distributed deformation across the Zagros mountain belt. The Iranian Plateau and the Lut Block show coherent motion with little internal deformation. The deformation is accommodated further north, in the Alborz and Kopet Dagh, with slip rates values of 12-14 mm/yr. To the west of the Caspian Basin, the modelled velocities are completely absorbed across the north-western Zagros belt, inconsistently with GPS data which indicate that most of the Arabia-Eurasia convergence east of the 50°E takes place in the Caucasus and its southern basin (Vernant et al., 2004). In the Himalaya-Tibetan orogen, the model velocity field represents a good first-order approximation to the GPS velocity field in the Himalaya Range and in the central to western Tibetan Plateau. Model velocities show a decrease from south to north without much changing in orientation, implying that the shortening in the plateau accommodates a large amount of the north-eastward advancement of India, consistently with geodetic observations. In the north-eastern Tibetan Plateau and in the Qilian Shan regions, the model velocities turn to the north-east, still fitting GPS data. However, the clockwise rotation of  $\sim 180^\circ$  degree around the eastern Himalaya syntaxis is not reproduced. Predicted velocities from the model are only slightly deflected toward the south-east from 104°E, but in the Yunnan and across the Shan Plateau they are directed eastwards instead of southwards.

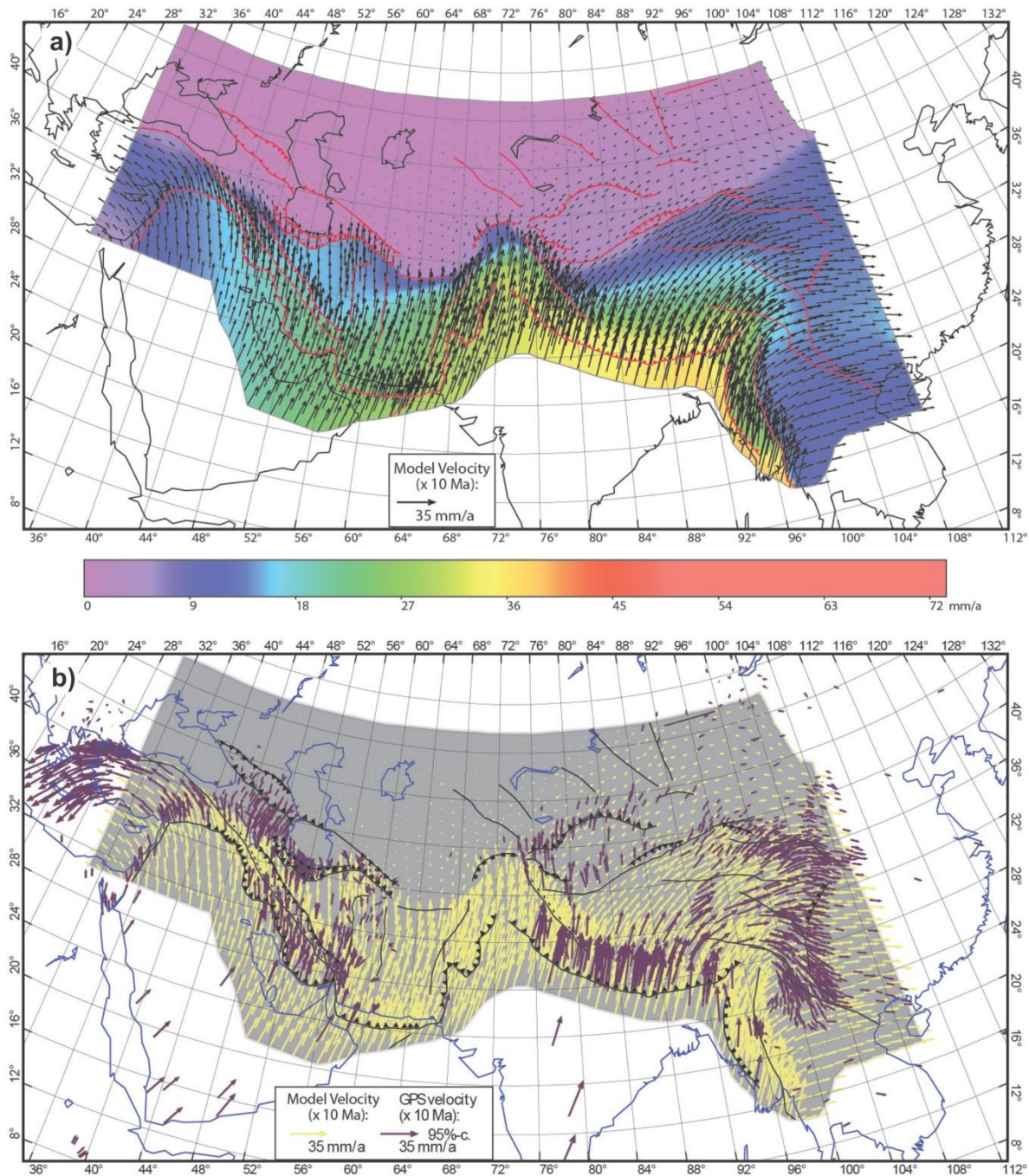


**Figure 7.4.** a) Surface velocity field respect to the Eurasia plate predicted by the reference model. b) Predicted surface velocities by the model (yellow) and GPS velocities (purple, references in Section 6.4). Friction coefficient on faults is  $\mu_f=0.1$ .

Figure 7.5 shows the orientations of most compressive horizontal principal stresses, compared stress data coming from the World Stress Map WSM2008 (Heidbach et al., 2008). The stress field plot shows a general agreement between predicted stress orientations and tectonic regime with the observations for the Arabia/Eurasia collision zone. The results indicate thrusting with changing direction from N-S in north-western Iran and Caucasus region to NNE-SSW in southern and eastern Iran, but also strike-slip in the Zagros fold-and-

thrust belt and in the northern ranges (Alborz and Kopet Dagh). However, the area extending from the south Caspian Basin to Anatolia remains controversial. Stress data indicate strike-slip regime in the Caucasus and joint extensional and strike-slip deformation in eastern Anatolia, which are not reproduced in the model. This extension is probably due to the Hellenic arc subduction (in the Aegean region) which I don't consider in this model. In the Himalayan-Tibetan orogen, the model stress field simulates correctly the compressive regime in the Karakorum, Pamir, middle to western Himalaya, Kunlun Shan and southern Tian Shan, and the joint strike-slip and compressive regime in the Qilian Shan, eastern Himalaya and in the Shan Plateau. In the northern Tian Shan and Altai Range the model predicts strike-slip, meanwhile data indicate mainly thrusting with some strike-slip. In addition, the predicted stress orientations do not allow for extension throughout the Tibetan Plateau, nor in the eastern end of the plateau, between the eastern syntaxis and the Sichuan Basin (Yunnan province) as indicated by focal mechanisms.

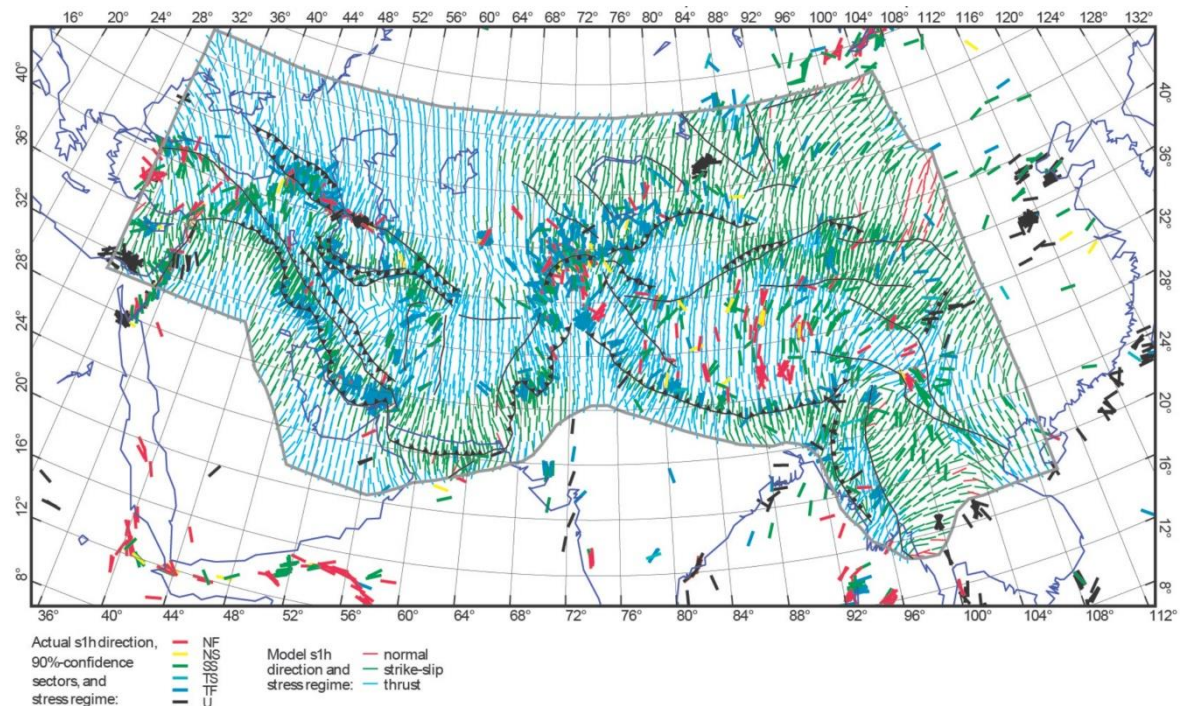


**Figure 7.5.** Directions of the most-compressive horizontal principal stresses predicted by the reference model (thinner lines), and stress data from WSM2008 (thicker lines, Heidbach et al., 2008). Friction coefficient on faults is  $\mu_f = 0.1$ .

The predicted fault slip rates show excessively low values ( $\leq 1$  mm/yr) along the deformation front of the Zagros Himalaya ranges, as well as in the Tian Shan, Junggar and Altai Range or along the Altyn Tagh Fault. The Karakorum Fault shows values between 13-15 mm/yr, indicating thrusting instead of dextral shearing, whereas the Northern Anatolian Fault is moving slowly at  $\sim 6$  mm/yr, compared the observed rate of  $\sim 26$  mm/yr (Reilinger et al., 2006).

## 7.2 Change in the rheological parameters

I tested different rheological parameters (Table 7.2, e.g. Figure 7.6), with values that have been used in previous neotectonic studies (Bird and Kong, 1994; Negredo et al., 2002, 2004; Burbidge, 2004; Petit and Fournier, 2005; Vergnolle et al., 2007; Barba et al., 2010).

**Table 7.2.** Rheological parameters used in the model.

Parameter	Tested range	Preferred value for “soft rheology” model
ACREEP crust [ $\text{Pa}\cdot\text{s}^{-1/n}$ ]	$2.11\cdot 10^6 / 2.3\cdot 10^9$	$2.3\cdot 10^9$
ACREEP mantle [ $\text{Pa}\cdot\text{s}^{-1/n}$ ]	$1.00\cdot 10^4 / 1.4\cdot 10^5$	$1.00\cdot 10^4$
BCREEP crust [K]	4000 / 8625	4000
BCREEP mantle [K]	10000 / 18314	16000
Resulting vertical integral of shear stress [ $\text{Pa}\cdot\text{m}$ ]		$1.03\cdot 10^{12}$

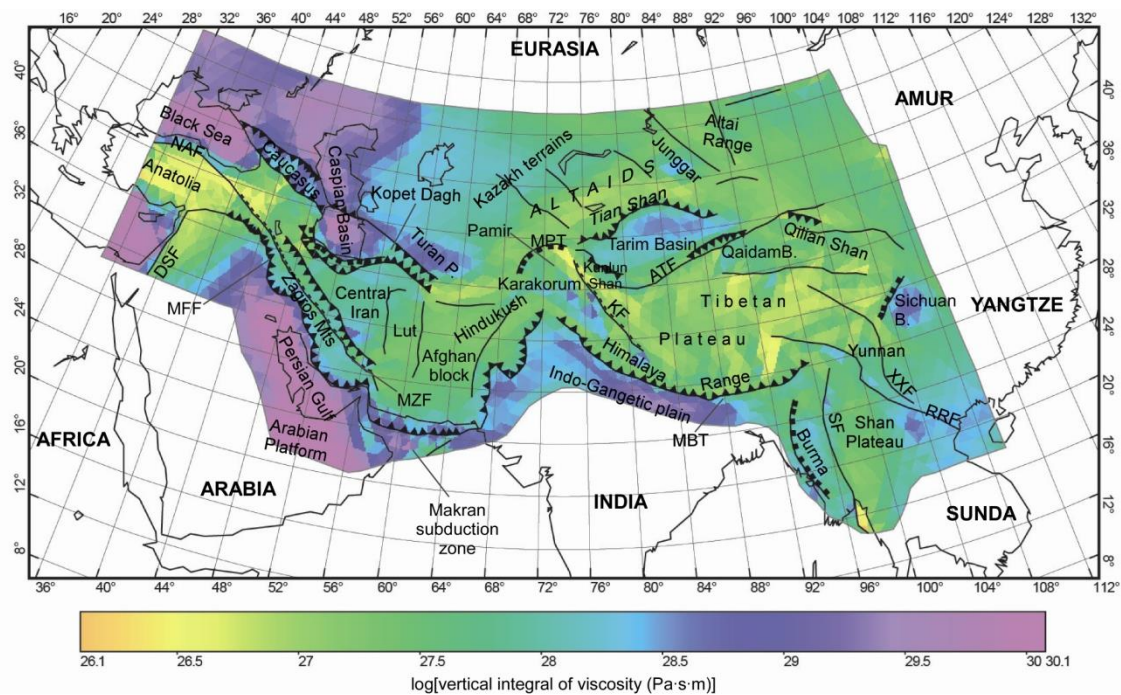


**Figure 7.6.** Vertical integral of viscosity in the “soft-rheology model”. Friction coefficient on faults  $\mu_f=0.1$ . ATF: Altyn Tagh Fault; DSF: Dead Sea Fault; MBT: Main Boundary Thrust; MFF: Main Frontal Front; MPT: Main Pamir Thrust; MZF: Main Zagros Fault; NAF: North Anatolia Fault; RRF: Red River Fault; SF: Sagaing Fault; XXF: Xiangshuihe-Xiaojiang Fault.

The vertical integral of viscosity in the region (Figure 7.6) has lower values with respect to the reference model (Figure 7.2), in particular in the Himalaya-Tibetan orogen. The values

of the majority of the more rigid blocks are two or three orders of magnitude lower than in the reference model (Tarim Basin, Caucasus and western Indo-Gangetic plain:  $\sim 2 \cdot 10^{28}$  Pa·s·m compared to  $10^{30}$  Pa·s·m; Qaidam Basin:  $\sim 4 \cdot 10^{27}$  Pa·s·m compared to  $10^{29}$  Pa·s·m; Central Iran:  $\sim 10^{28}$  Pa·s·m compared to  $10^{30}$  Pa·s·m). However, the southern Caspian Basin, the Arabian Platform and the Sichuan Basin show values similar to those shown in the reference model ( $\sim 10^{30}$  Pa·s·m).

The strain rate plot (Figure 7.7) shows that the resulting strain rate is higher than  $10^{-16} \text{ s}^{-1}$  in most of the study area, except for the Arabian Platform, the Caspian Basin, the Caucasus and the region north of it. Although the frontal parts of the Zagros and Himalayan belts result slowly deforming (strain rates of  $\sim 10^{-16} \text{ s}^{-1}$  in the Zagros and  $\sim 10^{-15} \text{ s}^{-1}$  in Himalaya fronts, compared to  $\sim 10^{-17} \text{ s}^{-1}$  in the reference model), the deformation is primarily taken up in Anatolia, Tian Shan and Altai Range, where the strain rate is  $\sim 10^{-15} \text{ s}^{-1}$ .

Resulting surface velocities are shown in Figure 7.8. The predicted surface velocities are higher than the observations in many regions, and in general the deformation is transmitted better inside the continent, where the convergence velocity decrease is lower. The model overestimates the velocity values in Central Iran ( $\sim 16$  mm/yr against  $\sim 12$  mm/yr observed), Tarim Basin ( $\sim 27$  mm/yr against  $\sim 9.4$  mm/yr) and Tian Shan ( $\sim 18$  mm/yr against  $\sim 15$  mm/yr), without reproducing the accommodation of the shortening across the Tibetan Plateau. Conversely, in the north-western Iran, model velocities are lower than the observations ( $\sim 27$  mm/yr against  $\sim 33$  mm/yr) as well as in the Caucasus region with respect to the previous model ( $\sim 8$  mm/yr against  $10$  mm/yr).

The predicted stress orientations (Figure 7.9) show normal faulting in the middle to western Tibetan Plateau, in agreement with the observations. The soft-rheology model provides a better fit of the compressional regime in the northern mountain belts of the Himalaya-Tibetan orogen, like in the Qilian Shan, Tian Shan and Altai ranges, mostly oriented N-S. In the Zagros orogen, the change in the rheological parameters only affects the Anatolia region, showing strike-slip and normal faulting, with the most compressive stress directions varying from nearly N-S direction to NNW-SSE from the NW-Iran to eastern Anatolia in agreement with the anticlockwise rotation of the regional trend.

Predicted long-term-average slip-rates show negligible movement in the Karakorum Fault (0.5-0.7 mm/yr of dextral strike-slip), whereas the Tian Shan Thrust is slipping at 3-5.4 mm/yr (against to values of 0.12-0.17 mm/yr obtained in the reference model), the Altyn Tagh Fault is left-lateral moving up to 6.5 mm/yr in the north-easternmost segment, and the NW-trending faults north of the Tian Shan show right-lateral strike-slip up to 3.7 mm/yr.

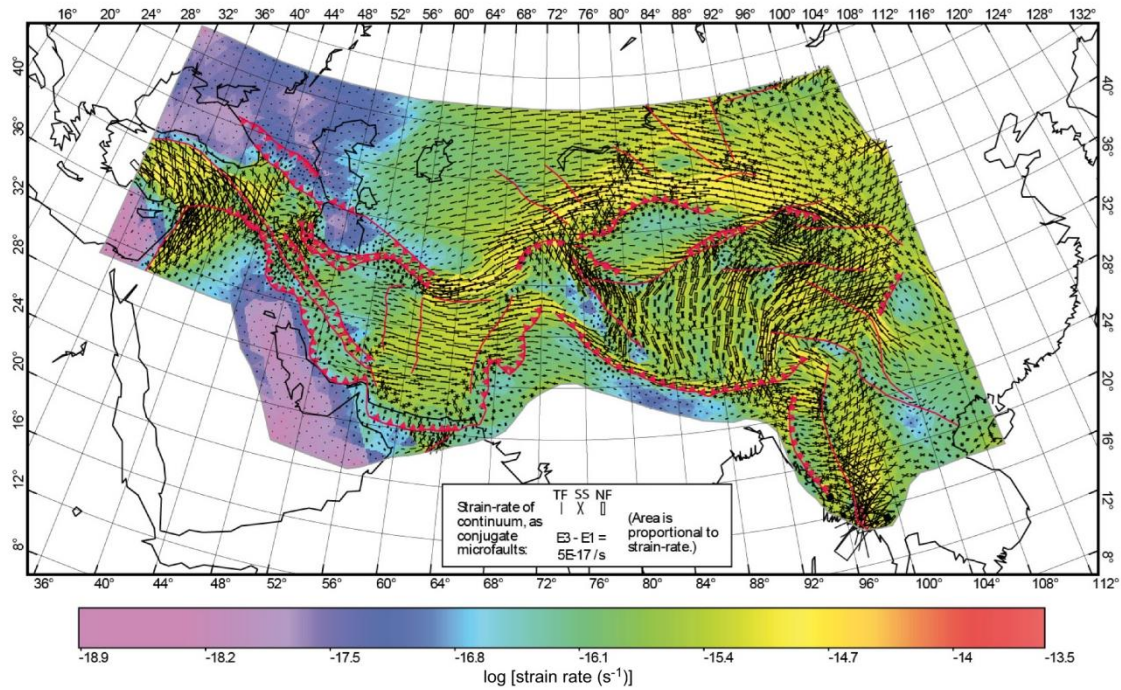


**Figure 7.7.** Strain-rate field, using the soft rheology detailed in Table 7.2. Coloured background shows logarithm of the magnitude of the greatest strain rate. Overlying icons show total strain rate tensor. The fault symbols are sized with an area proportional to the strain rate. Friction coefficient on faults  $\mu_f=0.1$ . TF=thrust faulting; SS=strike-slip faulting; NF=normal faulting.

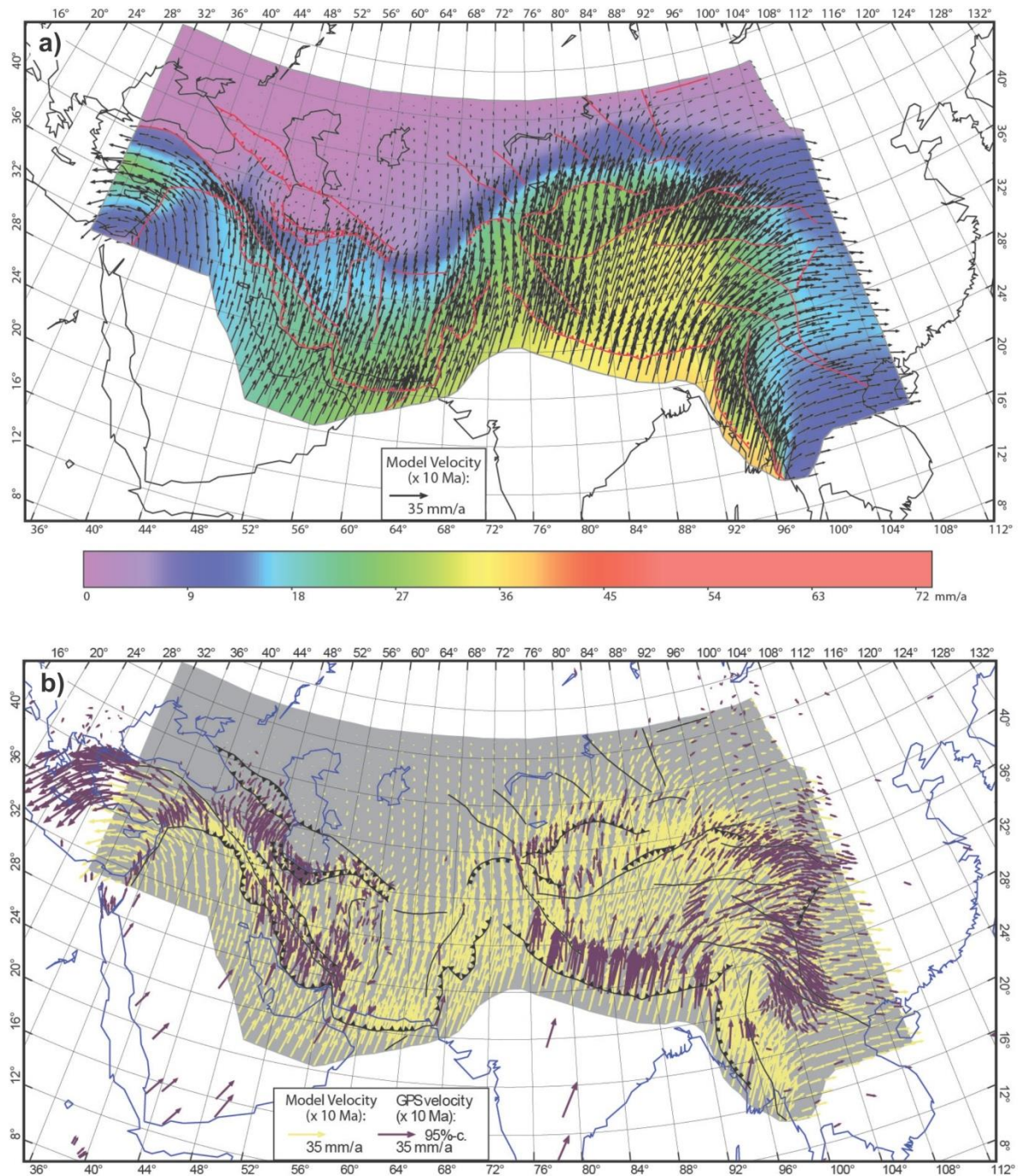


**Figure 7.8.** a) Surface velocity field respect to the Eurasia plate predicted by the “soft-rheology” model. b) Predicted surface velocities by the model (yellow) and GPS velocities (purple, see references in Section 6.4). Friction coefficient on faults is  $\mu_f=0.1$ .

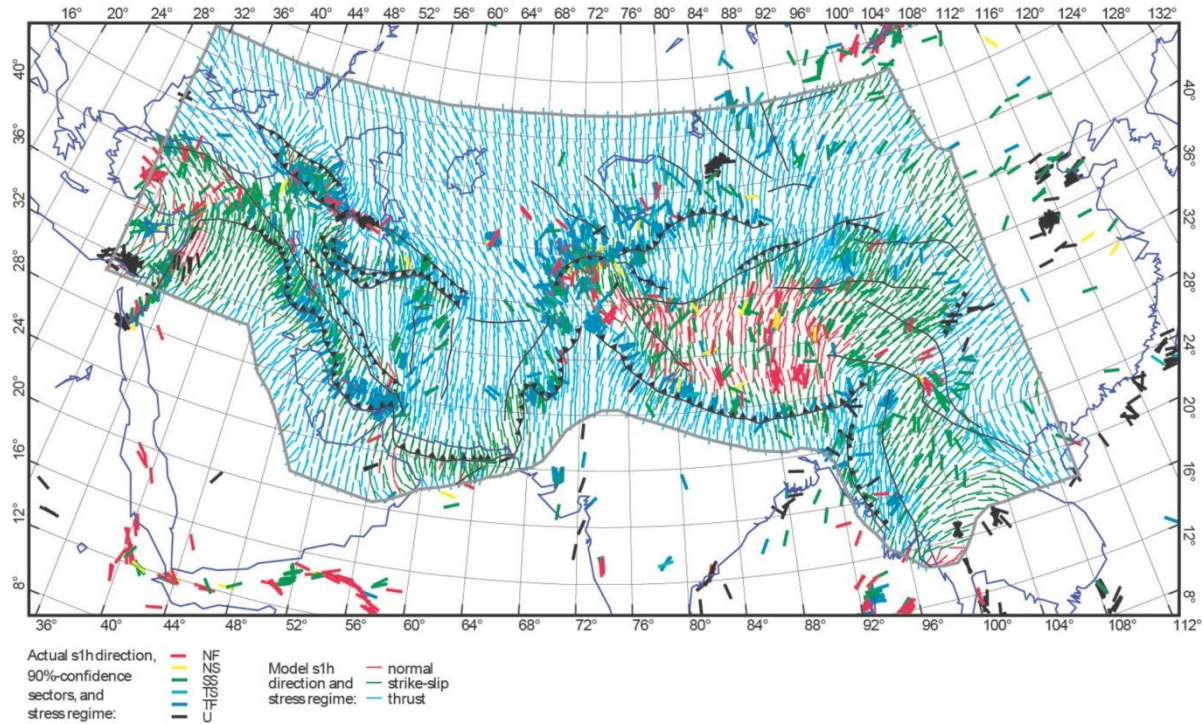


**Figure 7.9.** Direction of the most compressive horizontal principal stresses predicted by the model (thinner lines), using the soft rheology detailed in Table 7.2, and stress data from WSM2008 (thicker lines, Heidbach et al., 2008). Friction coefficient on faults is  $\mu_f = 0.1$ .

### 7.3 Change of the lithospheric mantle thickness in NE-Tibet

As mentioned in Section 5.2.4, several geophysical studies and tomographic models (Kumar et al., 2006; Jiménez-Munt and Platt, 2006; Jiménez-Munt et al., 2008; Barron and Priestley, 2009; Zhao et al., 2010; Ceylan et al., 2012; Agius and Lebedev, 2013) suggest the occurrence of a lithosphere thinning and/or the presence of shallow asthenospheric layer beneath the north-eastern Tibetan Plateau, north of the Bangong-Nujiang Suture (BNS) to explain the low body waves and surface waves velocity anomalies, the high attenuation, high conductivity and high heat flow values in the region. All these characteristics call for a hot environment throughout the crust and upper mantle (Yue et al., 2012; and references therein). Results from the geophysical-petrological study carried out in this Thesis (Chapter 5) also confirm the presence of a shallower LAB in the north-eastern Tibetan Plateau with respect to its southern sector. The base of the lithosphere is found at  $\sim 120$  km depth beneath the Bangong-Nujiang Suture and northwards up to latitude  $36^\circ\text{N}$ , whereas it deepens southwards beneath the Lhasa terrain, reaching  $\sim 280$  km depth at latitude  $30^\circ\text{N}$  (see Figure 5.6, in Section 5.2.4 and localization on Figure 5.1).

In this Chapter, I study the effect of this lithosphere thinning of north-eastern Tibetan Plateau on the surface deformation. In an area characterized by poor Sn-phase velocity propagation, consistently with Barron and Priestley (2009) study, I imposed the thickness of the lithosphere at 120 km on the north-eastern Tibetan Plateau (Figure 7.10a), following the

resulting lithospheric thickness obtained along profile D-D' (Chapter 5). The temperature at the Moho boundary in the north-eastern Tibet increases by  $\sim 200^\circ\text{C}$  with respect to the previous models, and the integral of the viscosity decreases from  $\sim 4 \cdot 10^{27}$  Pa·s·m to  $\sim 5 \cdot 10^{26}$  Pa·s·m. Figure 7.10b shows that in the most of the Central Asia the lithosphere density has to be higher than the input density parameters (Table 7.1) in order to keep the local isostatic condition. However, the lithosphere thinning in the NE-Tibet requires an additional density anomaly of  $\sim 25 \text{ kg/m}^3$ . The reduction of the lithosphere thickness by  $\sim 200$  km leads to a localization of the deformation in the thinned region. The NE-Tibet shows an increase of  $\sim 16\%$  in the predicted strain rates (Figure 7.10c) and of  $\sim 40\%$  in the predicted surface velocities (Figure 7.11) compared to the model with a thick lithosphere in the whole Tibet (Section 7.1).

The models with thick and thin lithosphere in the north-eastern Tibet have been evaluated by scoring the predictions against geodetic velocities and stress data using the root-mean-square (RMS) misfit. The coefficient of friction on faults ( $\mu_f$ ) has been varied systematically from 0.01 (weak) to 0.2 (moderately strong); for higher values the RMS remains constant. The Figure 7.12 gives model errors for different  $\mu_f$ . I separated the Arabia-Eurasia collision zone (from the western border of the study region to  $62^\circ\text{E}$  longitude) from the India-Eurasia collision zone (from  $72^\circ\text{E}$  to the eastern border of the study region) in order to better discuss the scoring results. Although the scoring has been applied also to the region in between the two collision zones (from  $60^\circ\text{E}$  to  $72^\circ\text{E}$ ), I do not show the relative graph since the results can be misleading due to the scarcity of measured data, especially GPS velocities.

Figure 7.12 shows that velocity errors increase with increasing  $\mu_f$ , whereas stress orientations show a decreasing misfit with increasing  $\mu_f$ . Therefore, the best fitting model is, reasonably, a model using a  $\mu_f$  coefficient between 0.05 and 0.1. The graph shows that the errors are higher in the Arabia-Eurasia collision zone than in the India-Eurasia collision area, with  $\sim 5\text{-}9$  mm/yr and  $\sim 1\text{-}3$  mm/yr misfit in the velocities, and  $33^\circ\text{-}39^\circ$  and  $31^\circ\text{-}34^\circ$  misfits in the stress azimuths, respectively. The change of the lithosphere thickness in the north-eastern Tibetan Plateau (Figure 7.10b) has a low effect on the geodetic velocities,  $\sim 0.05$  mm/yr difference between thick- and thin-lithosphere models, which is a  $\sim 3\%$  RMS higher considering a thinner lithosphere. But it produces an improvement of  $\sim 0.5^\circ$  (2%) on the stress orientations assuming a thinner lithosphere in NE-Tibet. Rheology exerts a more important control on the model predictions, both on surface velocities and stress directions. The “soft-rheology” model generates higher errors in the predictions. Misfits in the velocities of  $\sim 8$  mm/yr and  $\sim 2$  mm/yr are found in the Arabia-Eurasia and India-Eurasia collision zones, respectively. Misfits in the stress directions show values ranging between  $34^\circ\text{-}37^\circ$  and  $31.5^\circ\text{-}33.5^\circ$  in the same regions. Using the rheology of the reference model (Table 7.1), the misfit decreases to ranges of  $\sim 5\text{-}6$  mm/yr and  $\sim 1\text{-}2$  mm/yr in the velocities, and  $\sim 34^\circ\text{-}37^\circ$  and  $\sim 31^\circ\text{-}32^\circ$  in the stress directions, in the Arabia-Eurasia and India-Eurasia collision zones, respectively.

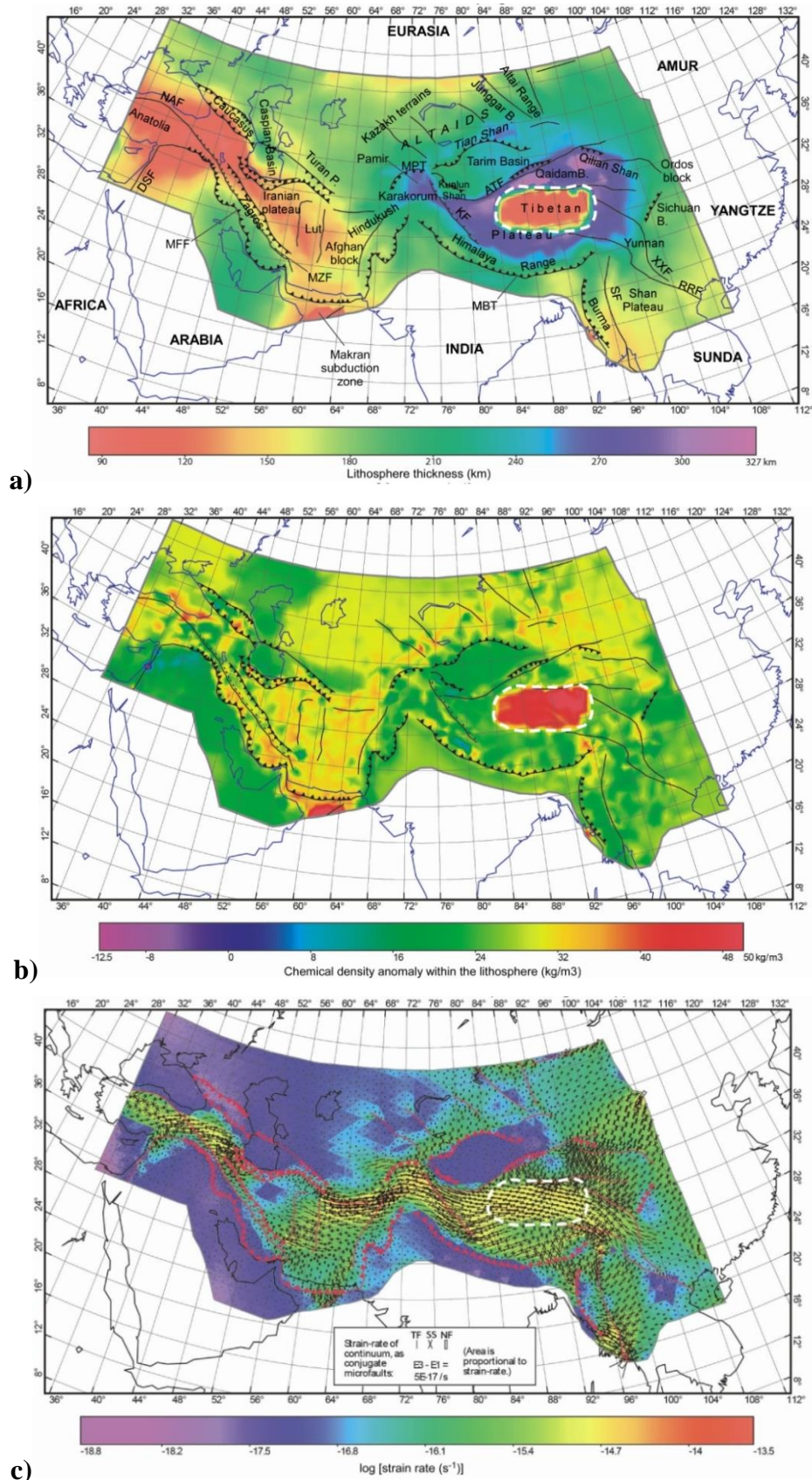


**Figure 7.10.** Model with a thin lithosphere (LAB at 120 km depth) in the north-eastern Tibetan Plateau (dashed-line bordered area), and with  $\mu_f = 0.1$ . a) Lithosphere thickness; b) lithosphere density anomalies (with respect to the input density parameters, Table 7.1) attributed to compositional heterogeneities; c) strain rate. Refer to caption of Figure 7.2 for fault names.

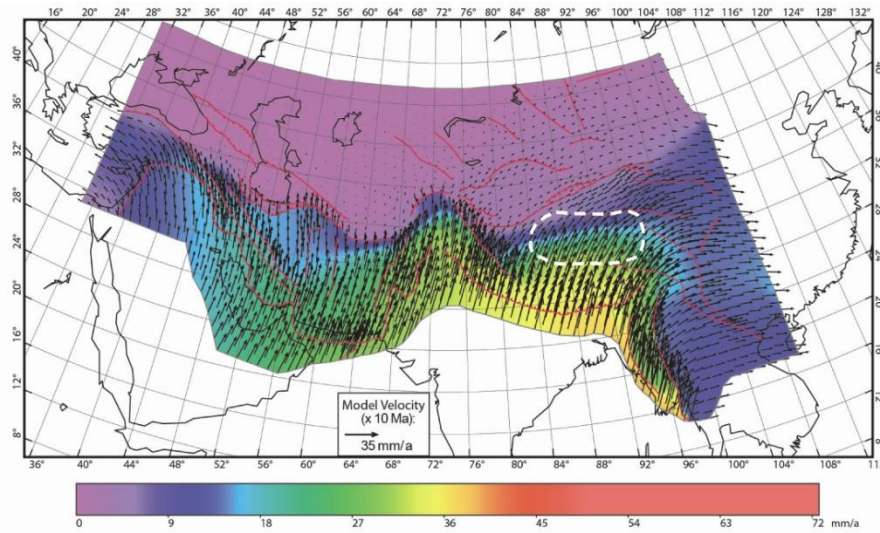


**Figure 7.11.** Predicted surface velocity in a model with a thin lithosphere (LAB at 120 km depth) in the north-eastern Tibetan Plateau (dashed line bordered area), and with  $\mu_f = 0.1$ .

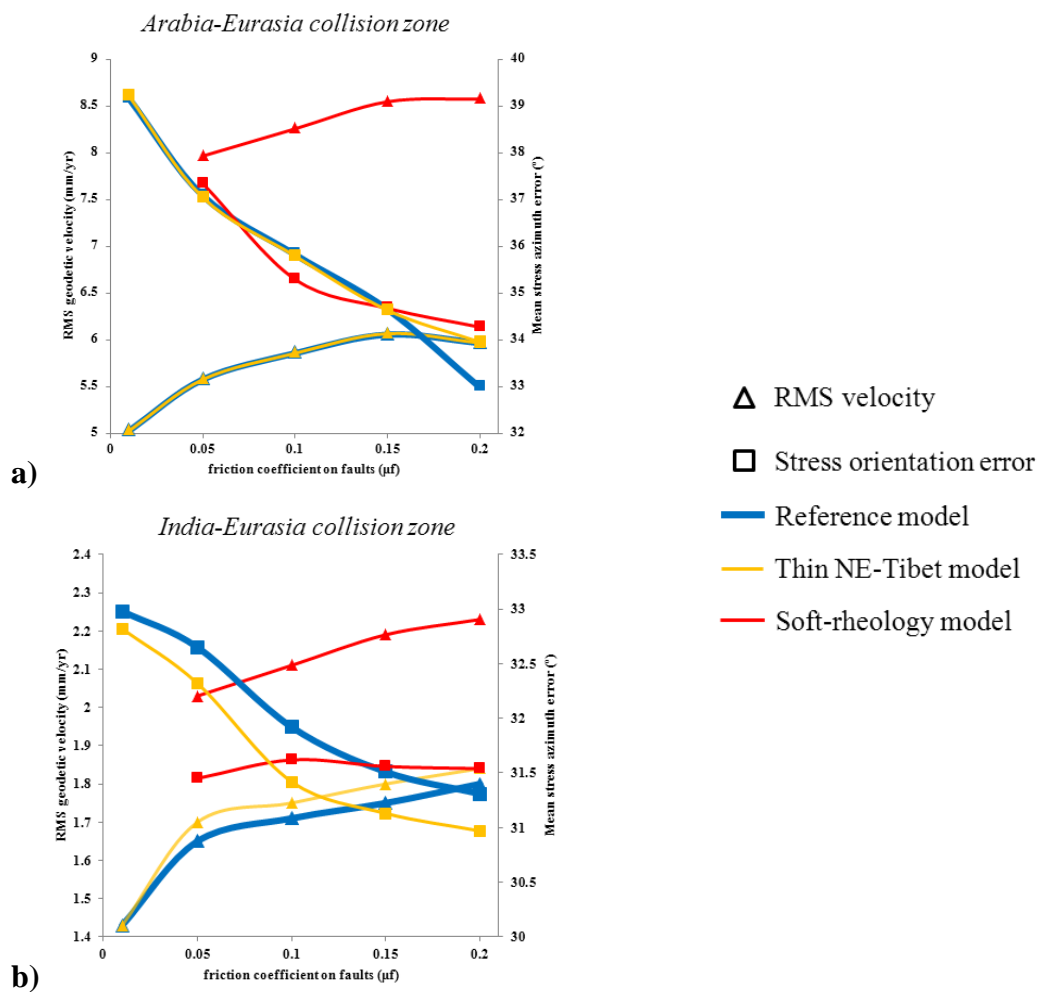


**Figure 7.12.** Model scores against geodetic velocities (triangles) and stress direction (squares) data for different  $\mu_f$  in the (a) Arabia-Eurasia and (b) India-Eurasia collision zones.

Finally, in the region from 60°E to 72°E, the soft-rheology allows to improve model predictions, reducing the errors by ~2 mm/yr and 3° in the velocity and stress orientations, respectively. However, the geodetic observations within this area are too scarce to obtain a meaningful scoring. Therefore, for this region, the results will be discussed only in terms of the distribution of the seismic strain rates, and stress directions.

## 7.4 Changing the velocity conditions in the south-eastern boundary

The surface velocities predicted by the models (Figures 7.4, 7.8 and 7.11) are particularly in disagreement in the south-eastern corner of the Central Asia (south of 32°N latitude) with the velocities inferred by geodetic studies which draw a tight southward flow around the eastern Himalayan syntaxis.

The kinematics of this region is controlled by the competing movements of the three major plates: India, Eurasia and Sunda plates. As shown in Figure 7.13 at the latitude of Burma region (Myanmar), the Indian plate slides northward past the Sunda plate.

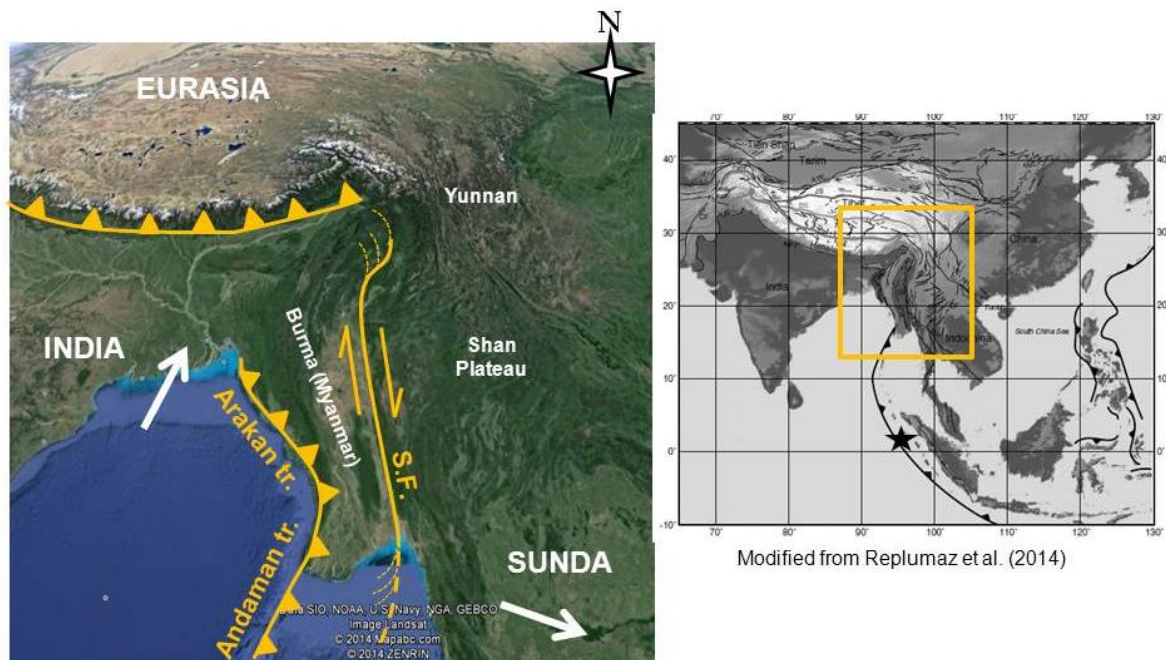


**Figure 7.13.** Simplified scheme of the tectonic setting in the south-eastern part of the Central Asia region. White arrows indicate the approximate direction of Indian and Sunda plates' motion with respect to Eurasia. The black star on the right figure indicates the location of the Sumatra-2004 earthquake. S.F.: Sagaing Fault.

Geodetic studies reveal that the India-Sunda motion is partitioned between the right-lateral strike-slip Sagaing Fault, slipping at a rate of 18 mm/yr, and the Arakan-Andaman trenches farther west, accommodating 20 mm/yr of oblique Indian convergence oriented  $\sim 30^\circ\text{N}$  (Socquet et al., 2006). The Sagaing Fault is linked to the Himalayan fault system by a compressional horsetail directed northwards in the Himalayan syntaxis area, while it ends in an extensional horsetail toward the south in the Andaman pull-apart basin (Socquet et al., 2006).

As mentioned in Section 6.4, the Burma region is also affected by moderate seismicity ( $3 < M < 6$ , Figure 6.6) related to an eastward subducting plane. The subduction continues southward. The Arakan-Andaman trenches and their southern propagation, the Sumatra trench, form a huge subduction boundary between India, Australia and Sunda plates. Fast slipping on faults and high seismicity level reveal that this plate boundary is currently extremely active. The Sumatra-2004 earthquake occurred along the Sumatra trench, near the triple junction between India-Sunda-Australia plates (Figure 7.13).

In order to reproduce the clockwise turn of the velocity vectors around the eastern Himalaya syntaxis, different velocity conditions in the south-eastern boundary of the Central Asia have been tested (Figure 7.14). We use the same model parameters detailed in Table 7.1 and the  $\mu_f$  value of 0.05 since it provides the minimum errors against the observations (see Section 7.3). Boundary conditions BCS1 and BCS2 consider a southward velocity of Sunda plate referred to Eurasia, trying to reproduce the southward movement in the Yunnan and Shan Plateau regions. In BCS2 conditions, Burma is free, moving subjected to the normal tractions equal to lithostatic vertical stress, based on density structure just in the boundary. BCS3 leaves Sunda boundary free, and a SSE velocity is imposed to Burma plate simulating a roll back subduction.

Figure 7.15 shows the predicted stress orientations using these three boundary conditions. In the three cases, the model predicts NE-SW extensional deformation to the south of the Sichuan Basin (east of  $104^\circ\text{E}$ ). However, with respect to the previous models, while in the first case (BCS1) any further no variations in the tectonic regime are predicted, in the other two cases (BCS2 and BCS3) the tectonic regime of south-eastern Asia changes considerably. The modification of the velocity conditions along the western Burma margin affects the tectonic regime not only in the Burma and Shan Plateau, but also in the eastern Tibetan Plateau, where strike-slip tectonics is predicted. Additionally, normal faulting is predicted to the east of the syntaxis, across the Yunnan.

Furthermore, the results of Figure 7.15 indicate that: i) the compressive deformation of the Burma region can be reproduced only when the NE-wards advancement of India plate is applied to the India-Burma boundary (BCS1); ii) normal faulting in the Yunnan province can be reproduced only applying southward or south-westward directed velocities along the India-Burma boundary (BCS2 and BCS3), likely due to back-arc extension tectonics associated with the subducting slab.

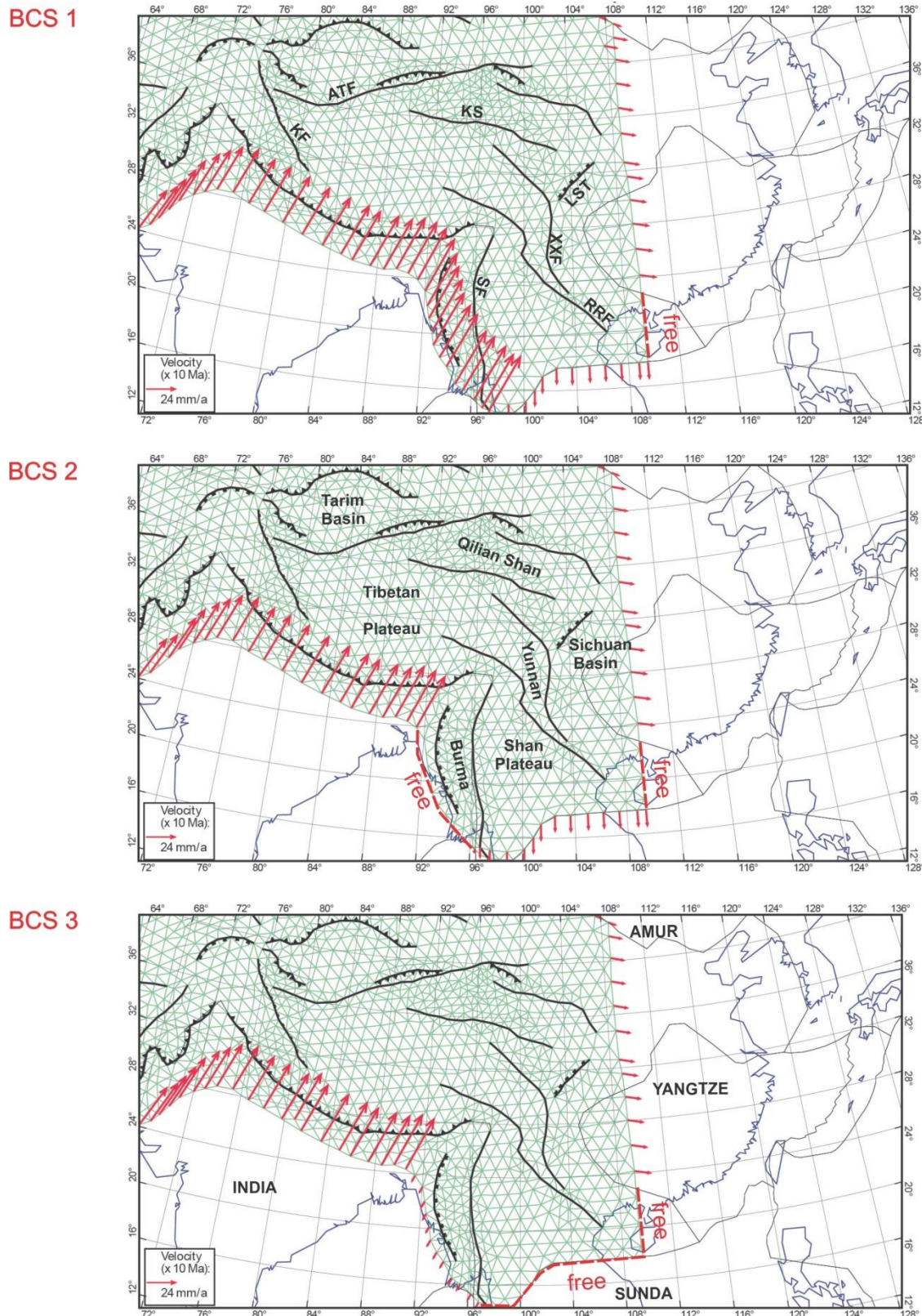
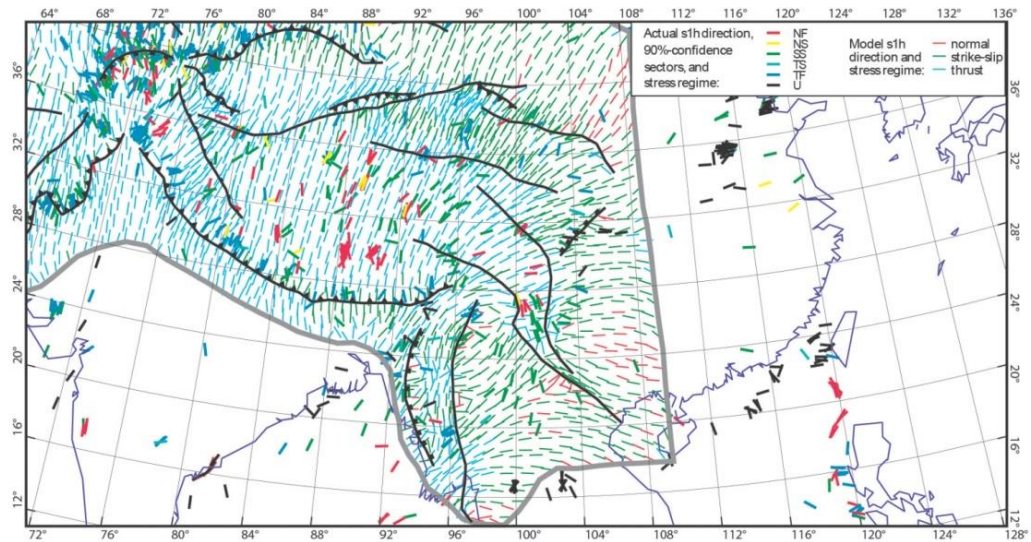
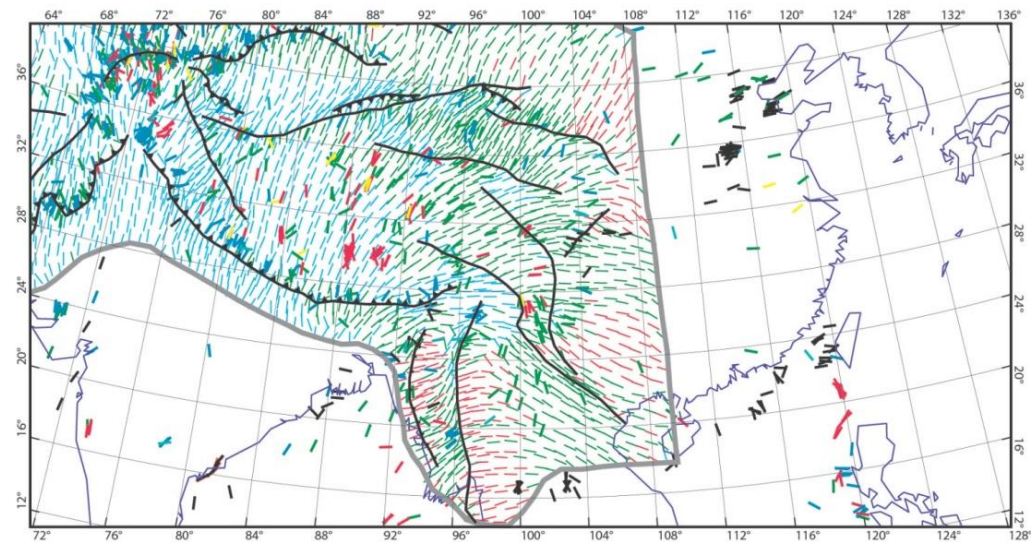


**Figure 7.14.** Different boundary conditions in south-eastern Asia. BCS1 and BCS2 indicate southward-directed Sunda plate velocities with values between 12-12.3 mm/yr; BCS3 shows south-westward velocities in Burma region, with values between 4.8-5.1 mm/yr. In the rest, the boundary condition is motion free or according to the Euler pole of the tectonic plate of the boundary. ATF: Altyn Tagh Fault; KF: Karakorum fault; KS: Kunlun suture or fault; LST: Longmen Shan Thrust; RRF: Red River Fault; SF: Sagaing Fault; XXF: Xiangshuihe-Xiaojiang Fault.

BCS 1



BCS 2



BCS 3

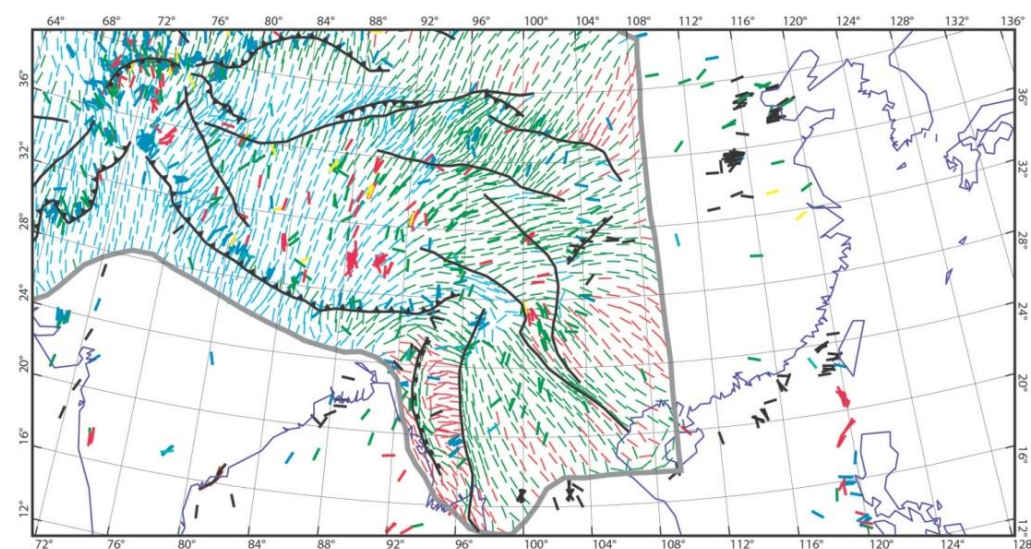
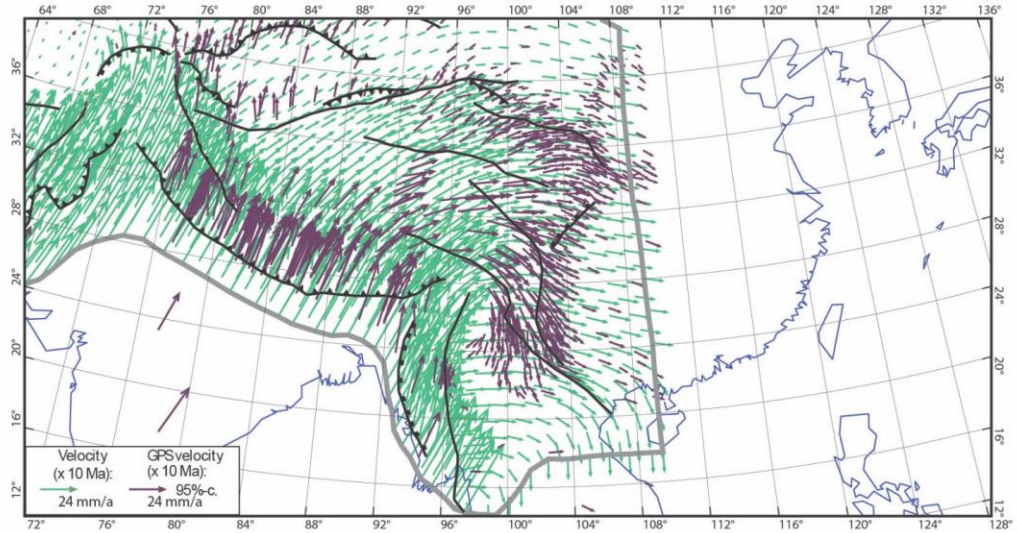
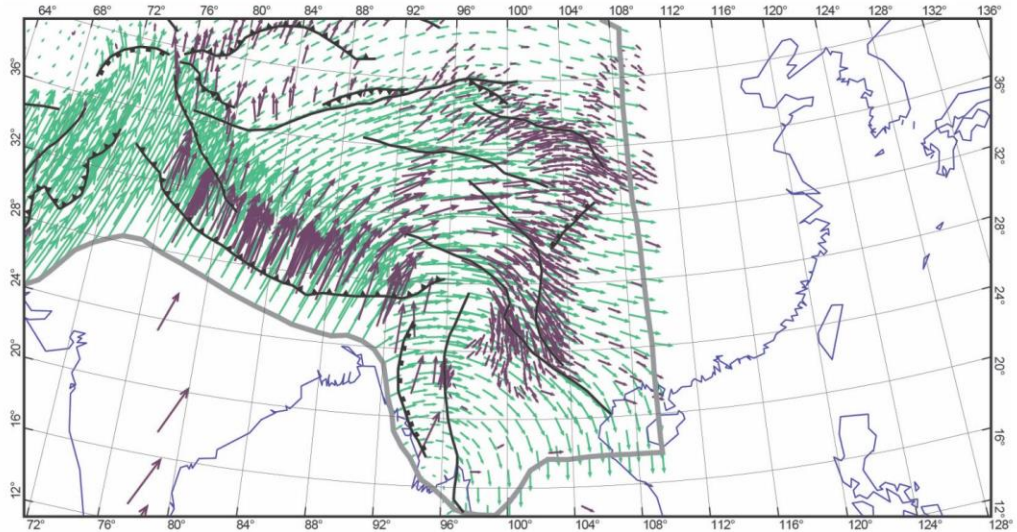


**Figure 7.15.** Most compressive horizontal principal stresses, using the parameters detailed in Table 7.1 and with  $\mu_f = 0.05$ , with different boundary conditions (BCS type referred to Figure 7.14) and the lithosphere structure from the reference model (see Figure 6.3).

BCS 1



BCS 2



BCS 3

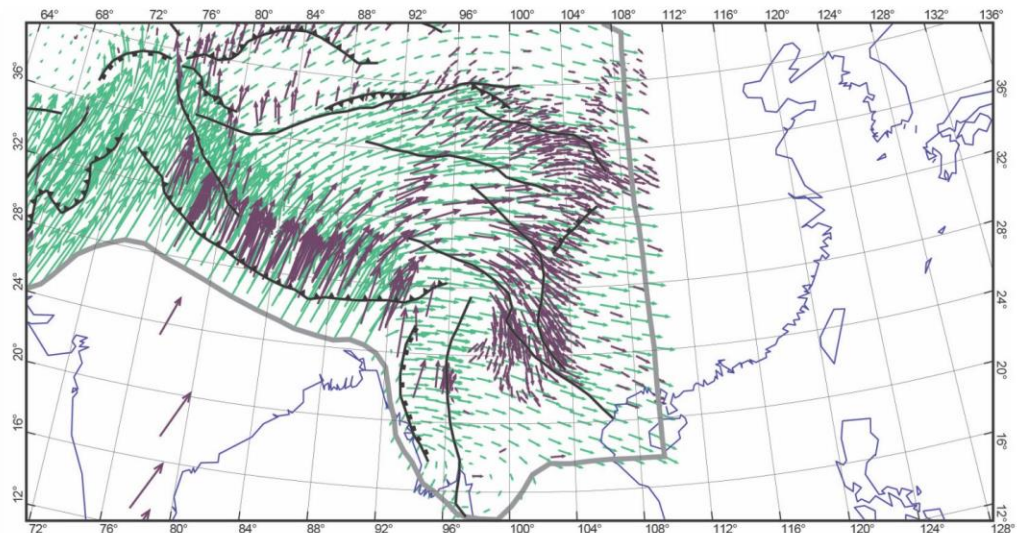


**Figure 7.16.** Predicted velocity field for different boundary conditions (refer to Figure 7.14) and under the same conditions than in Figure 7.15 (assuming a friction coefficient on faults of 0.05 and a lithosphere structure as in the reference model).

The predicted velocity field for the three different boundary conditions is shown in Figure 7.16. The three boundary conditions predict south-eastward velocities fitting the geodetic observations to the east of the Red River Fault (i.e. east of 102°E). However, the tight clockwise turn of 180° of the velocity field around the syntaxis with the southward flow toward the Shan Plateau is not reproduced by the models and remains an unresolved problem in this study.

## Chapter 8: Discussion and concluding remarks

### 8.1 Discussion

This study shows that the SHELLS program provides valuable information on the accommodation of deformation in Central Asia related to the tectonic convergence of the Arabia and the India plates, although the results do not permit leaning toward a single model.

The results show that the contribution of rheology in controlling the deformation patterns is significant. The rheology used for the reference model provides the best fit of the geodetic velocities and stress data in the whole region (Figure 7.4 and 7.5). The scoring shows that the crustal motion, including magnitude and orientation of the velocity vectors, is consistently reproduced in the Himalaya Range and in the central to western sector of the Tibetan Plateau with a RMS error lower than 2 mm/yr (8%) (Figure 7.11b). Similarly, the counter-clockwise rotation trend of the velocities in Arabia and Iran and the westward movement of Anatolia with respect to Eurasia are equally well-reproduced by the model (Figure 7.4), although with an average misfit in the magnitude of the velocity vectors of 5-6 mm/yr (~20%).

The thin-shell approach also allows a good first-order approximation to the stress field in Central Asia, although the results suggest that the implementation of laterally-varying rheological parameters would prevent or, at least reduce, the local misfits on the stress orientations (31°-34° are the obtained least misfits in this study). The model with the rheology as in the reference model) (parameters in Table 7.1), and a thin lithosphere in NE-Tibet shows a general agreement between predicted thrusting and strike-slip features and the observations (Figure 7.10). The introduction of a thinner lithosphere in the north-eastern Tibet allows for a slight improvement in the stress orientations. The 120-km-thick lithosphere decreases ten times the vertical integral of viscosity and increases the Moho-temperature of the north-eastern Tibet to ~960°C (compared to ~750°C of the reference model), which is in agreement with previous studies (Hacker et al., 2000; Galve et al., 2006; Jiménez-Munt et al., 2008) and with the results along D-D' profile (Section 5.2.4). However, the stiffness of the surrounding terrains (i.e. Tarim, Sichuan and Qaidam basins) does not allow reproducing the E-W extension within the Tibetan Plateau. The “soft-rheology” model (Section 7.3), which results in a lower viscous (weaker) lithosphere in the whole Himalaya-Tibetan orogen with respect to the reference model (Figure 7.7), allows the E-W extension (normal and strike-slip faulting) within the plateau. The strike-slip regime in the Caucasus in agreement with Vernant et al. (2004) and Masson et al. (2006) and the normal faulting in eastern Anatolia are also reproduced with in the soft-rheology model, making the results consistent with Le Pichon and Kremer (2010) and the stress data (Figure 7.9). However, the study on the geodetic velocities and strain patterns by Jiménez-Munt and Sabadini (2002) shows that the Anatolia region is rather a rigid block, characterized by a hard lithosphere and slow strain-rates in the centre of the peninsula. The authors suggest that the observed normal faulting is not due to rheological weakness but to the subduction of the Hellenic arc in the Aegean region.

Plots of the predicted strain-rates highlight the presence of rigid (very low deforming rate) blocks surrounded by zones of distributed deformation: the Central Iran, the Tarim, the Sichuan and Qaidam basins, and the south-eastern Yunnan province. The whole north-western corner of the study region, including the Caucasus, the Black Sea and the Caspian Basin, shows negligible deformation in all the models performed.

Considering the location of the rigid blocks and the velocity field derived by GPS observations (Figure 6.5), it seems that these blocks act as boundaries for the observed velocity field outlined in Figure 8.1. The presence of the Black Sea and of the rigid southern Caspian Basin seems to deflect northwards the counter-clockwise motion involving Arabia and Iran. Similarly the presence of the Tarim Basin deflects the velocity field of the western sector of the Himalaya-Tibetan orogen toward the NNW, as observed in the Pamir, Karakorum, and western Tibetan Plateau. The central and eastern sector of the orogen, instead, are moving north-eastwards following the push of the advancing India plate. Eastwards, the presence of the Sichuan Basin deflects again the velocity field towards the southeast. The geodetic observations show also the southward motion in the Yunnan and the Shan Plateau. Different authors propose the presence of a lower crust channel flow in the Yunnan region, driving the upper crust southward (Shen et al., 2001; Gan et al., 2007; Shin et al., 2009). The channel flow would be generated at the later stage of development of the plateau by lateral compression of the Sichuan and the eastern India indenter and gravitational buoyancy.

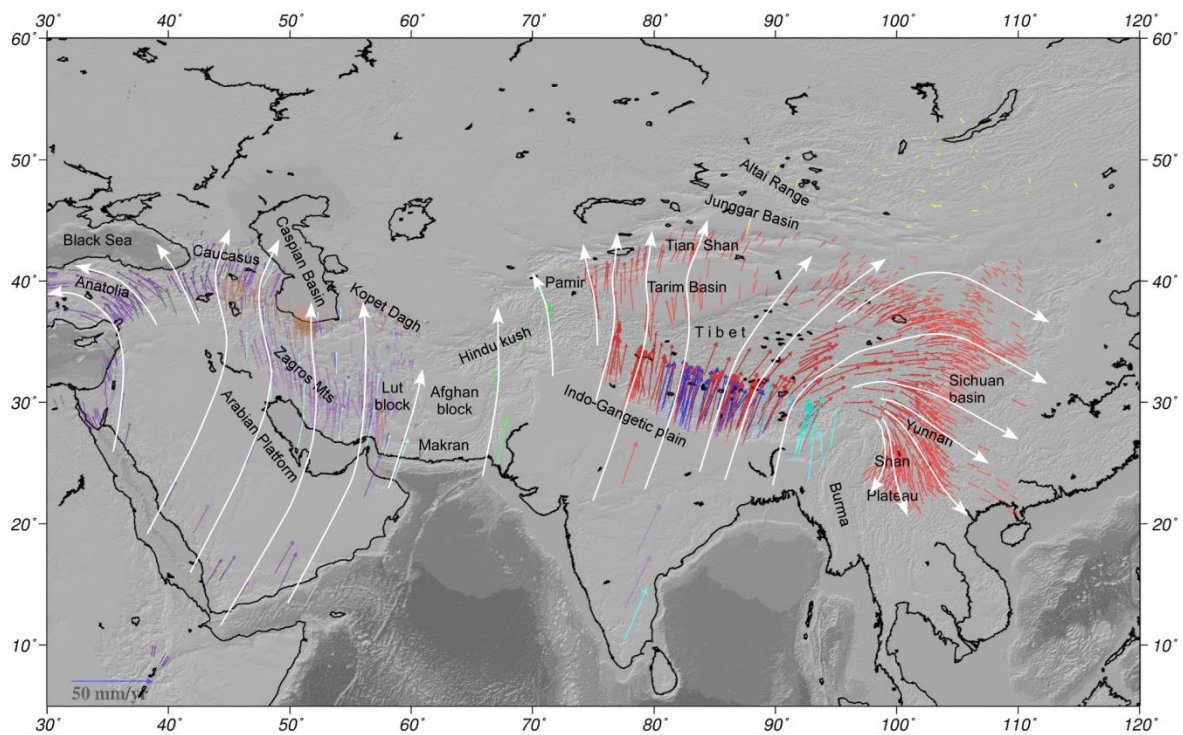


**Figure 8.1.** Flow lines (main directions) of the velocity field in the Central Asia (referred to Eurasia) as inferred by GPS measurements (coloured arrows; see legend in Figure 6.5).

The SHELLS program allows reproducing the main directions (Figure 8.1) of the observed velocity field in the whole Central Asia. In the “soft-rheology” model the splitting of the velocity field west of 48°E longitude toward the Anatolia and the Caucasus regions is appreciable (Figure 7.8). The nearly N-S trending velocities in the western Himalaya-Tibetan orogen are also well reproduced in the models as well as the north-eastward motion in the central and eastern Tibetan Plateau (Figure 7.4, 7.8 and 7.11) and the south-eastern movement south of the Sichuan Basin (Figure 7.16). Only the southward flow around the eastern Himalaya syntaxis is not reproduced. The same result was obtained also by Vergnolle et al. (2007) which, by using the thin viscous sheet approach to model the deformation in the eastern Asia, including the Sunda and the Philippine Sea plates, found that the predicted velocities are systematically rotated counter-clockwise by 10°-15° compared to the geodetic observations in northern and eastern China. The impossibility to simulate the southward flow by using a coupled crust-mantle lithosphere as in the SHELLS program, suggests that it is probably a feature just superficial, decoupled from the rest of the lithosphere. We suggest that the southward motion is generated by the squeezing of the continental block between the strong north-eastward advance of the India plate to the west and the strong Sichuan Basin to the east.

The resulting strain rate plots of the performed models show, in general, a good correlation with the earthquake distribution, especially in the Zagros and Himalaya-Tibetan orogens, if the rheology of the reference model is considered. The faster deforming areas (strain rate of  $10^{-15}$ - $10^{-16}$  s<sup>-1</sup>) are characterized by numerous seismic events with magnitudes up to M=7.9 (Figure 7.3), with the earthquakes occurring mostly in the first 50 km depth. In the Zagros orogen, the deformation is accommodated in the region surrounding the rigid Central Iran block, whereas in the Himalaya-Tibetan orogen the deformation is accommodated in the belts surrounding the rigid Tarim and Sichuan basins and the southern Shan Plateau (Figure 7.3). Similarly, the earthquakes are located in the different belts surrounding the rigid blocks, but also throughout the Tibetan Plateau and its south-eastern propagation. The Arabian Platform and the north-western corner of the Central Asia region are characterized by an absence of seismicity, which is in agreement with the high viscosity and low strain-rate of the reference model.

There are, however, zones of scarce correlation between the strain rates predicted by the models and the earthquake distribution. One of these areas is the Caucasus range, which behaves rigidly in all the tested models (see results in Sections 7.1 and 7.2), but the seismicity is moderate (5-7 magnitude earthquakes), and geodetic observations indicate N-S directed motion (Reilinger et al., 2006). The high lithospheric strength of this area is due to the thick lithospheric mantle (>100 km thick), the low surface heat flow ( $\sim 0.48$  W/m<sup>2</sup>) (Figure 6.3) and then resulting in a high viscous lithosphere ( $\sim 10^{25}$  Pa·s) (Figure 7.2 and 7.6). Consequently, the deformation related to the Arabian convergence in our models is accommodated further south, i.e. in the north-western Zagros and Anatolia, which show low viscosity ( $\sim 10^{22}$  Pa·s), high strain rates ( $\sim 10^{-15}$  s<sup>-1</sup>) and moderate slip on faults (5-7 mm/yr along the North Anatolia Fault and the northern segment of the High Zagros Fault). One possibility to decrease the

lithosphere strength and allow for deformation to be accommodated in the Caucasus region would be to consider higher heat flow values ( $\sim 80 \text{ mW/m}^2$ ) according to Kutas et al. (1998).

The front of the Zagros range is another area of weak correlation between the model-derived strain rates and the seismic events distribution. Although, the Zagros fold-and-thrust belt is affected by high seismicity (Figure 6.6), the results of this study do not evidence significant deformation ( $\leq 1 \text{ mm/yr}$  of slip rate along the Main Frontal Front and  $10^{-16} \text{ s}^{-1}$  of strain rate). The reason stands in the fact that, due to the shallow dip of the MFF discontinuity ( $25^\circ$  dip, Figure 6.2) and its location on the strongly viscous Arabian lithosphere, the deformation can occur only at shallowest crustal levels in this region. The model, which performs vertical integrals of the viscosity, is not able to show motion on the discontinuity due to the  $\sim 180\text{-km}$  of thickness of highly viscous Arabian lithosphere. Therefore, the deformation is accommodated farther inwards, with slip on the MZT and CIT discontinuities in the Zagros (Figure 6.2). A similar problem characterizes also the front of the Himalaya Range, where the Main Boundary Thrust is not showing slip motion in the modelling results

By adopting a softer rheology in the mantle (Section 7.2), the fit of the observed slip-rates has been improved on selected faults. The slip-rate along the North Anatolia and Main Zagros faults has been increased to 7-10 mm/yr, compared to 5-6 mm/yr of the reference model with “stiffer” rheology. However, this value is too low to reconcile with the observations which claim for a slip of  $\sim 26 \text{ mm/yr}$  (Reilinger et al., 2006; Le Pichon and Kreemer, 2010). Probably, by imposing the westward motion of Anatolia with respect to Eurasia, the slip-rate on the North Anatolian Fault would have decrease the misfit. The Altyn Tagh Fault, which is characterized by only  $\sim 4 \text{ mm/yr}$  of left-lateral slip-rate in the reference model, show values of 4-6.5 mm/yr in the “soft-rheology” model, in agreement with GPS measurements (5-6 mm/yr, Zhang et al. 2004). Reasonable slip-rate values are obtained in the soft-rheology model also for the Tian Shan and Main Pamir thrusts if compared to those obtained by Liu and Bird (2008) (average of 4.5 mm/yr and 6 mm/yr compared to 5 mm/yr and 10 mm/yr in the Tian Shan Thrust and in the Main Pamir Thrust, respectively). The Sagaing Fault motion is slipping with a rate up to 15-18 mm/yr, which is consistent with the value of 18 mm/yr obtained by geodetic measurements (Vigny et al., 2003) or elastic modelling (Socquet et al., 2006), but not with the values proposed by Meade (2007) and Liu and Bird (2008), respectively of 31-49 mm/yr and 22-35 mm/yr of slip-rate.

The tests on changing the boundary conditions point out that the strike-slip tectonic regime observed in the easternmost sector of the Tibetan Plateau is controlled by the boundary conditions imposed along the India-Burma boundary, being reproduced only when the Indian convergence is neglected (BCS2 and BCS3, Figure 7.15). On the other hand, the absence of tectonic convergence along the western Burma margin does not impede the south-eastward extrusion of the material north of the eastern Indian indenter. Even removing completely the Indian convergence (i.e. no velocity conditions imposed at the India-Eurasia boundary), the results show a south-eastward material flow, similar to the models by Vergnolle et al. (2007).

An important result is that reproducing the N-S extensional features observed to the east of the eastern Himalaya syntaxis, (in the Yunnan region between the Red River Fault and the Xiangshuihe-Xiaojiang Fault) demands a free condition or south-westward motion to the western Burma border. Since the upper crust of Burma region is affected by shortening due to the Indian convergence along the Arakan trench (Socquet et al., 2006), the south-westward motion of this margin must be associated with the mantle part, likely suggesting a retreating of the subducting slab, and consequent back-arc extension in the continental interiors. This theory is supported by a recent study on the distribution of the lithospheric strength in the south-eastern Tibet and Yunnan provinces (Chen et al., 2014b, Figure 8.2). The study analyses the relation between elastic thickness anisotropy and other proxies for the lithosphere stress and strain, and points out the weak and highly anisotropic nature of the lithosphere at regional scale. The authors suggest that the area is characterized by a geodynamic transition from the post-collision compression tectonics within the Tibetan Plateau to the back-arc extension related to the Burma plate subduction off the plateau (Chen et al., 2014b).

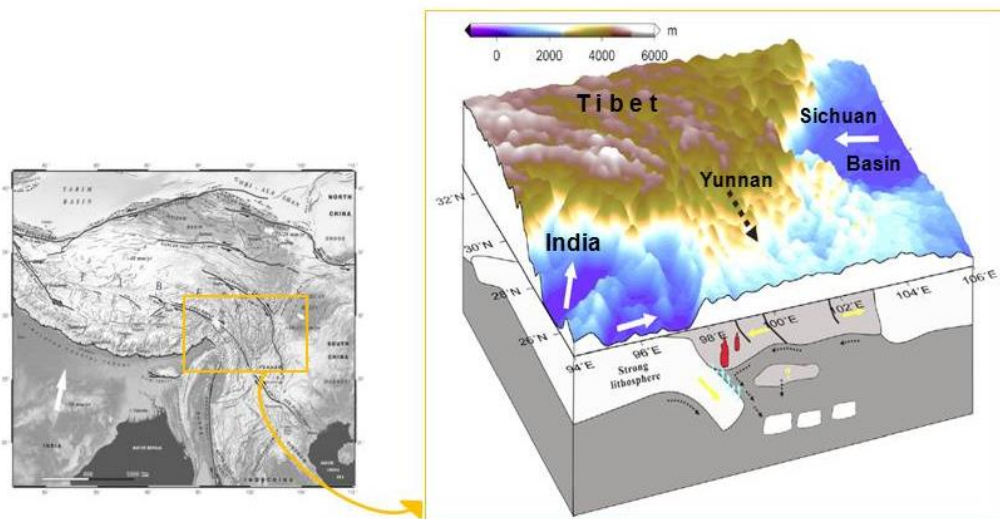


**Figure 8.2.** Cartoon of the interaction and deformation of the lithosphere in the south-eastern Tibetan Plateau, modified from Chen et al. (2014b). Solid arrows illustrate the direction of the forces acting upon (white) and within (yellow) the lithosphere. Black dashed arrow on the topographic surface indicates the direction of the crust flow. Thin dashed arrows represent the sublithospheric mantle flow. Localization figure (on the left) modified from Tapponnier et al. (2001).

## 8.2 Concluding remarks

The thin viscous sheet approach used in this study is suitable to reproduce a first order approximation of the velocity and stress fields in the Central Asia region related to the collision of the Arabia and India plates with Eurasia. Besides the large scale, this study offers

a coherent result in regions with little or no data coverage, as in the case of the Arabia-India inter-collision zone, over large areas of Pakistan and entire Afghanistan. The results obtained allow delineating the following concluding remarks:

- The SHELLS program allows reproducing the main directions of the velocity vectors in the study region by only imposing the convergence of Arabia and India plates respect to the fix Eurasia, and varying the rheology parameters. The models are able to simulate the observed kinematics including the counter-clockwise rotation of Arabia and Iran triggering the westward escape of Anatolia, and the eastward extrusion of the northern Tibetan Plateau structural domains.
- The reference model provides the least misfits in the Arabia-Eurasia and India-Eurasia collision zones. The errors in the predicted GPS velocities and stress directions are, respectively, 5.7 mm/yr (~20%) and 36° (~10%) for the Arabia-Eurasia and ~1.7 mm/yr (~7%) and 32° (~8%) for the India-Eurasia collision zone.
- The minimum misfits are obtained with friction coefficient on faults ( $\mu_f$ ) between 0.05 and 0.1, given the divergent trends of the errors for the geodetic observations and stress data.
- A soft lithosphere is required to reproduce the normal and strike-slip faulting within the Tibetan Plateau. This can be achieved by changing the rheological parameters or by thinning the lithosphere, or by the combination of both.
- The results show that the thinning of the north-eastern part of the Tibetan Plateau result in an increase of the Moho temperature that would permit to reconcile the model with the high heat flow values and the low mantle seismic velocities observed in this area, as well as with the results of the geophysical-petrological study presented in this Thesis.
- The southward flow of material from the south-eastern Tibetan Plateau towards the Shan Plateau observed by the geodetic studies cannot be reproduced with the thin-sheet approach. This odd flow is interpreted in this work as probably resulting from the squeezing of the continental block sandwiched between the strong NE-ward advancing of the India plate and the rigid Sichuan Basin block.
- The tectonic regime of the eastern Tibetan Plateau is controlled by the boundary conditions along the India-Burma boundary. The eastward subducting slab beneath Burma is probably retreating and producing back-arc extension in the continental interiors, which is expressed by normal faulting in the Yunnan region, between the Red River and the Xiangshuihe-Xiaojiang faults.

## **PART IV:**

# **GENERAL CONCLUSIONS**

---



## Chapter 9: General conclusions

The Central Asia collision zone has been studied in this Thesis by using two different numerical methodologies: 1) the geophysical-petrological approach which allowed the characterization of the present-day lithosphere structure beneath the Arabia-Eurasia and the India-Eurasia collision zones along four geo-transects, and 2) the thin viscous sheet approach which allowed investigating the large scale neotectonic deformation in the whole Central Asia region on map view.

In the integrated geophysical-petrological approach, geological, geophysical and petrological data are combined within an internally consistent thermodynamic-geophysical framework. This technique has proven to be a valuable tool for the characterization of the lithosphere structure from the thermal, compositional and seismological point of view. Since density in the lithospheric mantle is a function of P-T conditions and the chemical composition, the resulting lithospheric structure allows taking into account mineral phase changes and lateral compositional heterogeneities within the lithospheric mantle of the Zagros and the Himalaya-Tibetan orogens.

The four 2D lithospheric models are in agreement with geophysical observables, geological data and seismic tomography studies. The results show that the present-day lithosphere mantle structure of the Arabia-Eurasia and India-Eurasia collision zones are laterally-varying along the strike of the Zagros and the Himalaya-Tibetan orogens, not just in terms of crust and lithospheric mantle thickness, but also in mantle density, temperature and composition. The study also allowed distinguishing different lithospheric domains within the Zagros and the Himalaya-Tibetan orogens. The 2D-models obtained along the four selected profiles show that the ranges of the Central Asia (Zagros, Alborz, Himalaya, Tian Shan, Qilian Shan) are characterized by the presence of crustal roots, but not necessarily underlain by lithospheric mantle roots.

In the Zagros orogen, the resulting crustal thickness is smaller beneath the Arabia platform and Central Iran, and greater beneath the Sanandaj Sirjan Zone and the Alborz range. The lithospheric mantle thickness is greater beneath the Arabian Platform, the Mesopotamian Foreland Basin and the frontal sector of the Zagros range than beneath the continent interiors. In the northern profile (northern Zagros) the LAB rises sharply below the Sanandaj Sirjan Zone in a ~90 km narrow region, whereas in the southern profile (central Zagros) the thinning is smoother and affects a wider region, from the Zagros Fold-and-Thrust Belt to the Central Iran. The transition from the Arabian to the Eurasian lithospheric domain is located beneath the Zagros range, and it is marked by a change in the mantle velocity anomaly and in the lithospheric mantle composition.

In the Himalaya-Tibetan orogen, the crustal and lithospheric mantle thickness increase from the Indo-Gangetic plain to the Tibetan Plateau, but in different ways from east to west.

In the western sector, the thickening is gradually and it reaches the maximum below the northern edge of the Plateau and the western Kunlun Shan. In the eastern sector, the thickening generates sharp steps at both Moho and LAB discontinuities beneath the Himalaya Range, but it affects only the southern part of the plateau. The lithospheric mantle thins abruptly beneath the Qiangtang and the Songpan Ganzi terrains, even without comparable crustal thinning. Beyond the Tibetan Plateau, the lithospheric mantle thins below the Tarim and Junggar basins, although with smaller extent compared to the thinning in the north-eastern Tibet. The transition from the Indian to the Eurasian lithospheric domain is located within Tibet, but with conspicuous differences in the amount of the northward underthrusting from east to west. In the western sector, the Indian lithospheric mantle underlies the whole Tibetan Plateau up to the boundary with the Tarim Basin, while in the eastern sector the underthrusting is restricted to the north up to the Bangong-Nujiang Suture. Different Eurasian domains have been also identified beneath the Tarim Basin and the Altaids region (i.e. Tian Shan, Junggar and Altai range) by means of different lithospheric mantle compositions.

The location of the lateral changes in the lithospheric mantle thickness roughly coincides with the position of the lateral variations in the lithospheric mantle compositions (Figure 9.1). Although the non-uniqueness of the compositional space remains an intrinsic problem since a wide range of compositions can explain multiple geophysical data, the chosen compositions fit the seismic velocity anomalies of both P- and S-waves and are compatible with available xenolith data and with the tectonothermal age. A generic lherzolitic mantle composition is dominant along the four profiles, being suitable for the lithospheric mantle beneath the Mesopotamian Foreland Basin and Persian Gulf, the Indo-Gangetic plain, the Himalaya Range and the western Tibetan Plateau, the Qaidam Basin, Qilian Shan, North China Block as well as the accreted terrains on the Eurasian side of the Arabia-Eurasia collision zone (Urumieh Dokhtar Magmatic Arc and Central Iran). However, the results show a change to a more fertile mantle composition beneath the Tarim Basin, and a relative enrichment in FeO and MgO beneath the northern Eurasian domains of the Himalaya-Tibetan orogen (Tian Shan, Junggar and Altai Range). Furthermore, the frontal parts of the Zagros range (Zagros Fold-and-thrust belt and Imbricated Zone) are compatible with a Phanerozoic harzburgitic-type mantle composition, and a refertilized dunitic lithospheric mantle is proposed for the thin lithospheric mantle of the north-eastern Tibetan Plateau.

In terms of major element composition, the transition from the Arabian-Indian to the Eurasia lithospheric mantle portion is recorded by a MgO depletion and  $\text{Al}_2\text{O}_3$  as well as CaO enrichments in the Eurasian plate lithospheric mantle. The subductions of the Arabian and Indian plates beneath Iran and eastern Tibet (up to the Bangong-Nujiang Suture) respectively, are most probably responsible for metasomatic processes in the upper (Eurasian) plate induced by Al-Ca-rich slab released fluids. However, whether additional processes represented by partial or extensive melting, slab breakoff or delamination, have contributed or not in producing the solid assemblage defined by the NCFMAS chemical composition is hard to discern from this study.

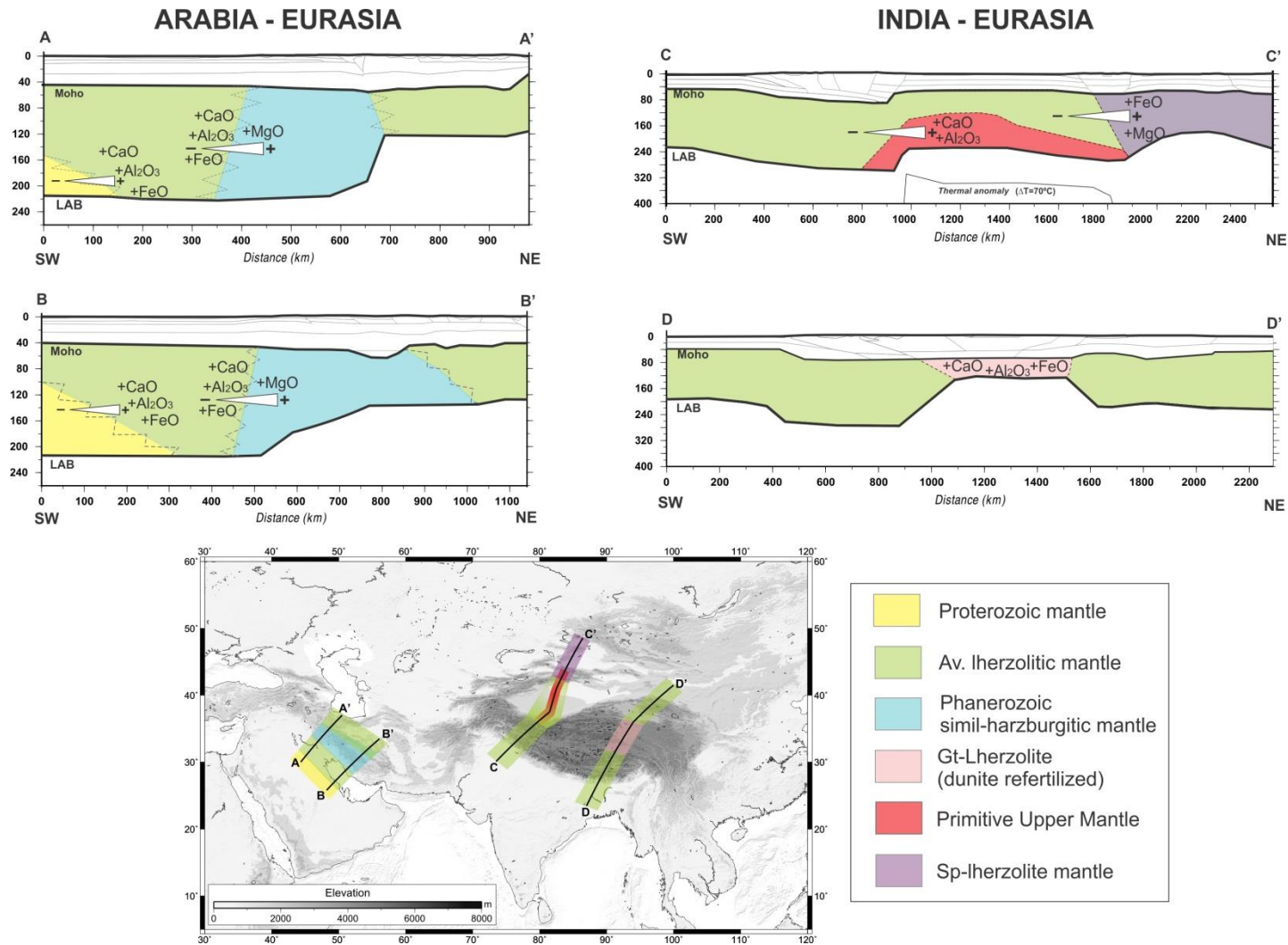


**Figure 9.1.** Scheme to summarize the results on the lateral compositional variations within the lithospheric mantle obtained beneath the Arabia-Eurasia (A-A' and B-B' profiles) and India-Eurasia (C-C' and D-D' profiles) collision zones. Composition colour for the asthenosphere domain (i.e. Primitive Upper mantle) has been omitted for clarity.

In fact, mantle composition in terms of major elements should be supported by trace element geochemistry and isotopic data to distinguish between different mantle processes. In this way it would be possible to decipher the long-term chemical evolution of the subcontinental lithospheric mantle and, hence, to evaluate the mechanism responsible for the present-day lithospheric mantle composition and thickness.

The neotectonic modelling permitted to match the results on the present-day lithospheric structure of the Zagros and the Himalaya-Tibetan orogens with the present-day kinematics, GPS observations and fault activities related to the collision of the Arabia and India plate with Eurasia. The variations in the lithospheric structure obtained in the Zagros and the Himalaya-Tibetan orogens have significantly affected the lithospheric strength and, hence, the distribution of the surface deformation. The SHELLS program considers a vertically-integrated viscosity in a laterally-varying thermal and lithosphere structure and, therefore, it allows showing clearly the relative strengths of the different parts of the lithosphere. The neotectonic modelling based on this thin-shell approach has proven to be a valuable tool to investigate the effect of the lithospheric structure, rheology, boundary conditions, and friction coefficient values on the predicted surface velocities, deformation patterns, stress orientations and tectonic regime in Central Asia.

Although the results obtained using the SHELLS code do not permit leaning toward a single model to fit all the kinematic features of such a complex geodynamic setting, the study shows that a model considering a “typical” rheology (e.g. the reference model), allows obtaining a first order approximation of the velocity field and of the stress directions in the whole Central Asia. The model reproduces the counter-clockwise rotation of Arabia and Iran, the westward escape of Anatolia, and the eastward extrusion of the northern Tibetan Plateau by only imposing the convergence of Arabia and India plates respect to the fix Eurasia. The simulation of observed extensional tectonics within the Tibetan Plateau requires, instead, a weaker lithosphere, which can be provided by i) a change in the rheological parameters or ii) a reduction of the lithosphere thickness in the NE-Tibet. The results show that the temperature increase generated by the lithospheric thinning in the NE-Tibet would permit to reconcile the model with the high heat flow values and the low mantle seismic velocities observed in this area. Furthermore, the thinning affects the strain distribution within the Tibetan Plateau, showing that the northern-eastern sector is faster deforming than the southern and western parts. The anisotropic distribution of the deformation within the plateau, as well as the lateral strength variations throughout the Himalaya-Tibetan orogen, characterized by the presence of the rigid Tarim and Sichuan basins, can produce changes in the mass distribution and in the transmission of the deformation into the continent interior, with further consequences in the topography evolution of this region. In the Zagros orogen, the modelling results show lower strain rates compared to the Himalaya-Tibetan orogen, with the deformation concentrated in the ranges surrounding the rigid Central Iran block. The lithosphere weakness generated by the thinning of the lithospheric mantle is compensated by the presence of this rigid block, resulting in a lithosphere overall more viscous in the Arabia-Eurasia collision zone than in the India-Eurasia collision zone. This characteristic combined with the slower advancement of the Arabia plate against Eurasia result in a lower deforming

orogen in which the tectonic convergence of the Arabia plate is mainly accommodated at the sides of the Zagros range, i.e. toward the west in the Anatolia region and toward the east, in the Arabia-India inter-collision zone.

With this approach, it has not been possible to simulate the tight clockwise flow of crustal material around the eastern Himalaya syntaxis observed by GPS measurements. It is probably describing a surficial feature derived by the squeezing of the continental block sandwiched between the strong NE-ward advancing of the India plate and the rigid Sichuan Basin. An improvement on the program would be to implement the possibility to vary laterally the rheological parameters and the friction coefficient between the different faults inside the model. It would be more realistic, permitting to fit the observed geological slip-rates.

In summary, this Thesis has provided new insights on the present-day lithosphere structure of the Zagros and the Himalaya-Tibetan orogens, consistently with tomography images and integrated geophysical models, and new insights on the accommodation of the deformation related to the collision of the Arabia and India with Eurasia. I hope that the results obtained will help to further understand the close relations between lithospheric mantle structure, upper mantle processes and the tectonic behaviour in the Central Asia collision zone.



## List of figures and tables

- Figure 1.1.** Topographic map of the study region (roughly defined by the white line). This Thesis shows the results on the present-day lithospheric structure along four profiles (orange lines) obtained by using an integrated geophysical-petrological methodology, and the study of the present-day deformation in the whole Central Asia obtained by applying a thin viscous sheet approach. 3
- Figure 2.1.** Topography map of the Central Asia region and localization of the three major zones selected to introduce the geodynamic and tectonic setting. The shaded relief has been obtained from ETOPO1 database (Amante and Eakins, 2009). 10
- Figure 2.2.** Simplified map of the Arabian and surrounding plates, with plate boundaries (red) and convergence vectors (red arrows). Grey areas represent exposed basement. Fig. from Stern and Johnson (2008). 11
- Figure 2.3.** Structural map showing the main tectonic units of the Zagros Mountains and adjacent areas (modified after Jiménez-Munt et al., 2012). The colours assigned to the different tectonic units are not related to age or lithology, but are used to highlight their limits. White arrows correspond to the relative plate velocities of the Arabian plate with respect to a fixed Eurasian plate. ZDF: Zagros deformation front; MFF: Main Frontal Fault; HZF: High Zagros Fault; MZF: Main Zagros Fault; Qb: Qom basin; GKB: Great Kabir basin; and AFB: Alborz foredeep basin; OFB: Oman foreland basin; SH: Strait of Hormuz; MF: Minab Fault; MFT: Makran Frontal Thrust. 12
- Figure 2.4.** Geological map of the Indian Shield showing the age and exposure of the Precambrian basement. SGT: Southern Granulite Terrain; WDC: Western Dharwar Craton; EDC: Eastern Dharwar Craton; EGMB: Eastern Ghat Mobile Belt; CB: Cudappah Basin; DVP: Deccan Volcanic Province; GRP: Godavari Rift Province; BC: Bhandara Craton; SC: Singhbhum Craton; BhC: Bundhelkhand Complex; DAFB: Delhi Aravalli Fold Belt; CITZ: Central Indian Tectonic Zone. Figure from Rajesh and Mishra (2004). 14
- Figure 2.5.** Tectonic map of the Himalaya-Tibetan Plateau and surrounding areas. The names for the different terrains (coloured areas) are taken from van Hinsbergen et al. (2011). ATF: Altyn Tagh Fault; BNS: Bangong Nujiang Suture; CAOB: Central Asia Orogenic Belt; HFF: Himalaya Frontal Front; ITS: Indus-Tsangpo Suture; JS: Jinsha Suture; KF: Karakorum Fault; KS: Kunlun suture or fault; MBT: Main Boundary Thrust; MCT: Main Central Thrust; NBT: North Border Thrust; NTST: Northern Tian Shan Thrust; S.-G: Songpan-Ganzi; STST: Southern Tian Shan Thrust. 16
- Figure 2.6.** Topography map and main structural lines of the region between the Arabia-Eurasia and the India-Eurasia collision zones. CF: Chaman Fault; HRF: Herat Fault; KF: Karakorum Fault; MFF: Main Frontal Front; MPT: Main Pamir Thrust; MZF: Main Zagros Fault; SIF: Sistan Fault. 18
- Figure 3.1.** Simplified scheme of the LitMod program. A: radiogenic heat production;  $\rho_c$ : crustal density;  $\rho_m$ : lithospheric mantle density; T: temperature; Zc: crustal thickness; Zm: lithospheric mantle thickness. 24
- Figure 3.2.** Schematics of diffusive vs. direct radiative transfer in an internally heated medium comprised of grains. In a low temperature gradient, each grain is effectively isothermal. The shades of the grains indicate the gradual temperature change. White arrows indicate diffusion. Black arrow denotes direct transfer of a photon from a hot to a cold grain: here, negligible interaction with the intervening grains occurs. Figure from Hofmeister (2005). 27

- Figure 3.3.** Secular evolution of subcontinental lithospheric mantle composition, using estimates for single areas based on garnet xenocrystals and xenolith suites and classified in terms of tectonothermal age (from Griffin et al., 2008). 33
- Figure 3.4.** Classifications of the crustal domains in terms of the age of the last tectonothermal event. Figure from IUGS web page (<http://iugs.org/index.php>). 35
- Figure 3.5.** Density-depth (panel a) and velocity-depth (panels b, c) ranges for different lithospheric mantle compositions, calculated considering the Moho and the LAB discontinuity at 35 km and 150 km depth, respectively. Compositions are taken from Griffin et al. (2008). PUM: Primitive Upper Mantle. 36
- Figure 4.1.** Structural map showing the main tectonic units of the Zagros Mountains and adjacent areas, including major igneous and ophiolitic complexes, and location of the selected profiles (thick grey lines) A-A' and B-B' (modified after Jiménez-Munt et al., 2012). The colours assigned to the different tectonic units are not related to age or lithology but are used to highlight their limits. White arrows correspond to the relative plate velocities of the Arabian plate with respect to a fixed Eurasian plate. Light-blue line indicates the balanced geological cross-section by Vergés et al. (2011). ZDF: Zagros deformation front; MFF: Mountain Frontal Fault; HZF: High Zagros Fault; MZF: Main Zagros Fault; Qb: Qom basin; GKB: Great Kabir basin; and AFB: Alborz foredeep basin; OFB: Oman foreland basin; SH: Strait of Hormuz; MF: Minab Fault; MFT: Makran Frontal Thrust. 39
- Figure 4.2.** Potential fields in the study area. (a) Bouguer anomaly from Getech data in Iran and calculated from satellite free-air anomaly in the rest of the region (see text for details). (b) Geoid height from EGM2008 model. Spherical harmonics up to degree and order 9 have been removed. Shading indicates elevation. 41
- Figure 4.3.** Heat flow measurements in the Arabian plate, Red Sea, Gulf of Aden, Eastern Mediterranean Sea, Anatolia region, Caspian Sea and Zagros Mountain region. 42
- Figure 4.4.** Topography map of the study area, crustal thickness values (numbers) and 2D-lithospheric modelling profiles (heavy continuous lines, grey and pink) from other studies (modified after Jiménez-Munt et al., 2012). Black dashed contours are the results from regional tomographic models (Manaman et al., 2011). Grey wide lines denote the localisation of A-A' and B-B' profiles of this study. Grey thin lines correspond to the main structural boundaries (see Figure 4.1). 43
- Figure 4.5.** P-wave tomography along A-A' (a) and B-B' (b) profiles from 35 to 400 km depth. Global reference model used - AK135 (Kennett et al., 1995). HZF: High Zagros Fault; MFF: Main Frontal Fault; MZF: Main Zagros Fault. 45
- Figure 4.6.** Density and velocity variations with depth for each mantle composition, considering a Moho discontinuity at 42 km depth and LAB at 210 km depth. Mantle compositions refer to Table 4.1. 48
- Figure 4.7.** Crustal model for A-A' (a) and B-B' (b) profiles. Dashed lines indicate the Moho discontinuity from published 2-D lithospheric profiles (Molinaro et al. 2005; Motavalli-Anbaran et al. 2011). Physical properties of crustal bodies are reported in Table 4.2. HZF: High Zagros Fault; IZ: Imbricated Zone; MFF: Main Frontal Fault; MZF: Main Zagros Fault; SSZ: Sanandaj Sirjan Zone; UDMA: Urumieh Dokhtar Magmatic Arc; ZFTB: Zagros Fold-and-Thrust Belt. 51
- Figure 4.8.** Modelling results for A-A' profile. Red dots denote measured values and vertical dispersion bars with the standard deviation calculated on a strip of 50 km. Continuous blue lines represent the calculated values from the model. Dashed grey lines represent the transition between different chemical compositions or mantle domains. Numbers indicate different mantle composition (Table 4.1). Discontinuous lines indicate Moho and/or LAB depth geometry from Motavalli-Anbaran et al. (2011)

(profile I, black) and Jiménez-Munt et al. (2012) (red). HZF: High Zagros Fault; IZ: Imbricated Zone; MFF: Main Frontal Fault; MZF: Main Zagros Fault; SSZ: Sanandaj Sirjan Zone; UDMA: Urumieh Dokhtar Magmatic Arc; ZFTB: Zagros Fold-and-Thrust Belt. 52

**Figure 4.9.** Modelling results for B-B' profile. Red dots denote measured values and vertical dispersion bars with the standard deviation calculated on a strip of 50 km. Continuous blue lines represent the calculated values from the model. Dashed grey lines represent the transition between different chemical compositions or mantle domains. Numbers indicate different mantle composition (Table 4.1). Discontinuous lines indicate Moho and/or LAB geometry by Molinaro et al. (2005) (purple), Motavalli-Anbaran et al. (2011) (profile III, black), and Jiménez-Munt et al. (2012) (red). HZF: High Zagros Fault; IZ: Imbricated Zone; MFF: Main Frontal Fault; MZF: Main Zagros Fault; SSZ: Sanandaj Sirjan Zone; UDMA: Urumieh Dokhtar Magmatic Arc; ZFTB: Zagros Fold-and-Thrust Belt. 53

**Figure 4.10.** A-A' profile. (a) P-wave mantle velocity distribution; (b) P-wave seismic velocity anomaly with respect to AK135 reference velocity model (Kennett et al., 1995); (c) S-wave mantle velocity distribution; (d) S-wave seismic velocity anomaly with respect to AK135 reference velocity model (Kennett et al., 1995). Numbers along dashed line (in panel a) represent velocity values from tomography model by Simmons et al. (2011). 54

**Figure 4.11.** B-B' profile. (a) P-wave mantle velocity distribution; (b) P-wave seismic velocity anomaly with respect to AK135 reference velocity model (Kennett et al., 1995); (c) S-wave mantle velocity distribution; (d) S-wave seismic velocity anomaly with respect to AK135 reference velocity model (Kennett et al., 1995). Numbers along dashed blue and black lines represent velocity values from tomography model by Simmons et al. (2011) (panel a) and from Kaviani et al. (2007) (panel c). 55

**Figure 4.12.** Calculated Bouguer and geoid anomalies, elevation, and seismic velocities for different lithospheric mantle compositions (Archean, Proterozoic, Phanerozoic) along the A-A' profile. Grey dots with error bars indicate the geophysical observables. Velocity profiles correspond to are calculated at 400 km (top right) and 800 km (bottom right) from the beginning of the profile. 58

**Figure 5.1.** Tectonic map of the Himalaya-Tibetan Plateau and surrounding areas and Moho data from previous studies (color-coded symbols). Thick grey lines show the location of C-C' and D-D' profiles. Black stars indicate mantle xenolith suites localities from Bagdassarov et al. (2011) and Song et al. (2007) considered in this study. ATF: Altyn Tagh Fault; BNS: Bangong Nujiang Suture; CAO: Central Asia Orogenic Belt; HFF: Himalaya Frontal Front; ITS: Indus-Tsangpo Suture; JS: Jinsha Suture; KF: Karakorum Fault; KS: Kunlun Suture (or Kunlun fault); MBT: Main Boundary Thrust; MCT: Main Central Thrust; NBT: North Border Thrust; NTST: Northern Tian Shan Thrust; S.-G.: Songpan-Ganzi; STST: Southern Tian Shan Thrust. 66

**Figure 5.2.** Geophysical observables in the study region. a) Topography; b) Bouguer anomaly calculated from global free-air anomaly (Sandwell and Smith, 1997) with 3D topographic correction; c) geoid height from filtered EGM2008 model; d) heat flow measurements from global dataset (Pollack et al., 1993). 68

**Figure 5.3.** P-wave seismic tomography image along C-C' profile (see location on Figure 5.1) White circles represent the earthquakes used in the tomography (Engdhal et al., 1998). Contour lines interval: 1%. Global reference model used - AK135 (Kennett et al., 1995). HFF: Himalaya Frontal Fault; MCT: Main Central Thrust; NTST: Northern Tian Shan Thrust; STST: Southern Tian Shan Thrust. 73

**Figure 5.4.** Crustal model of C-C' profile. Physical properties of the crustal bodies (numbers) are reported in Table 5.2. HFF: Himalaya Frontal Fault; ITS: Indus-Tsangpo Suture; JS: Jinsha Suture; KF: Karakorum Fault; MCT: Main Central Thrust; NTST: Northern Tian Shan Thrust; NTSF: Northern Tian Shan Fault; STST: Southern Tian Shan Thrust; ZSZ: Zaskar Shear Zone. 77

- Figure 5.5.** Modelling results along C-C' profile. Red dots represent the data and vertical dispersion bars the standard deviation calculated on a strip of 50 km for gravity, geoid and topography, and on a strip of 500 km for surface heat flow. Yellow and green dots are mean heat flow values from Wang (2001) and An and Shi (2007), respectively. Continuous blue lines represent the calculated observables from the model. Thick horizontal bars are temperatures from different studies ([A] An and Shi, 2007; [B] Liu et al., 2004; [C] Bagdassarov et al., 2011). Numbers indicate different mantle bodies defined by their own NCFMAS composition (Table 5.3). HFF: Himalaya Frontal Fault; MCT: Main Central Thrust; NTST: Northern Tian Shan Thrust; STST: Southern Tian Shan Thrust. 80
- Figure 5.6.** Resulting distribution of mantle seismic velocities and mantle seismic velocity anomalies for both P- and S-waves along C-C' profile. Velocity anomalies are calculated respect to the column at 2100 km from the beginning of the profile. 82
- Figure 5.7.** Modelling results along D-D' profile. Only small differences in the Moho depth have been applied to update the crustal thickness values of the previous model by Jiménez-Munt et al. (2008) (dashed line) with the most recent data (see text for details). Thick horizontal bars are temperatures taken from: [A] Priestley and McKenzie (2006); [B] An and Shi (2007); [C] Galve et al. (2006); [D] Mechie et al. (2004); [E] Hacker et al. (2000). BNS: Bangong Nujiang Suture; HFF: Himalaya Frontal Fault; ITS: Indus-Tsangpo Suture; JS: Jinsha Suture; KS: Kunlun Suture; NBT: North Border Thrust. 84
- Figure 5.8.** D-D' profile. (a) P-wave mantle velocities; (b) mantle velocity anomalies calculated respect to the selected column at 1500 km from the beginning of the profile; (c) P-wave seismic tomography image (see text for details). 85
- Figure 5.9.** Simplified 3D diagram showing the resulting crustal and lithospheric structures from our modelling along the two studied profiles, superimposed to the seismic tomography. The Figure on the right lower corner is modified from Figure 1 in Jiménez-Munt et al. (2008). 87
- Figure 5.10.** Density and P-wave velocity variations on depth for each composition, considering a flat model with parallel layers, where Moho and LAB discontinuities are located at 42 km and 210 km depth, respectively. Mantle composition names refer to Table 5.3. 88
- Figure 6.1.** Plate boundaries (black thin lines) in the Central Asia region from PB2002 plate model (Bird, 2003). Colours indicate surface topography from ETOPO1 model (Amante and Eakins, 2009). ATF: Altn Tagh Fault; DSF: Dead Sea Fault; MBT: Main Boundary Thrust; MFF: Main Frontal Front; MPT: Main Pamir Thrust; MZF: Main Zagros Fault; NAF: North Anatolia Fault; RRF: Red River Fault; SF: Sagaing Fault; XXF: Xiangshuihe-Xiaojiang Fault. 98
- Figure 6.2.** Finite element grid and faults in the study region. Plate boundaries (thin black lines) and plate names (bold characters) derive from PB2002 plate model (Bird, 2003). AIF: Arabia-India transform Fault; ATF: Altn Tagh Fault; BFF: Burmese Fold Belt; CF: Chaman Fault; CIT: Central Iran Thrust; DSF: Dead Sea Fault; GTF: Gobi-Tian Shan Fault; HRF: Herat Fault; IMTB: Indus-Makran thrust belt; KF: Karakorum Fault; KS: Kunlun Suture (or Kunlun Fault); LST: Longmen Shan Thrust; MBT: Main Boundary Thrust; MFF: Main Frontal Front; MPT: Main Pamir Thrust; MZF: Main Zagros Fault; NAF: North Anatolia Fault; NBT: North Border thrust; NF: Nayband fault; RRF: Red River Fault; SF: Sagaing Fault; SIF: Sistan Fault; TF: Talas-Fergana fault; TST: Tian Shan Thrust; WKT: Western Kunlun Thrust; XXF: Xiangshuihe-Xiaojiang Fault. 99
- Figure 6.3.** Input data for the neotectonic model. (a) Crustal thickness; (b) Lithosphere (crust + lithospheric mantle) thickness and (c) Surface heat flow in the Central Asia, derived from the combination of elevation, geoid anomaly and thermal analysis (Robert et al., 2015). Refer to the caption of Figure 6.2 for the fault names. 101

- Figure 6.4.** Velocity boundary conditions calculated using the Euler poles of Table 6.1 (Eurasia-fixed reference frame). 104
- Figure 6.5.** GPS velocities in the Eurasia reference frame. Note the more rapid convergence of India than Arabia with respect Eurasia, and the rapid westward escape of north-western Arabia, and the eastward and southward extrusion of material from the eastern Tibetan Plateau around the eastern Himalaya syntaxis. 105
- Figure 6.6.** Distribution of earthquake with  $M > 3$  from Enghdal seismic catalogue (Enghdal et al. 1998). Colours indicate the depth of the seismic events and the size indicates the magnitude. The maximum magnitude in the Central Asia region is  $M=7.9$ . Two larger earthquakes of magnitude  $M=8.6$  and  $M=9.0$  are located in the subduction zone south of Burma, at  $2^\circ\text{N}$  and  $3^\circ\text{N}$  latitudes respectively. 106
- Figure 6.7.** Stress data compilation in the Central Asia region extracted from the World Stress Map WSM2008 (Heidbach et al., 2008). Data have been filtered to quality C (stress orientations are accurate to within  $25^\circ$ ). Depths are less than 50 km. 108
- Figure 7.1.** Finite element grid, fault traces and kinematic setting of the reference model. Coastline is shown in blue. Tectonic plate boundaries are shown in thin black line. 110
- Figure 7.2.** Vertical integral of viscosity in the study region for the reference model. Modelling parameters used are show in Table 7.1. Friction coefficient on faults is  $\mu_f=0.1$ . ATF: Altyn Tagh Fault; DSF: Dead Sea Fault; MBT: Main Boundary Thrust; MFF: Main Frontal Front; MPT: Main Pamir Thrust; MZF: Main Zagros Fault; NAF: North Anatolia Fault; RRF: Red River Fault; SF: Sagaing Fault; XXF: Xiangshuihe-Xiaojiang Fault. 111
- Figure 7.3.** Long-term-average anelastic strain rate field. Straining due to slip rates of fault elements is not included. Coloured background shows logarithm of the magnitude of the greatest strain rate. Overlying icons show total strain rate tensor. The fault symbols are sized with an area proportional to the strain rate. Friction coefficient on faults is  $\mu_f=0.1$ . TF = thrust faulting; SS = strike-slip faulting; NF = normal faulting. 112
- Figure 7.4.** a) Surface velocity field respect to the Eurasia plate predicted by the reference model. b) Predicted surface velocities by the model (yellow) and GPS velocities (purple, references in Section 6.4). Friction coefficient on faults is  $\mu_f=0.1$ . 113
- Figure 7.5.** Directions of the most-compressive horizontal principal stresses predicted by the reference model (thinner lines), and stress data from WSM2008 (thicker lines, Heidbach et al., 2008). Friction coefficient on faults is  $\mu_f = 0.1$ . 114
- Figure 7.6.** Vertical integral of viscosity in the “soft-rheology model”. Friction coefficient on faults  $\mu_f=0.1$ . ATF: Altyn Tagh Fault; DSF: Dead Sea Fault; MBT: Main Boundary Thrust; MFF: Main Frontal Front; MPT: Main Pamir Thrust; MZF: Main Zagros Fault; NAF: North Anatolia Fault; RRF: Red River Fault; SF: Sagaing Fault; XXF: Xiangshuihe-Xiaojiang Fault. 115
- Figure 7.7.** Strain-rate field, using the soft rheology detailed in Table 7.2. Coloured background shows logarithm of the magnitude of the greatest strain rate. Overlying icons show total strain rate tensor. The fault symbols are sized with an area proportional to the strain rate. Friction coefficient on faults  $\mu_f=0.1$ . TF = thrust faulting; SS = strike-slip faulting; NF = normal faulting. 117
- Figure 7.8.** a) Surface velocity field respect to the Eurasia plate predicted by the “soft-rheology” model. b) Predicted surface velocities by the model (yellow) and GPS velocities (purple, see references in Section 6.4). Friction coefficient on faults is  $\mu_f=0.1$ . 118

- Figure 7.9.** Direction of the most compressive horizontal principal stresses predicted by the model (thinner lines), using the soft rheology detailed in Table 7.2, and stress data from WSM2008 (thicker lines, Heidbach et al., 2008). Friction coefficient on faults is  $\mu_f=0.1$ . 119
- Figure 7.10.** Model with a thin lithosphere (LAB at 120 km depth) in the north-eastern Tibetan Plateau (dashed-line bordered area), and with  $\mu_f=0.1$ . a) Lithosphere thickness; b) lithosphere density anomalies (with respect to the input density parameters, Table 7.1) attributed to compositional heterogeneities; c) strain rate. Refer to caption of Figure 7.2 for fault names. 121
- Figure 7.11.** Predicted surface velocity in a model with a thin lithosphere (LAB at 120 km depth) in the north-eastern Tibetan Plateau (dashed line bordered area), and with  $\mu_f=0.1$ . 122
- Figure 7.12.** Model scores against geodetic velocities (triangles) and stress direction (squares) data for different  $\mu_f$  in the (a) Arabia-Eurasia and (b) India-Eurasia collision zones. 122
- Figure 7.13.** Simplified scheme of the tectonic setting in the south-eastern part of the Central Asia region. White arrows indicate the approximate direction of Indian and Sunda plates' motion with respect to Eurasia. The black star on the right figure indicates the location of the Sumatra-2004 earthquake. S.F.: Sagaing Fault. 123
- Figure 7.14.** Different boundary conditions in south-eastern Asia. BCS1 and BCS2 indicate southward-directed Sunda plate velocities with values between 12-12.3 mm/yr; BCS3 shows south-westward velocities in Burma region, with values between 4.8-5.1 mm/yr. In the rest, the boundary condition is motion free or according to the Euler pole of the tectonic plate of the boundary. ATF: Altyn Tagh Fault; KF: Karakorum fault; KS: Kunlun suture or fault; LST: Longmen Shan Thrust; RRF: Red River Fault; SF: Sagaing Fault; XXF: Xiangshuihe-Xiaojiang Fault. 125
- Figure 7.15.** Most compressive horizontal principal stresses, using the parameters detailed in Table 7.1 and with  $\mu_f=0.05$ , with different boundary conditions (BCS type referred to Figure 7.14) and the lithosphere structure from the reference model (see Figure 6.3). 126
- Figure 7.16.** Predicted velocity field for different boundary conditions (refer to Figure 7.14) and under the same conditions than in Figure 7.15 (assuming a friction coefficient on faults of 0.05 and a lithosphere structure as in the reference model). 127
- Figure 8.1.** Flow lines (main directions) of the velocity field in the Central Asia (referred to Eurasia) as inferred by GPS measurements (coloured arrows; see legend in Figure 6.5). 130
- Figure 8.2.** Cartoon of the interaction and deformation of the lithosphere in the south-eastern Tibetan Plateau, modified from Chen et al. (2014). Solid arrows illustrate the direction of the forces acting upon (white) and within (yellow) the lithosphere. Black dashed arrow on the topographic surface indicates the direction of the crust flow. Thin dashed arrows represent the sublithospheric mantle flow. Localization figure (on the left) modified from Tapponnier et al. (2001). 133
- Figure 9.1.** Scheme to summarize the results on the lateral compositional variations within the lithospheric mantle obtained beneath the Arabia-Eurasia (A-A' and B-B' profiles) and India-Eurasia (C-C' and D-D' profiles) collision zones. Composition colour for the asthenosphere domain (i.e. Primitive Upper mantle) has been omitted for clarity. 139

<b>Table 3.1.</b> Lithospheric mantles are classified into Archons, Protons and Tectons in terms of the tectonothermal age (Janse, 1994; Griffin et al., 2003). Bulk compositions, expressed in weight %, come from Griffin et al. (2008) and references therein. PUM: Primitive Upper Mantle.	33
<b>Table 4.1.</b> Chemical compositions used in the models for mantle bodies (see Figures 4.8 and 4.9).	47
<b>Table 4.2.</b> Physical properties of the materials used in the modelling: depth-varying density $\rho$ ; thermal conductivity $K$ ; radiogenic heat production $H$ . The heat production in the lithospheric mantle is $0.02 \mu\text{W}/\text{m}^3$ .	49
<b>Table 4.3.</b> The RMSE between measurements and calculated data for the profiles A-A' and B-B' (see Figures 4.8 and 4.9) and test models (see Figure 4.12 in Section 4.2.3)	50
<b>Table 4.4.</b> Chemical compositions used in test models for mantle bodies (Figure 4.12).	59
<b>Table 5.1.</b> Lithology and structural relations among the different terrains along C-C' profile.	70
<b>Table 5.2.</b> Physical properties of the different tectonic units used in the crustal model of Figure 5.4: depth-varying density $\rho$ ; thermal conductivity $K$ ; depth-varying radiogenic heat production $H$ ; $z$ is the depth in km. UC: upper crust; MC: middle crust; LC: lower crust.	75
<b>Table 5.3.</b> Major elements composition in the NCFMAS system for the lithospheric mantle and asthenosphere domains used in the modelling (Figures 5.5 and 5.7). Mantle 2 and Mantle 4 derive from published petrological studies on mantle xenoliths. Gt: garnet; Lherz.: Lherzolite; Sp: Spinel.	79
<b>Table 5.4.</b> The RMSE (Eq. 4.1) between measurements and calculated data for eastern profile (see explanations in the text).	86
<b>Table 6.1.</b> Euler poles from Liu and Bird (2008) of the 5 tectonic plates in the Central Asia region referred to the fixed Eurasia plate.	103
<b>Table 7.1.</b> Model parameters.	110
<b>Table 7.2.</b> Rheological parameters used in the model.	115



## References

- Adams, A., R. Brazier, A. Nyblade, A. Rodgers, and A. Al-Amri (2009), Source parameters for moderate earthquakes in the Zagros mountains with implications for the depth extent of seismicity, *Bull. Seis. Soc. Am.*, 99, 2044–2049.
- Afonso, J.C., G. Ranalli, M. Fernandez (2005), Thermal expansivity and elastic properties of the lithospheric mantle: results from mineral physics of composites, *Phys. Earth Int.*, 149, 279-306.
- Afonso, C., M. Fernandez, G. Ranalli, W.L. Griffin, J.A.D. Connolly (2008), Integrated geophysical-petrological modeling of the lithosphere and sub-lithospheric upper mantle: methodology and applications, *Geochem. Geophys. Geosyst.*, v.9, Q05008, doi:10.1029/2007GC001834.
- Afonso, J.C., and S. Zlotnik (2011), The subductability of the continental lithosphere: the before and after story, in *Arc-continent collision*, *Frontiers in Earth Sciences* edited by D. Brown and P.D. Ryan, 53-86, doi:10.1007/978-3-540-88558, Springer.
- Afonso, J.C., J. Fullea, W.L. Griffin, Y. Yang, A.G. Jones, J.A.D. Connolly, S.Y. O'Reilly, (2013a), 3-D multi-observable probabilistic inversion for the compositional and thermal structure of the lithosphere and upper mantle. I: a priori petrological information and geophysical observables, *J. Geophys. Res.*, 118, 2586-2617.
- Afonso, J.C., J. Fullea, Y. Yang, J.A.D. Connolly, A.G. Jones, (2013b), 3-D multi-observable probabilistic inversion for the compositional and thermal structure of the lithosphere and upper mantle. II: General methodology and resolution analysis, *J. Geophys. Res.*, 118, 1650-1676.
- Agard, P., P. Monié, W. Gerber, J. Omrani, M. Molinaro, B. Meyer, L. Labrousse, B. Vrielynck, L. Jolivet, and P. Yamato (2006), Transient, synobduction exhumation of Zagros blueschists inferred from P-T, deformation, time, and kinematic constraints: Implications for Neotethyan wedge dynamics, *J. Geophys. Res.*, 111, B11401, doi:10.1029/2005JB004103.
- Agard, P., J. Omrani, L. Jolivet, H. Whitechurch, B. Vrielynck, W. Spakman, P. Monié, B. Meyer, and R. Wortel, (2011), Zagros orogeny: a subduction-dominated process, in: *Geodynamic Evolution of the Zagros*, pp. 692–725, Lacombe, O., Grasemann, B., Simpson, G. (Eds.), *Geol. Magazine*.
- Agius, M. R. and S. Lebedev (2013), Tibetan and Indian lithospheres in the upper mantle beneath Tibet: Evidence from broadband surface-wave dispersion, *Geochem. Geophys. Geosyst.*, 14, doi:10.1002/ggge.20274.
- Alinaghi, A., I. Kolakov, and H. Thybo, (2007), Seismic tomographic imaging of P- and S-waves velocity perturbations in the upper mantle beneath Iran, *Geophys. J. Int.*, 169, 1089– 1102, doi: 10.1111/j.1365-246X.2007.03317.x.
- Allen, M., M.R. Ghassemi, M. Shahrabi and M. Qorashi, M. (2003), Accommodation of late Cenozoic oblique shortening in the Alborz range, northern Iran, *J. Struct. Geol.*, 25 (5), 659–672.
- Amante, C. and B.W. Eakins (2009), ETOPO1 Arc-Minute Global Relief model: Procedures, Data Sources and Analysis, NOAA Technical Memorandum NESDIS NGDC-24, 19 pp. Available at: <http://www.ngdc.noaa.gov>

- An, M. and Y. Shi (2006), Lithospheric thickness of the Chinese continent, *Physics of the Earth and Planetary Interiors*, 159, 257-266.
- An, M. and Y. Shi (2007), Three-dimensional thermal structure of the Chinese continental crust and upper mantle, *Science China Earth Science*, 50, 10, 1441-1451.
- Anderson, O.L. and D.G. Isaak (1995), Elastic constants of mantle minerals at high temperature. In: Ahrens TJ (ed.) *Handbook of Physical Constants*, vol. 3, pp. 64–96. Washington, DC, American Geophysical Union.
- Artemieva, I. M (2006), Global 1 x 1 thermal model TC1 for the continental lithosphere: implications for lithosphere secular evolution, *Tectonophysics*, 426, 245-277.
- Audet, P. and R. Bürgmann (2011), Dominant role of tectonic inheritance in super-continent cycles, *Nature geoscience*, 4, 184–187.
- Austermann, J. and G. Iaffaldano (2013), The role of the Zagros orogeny in slowing down Arabia-Eurasia convergence since ~5 Ma, *Tectonics*, 32, doi:10.1002/tect.20027.
- Bagdassarov, N., V. Batalev, V. Egorova (2011), State of lithosphere beneath Tien Shan from petrology and electrical conductivity of xenoliths, *J. Geophys. Res.*, 116, B01202, doi:10.1029/2009JB007125
- Ballato, P and M. R. Strecker (2014), Assessing tectonic and climatic causal mechanisms in foreland-basin stratal architecture: insights from the Alborz Mountains, northern Iran, *Earth Surf. Process Landforms*, 39, 110–125.
- Barba, S., M.M.C. Carafa, M.T. Mariucci, P. Montone, S. Pierdominici (2010), Present-day stress-field modelling of southern Italy constrained by stress and GPS data, *Tectonophysics* 482, 193–204.
- Barron, J. and Priestley K (2009) Observations of frequency-dependent Sn propagation in northern Tibet. *Geophys. J. Int.* 179:474–488.
- Beydoun, Z.R., M.W.H. Clarke, R. Stoneley (1992), Petroleum in the Zagros Basin; a late Tertiary foreland basin overprinted onto the outer edge of a vast hydrocarbon-rich Paleozoic–Mesozoic passive-margin shelf, In: Macqueen, R.W., Leckie, D.A. (Eds.), *Foreland Basins and Fold Belts*, pp. 309–339.
- Berberian, F. and M. Berberian (1981), Tectono-plutonic episodes in Iran, In: Gupta, H.K., Delany, F.M. (Eds.), *Zagros–Hindu Kush–Himalaya Geodynamic Evolution*, American Geophysical Union & Geological Society of America, Washington, pp. 5–32.
- Berberian, M. and G.C.P. King (1981), Towards a paleogeography and tectonic evolution of Iran, *Can. J. Earth Sc.*, 18 (2).
- Berberian, F., I.D. Muir, R.J. Pankhurst, M. Berberian (1982), Late Cretaceous and early Miocene Andean-type plutonic activity in northern Makran and Central Iran, *Journal of Geol. Soc. London*, 139, 605–614.

- Bettinelli, P., J.-P. Avouac, M. Flouzat, F. Jouanne, L. Bollinger, P. Willis, and G. R. Chitrakar (2006), Plate motion of India and interseismic strain in the Nepal Himalayan from GPS and DORIS measurements, *J. Geod.*, 80, 567–589, doi:10.1007/s00190-006-0030-3.
- Bijwaard, H., W. Spakman, E. R. Engdahl (1998), Closing the gap between regional and global travel time tomography, *J. Geophys. Res.*, 103, 30055–30078.
- Bird, P. (1978), Finite element modeling of lithosphere deformation: the Zagros collision orogeny, *Tectonophysics*, 50, 307–336.
- Bird, P. (1999), Thin-plate and thin-shell finite element programs for forward dynamic modeling of plate deformation and faulting, *Comput. Geosci.*, 25, 383–394.
- Bird, P., Kong, X., 1994. Computer simulations of California tectonics confirm very low strength of major faults. *Geol. Soc. Amer. Bull.* 106, 159–174.
- Bird, P. (2003), An updated digital model of plate boundaries, *Geochem., Geophys., Geosys.*, 4(3), doi:10.1029/2001GC000252.
- Bird, P., Z. Liu, and W. K. Rucker (2008), Stresses that drive the plates from below: Definitions, computational path, model optimization, and error analysis, *J. Geophys. Res.*, 113, B11406, doi:10.1029/2007JB005460.
- Bonini, M., G. Corti, D. Sokoutis, G. Vannucci, P. Gasperini, S. Cloetingh (2003), Insights from scaled analogue modelling into the seismotectonics of the Iranian region, *Tectonophysics*, 376, 137–1493.
- Bowin, C. (2000), Mass anomalies and the structure of the Earth, *Phys. Chem. Earth*, 25 (4), 343–353.
- Braitenberg, C., M. Zadro, J. Fang, Y. Wang, H.T. Hsu (2000), Gravity inversion in Qinghai-Tibet Plateau, *Physics and Chemistry of the Earth, Part A: Solid Earth and Geodesy*, 25 (4), 381–386.
- Braitenberg, C., Y. Wang, J. Fang, H.T. Hsu (2003), Spatial variations of flexure parameters over the Tibet-Qinghai plateau, *Earth Planet. Science Lett.*, 205, 211–224.
- Braun, I. and L.M. Kriegsman (2003), Proterozoic crustal evolution of southern most India and Sri Lanka, In: Yoshida, M., Windley, B.F., Dasgupta, S. (Eds.), *Proterozoic East Gondwana: Supercontinent Assembly and Breakup*. The Geological Society of London Special Pub, 206, 169–202. doi: <http://dx.doi.org/10.1144/GSL.SP.2003.206.01.10>.
- Briaux, A., Ph. Patriat, P. Tapponnier (1993), Updated interpretation of magnetic anomalies and seafloor spreading stages in the South China Sea, implications for the Tertiary tectonics of SE Asia, *J. Geophys. Res.* 98, 6299–6328.
- Burbidge, D.R. (2004), Thin plate neotectonic models of the Australian plate. *J. Geophys. Res.* 109, B10405. doi:10.1029/2004JB003156.
- Burg, J.-P., D. Bernoulli, J. Smit, A. Dolati, and A. Bahroudi (2008), A giant catastrophic mud-and-debris flow in the Miocene Makran, *Terra Nova*, 20, 188–193, doi:10.1111/j.1365-3121.2008.00804.x.

- Burtman, V. S., and P. Molnar (1993), Geological and geophysical evidence for deep subduction of continental crust beneath the Pamir, Geological Society of America, Special Paper, 281, pp. 76, Boulder, Colorado.
- Byrne, D.E., L.R. Sykes and D.M. Davis (1992), Great thrust earthquakes and aseismic slip along the plate boundary of the Makran subduction zone, *J. Geophys. Res.*, 97, 449–478.
- Calais, E., M. Vergnolle, V. Sankov, A. Lukhnev, A. Miroshnitchenko, S. Amarjargal, and J. Deverchere (2003), GPS measurements of crustal deformation in the Baikal-Mongolia area (1994–2002): Implications for current kinematics of Asia, *J. Geophys. Res.*, 108(B10), 2501, doi:10.1029/2002JB002373.
- Calais, E., L. Dong, M. Wang, Z. Shen, and M. Vergnolle (2006), Continental deformation in Asia from a combined GPS solution, *Geophys. Res. Lett.*, 33, L24319, doi:10.1029/2006GL028433.
- Capitanio, F. A. (2014), The dynamics of extrusion tectonics: Insights from numerical modeling, *Tectonics*, 33, 2361–2381, doi:10.1002/2014TC003688.
- Carballo, A., M. Fernandez, M. Torne, I. Jimenez-Munt, and A. Villaseñor, (2014), Thermal and petrophysical characterization of the lithospheric mantle along the northeastern Iberia geo-Transect, *Gondwana Research*, doi: 10.1016/j.gr.2013.12.012
- Casciello, E., J. Vergés, E. Saura, G. Casini, M. Fernandez, E. Blanc, S. Homke and D. Hunt, (2009), Fold patterns and multilayer rheology of the Lurestan Province, Zagros Simply Folded Belt (Iran), *Geol. Soc. London*, 166, 1-13, DOI 10.1144/0016-7649.2008-1138.
- Ceylan, S., J. Ni, J. Y. Chen, Q. Zhang, F. Tilmann, E. Sandvol (2012), Fragmented Indian plate and vertically coherent deformation beneath eastern Tibet, *J. Geophys. Res.*, 117, B11303, doi:10.1029/2012JB009210.
- Charvet J., L.S. Shu, S. Laurent-Charvet, B. Wang, F. Michel, C. Dominique, Y. Chen, D.J. Koen (2011), Paleozoic tectonic evolution of the Tianshan belt, NW China, *Science China Earth Science* 54(2):166–184.
- Chatelain, J.L., Roecker, S.W., Hatzfeld, D., Molnar, P., 1980. Microearthquake seismicity and fault plane solutions in the Hindu Kush region and their tectonic implications. *Journal of Geophysical Research* 85, 1365–1387.
- Chen, W., Yang, Z., 2004. Earthquakes beneath the Himalayas and Tibet: evidence for strong lithospheric mantle. *Science* 304, 1949–1952.
- Chen, W.-P., and T.-L. Tseng (2007), Small 660-km seismic discontinuity beneath Tibet implies resting ground for detached lithosphere, *J. Geophys. Res.*, 112, B05309, doi:10.1029/2006JB004607.
- Chen, M.-M., W. Tian, K. Suzuki, M.-L.-G. Tejada, F.L. Liu, R. Senda, C.-J. W., B. Chen, Z.Y. Chu (2014), Peridotite and pyroxenite xenoliths from Tarim, NW China: Evidences for melt depletion and mantle refertilization in the mantle source region of the Tarim flood basalt, *Lithos*, <http://dx.doi.org/10.1016/j.lithos.2014.01.005>.

- Chen, B., J. Liu, M.K. Kaban, Y. Sun, C. Chen, J. Du (2014b), Elastic thickness, mechanical anisotropy and deformation of the southeastern Tibetan Plateau, *Tectonophysics*, 637, 45–56, <http://dx.doi.org/10.1016/j.tecto.2014.09.007>.
- Chetty, T.R.K. and M. Santosh (2013), Proterozoic orogens in southern Peninsular India: contiguities and complexities, *J. Asian Earth Sci.*, 78, 39–53.
- Chung, S.L., M. F. Chua, Y. Zhang, Y. Xie, C. Lo, T.Y. Lee, C.Y. Lan, X. Li, Q. Zhang, Y. Wang (2005), Tibetan tectonic evolution inferred from spatial and temporal variations in post-collisional magmatism, *Earth-Science Reviews*, 68, 173–196.
- Connolly, J. (2005), Computation of phase equilibria by linear programming: a tool for geodynamic modeling and an application to subduction zone decarbonation, *Earth Planet. Science Lett.*, 236, 524–541.
- Cook, K. L., and L. H. Royden (2008), The role of crustal strength variations in shaping orogenic plateaus, with application to Tibet, *J. Geophys. Res.*, 113, B08407, doi:10.1029/2007JB005457.
- Cunha, T.A., Matias L.M., Terrinha P., Negredo A. M., Rosas F., Fernandes M.S., Pinheiro L. M., 2012, Neotectonics of the SW Iberia margin, Gulf of Cadiz and Alboran Sea: a reassessment including recent structural, seismic and geodetic data, *Geophys. J. Int.*, doi: 10.1111/j.1365-246X.2011.05328.x
- de la Torre, T. and A. Sheehan (2005), Broadband seismic noise analysis of the Himalayan Nepal Tibet seismic experiment, *Bull. Seismol. Soc. Am.*, 95, 1202–1208.
- DeCelles, P.G., D.M. Robinson, G. Zandt (2002), Implications of shortening in the Himalayan fold-thrust belt for uplift of the Tibetan Plateau, *Tectonics* 21, 286–299. doi:10.1029/2001tc001322.
- DeMets, C., R. G. Gordon, D. F. Argus, and S. Stein (1990), Current plate motions, *Geophys. J. Int.*, 101, 425–478, 1990.
- DeMets, C., R.G. Gordon, D. F. Argus (2010), Geologically current plate motions, *Geophys. J. Int.*, 181, 1–80, doi: 10.1111/j.1365-246X.2009.04491.x.
- Dewey, J. F., Robert M. Shackleton, C. Chengfa, S. Yiyin (1988), The tectonic evolution of the Tibetan plateau. *Phil. Trans. R. Soc. Lond.*, 327, 379–413.
- Eaton, D.W., F. Darbyshire, R.L. Evans, H. Grütter, A.G. Jones, and X. Yuan (2009), The elusive lithosphere-asthenosphere boundary (LAB) beneath cratons, *Lithos*, 109, 1–22.
- Egan, S. S., J. Mosar, M.-F. Brunet and T. Kangarli (2009), Subsidence and uplift mechanisms within the South Caspian Basin: Insights from the onshore and offshore Azerbaijan region, *Geol. Soc. Spec. Publ.*, 312, 219–240, doi:10.1144/SP312.11.
- Emami, H., J. Vergés, T. Nalpas, P. Gillespie, I. Sharp, R. Karpuz, E. J.-P. Blanc, E. and M.G.H. Goodarzi (2010), Structure of the Mountain Front Flexure along the Anaran anticline in the Pusht-e Kuh Arc (NW Zagros, Iran): insights from sand box models, in: *Tectonic and Stratigraphic Evolution of Zagros and Makran during the Mesozoic-Cenozoic*, eds. P. Leturmy & C. Robin, pp.155–78, *Geol. Soc. London Spec. Pub.* no. 330.

- England, P., and G. Housemann (1989), Extension during continental convergence, with application to the Tibetan Plateau, *J. Geophys. Res. Solid Earth*, 94, 17561-17579.
- England, P.C. and P. Molnar (1997), The field of crustal velocity in Asia calculated from Quaternary rates of slip on faults, *Geophys. J. Int.*, 130, 551–582.
- England, P. and P. Molnar (2005), Late Quaternary to decadal velocity fields in Asia, *J. Geophys. Res.*, 110, B12401, doi: 10.129/2004JB003541.
- Engdahl, E.R., R. van der Hilst, R.P. Buland (1998), Global teleseismic earthquake relocation with improved travel times and procedures for depth determination, *Bull. Seismol. Soc. Am.* 88, 3295-3314.
- Fan, G., Ni, J.F., Wallace, T.C. (1994), Active tectonics of the Pamirs and Karakorum, *J. Geophys. Res.*, 99, 7131–7160.
- Fischer, K. M., H.A. Ford, D.L. Abt, C.A. Rychert (2010), The lithosphere-asthenosphere boundary, *Annual Review of Earth and Planetary Sciences*, 38, 551–575, doi:10.1146/annurev-earth-040809-152438.
- Förster, A., H.J. Förster, R. Masarweh, A. Masri and K. Tarawneh (2007), The surface heat flow of the Arabian Shield in Jordan, *Journal of Asian Earth Sciences*, 30, 271-284.
- Fullea, J., M. Fernandez, H. Zeyen, (2008), FA2BOUG - A FORTRAN 90 code to compute Bouguer gravity anomalies from gridded free-air anomalies: Application to the Atlantic-Mediterranean transition zone, *Computers & Geosciences*, 34 (12), 1665-1681, ISSN:0098-3004, DOI: 10.1016/j.cageo.2008.02.018.
- Fullea, J., J.C. Afonso, J.A.D. Connolly, M. Fernandez, D. García-Castellanos, H. Zeyen (2009), LitMod 3D: An interactive 3D software to model the thermal, compositional, density, seismological, and rheological structure of the lithosphere and sublithospheric upper mantle, *Geochem, Geophys, Geosystem*, 10, 8, doi: 10.129/2009GC002391.
- Ghasemi, A. and C.J. Talbot (2006), A new tectonic scenario for the Sanandaj Sirjan Zone (Iran), *J. Asian Earth Science*, 26,683-693.
- Galve A., M. Jiang, A. Hirn, M. Sapin, M. Laigle, B. de Voogd, J. Gallart, H. Qian (2006), Explosion seismic P and S velocity and attenuation constraints on the lower crust of the North-Central Tibetan Plateau, and comparison with the Tethyan Himalayas: Implications on composition, mineralogy, temperature, and tectonic evolution, *Tectonophysics*, 412, 141-157.
- Gan, W., P. Zhang, Z.-K. Shen, Z. Niu, M. Wang, Y. Wan, D. Zhou, and J. Cheng (2007), Present-day crustal motion within the Tibetan Plateau inferred from GPS measurements, *J. Geophys. Res.*, 112, B08416, doi:10.1029/2005JB004120.
- Gaul, O.F., W.L. Griffin, S.Y. O'Reilly, N.J. Pearson, N.J. (2000), Mapping olivine composition in the lithospheric mantle, *Earth Planet. Science Lett.*, 182, 223–235.
- Ghosh, A., W. E. Holt, L. M. Flesch, and A. J. Haines (2006), Gravitational potential energy of the Tibetan Plateau and the forces driving the Indian Plate, *Geology*, 34(5), 321–324.

- Giardini, D., G. Grunthal, K. Shedlock, and P. Zhang (1999), Global Seismic Hazard Map, 1:35,000,000, Global Seismic Hazard Assessment Program, UN/International Decade of Natural Disaster Reduction, International Lithosphere Program (Available at <http://seismo.ethz.ch/GSHAP>)
- Gök, R., H. Mahdi, H. al-Shukri and A. Rodgers (2008), Crustal structure of Iraq from receiver functions and surface wave dispersion; implications for understanding the deformation history of the Arabian-Eurasian collision, *Geophys. J. Int.*, 172, 1179-1187.
- Gordon, S.M., P. Luffi, B. Hacker, J. Valley, M. Spicuzza, R. Kozdon, P. Kelemen, L. Ratschbacher, V. Minaev (2012), The thermal structure of continental crust in active orogens: insight from Miocene eclogite and granulite xenoliths of the Pamir Mountains, *J. Metamorph. Geol.* 30, 413–434.
- Griffin, W., S.Y. O'Reilly, S.Y. Abe, S.Y., N. Aulbach, S. Davies, R.M. Pearson, N.J. Doyle, and B.J. Kivi (2003), The origin and evolution of Archean lithospheric mantle *Precambrian Research*, 127, pp. 19-41.
- Griffin, W.L., S.Y. O'Reilly, J.C. Afonso, G.C. Begg (2009), The composition and evolution of lithospheric mantle: a re-evaluation and its tectonic implications, *J. Petrology*, 50, 1185–1204.
- Gritto, R., M.S. Sibol, J.E. Siegel, H.A. Ghalib, Y. Chen, R.B. Herrmann, G.I. Alequabi, H. Tkalcic, B.S. Ali, B.I. Saleh, D.S. Mahmood, O.K. Shaswar, A. Mahmood, S. Abdullah, F. Ibrahim, R. Zand, B. Ali, L. Omar, N.I. Aziz, N.H. Ahmed, T. Al-Nasiri, A.A. Ali, A.A. Taqi, and S.R. Khalaf (2008), Crustal structure of North Iraq from receiver function analyses, in: *Monitoring Research Review: Ground-Based Nuclear Explosion Monitoring Technologies*.
- Grose, C. and J.C. Afonso (2013), Comprehensive plate models for the thermal evolution of oceanic lithosphere, *Geochem., Geophys. Geosyst.*, 14, 3751–3778, doi:10.1002/ggge.20232.
- Guillot, S., E. Garzanti, D. Baratoux, D. Marquer, G. Maheo, J. de Sigoyer (2003), Reconstructing the total shortening history of the NW Himalaya, *Geochem. Geophys. Geosyst.*, 4(7), 1064, doi:10.1029/2002GC000484
- Haines, S. S., S. L. Klemperer, L. Brown, J. Guo, J. Mechie, R. Meissner, A. Ross, W. Zhao (2003), INDEPTH III seismic data: From surface observations to deep crustal processes in Tibet, *Tectonics*, 22(1), 1001, doi:10.1029/2001TC001305.
- Hacker, B. R., E. Gnos, L. Ratschbacher, M. Grove, M. McWilliams, S. V. Sobolev, J. Wan and W. Zhenhan (2000), Hot and dry deep crustal xenoliths from Tibet, *Science*, 287, 2463–2466.
- Hacker, B., P. Luffi, V. Lutkov, V. Minaev, L. Ratschbacher, T. Plank, M. Ducea, A. Patino-Douce, M. McWilliams and J. Metcalf (2005), Near-ultrahigh pressure processing of continental crust: Miocene crustal xenoliths from the Pamir, *J. Petrol.*, 46, 1661-1687.
- Hansen, S.E., A.J. Rodgers, S.Y. Schwartz and A.M.S. Al-Amri (2007), Imaging ruptured lithosphere beneath the Red Sea and Arabian Peninsula, *Earth Planet. Science Lett.*, 259, 256-265.
- Hargrove, U.S., R.J. Stern, J.-L. Kimura, W.I. Manton and P.R. Johnson (2006), How juvenile is the Arabian–Nubian Shield? Evidence from Nd isotopes and pre-Neoproterozoic inherited zircon in the Birumq suture zone, Saudi Arabia, *Earth Planet. Science Lett.* 252, 308–326.

- Hatzfeld, D., and P. Molnar (2010), Comparisons of the kinematics and deep structures of the Zagros and Himalaya and of the Iranian and Tibetan plateaus and geodynamic implications, *Rev. Geophys.*, 48, RG2005, doi:10.1029/2009RG000304.
- Hawkesworth, C.J., D.G. Pearson, S.P. Turner, S.P. (1999), Chemical and temporal variations in the Earth's lithosphere, *Phil. Trans. Roy. Soc. London, A* 357, 647–669.
- Hearn, T. M. and J.F. Ni (1994), Pn velocities beneath continental collision zones: the Turkish-Iranian Plateau, *Geophys. J. Int.*, 117(2), 273–283.
- Heidbach, O., M. Tingay, A. Barth, J. Reinecker, D. Kurfeß, and B. Müller (2008), The 2008 release of the World Stress Map, <http://www.world-stress-map.org>, Helmholtz Centre Potsdam, Potsdam, Germany.
- Heki, K., S. Miyazaki, H. Takahashi, M. Kasahara, F. Kimata, S. Miura, N. F. Vasilenko, A. Ivaschenko, and K.-D. An (1999), The Amurian plate motion and current plate kinematics in eastern Asia, *J. Geophys. Res.*, 104, 29,147–29,155.
- Hetényi, G., R. Cattin, F. Brunet, L. Bollinger, J. Vergne, J.L. Nabelek, M. Diament (2007), Density distribution of the India plate beneath the Tibetan Plateau: Geophysical and petrological constraints on the kinetics of lower crustal eclogitization, *Earth Planet. Science Lett.*, 264, 226– 244.
- Hofmeister, A. M. (1999), Mantle values of thermal conductivity and the geotherm from phonon lifetimes, *Science*, 283, 1699–1706.
- Hofmeister, A. M. (2005), Dependence of diffusive radiative transfer on grain-size, temperature, and Fe-content: Implications for mantle processes, *J. Geodyn.*, 40, 51–72.
- Holbig, E. S., and T. L. Grove (2008), Mantle melting beneath the Tibetan Plateau: Experimental constraints on ultrapotassic magmatism, *J. Geophys. Res.*, 113, B04210, doi:10.1029/2007JB005149.
- Holland, T., and R. Powell (1998), An internally consistent thermodynamic data set for phases of petrological interest, *J. Metamorph. Geol.*, 16, 309–343.
- Hollingsworth, J., J. Jackson, R. Walker, and H. Nazari (2008), Extrusion tectonics and subduction in the eastern South Caspian region since 10 Ma, *Geology*, 36,763–766, doi:10.1130/G25008A.1
- Holt, W.E., N. Chamot-Rooke, X. Le Pichon, A.J. Haines, B. Shen-Tu and J. Ren (2000), Velocity field in Asia inferred from Quaternary fault slip rates and Global Positioning System observations, *J. Geophys. Res.*, 105(B8), 19185–19209.
- Homke, S., J. Vergés, J. Serra-Kiel, G. Bernaola, I. Sharp, M. Garcés, I. Montero-Verdú, R. Karpuz, M.H. Goodarzi (2009), Late Cretaceous–Paleocene formation of the proto-Zagros foreland basin, Lurestan Province, SW Iran, *Geological Society of America Bulletin* 121 (7–8), 963–978.
- Houseman, G.A. and P. England (1993), Crustal thickening versus lateral expulsion in the India-Asian continental collision, *J. Geophys. Res.*, 98, 12233-12249.
- Howe, T. C., and P. Bird (2010), Exploratory models of long-term crustal flow and resulting seismicity across the Alpine-Aegean orogen, *Tectonics*, 29, TC4023, doi:10.1029/2009TC002565.

- Huang, W.-C., J. F. Ni, F. Tilmann, D. Nelson, J. Guo, W. Zhao, J. Mechie, R. Kind, J. Saul, R. Rapine, and T. M. Hearn (2000), Seismic polarization anisotropy beneath the central Tibetan Plateau, *J. Geophys. Res.*, 105(B12), 27, 979-27,989, doi:10.1029/2000JB900339.
- Huang, J., and D. Zhao (2006), High-resolution mantle tomography of China and surrounding regions, *J. Geophys. Res.*, 111, B09305, doi:10.1029/2005JB004066.
- Jackson, J., H. Austrheim, D. McKenzie, K. Priestley (2004), Metastability, mechanical strength, and the support of mountain belts, *Geology*, 32, 625–628.
- Janse, A.J.A. (1994), Is Clifford's Rule still valid? Affirmative examples from around the world. In: Meyer, H.O.A., Leonardos, O. (Eds.), *Diamonds: Characterization, Genesis and Exploration*. Dept. Nacional da Prod. Mineral, Brazilia, pp. 215–235.
- Jiang, M., A. Galvé, A. Hirn, B. deVoogd, M. Laigle, H.P. Su, J. Diaz, J.C. Lepine, Y.X. Wang (2006), Crustal thickening and variations in architecture from the Qaidam Basin to the Qang Tang (North-Central Tibetan Plateau) from wide-angle reflection seismology, *Tectonophysics*, 412, 121–140.
- Jiménez-Munt, I., M. Fernandez, M. Torne, P. Bird (2001), The transition from linear to diffuse plate boundary in the Azores–Gibraltar region: results from a thin-sheet model, *Earth Planet. Sci. Lett.*, 192, 175 – 189.
- Jiménez-Munt, I. and R. Sabadini (2002), The block-like behaviour of Anatolia envisaged in the modeled and geodetic strain rates, *Geophys. Res. Lett.*, 29(30), 1978, doi: 10.129/2002GL015995.
- Jiménez-Munt, I., R. Sabadini, A. Gardi, G. Bianco (2003), Active deformation in the Mediterranean from Gibraltar to Anatolia inferred from numerical modeling and geodetic and seismological data, *J. Geophys. Res.*, 108, doi:10.1029/2001JB001544.
- Jiménez-Munt, I., D. Garcia-Castellanos, M. Fernandez (2005), Thin-sheet modelling of lithospheric deformation and surface mass transport, *Tectonophysics*, 407, 239-255, doi:10.1016/j.tecto.2005.08.015.
- Jiménez-Munt, I. and J. P. Platt (2006), Influence of mantle dynamics on the topographic evolution of the Tibetan Plateau: Results from numerical modeling, *Tectonics*, 25, TC6002, doi: 10.1029/2006TC001963.
- Jiménez-Munt I., M. Fernandez, J. Vergés, J.P. Platt (2008), Lithosphere structure underneath the Tibetan Plateau inferred from elevation, gravity and geoid anomalies, *Earth Planet. Science Lett.*, 267, 276-289. doi:10.1016/j.epsl.2007.11.045.
- Jiménez-Munt, I., M. Fernandez, E. Saura, J. Vergés, J. and D. García-Castellanos (2012), 3D lithospheric structure and regional/residual Bouguer anomalies from Arabia-Eurasia collision (Iran), *Geophys. J. Int.*, 190, 1311–1324, doi:10.1111/j.1365-246X.2012.05580.x
- Ju, W. and G. Hou (2014), Late Permian to Triassic intraplate orogeny of the southern Tianshan and adjacent regions, NW China, *Geoscience Frontiers*, 5, 83-93.
- Kao, H., R. Gao, R-J Rau, D. Shi, R-Y Chen, T. Guan and F.T. Wu (2001), Seismic image of the Tarim basin and its collision with Tibet, *Geology*, 29, 575–578.

- Kaviani, A., A. Paul, E. Bourova, D. Hatzfeld, H. Pedersen and M. Mokhtari (2007), A strong seismic velocity contrast in the shallow mantle across the Zagros collision zone (Iran), *Geophys. J. Int.*, 171, 399–410, doi: 10.1111/j.1365-246X.2007.03535.x
- Kennett, B.L.N., E.R. Engdahl and R. Buland (1995), Constraints on seismic velocities in the Earth from travel times, *Geophys. J. Int.*, 122, 108–124.
- Keskin, M. (2003), Magma generation by slab steepening and breakoff beneath a subduction–accretion complex: an alternative model for collision-related volcanism in Eastern Anatolia, Turkey, *Geophys. Res. Lett.*, 30 (24), 8046. doi:10.1029/2003GL018019.
- Kind, R., et al. (2002), Seismic images of crust and upper mantle beneath Tibet: Evidence for Eurasian plate subduction, *Science*, 298(5596), 1219–1221, doi:10.1126/science.1078115.
- Kirby, S.H. (1983), Rheology of the lithosphere, *Rev. Geophys. Space Phys.*, 21(6), 1458–1487.
- Konert, G., A.M. Afifi, S.A. Al-Harjri, H.J. Droste (2001), Paleozoic stratigraphic and hydrocarbon habitat of the Arabian Plate, *GeoArabia*, 6, 407–442.
- Koop, W. and Stoneley, R. (1982), Subsidence history of the middle East Zagros basin, Permian to Recent, *Philosophical Transactions of the Royal Society of London* 305, 149–168.
- Kumar, P., X. Yuan, R. Kind, G. Kosarev (2005), The lithosphere-asthenosphere boundary in the Tien Shan-Karakorum region from S receiver function: Evidence for continental subduction, *Geophys. Res. Lett.*, 32, L07305, doi:10.1029/2004GL022291.
- Kumar, P., X. Yuan, R. Kind, J. Ni (2006), Imaging the colliding India and Asian lithospheric plates beneath Tibet, *J. Geophys. Res.*, 111, B06308, doi:10.1029/2005JB003930.
- Kumar, P., X. Yuan, M.R. Kumar, R. Kind, X. Li and R.K. Chadha (2007), The rapid drift of the Indian tectonic plate, *Nature*, 449.
- Kutas, R., V. P. Kobolev and V.A. Tsvyashchenko (1998), Heat flow and geothermal model of the Black Sea depression, *Tectonophysics*, 291, 91–100.
- Lachenbruch, A.H. and P. Morgan, P. (1990), Continental extension, magmatism and elevation: formal relations and rules of thumb, *Tectonophysics*, 174, 39–62.
- Lei, J. (2011), Seismic tomographic imaging of the crust and upper mantle under the central and western Tien Shan orogenic belt, *J. Geophys. Res.*, 116, B09305, doi:10.1029/2010JB008000.
- Lei, J. and D. Zhao (2007), Teleseismic P-wave tomography and the upper mantle structure of the central Tien Shan orogenic belt, *Physics of the Earth and Planetary Interiors*, 162, 165–185.
- Leloup, P.H., N. Arnaud, R. Lacassin, J.R. Kienast, T.M. Harrison, T.T.P. Trong, A. Replumaz, P. Tapponnier (2001), New constraints on the structure, thermochronology, and timing of the Ailao Shan–Red River shear zone, SE Asia, *J. Geophys. Res.* 106, 6683–6732
- Le Pichon, X., P. Henry, B. Goffée (1999), Uplift of Tibet from eclogites to granulites – implications for the Andean Plateau and the Variscan belt, *Tectonophysics*, 273, 57–76.

- Le Pichon, X., and C. Kreemer (2010), The Miocene-to-present kinematic evolution of the eastern Mediterranean and Middle East and its implications for dynamics, *Annu. Rev. Earth Planet. Sci.*, 38, 323–351.
- Lenardic, A. and L.-N. Moresi (1999), Some thoughts on the stability of cratonic lithosphere: effects of buoyancy and viscosity, *J. Geophys. Res.*, 104, B6, 12747-12758.
- Li, S., W. D. Mooney, J. Fan (2006), Crustal structure of mainland China from deep seismic sounding data, *Tectonophysics*, 420, 239–252.
- Li, Y., Q. Liu, J. Chen, S. Li, B. Guo, Y. Lai (2007), Shear wave velocity structure of the crust and upper mantle underneath the Tianshan orogenic belt, *Science in China Earth Science*, 50, 3, 321-330.
- Li, C., R. van der Hilst, A. Meltzer, E. Engdahl (2008), Subduction of the Indian lithosphere beneath the Tibet Plateau and Burma, *Earth Planet. Science Lett.*, 274, 157-168.
- Li, Y., C. Wang, C. Ma, G. Xu, and X. Zhao (2011), Balanced cross-section and crustal shortening analysis in the Tanggula-Tuotuohe Area, Northern Tibet, *J. Earth Sci.*, 22(1), 1–10, doi:10.1007/s12583-011-0152-2.
- Liang, C., X. Song, J. Huang (2004), Tomographic inversion of Pn travel times in China, *J. Geophys. Res.*, 109, B11304, doi:10.1029/2003JB002789.
- Liang, C., and X. Song, X. (2006), A low velocity belt beneath northern and eastern Tibetan Plateau from Pn tomography, *Geophys. Res. Lett.*, 33, L22306, doi:10.1029/2006GL027926.
- Liang, X., Y. Shen, Y. J. Chen, Y. Ren (2011), Crustal and mantle velocity models of southern Tibet from finite frequency tomography, *J. Geophys. Res.*, 116, B02408, doi:10.1029/2009JB007159.
- Liang, X., E. Sandvol, Y. J. Chen, T. Hearn, J. Ni, S. Klemperer, Y. Shen, F. Tilmann (2012), A complex Tibetan upper mantle: A fragmented Indian slab and no south-verging subduction of Eurasian lithosphere, *Earth Planet. Science Lett.*, 333-334, 101-111, doi:10.1016/j.epsl.2012.03.036.
- Liu S., L. Wang, C. Li, H. Li, Y. Han, C. Jia and G. Wei (2004), Thermal-rheological structure of lithosphere beneath the northern flank of Tarim Basin, western China: Implication for geodynamics, *Science in China Series D: Earth Sciences* 2004, Vol. 47, 7, 659-672.
- Liu, Z., and P. Bird (2008), Kinematic modelling of neotectonics in the Persia-Tibet-Burma orogen, *Geophys. J. Int.*, 172(2), 779 – 797, doi:10.1111/j.1365-246X.2007.03640.x.
- Lu, S.N., H.K. Li, C.L. Zhang, G.H. Niu (2008), Geological and geochronological evidence for the Precambrian evolution of the Tarim craton and surrounding continental fragments, *Precambrian Research*, 160, 94-107.
- Lucazeau, F., S. Leroy, F. Rolandone, E. d'Acremont, L. Watremez, A. Bonneville, B. Goutorbe and D. Düsünür (2010), Heat-flow and hydrothermal circulation at the ocean-continent transition of the eastern Gulf of Aden, *Earth Planet. Science Lett.*, 295. <http://dx.doi.org/10.1016/j.epsl.2010.04.039>.
- Maggi, A., J. A. Jackson, K. Priestley, and C. Baker (2000), A re-assessment of focal depth distributions in southern Iran, the Tien Shan and northern India: Do earthquakes really occur in the

- continental mantle?, *Geophys. J. Int.*, 143,629–661.
- Maggi, A. and K. Priestley (2005), Surface waveform tomography of the Turkish–Iranian plateau, *Geophys. J. Int.*, 160, 1068–1080.
- Manaman, N.S. and H. Shomali, H. (2010), Upper mantle S-velocity structure and Moho depth variations across Zagros belt, Arabian–Eurasian plate boundary, *Phys. Earth Planet. Int.*, 180, 92–103, doi:10.1016/j.pepi.2010.01.011.
- Manaman, N. S., H. Shomali and H. Koyi (2011), New constraints on upper-mantle S-velocity structure and crustal thickness of the Iranian plateau using partitioned waveform inversion, *Geophys. J. Int.*, 184, 247–267, doi:10.1111/j.1365-246X.2010.04822.x.
- Masle, G., A. Pecher, S. Guillot, S.M. Rai and A.P. Gajurel (2012), *The Himalaya-Tibet collision*, Ed. Nepal Geological Society, Societe Geologique de France, Vuibert, 264 pp.
- Masson, F., Y. Djamour, S. Van Gorp, J. Chery, M. Tatar., F. Tavakoli, H. Nankali., P. Vernant (2006), Extension in NW Iran driven by the motion of the South Caspian Basin.
- Masson, F., M. Anvari, Y. Djamour, A. Walsperdorf, F. Tavakoli, M. Daignières, H. Nankali, and S. Van Gorp (2007), Large-scale velocity field and strain tensor in Iran inferred from GPS measurements: new insight for the present-day deformation pattern within NE Iran, *Geophys. J. Int.*, 170, 436–440.
- McClusky, S., R. Reilinger, S. Mahmoud, D. B. Sari, and A. Tealeb (2003), GPS constraints on Africa (Nubia) and Arabia plate motions, *Geophys. J. Int.*, 155, 126–138, doi:10.1046/j.1365-246X.2003.02023.x.
- McDonough, W.F. and S.-s. Sun (1995), The composition of the Earth, *Chem. Geol.*, 120, 223–253.
- McKenzie, D. P. (1972), Active tectonics of the Mediterranean region, *Geophys. J. R. Astr. Soc.*, 30, 109–185.
- McNamara, D. E., W. R. Walter, T. J. Owens, and C. J. Ammon (1997), Upper mantle velocity structure beneath the Tibetan Plateau from Pn travel time tomography, *J. Geophys. Res.*, 102(B1), 493-505, doi:10.1029/96JB02112.
- McQuarrie, N. (2004), Crustal scale geometry of the Zagros fold-thrust belt, Iran. *J. Struct. Geology*, 26,519-535.
- McQuarrie, N. and D.J.J. van Hinsbergen (2013), Retro-deforming the Arabia-Eurasia collision zone: Age of collision versus magnitude of continental subduction, *Geology*, 41, 315-318.
- Meade, B.J. (2007), Present-day kinematics at the India–Asia collision zone, *Geology*, 35, 81–84.
- Mechie, J., S.V. Sobolev L. Ratschbacher, A.Y. Babeiko, G. Bock, A.G. Jones, K.D. Nelson, K.D. Solon, L.D. Brown, W. Zhao (2004), Precise temperature estimation in the Tibetan crust from seismic detection of the  $\alpha$ - $\beta$  quartz transition, *Geology*, 32, 601-604.
- Meert, J.G., M.K. Pandit, V.R. Pradhan, J., Banks, R. Sirianni, M. Stroud, B. Newstead, J. Gifford

- (2010), Precambrian crustal evolution of Peninsular India: a 3.0 billion year odyssey, *J. Asian Earth Science*, 39, 483–515.
- Mishra, D.C., M. Ravi Kumar, K. L. Arora (2012), Long wavelength satellite gravity and geoid anomalies over Himalaya, and Tibet: Lithospheric structures and seismotectonics of deep focus earthquakes of Hindu Kush–Pamir and Burmese arc, *J. Asian Earth Sci*, doi:10.1016/j.jseaes.2011.12.00.
- Mitra, S., K. Priestley, A. Kr. Bhattacharya and V. K. Gaur (2005), Crustal structure and earthquake focal depths beneath northeastern India and southern Tibet, *Geophys. J. Int.* 160, 227-248.
- Mohammadi, N., F. Sodoudi, E. Mohammadi and A. Sadidkhoy (2013), New constraints on lithospheric thickness of the Iranian plateau using converted waves, *J. Seismol.*, doi: 10.1007/s10950-013-9359-2.
- Mohadjer, S., et al. (2010), Partitioning of India-Eurasia convergence in the Pamir-HinduKush from GPS measurements, *Geophys. Res. Lett.*, 37, L04305, doi:10.1029/2009GL041737.
- Mokhtar, T.A., C.A. Ammon, R.B. Herrmann and A.A. Ghalib (2001), Surface wave velocity across Arabia, *Pure appl. Geophys.*, 158, 1425–1444.
- Molinaro, M., H. Zeyen and X. Laurencin (2005), Lithospheric structure beneath the southeastern Zagros Mountains, Iran: recent slab break-off?, *Terra Nova*, 17, 1–6.
- Molnar, P. and P. Tapponnier (1975), Cenozoic tectonics of Asia; effects of a continental collision, *Science*, 189, 419-426
- Molnar, P., P. England, J. Martinod (1993), Mantle dynamics, uplift of the Tibetan plateau and Indian monsoon, *Rev. Geophys.*, 31, 357-396.
- Monsalve, G., Sheehan, A., Schulte-Pelkum, V., Rajaure, S., Pandey, M., Wu, F., 2006. Seismicity and 1-D velocity structure of the Himalayan collision zone. *J. Geophys. Res.* 111, B10301. doi:10.1029/2005JB004062.
- Morley, C. K., B. Kongwung, A.A. Julapour, M. Abdolghafourian, M. Hajian, D. Waples, J. Warren, H. Otterdoom, K. Srisuriyon and H. Kazemi (2009), Structural development of a major late Cenozoic basin and transpressional belt in central Iran: The Central Basin in the Qom-Saveh area, *Geosphere*, 5(4), 325-362.
- Mosar, J., T. Kangarli, M. Bochud, U.A. Glasmacher, A. Rast, M.-F. Brunet, M. Sosson (2010), Cenozoic-recent tectonics and uplift in the Greater Caucasus: a perspective from Azerbaijan, *Sedimentary Basin Tectonics from the Black Sea and Caucasus to the Arabian Plateform*, Geological Society, London, Special Publications, 340, p. 161-180.
- Motavalli-Anbaran, S.-H., H. Zeyen, M.-F. Brunet and V.E. Ardestani (2011), Crustal and lithospheric structure of the Alborz Mountains, Iran, and surrounding areas from integrated geophysical modeling, *Tectonics*, 30, TC5012, doi:10.1029/2011TC002934.
- Mouthereau, F., J. Tensi, N. Bellahsen, O. Lacombe, T. De Boisgrollier and S. Kargar (2007), Tertiary sequence of deformation in a thin-skinned/thick-skinned collision belt: The Zagros Folded Belt (Fars,

- Iran), *Tectonics*, 26, TC5006, doi:10.1029/2007TC002098.
- Mouthereau, F., O. Lacombe and J. Vergés (2012), Building the Zagros collisional orogen: Timing, strain distribution and the dynamics of Arabia/ Eurasia plate convergence, *Tectonophysics*, doi:10.1016/j.tecto.2012.01.022
- Nabelek, J., G. Hetenyi, J. Vergne, S. Sapkota, B. Kafle, M. Jiang, H. Su, J. Chen, B. S. Huang, and Hi-CLIMB Team (2009), Underplating in the Himalaya-Tibet Collision Zone Revealed by the Hi-CLIMB Experiment, *Science*, 325, doi: 10.1126/science.1167719.
- Nasrabadi, A., M. Tatar, K. Priestley and M.R. Sepahvand (2008), Continental lithosphere structure beneath the Iranian plateau, from analysis of receiver functions and surface waves dispersion, 14th World Conference on Earthquake Engineering, October 12-17, 2008, Beijing, China.
- Negredo, A.M., P. Bird, C. Sanz de Galdeano, E. Buforn (2002), Neotectonic modeling of the Ibero-Maghrebian region, *J. Geophys. Res.*, 107 (B11), 2292, doi:10.1029/2001JB000743.
- Negredo, A. M., I. Jiménez-Munt, and A. Villaseñor (2004), Evidence for eastward mantle flow beneath the Caribbean plate from neotectonic modeling, *Geophys. Res. Lett.*, 31, L06615, doi:10.1029/2003GL019315.
- Negredo, A. M., A. Replumaz, A. Villaseñor, and S. Guillot (2007), Modeling the evolution of continental subduction processes in the Pamir–Hindu Kush region, *Earth Planet. Sci. Lett.*, 259, 212–225, doi:10.1016/j.epsl.2007.04.043.
- Nelson, K. D. et al. (1996), Partially molten middle crust beneath southern Tibet: Synthesis of project INDEPTH results, *Science*, 274(5293), 1684-1688, doi:10.1126/science.274.5293.1684.
- Nissen, E., M. Tatar, J. A. Jackson, and M. B. Allen (2011), New views on earthquake faulting in the Zagros fold-and-thrust belt of Iran, *Geophys. J. Int.*, 186, 928–944.
- Nowrouzi, G., M. Ghafoury, M. Ashtiany and G. Javan Doley (2007), Crustal velocity structure of northeast of central Iran and Binalud zone, using teleseismic receiver functions, *J. Earth Space phys.*, 33, 1205-8647.
- O'Reilly, S.Y., W.L. Griffin, Y.H. Poudjom-Djomani, P. Morgan (2001), Are lithospheres forever? Tracking changes in subcontinental lithospheric mantle through time, *GSA Today* 11, 4–10.
- O'Reilly, S. Y. and W.L. Griffin (2006), Imaging chemical and thermal heterogeneity in the subcontinental lithospheric mantle with garnets and xenoliths. Geophysical implications, *Tectonophysics*, 416, 289-309.
- Owens, T.J. and G. Zandt (1997), Implications of crustal property variations for models of Tibetan plateau evolution, *Nature*, 387, 37-42.
- Paul, A., A. Kaviani, D. Hatzfeld, J. Vergne and M. Mokhtari (2006), Seismological evidence for crustal-scale thrusting in the Zagros mountain belt (Iran), *Geophys. J. Int.*, 166, 227–237, doi: 10.1111/j.1365-246X.2006.02920.x.
- Paul, A., D. Hatzfeld, A. Kaviani, M. Tatar and C. Péquegnat (2010), Seismic imaging of the

- lithospheric structure of the Zagros mountain belt (Iran), *Geol. Soc. London, Spec. Pub.*, 330, 5-18.
- Pavlis, N. K., S. A. Holmes, S. C. Kenyon, J. K. Factor (2008), An Earth Gravitational Model to degree 2160: EGM2008, *Geophys. Res. Abstr.*, 10, EGU2008-A-01891.
- Pearce, J.A., Bender, J.F., De Long, S.E., Kidd, W.S.F., Low, P.J., Guner, Y., Saroglu, F., Yilmaz, Y., Moorbath, S., Mitchell, J.G., 1990. Genesis of collision volcanism in Eastern Anatolia, Turkey. *J. Volcanology and Geothermal Res.* 44, 189–229.
- Petit, C., and M. Fournier (2005), Present-day velocity and stress fields of the Amurian Plate from thin-shell finite-element modelling, *Geophys. J. Int.*, 160(1), 357–369.
- Platt, J.P. and P. England (1994), Convective removal of lithosphere beneath mountain belts: thermal and mechanical consequences, *Am. J. Science* 294, 307–336.
- Pollack, H. N., S.J. Hurter, J.R. Johnson, (1993), Heat-Flow from the Earth's Interior-Analysis of the Global Data Set, *Rev. Geophys.*, 31, 267-280, 1977.
- Pollack, H. N., S.J. Hurter and J.R. Johnson (1993), Heat-Flow from the Earth's Interior-Analysis of the Global Data Set, *Rev. Geophys.*, 31, 267-280, 1977.
- Poudjom-Djomani, Y.H., S.Y. O'Reilly, W.L. Griffin and P. Morgan (2001), The density structure of subcontinental lithosphere through time, *Earth and Planet. Science Lett.*, 184, 605-621.
- Poupinet, G., J. Avouac, M. Jiang, S. Wei, E. Kissling, G. Herquel, J. Guilbert, A. Paul, G. Wittlinger, H. Su, J. Thomas (2002), Intracontinental subduction and Palaeozoic inheritance of the lithosphere suggested by a teleseismic experiment across the Chinese Tien Shan, *Terra Nova* 14 (1), 18–24.
- Priestley, K., C. Baker, J. Jackson (1994), Implications of earthquake focal mechanism data for the active tectonics of the south Caspian basin and surrounding regions, *Geophys. J. Int.* 118, 111–141.
- Priestley, K. and D. McKenzie (2006a), The thermal structure of the lithosphere from shear wave velocities, *Earth Planet. Science Lett.*, 244, 285-301.
- Priestley, K., E. Debayle, D. McKenzie, and S. Pilidou (2006b), Upper mantle structure of eastern Asia from multimode surface waveform tomography, *J. Geophys. Res.*, 111, B10304, doi:10.1029/2005JB004082
- Priestley, K., J. Jackson, D. McKenzie (2008), Lithospheric structure and deep earthquakes beneath India, the Himalaya and southern Tibet, *Geophys. J. Int.* 172, 345–362. doi:10.1111/j.1365-246X.2007.03636.x.
- Radjaee, A., D. Rham, M. Mokhtari, M., Tatar, K. Priestley and D. Hatzfeld, D. (2010), Variation of Moho depth in the central part of the Alborz Mountains, northern Iran, *Geophys. J. Int.*, 181, 173–184.
- Rai, S., K. Priestley, V. Gaur, S. Mitra, M. Singh, M.P. Searle (2006), Configuration of the Indian Moho beneath the Northwest Himalaya and Ladakh, *Geophys. Res. Lett.*, 33, doi:10.1029/2006GL026076.
- Rajesh, R.S. and D.C. Mishra (2004), Lithospheric thickness and mechanical strength of the Indian

- shield, *Earth and Planetary Science Letters*, 225, 319-328.
- Reilinger, R., et al. (2006), GPS constraints on continental deformation in the Africa-Arabia-Eurasia continental collision zone and implications for the dynamics of plate interactions, *J. Geophys. Res.*, 111(B05411), doi:10.1029/2005JB004051.
- Ren, Y. and Y. Shen (2008), Finite frequency tomography in southeastern Tibet: Evidence for the causal relationship between mantle lithosphere delamination and the north– south trending rifts, *J. Geophys. Res.*, 113, B10316, doi:10.1029/2008JB005615.
- Replumaz, A. and P. Tapponnier (2003), Reconstruction of the deformed collision zone between India and Asia by backward motion of lithospheric blocks. *J. Geophys. Res.* 108. doi:10.1029/2001jb000661.
- Replumaz, A., A. Negredo, S. Guillot, A. Villaseñor (2010), Multiple episodes of continental subduction during India/Asia convergence: insight from seismic tomography and tectonic reconstruction, *Tectonophysics*, 483, 125–134.
- Replumaz, A., F. Capitanio, S. Guillot, A. Negredo, A. Villaseñor (2014), The coupling of Indian subduction and Asian continental tectonics, *Gondwana Research*, <http://dx.doi.org/10.1016/j.gr.2014.04.003>
- Rezaei-Kahkhaei, M., A. Kananian, D. Esmaily, and A. Asiabanha (2010), Geochemistry of the Zargoli granite: Implications for development of the Sistan Suture Zone, southeastern Iran, *Isl. Arc*, 19, 259–276, doi:10.1111/j.1440-1738.2009.00704.x
- Ritzwoller, M.H., N.M. Shapiro, M.P. Barmin and A.L. Levshin (2002), Global surface wave diffraction tomography, *J. Geophys. Res.*, 107 (B12), 2335.
- Rizaoglu, T., O. Parlak, V. Höck, F. Koller, W. E. Hames, and Z. Billor (2009), Andean-type active margin formation in the eastern Taurides: Geochemical and geochronological evidence from the baskil granitoid (Elazig, SE Turkey), *Tectonophysics*, 473(1–2), 188–207, doi:10.1016/j.tecto.2008.08.011
- Robert, X., P. van der Beek, J. Braun, C. Perry, M. Dubille and J.-L. Mugnier (2009), Assessing Quaternary reactivation of the Main Central thrust zone (central Nepal Himalaya): New thermochronologic data and numerical modelling, *Geology*, August 2009; v. 37; no. 8; p. 731–734; doi: 10.1130/G25736A.1.
- Robert, A., J. Letouzey, C. Müller, M. Kavooosi, J. Vergés, S. Sherkati and A. Aghababei (2014), Structural evolution of the Kopeh Dagh fold-and-thrust belt (NE Iran) and interactions with the South Caspian and Amu Darya basins, *J. Marine and Petroleum Geology*, 57, 68-87.
- Robert, A., M. Fernandez, I. Jiménez-Munt, J. Vergés (2015), Lithospheric structures in Central Eurasia derived from elevation, geoid anomaly and thermal analysis, *J. Geol. Soc. London Spec. Pub.* (in press).
- Robinson, D.M., R.G. DeCelles, P.J. Patchett, C.N. Garzzone (2001), The kinematic evolution of the Nepalese Himalaya interpreted from Nd isotopes, *Earth Planet. Science Lett.*, 192, 507–521.
- Rolandone, F., F. Lucazeau, S. Leroy, J.-C. Mareschal, R. Jorand, B. Goutorbe, and H. Bouquerel

- (2013), New heat flow measurements in Oman and the thermal state of the Arabian Shield and Platform, *Tectonophysics*, 589, 77-89.
- Royden, L. H., B. C. Burchfiel, and R. D. Van der Hilst (2008), The Geological Evolution of the Tibetan Plateau, *Science*, 321, 1054-1058.
- Sandvol, E., D. Seber, M. Barazangi, F. Vernon, R. Mellors and A. Al-Amri (1998), Lithospheric seismic velocity discontinuities beneath the Arabian shield, *Geophys. Res. Lett.*, 25, (15), 287–2876.
- Sandwell, D. T. and H.W.F. Smith (1997), Marine gravity anomalies from GEOSAT and ERS-1 satellite altimetry, *J. Geophys. Res.*, 102, 10,039–10,054.
- Saura, E., J. Verges, S. Homke, E. Blanc, J. Serra-Kiel, G. Bernaola, E. Casciello, N. Fernandez, I. Romaire, G. Casini, J.C. Embry, I.R. Sharp and D.W. Hunt (2011), Basin architecture and growth folding of the NW Zagros early foreland basin during the Late Cretaceous and early Tertiary, *Journal of the Geological Society*, 168(1): 235-250.
- Schmidt, J., B. R. Hacker, L. Ratschbacher, K. Stübner, M. Stearns, A. Kylander-Clark, J. M. Cottle, A. A. G. Webb, G. Gehrels, and V. Minaev (2011), Cenozoic deep crust in the Pamir, *Earth and Planetary Science Letters*, 312(3-4), 411–421, doi:10.1016/j.epsl.2011.10.034
- Schulte-Pelkum, V., G. Monsalve, A. Sheehan et al. (2005), Imaging the Indian subcontinent beneath the Himalaya, *Nature*, 435, 1222-1225.
- Schurr, B., Ratschbacher L., Sippl C., Gloaguen R., Yuan X., and Mechie J., 2014, Seismotectonics of the Pamir, AGU, accepted.
- Schwab, M., L. Ratschbacher, W. Siebel, M. McWilliams, V. Minaev, V. Lutkov, F. Chen, K. Stanek, B. Nelson, W. Frisch, and J. L. Wooden (2004), Assembly of the Pamirs: Age and origin of magmatic belts from the southern Tien Shan to the southern Pamirs and their relation to Tibet, *Tectonics*, 23(4), TC4002, doi:10.1029/2003TC001583.
- Searle M.P. (2010), Geological evolution of the Karakoram ranges, *Ital. J. Geosci. Boll. Soc. Geol. It.*, Vol. 130, No. 2, pp. 147-159, DOI: 10.3301/IJG.2011.08.
- Searle, M. P., D. J. W. Cooper, A. J. Rex, Eveline Herren, A. J. Rex and M. Colchen (1988), Collision Tectonics of the Ladakh--Zaskar Himalaya [and Discussion]. Source: Vol. 326, No. 1589, *Tectonic Evolution of the Himalayas and Tibet* (Sep. 1, 1988), pp. 117-150 Published by: The Royal Society Stable.
- Sella, G. F., T. H. Dixon and A. Mao (2002), REVEL: A model for recent plate velocities from space geodesy, *J. Geophys. Res.*, 107(B4), 2081, doi:10.1029/2000JB000033.
- Sengör, A.M.C., D. Altiner, A. Cin, T. Ustaomer and K.J. Hsu (1988), Origin and assembly of the Tethyside orogenic collage at the expense of Gondwana Land, *Geol. Soc. London, Spec. Pub.* 37, 119–181.
- Sengör, A. M. C., S. Özeren, R. Genc, and E. Zor (2003), East Anatolian high plateau as a mantle-supported, north-south shortened domal structure, *Geophys. Res. Lett.*, 30(24), 8045, doi:10.1029/2003GL017858.

- Sepehr, M. and J.W. Cosgrove (2004), Structural framework of the Zagros Fold-Thrust Belt, Iran, *Marine and Petroleum Geol.*, 21, 7, 829-843.
- Shen, Z.-K., C. Zhao, A. Yin, Y. Li, D.D. Jackson, P. Fang and D. Dong (2000), Contemporary crustal deformation in east Asia constrained by Global Positioning System measurements, *J. Geophys. Res.*, 105, 5721– 5734.
- Shen, F., L.H. Royden and B.C. Burchfiel (2001), Large-scale crustal deformation of the Tibetan Plateau, *J. Geophys. Res.*, 106, 6793- 6816.
- Sherkati, S., Y. Letouzey and D. Frizon de Lamotte (2006), Central Zagros fold-thrust belt (Iran): New insights from seismic data, field observation and sandbox modeling, *Tectonics*, 25, TC4007, doi:10.1029/2004TC001766, 27 pp.
- Shervais, J.W. (2001), Birth, death, and resurrection: the life cycle of suprasubduction zone ophiolites, *Geochem., Geophys., Geosyst.*, 2, 1525-2027.
- Shi, R.D., W.L. Griffin, S.Y. O'Reilly, G.C. Zhao, Q.S. Huang, J. Li, J.F. Xu (2010), Evolution of the Lüliangshan peridotites in the North Qaidam UHP belt, Northern Tibetan Plateau: Constraints from Re-Os isotopes, *Lithos*, 117, 307-321.
- Shin, Y.H., H. Xu, C. Braitenberg, J. Fang, Y. Wang (2007), Moho undulations beneath Tibet from GRACE-integrated gravity data, *Geophys. J. Int.*, 170 (3), 971–985.
- Shin, Y.H., C.-K. Shum, C. Braitenberg, S. M. Lee, H. Xu, K. S. Choi, J. H. Baek and J. U. (2009), Three-dimensional fold structure of the Tibetan Moho from GRACE gravity data, *Geophys. Res. Lett.*, 36, L01302, doi:10.1029/2008GL036068.
- Shomali, Z.H., F. Keshvari, J. Hassanzadeh and N. Mirzaei (2011), Lithospheric structure beneath the Zagros collision zone resolved by non-linear teleseismic tomography, *Geophys. J. Int.*, 187 (1), 394–406, doi:10.1111/j.1365-246X.2011.05150.x.
- Shubert, G., D.L. Turcotte, P. Olson (2001), *Mantle convection in the Earth and planets*, 940 pp, Cambridge University Press, U.K.
- Simmons, N.A., S.C. Myers and G. Johannesson (2011), Global-scale P wave tomography optimized for prediction of teleseismic and regional travel times for Middle East events: 2. Tomographic inversion, *J. Geophys Res.* 116: (B04305), doi:10.1029/ 2010jb007969.
- Smit, H.W., S. Cloetingh, E. Burov, M. Tesauro, D. Sokoutis, M. Kaban (2013), Interference of lithospheric folding in western Central Asia by simultaneous Indian and Arabian plate indentation, *Tectonophysics*, 602, 176-193.
- Snyder, D. B. and M. Barazangi (1986), Deep crustal structure and flexure of the Arabian Plate beneath the Zagros collisional mountain belt as inferred from gravity observations, *Tectonics*, 5 (3), 361-373.
- Socquet, A., C. Vigny, N. Chamot-Rooke, W. Simons, C. Rangin, and B. Ambrosius (2006), India and Sunda plates motion and deformation along their boundary in Myanmar determined by GPS, *J. Geophys. Res.*, 111, B05406, doi:10.1029/2005JB003877

- Soudoudi, F., X. Yuan, R. Kind, B. Heit and A. Sadidkhouy (2009), Evidence for a missing crustal root and a thin lithosphere beneath the Central Alborz by receiver function studies, *Geophys. J. Int.*, 177, 733–742, doi:10.1111/j.1365-246X.2009.04115.x.
- Song, S.G., L. Su, Y.L. Niu, L.F. Zhang (2007), Petrological and geochemical constraints on the origin of garnet peridotite in the North Qaidam ultrahigh-pressure Metamorphic Belt, Northwestern China, *Lithos*, 96, 243–265.
- Spratt, J.E., A.G. Jones, K.D. Nelson, M.J. Unsworth and INDEPTH MT Team (2005), Crustal structure of the India–Asia collision zone, southern Tibet, from INDEPTH MT investigations, *Physics of the Earth and Planetary Interiors*, 150, 227–237.
- Stern, R.J., and M.G. Abdelsalam (1998), Formation of juvenile continental crust in the Arabian–Nubian shield: evidence from granitic rocks of the Nakasib suture, NE Sudan, *Geol. Rundsch.* 76, 150–160.
- Stern, R.J. and A. Kröner (1993), Late Precambrian crustal evolution in NE Sudan: isotopic and geochronological constraints, *J. Geol.* 101, 555–574.
- Stern, R.J. and P.R. Johnson (2008), Do variations in Arabian plate lithospheric structure control deformation in the Arabian–Eurasian convergence zone? Donald D. Harrington Symposium on the Geology of the Aegean. IOP Conf. Series, Earth & Environ. Science, 2, doi:10.1088/1755-1307/2/1/012005
- Stern, R. J. and P. Johnson (2010), Continental lithosphere of the Arabian plate: A geologic, petrologic, and geophysical synthesis, *Earth Science Rev.*, 101, 29–67, doi:10.1016/j.earscirev.2010.01.002.
- Su, B-X., S-L. Chung, M.H. Zarrinkoub, K-N. Pang, L. Chen, W-Q. Ji, A. Brewer, J-F. Ying and M.M. Kathib (2014), Composition and structure of the lithospheric mantle beneath NE-Iran: Constraints from mantle xenoliths, *Lithos*, 202-203, 267-282.
- Talebian, M., and J. Jackson (2004), A reappraisal of earthquake focal mechanisms and active shortening in the Zagros mountains of Iran, *Geophys. J. Int.*, 156, 506–526.
- Talwani, M., J. Worzel, and L. Landisman (1959), Rapid computations for two-dimensional bodies with application to the Mendocino submarine fracture zone, *J. Geophys. Res.*, 64, 49–59.
- Tapponnier, P., M. Mattauer, J.-N. Proust, and C. Cassaigneau (1981), Mesozoic ophiolites, sutures, and large-scale tectonic movements in Afghanistan, *Earth Planet. Science Lett.*, 52, 355–371, doi:10.1016/0012-821X(81)90189-8
- Tapponnier, P., X. Zhiqin, F. Roger, B. Meyer, N. Arnaud, G. Wittlinger, Y. Jingsui (2001), Oblique stepwise rise and growth of the Tibet Plateau, *Science*, 294 (5547), 1671–1677, doi:10.1126/science.105978.
- Tatar, M., D. Hatzfeld, and M. Ghafory-Ashtiany (2004), Tectonics of the Central Zagros (Iran) deduced from microearthquake seismicity, *Geophys. J. Int.*, 156, 255–266.
- Tavakoli, F., A. Walpersdorf, C. Authemayou, H.R. Nankali, D. Hatzfeld, M. Tatar, Y. Djamour, F.

- Nilforoushan, N. Cotte (2008), Distribution of the right-lateral strike slip motion from the Main Recent Fault to the Kazerun Fault System (Zagros, Iran): evidence from present-day GPS velocities, *Earth planet. Sci. Lett.*, 275, 342–347.
- Taylor, M., and A. Yin (2009), Active structures of the Himalayan-Tibetan orogen and their relationships to earthquake distribution, contemporary strain field, and Cenozoic volcanism, *Geosphere*, 5(3), 199–214, doi:10.1130/GES00217.1.
- Tilmann, F., J. Ni, and INDEPTH III Seismic Team (2003), Seismic imaging of the downwelling Indian lithosphere beneath central Tibet, *Science*, 300, 1424–1427, doi:10.1126/science.1082777.
- Tunini, L., I. Jiménez-Munt, M. Fernandez, J. Vergés, A. Villaseñor (2015), Lithospheric mantle heterogeneities below the Zagros Mountains and the Iranian Plateau: a petrological-geophysical study, *Geophys. J. Int.*, 200, 596–614.
- Tunini, L., I. Jiménez-Munt, M. Fernandez, J. Vergés, A. Villaseñor, A., J.C. Afonso, Looking at the roots of the highest mountains: the lithospheric structure of the Himalaya-Tibetan orogen from a geophysical-petrological study, under review in *Tectonics*.
- Turcotte, D. L., and G. Schubert (1982), *Geodynamics: Applications of Continuum Physics to Geological Problems*, John Wiley, New York.
- Unsworth, M., W. Wenbo, A. G. Jones, S. Li, P. Bedrosian, J. Booker, J. Sheng, D. Ming, and T. Handong (2004), Crustal and upper mantle structure of northern Tibet imaged with magnetotelluric data, *J. Geophys. Res.*, 109, B02403, doi:10.1029/2002JB002305.
- van Hinsbergen, D. J. J., P. Kapp, G. Dupont-Nivet, P. C. Lippert, P. G. DeCelles, and T. H. Torsvik (2011), Restoration of Cenozoic deformation in Asia and the size of Greater India, *Tectonics*, 30, TC5003, doi:10.1029/2011TC002908.
- Vergés, J., E. Saura, E., Casciello, M. Fernandez, A. Villaseñor, I. Jiménez-Munt and D. García-Castellanos (2011), Crustal-scale cross-section across the NW Zagros Belt: implications for the Arabian Margin reconstruction, in: *Geodynamic Evolution of the Zagros*, Lacombe, O., Grasemann, B., Simpson, G. (Eds.), *Geological Magazine*, 148, 739–761 (5–6).
- Vergnolle, M., E. Calais, and L. Dong (2007), Dynamics of continental deformation in Asia, *J. Geophys. Res.*, 112, B11403, doi:10.1029/2006JB004807
- Vernant, P., F. Nilforoushan, D. Hatzfeld, M.R. Abbassi, C. Vigny, F. Masson, H. Nankali, J. Martinod, A. Ashtiani, R. Bayer, F. Tavakoli, J. Chery (2004), Present-day crustal deformation and plate kinematics in the Middle East constrained by GPS measurements in Iran and northern Oman, *Geophys. J. Int.*, 157, 381–398.
- Vigny, C., A. Socquet, C. Rangin, N. Chamot-Rooke, M. Pubellier, M. Bouin, G. Bertrand, and M. Becker (2003), Present-day crustal deformation around Sagaing fault, Myanmar, *J. Geophys. Res.*, 108(B11), 2533, doi:10.1029/2002JB001999.
- Vilà, M., M. Fernandez, I. Jiménez-Munt (2010), Radiogenic heat production variability of some common lithological groups and its significance to lithospheric thermal modeling, *Tectonophysics*, 490, 152–164, doi:10.1016/j.tecto.2010.05.003.

- Villaseñor, A., M.H. Ritzwoller, A.L. Levshin, M.P. Barmin, E.R. Engdahl, W. Spakman and J. Trampert J. (2001), Shear velocity structure of central Eurasia from inversion of surface wave velocities, *Phys. Earth Planet. Int.*, 123, 169-184.
- Villaseñor, A., W. Spakman, E.R. Engdahl (2003), Influence of regional travel times in global tomographic models, *EGS-AGU-EUG Joint Assembly, Nice*.
- Vinnik, L. P., C. Reigber, I. M. Aleshin, G. L. Koserev, M. K. Kaban, S. I. Oreshin, S.W. Roecker (2004), Receiver function tomography of the central Tien Shan, *Earth Planet. Science Lett.*, 225, 131–146, doi:10.1016/j.epsl.2004.05.039
- Vozar, J., A. G. Jones, J. Fulla, M. R. Agius, S. Lebedev, F. Le Pape, W. Wei (2014), Integrated geophysical-petrological modeling of lithosphere-asthenosphere boundary in central Tibet using electromagnetic and seismic data, *Geochem. Geophys., Geosys.*, 15, doi: 10.1002/2014GC005365.
- Wang, Y. (2001), Heat flow pattern and lateral variations of lithosphere strength in China mainland: constraints on active deformation, *Physics of the Earth and Planetary Interiors*, 126, 121-146.
- Wang, Q., P.-Z. Zhang, J. T. Freymueller, R. Bilham, K. M. Larson, X. Lai, X. You, Z. Niu, J. Wu, Y. Li, J. Liu, Z. Yang, Q. Chen (2001), Present-day crustal deformation in China constrained by Global Positioning System measurements, *Science*, 294, 574–577, doi:10.1126/science.1063647.
- Wang, Y., W. D. Mooney, X. Yuan, R. G. Coleman (2003), The crustal structure from the Altai Mountains to the Altyn Tagh fault, northwest China, *J. Geophys. Res.*, 108(B6), 2322, doi:10.1029/2001JB000552.
- Wang, T. K., S.F. Lin, C.S. Lin, C.S. Wang (2004), Crustal structure of the southernmost Ryukyu subduction zone: OBS, MCS and gravity modeling, *Geophys. J. Int.*, 157, 147-163.
- Wang, T., D.W. Hong, B.M. Jahn, Y. Tong, Y.B. Wang, B.F. Han, X.X. Wang (2006), Zircon U-Pb geochronology and geochemistry of Paleozoic synorogenic intrusions from the Chinese Altai: implications for subduction–accretion processes, *J. Geology*, 114, 735–751.
- Watremez, L., E. Burov, E., d'Acrmont, S. Leroy, B. Huet, L. Le Pourhiet, N. Bellahsen (2013), Buoyancy and localizing properties of continental mantle lithosphere: Insights from thermomechanical models of the eastern Gulf of Aden, *Geochem., Geophys., Geosyst.*, 14, doi: 10.1002/ggge.20179.
- Wessel, P., and W. H. F. Smith (1995), New version of the Generic Mapping Tools released, *Eos Trans. AGU*, 76, 329, doi:10.1029/95EO00198
- Wittlinger, G., V. Farra, and J. Vergne (2004), Lithospheric and upper mantle stratifications beneath Tibet: New insights from Sp conversions, *Geophys. Res. Lett.*, 31, L19615, doi:10.1029/2004GL020955.
- Xiao, Q., G. Zhao, and Z. Dong (2011), Electrical resistivity structure at the northern margin of the Tibetan Plateau and tectonic implications, *J. Geophys. Res.*, 116, B12401, doi:10.1029/2010JB008163.
- Xu, Y.-G., X. Wei, Z.-Y. Luo, H.-Q. Liu, J. Cao, (2014) The Early Permian Tarim Large Igneous

- Province: Main characteristics and a plume incubation model, *Lithos*, <http://dx.doi.org/10.1016/j.lithos.2014.02.015>
- Yin, A., and T. M. Harrison (2000), Geologic evolution of the Himalayan-Tibetan orogen, *Annu. Rev. Earth Planet. Science*, 28, 211-280.
- Yin, A. (2006), Cenozoic tectonic evolution of the Himalayan orogen as constrained by along-strike variation of structural geometry, exhumation history, and foreland sedimentation, *Earth Sci. Rev.*, 76, 1-131.
- Yin, An (2009), Cenozoic tectonic evolution of Asia: A preliminary synthesis, *Tectonophysics*, doi:10.1016/j.tecto.2009.06.002
- Yuan, H. and B. Romanowicz (2010), Lithospheric layering in the North American craton. *Nature*, 466,1063-1068.
- Yue, H., X. J. Chen, E. Sandvol, J. Ni, T. Hearn, S. Zhou, Y. Feng, Z. Ge, A. Trujillo, Y. Wang, G. Jin, M. Jiang, Y. Tang, X. Liang, S. Wei, H. Wang, W. Fan, Z. Liu (2012), Lithospheric and upper mantle structure of the northeastern Tibetan Plateau, *J. Geophys. Res.*, 117, B05307, doi:10.1029/2011JB008545.
- Zarifi, Z., F. Nilfouroushan and M. Raeesi (2013), Crustal Stress Map of Iran: Insight From Seismic and Geodetic Computations, *Pure Appl. Geophys.* DOI 10.1007/s00024-013-0711-9
- Zarrinkoub, M.H., S.L. Chung, H.Y. Chiu, S. Mohammadi, M. Khatib, I.J. Lin (2010), Zircon U–Pb age and geochemical constraints from the northern Sistan suture zone on the Neotethyan magmatic and tectonic evolution in eastern Iran, *Abst. to GSA Conference on “Tectonic Crossroads: Evolving Orogens in Eurasia–Africa–Arabia”*. Ankara, Turkey.
- Zeyen, H. and M. Fernandez (1994), Integrated lithospheric modeling combining thermal, gravity, and local isostasy analysis: Application to the NE Spanish Geotranssect, *J. Geophys. Res.*, 99, 18,089 – 18,102.
- Zeyen, H., P. Ayarza, M. Fernandez and A. Rimi (2005), Lithospheric structure under the western African-European plate boundary: A transect across the Atlas Mountains and the Gulf of Cadiz, *Tectonics*, 24, TC2001, doi:10.1029/2004TC001639
- Zhang, Y.Q., J.-L. Mercier and P. Vergely (1998), Extension in the graben systems around the Ordos (China), and its contribution to the extrusion tectonics of south China with respect to Gobi-Mongolia, *Tectonophysics*, 285, 41–75.
- Zhang, P.-Z., Z. Shen, M. Wang, W. Gan, R. Bürgmann, P. Molnar, Q. Wang, Z. Niu, J. Sun, J. Wu, S. Hanrong, Y. Xinzhao (2004), Continuous deformation of the Tibetan Plateau from global positioning system data, *Geology*, 32, 809– 812, doi:10.1130/G20554.1.
- Zhang, Z.-J. and S.L. Klemperer (2005), West-east variation in crustal thickness in northern Lhasa block, central Tibet, from deep seismic sounding data, *J. Geophys. Res.*, 110, B09403, doi:10.1029/2004JB003139, pp.14
- Zhang, Y., J. Liu, Z. Guo (2010), Permian basaltic rocks in the Tarim basin, NW China: Implications

for plume–lithosphere interaction, *Gondwana Research*, 18, 596–610.

Zhang Z., S. Klemperer, Z. Bai, Y. Chen, J. Teng (2011), Crustal structure of the Paleozoic Kunlun orogeny from an active-source seismic profile between Moba and Guide in East Tibet, China, *Gondwana Research*, 19, 994-1007.

Zhang, H., D. Zhao, J. Zhao, Q. Xu (2012), Convergence of the Indian and Eurasian plates under eastern Tibet revealed by seismic tomography, *Geochem. Geophys. Geosyst.*, 13, Q06W14, doi:10.1029/2012GC004031.

Zhang, C.L., M. Santosh, H.B. Zou, Y.G. Xu, G. Zou, Y.G. Dong, R.F. Ding, H.Y. Wang (2012b), Revisiting the “Irtish tectonic belt”: implications for the Paleozoic evolution of the Altaid orogen, *J. Asian Earth Sciences*, 53, 117–133.

Zhang, C.-L. and H. Zou (2013), Comparison between the Permian mafic dykes in Tarim and the western part of Central Asian Orogenic Belt (CAOB), NW China: Implications for two mantle domains of the Permian Tarim Large Igneous Province, *Lithos* 174 (2013) 15–27.

Zhao, W., K. D. Nelson, J. Che, J. Quo, D. Lu, C. Wu, and X. Liu (1993), Deep seismic reflection evidence for continental underthrusting beneath southern Tibet, *Nature*, 366, 557-559, doi:10.1038/366557a0.

Zhao J., G. Liu, Z. Lu, X. Zhang, G. Zhao G. (2003), Lithospheric structure and dynamic processes of the Tianshan orogenic belt and the Junggar basin, *Tectonophysics*, 376, 199-239.

Zhao, J. M., X. Yuan, H. Liu, P. Kumar, S. Pei, R. Kind, Z. Zhang, J. Teng, L. Ding, X. Gao, Q. Xu, Q. Wang (2010), The boundary between the Indian and Asian tectonic plates below Tibet, *Proc. Natl. Acad. Science U. S. A.*, 107(25), 11,229–11,233, doi:10.1073/pnas.1001921107.

Zhao, W. J., P. Kumar, J. Mechie, R. Kind, R. Meissner, Z. Wu, D. Shi, H. Su, G. Xue, M. Karplus, F. Tilmann (2011), Tibetan plate overriding the Asian plate in central and northern Tibet, *Nat. Geosci.*, 4,870–873, doi:10.1038/ngeo1309.

Zheng, J., S.Y. O’Reilly, W.L. Griffin, F. Lu, M. Zhang, N.J. Pearson (2001), Relict refractory mantle beneath the eastern North China block: significance for the lithosphere evolution, *Lithos*, 57, 43–66.

Zheng, J., W. L. Griffin, S. Y. O’Reilly, M. Zhang, N. J. Pearson, and Z. Luo (2006), The lithospheric mantle beneath the southern Tianshan area, NW China, *Contrib. Mineral. Petrol.*, 151, 457–479.

Zhou, H. and M. A. Murphy (2005), Tomographic evidence for wholesale under- thrusting of India beneath the entire Tibetan plateau. *Journal of Asian Earth Sciences*, 25, 445–457.

Ziman, J.M. (1962), *Electrons and Phonons: The Theory of Transport Phenomena in Solids*, Clarendon Press, Oxford (Ch. 8 and 11), pp. 1-554